THE 2009 NNIN REU RESEARCH ACCOMPLISH~ MENTS

NNIN

Nanoscale Science, Engineering & Technology

The National Nanotechnology Infrastructure Network Research Experience for Undergraduates (NNIN REU) Program

Table of Contents

2009 NNIN REU Research Accomplishments

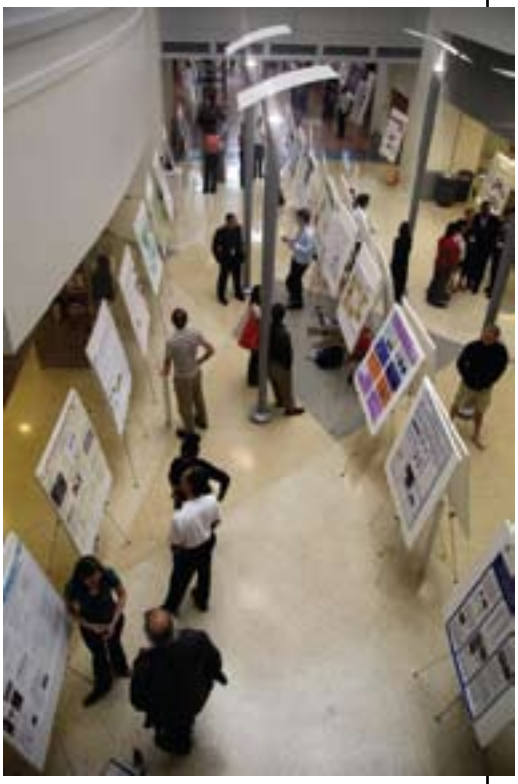

Photography Credits:

***COVER: Axel Palmstrom**, NNIN REU at UMinn, report on page 146*

*Table of Contents, Welcome, and Interns by Site Photos: **Edward Tang, Photographer***
(Edward is above right with Amanda Oehrlein, CNF REU)

The National Nanotechnology Infrastructure Network

www.nnin.org

is comprised of the following fourteen sites, supported by The National Science Foundation, the NNIN sites, our corporate sponsors and research users.

ASU NanoFab
Arizona State University
Ira A. Fulton School of Engineering
PO Box 876206 • Tempe, AZ 85287-6206
(480) 965-3808 • http://www.fulton.asu.edu/nanofab/

Cornell NanoScale Science & Technology Facility
Cornell University
250 Duffield Hall • Ithaca, NY 14853-2700
(607) 255-2329 • http://www.cnf.cornell.edu

Nanotechnology Research Center
Georgia Institute of Technology
791 Atlantic Dr NW • Atlanta, GA 30332-0269
(404) 385-4307 • http://www.mirc.gatech.edu/

Center for Nanoscale Systems
Harvard University
11 Oxford Street, LISE 306 • Cambridge, MA 02138
(617) 384-7411 • http://www.cns.fas.harvard.edu

Howard Nanoscale Science & Engineering Facility
Howard University
2300 6th St NW • Washington, DC 20059
(202) 806-6618 • http://www.msrce.howard.edu/

Penn State Nanofabrication Laboratory
The Pennsylvania State University
188 Materials Research Institute • University Park, PA 16802
(814) 865-3303 • http://www.mri.psu.edu/facilities/nnin/

Stanford Nanofabrication Facility
Stanford University
P.G. Allen Bldg, Rm 303x, 420 Via Palou • Stanford, CA 94305
(650) 725-3607 • http://snf.stanford.edu/

Nanotech@UCSB
University of California, Santa Barbara
ECE 1109E Engineering Sciences Bldg
Santa Barbara, CA 93106-9560
(805) 893-5999 • http://www.nanotech.ucsb.edu/

Colorado Nanofabrication Laboratory
University of Colorado at Boulder
ECEE Campus Box 425 • Boulder, CO 80309-0425
(303) 492-2809 • http://cnl.colorado.edu/

Lurie Nanofabrication Facility
The University of Michigan, Ann Arbor
1239 EECS 1301 Beal Ave • Ann Arbor, MI 48109-2122
(734) 763-6719 • www.lnf.umich.edu

Nanofabrication Center
University of Minnesota-Twin Cities
1-165 ECE Bldg 200 Union St SE • Minneapolis, MN 55455
(612) 625-3069 • http://www.nfc.umn.edu/

Microelectronics Research Center
The University of Texas at Austin
J.J. Pickle Research Campus • 10100 Burnet Rd, Bldg 160
Austin, TX 78758
(512) 471-6730 • http://www.mrc.utexas.edu/

Center for Nanotechnology
University of Washington
Box 352140 • Seattle, WA 98195-1721
(206) 616-9760 • http://www.nano.washington.edu/

Nano Research Facility
Washington University in St. Louis
Campus Box 1180, One Brookings Drive
Earth & Planetary Sciences Bldg 188, Danforth Campus
St. Louis, MO 63130-4899
(314) 935-8893 • http://www.nano.wustl.edu/

2009 NNIN REU Corporate Sponsors

Advanced Micro Devices
Agilent Technologies
Analog Devices
Applied Materials
Canon
Daihen Corporation
Ebara Corporation
Ericsson
Hewlett-Packard Company
Hitachi, Ltd
IBM Corporation
Infineon
Intel Corporation
Intel Foundation
LG Electronics, Incorporated
National Semiconductor Corporation
NEC Corporation
NXP Semiconductors
Olympus Corporation
Panasonic
Qualcomm
Renesas Technology Corporation
Robert Bosch Corporation
Seiko Epson Corporation
Sony Corporation
STMicroelectronics
Texas Instruments, Incorporated
Toshiba

Welcome from Prof. Sandip Tiwari NNIN Director

The 2009 NNIN REU Interns at the network-wide convocation, University of Michigan, August 2009

The summer of 2009 was quite a successful time for the NNIN and its two REU programs. Seventy-four students participated in our Research Experience for Undergraduates (REU) Program, and 10 students, from the 2008 NNIN REU Program, participated in our International Research Experience for Undergraduates (iREU) Program.

This publication reflects the hard work of our interns, but also the dedication of the principal investigators, mentors, program coordinators and site staff. Taking on the challenge of completing comprehensive experimental research in ten weeks can be a very formative and defining experience for everyone involved, most especially the undergraduate intern. Our programs test the many skills of learning and applying that learning, and help determine the course of a student's life at a very critical stage when one is coming into one's own.

NNIN attempts to provide such an experience by bringing strong collaborations and interesting research problems in which undergraduate students can participate. Many of our interns get their first taste of advanced hands-on research as part of our program, and we work diligently to make this a positive experience; focusing on advanced research and knowledge, seeking strong mentors and staff support, exposing our interns to a professional research environment, and having high expectations built into the research projects, the convocation, and the final reports included here. In addition, we expect that at each site, students will enjoy the wider variety of research conducted by peers and other users across diverse disciplines of science and engineering within the unifying facilities.

My thanks to the staff, the graduate student mentors and the faculty for their participation and involvement. Particular thanks are due to Melanie-Claire Mallison and Lynn Rathbun at Cornell University, and Nancy Healy at Georgia Institute of Technology for their contributions in organizing the logistics of both programs, and many thanks to Sandrine Martin, Trasa Burkhardt and Brandon Lucas at the University of Michigan for organizing the August convocation.

I wish all our program participants the best wishes for future technical careers; the NNIN hopes to see you build on this summer's experience! Please keep in touch!

Sandip Tiwari
Director, NNIN
st222@cornell.edu

Intern Reports; Quick Reference

2009 NNIN REU Interns at Arizona State University

2009 NNIN REU Interns at Cornell University

2009 NNIN REU Interns at Georgia Tech

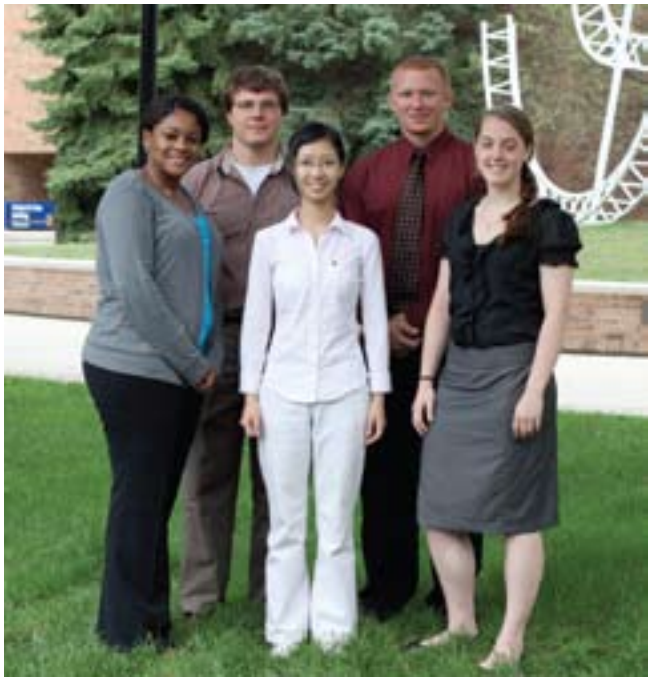

2009 NNIN REU Interns at Harvard University

2009 NNIN REU Interns at Howard University

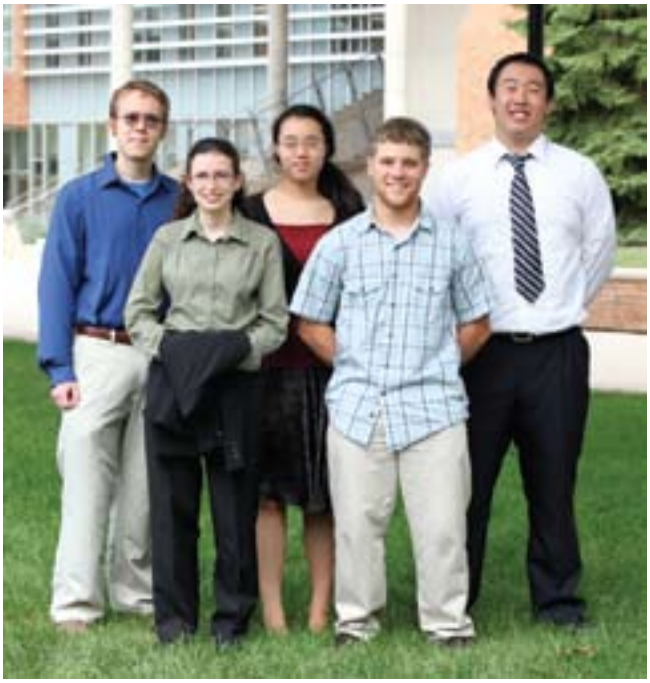

2009 NNIN REU Interns at the Pennsylvania State University

2009 NNIN REU Interns at Stanford University

2009 NNIN REU Interns at the University of California, Santa Barbara

2009 NNIN REU Interns at the University of Colorado

2009 NNIN REU Interns at the University of Michigan

2009 NNIN REU Interns at the University of Minnesota

2009 NNIN REU Interns at the University of Texas at Austin

2009 NNIN REU Interns at the University of Washington

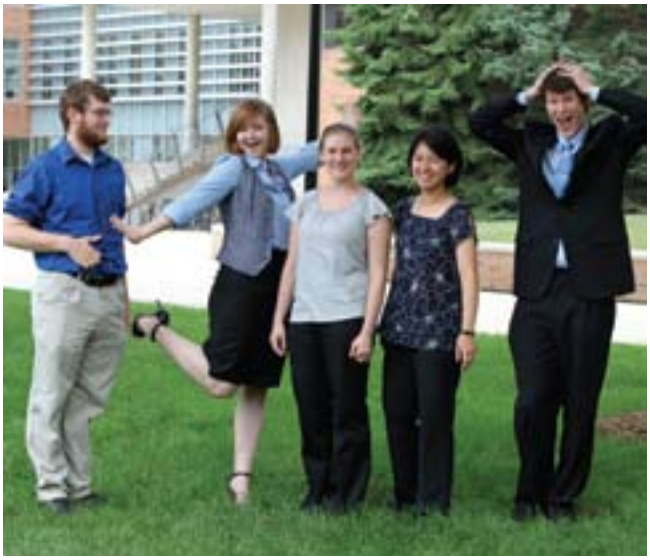

2009 NNIN REU Interns at Washington University in St. Louis

Traveling to Japan was my first time abroad—I was ecstatic to find out I was going and I started getting prepared to work and live in another society. It was an exciting prospect to get to see the parts of Japanese culture I had heard about previously, like sushi (my favorite), sake, wandering around central Tokyo, and visiting lots of shrines and temples. Seeing the world is something I have always wished to do, and getting to stay for three months in a foreign country was really a unique opportunity.

Living in Japan is like being on another planet—I had a conversation with another foreign researcher about how amazing it is that our societies have evolved so differently, but still, each manages to get along fine. I chose the Japan site both for the research and to get a taste of a society that's very orthogonal to our own. It's hard to convey in words how different things are, and how staying for more than a few weeks allows one to get a real taste of the culture. While I was there, there was a wide spectrum of emotions I felt, from excitement and amazement, to bafflement, and even sometimes loneliness. What was always constant was having new experiences every week travelling around greater Tokyo, Kyoto, Nagoya, Nara and other areas, experiencing plenty of what Japan had to offer.

Reflecting back, it really was one of those unique experiences one has in life that you always cherish and wish you could get back... running through subways to chase the last train out of Tokyo, stuffing ourselves at Hama-zushi, waterfall jumping in Minakami, crossing the bridge in Uji, singing 2Pac at karaoke, and boating on Lake Biwa with Sakaki-san. I really cannot do justice to how life changing it was—with how fond I had grown of our group of interns and all the fun we had. When our time was up, I found it poignantly difficult to leave this place to which I had become so attached. Well-rested after returning, I can't wait to go back. I wholeheartedly recommend the whole iREU experience in Japan.

Best, David Christle

The NNIN International Research Experience for Undergraduates was amazing. Living in Julich was a great way to experience life in a small German town and meet other international students. Acclimating to the weather and lifestyle in Julich was easy and I felt at home quickly.

Conducting research at the Institute for Bio- and Nanosystems, I was exposed to the forefront of nanotechnology research. There were a wide variety of graduate students with different scientific backgrounds, from all parts of the world that I could rely on for help with my research. Forschungszentrum is a friendly and professional work place where I felt that I could not only research my assigned project, but explore other subjects as well.

Being placed in the center of Europe put me in close proximity to many famous countries and cities. Using the train system was a convenient and affordable means of transportation when I traveled over the summer, namely to Amsterdam, Bruges, Zurich, Paris, Prague, and Munich. Traveling to all these cities, I learned a great deal of the history of Europe and met many interesting people from all over the world.

Jose Guevarra, Mechanical Engineering, UCSB

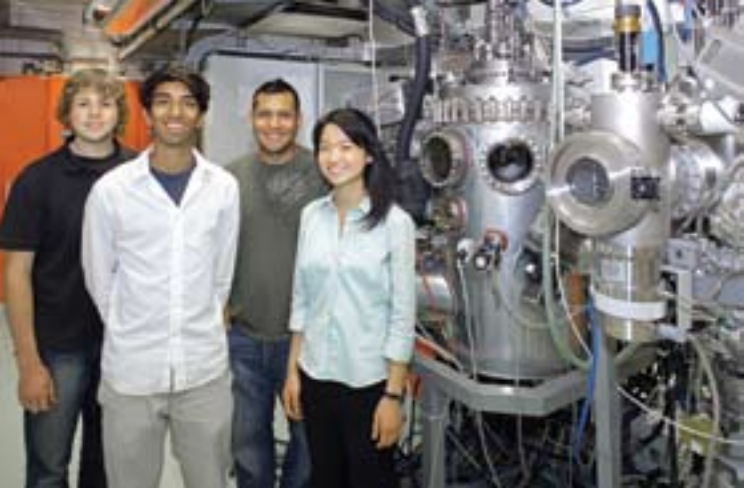

Photography Credits:

The photographs on these two iREU pages were taken by various members of the 2009 NNIN iREU Program

Having never been to Europe, I knew that my summer internship would definitely be enlightening. However, I never imagined that I would be able to weave together my research and travel experiences so well. During the weekdays, I was an international researcher, working on cutting edge technology. On the weekends, I was a country-trotting traveler, exploring the culture of Europe's greatest cities.

The central location of Jülich enabled us to easily traverse, by train, most of Europe, from nearby Paris to faraway Prague. Having a "home base" let us follow a "one weekend, one city" philosophy throughout the summer. This gave us the advantage of recharging ourselves during the week all while getting roused up for the upcoming weekend.

However, the most illuminating experiences came from submerging myself in the work environment of the research center. Despite the fact that science is considered a universal language, there were still cultural differences that made the summer very interesting, e.g., unusually long coffee breaks! After a summer of conferences, presentations, collaborations, and discussions, it dawned on me how truly global the research community is. The scientists in Germany, and other countries, were conducting research just as innovative and relevant as that conducted in the U.S. It definitely opened up the realm of possibilities for my research career. All in all, it was a very successful summer!

Kishore Padmaraju, University of Rochester

A summer in Japan inevitably brings about a wide variety of experiences. Over the 80 days of my summer, I went mountain biking in the Japanese Alps, saw a sumo tournament in Nagoya and a geisha performance in the Gion district, watched a traditional Japanese drumming performance, and experienced my first earthquake. The food was another experience in and of itself. Sea urchin sushi, as it turns out, is one of the more disgusting things I've ever tasted. Raw horse meat, on the other hand, is surprisingly palatable. But beyond the weekly trips and adventurous dinners, it wasn't all fun and glory. There were seemingly endless difficulties of adjusting to a new culture. Sometimes, just figuring out how to dry my clothes or how to order at a restaurant seemed like an insurmountable challenge. But I'd like to think that the frustrations of the perpetual language barrier and cultural differences were well worth it. Without a doubt, I've come out of this summer with a greater understanding of myself and my own strengths and limitations, as well as increased cultural awareness and sensitivity.

Jillian Kiser, M.Eng., Olin College of Engineering

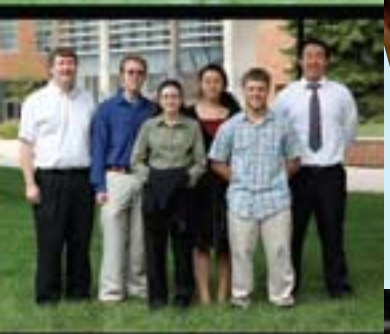

The NNIN REU Program Coordinators wish to thank everyone for a successful summer!

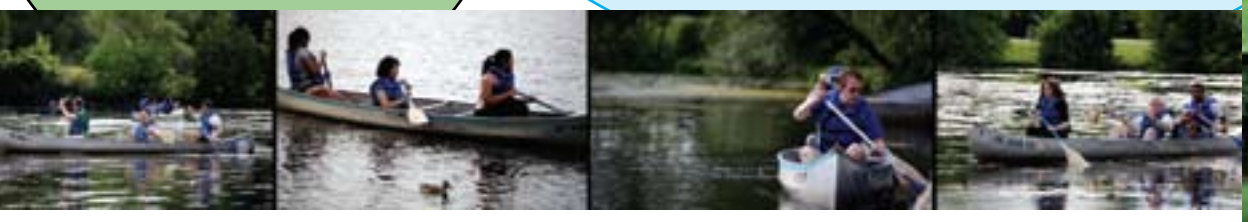

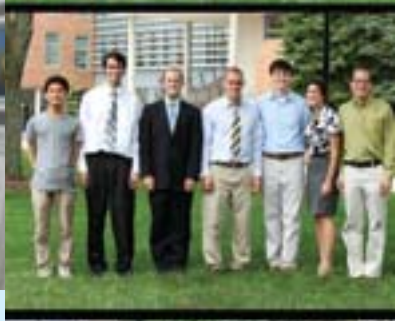

The National Nanotechnology Infrastructure Network

Research Experience for Undergraduates (NNIN REU) Program

2009 Research Accomplishments

Role of Reactive Oxygen Species in Nanotoxicity

Sarah Connolly
Biochemistry/Microbiology, University of Florida

NNIN REU Site: Nanofabrication Center, University of Minnesota-Twin Cities, Minneapolis, MN
NNIN REU Principal Investigator(s): Dr. Christy Haynes, Chemistry, University of Minnesota
NNIN REU Mentor(s): Melissa Maurer-Jones, Chemistry, University of Minnesota
Contact: sarahsconnolly@ufl.edu, chaynes@umn.edu, jone1317@umn.edu

Abstract:

Though the emergence of the nanotechnology field has increased the incorporation of nanomaterials into commercially available products, we have limited understanding of how its widespread applications can affect us personally. This project focused on observing the presence of reactive oxygen species (ROS) in mouse fibroblast model cells when exposed to nano-titanium dioxide ($nTiO_2$) utilizing various fluorescent probe assays including 4-((9-acridinecarbonyl) amino)-2,2,6,6-tetramethylpiperidin-1-oxyl (TEMPO-9-AC) and 2',7'-dichlorodihydrofluorescein diacetate (H_2DCFDA). ROS can cause oxidative stress in cells, which may lead to cell dysfunction, mutation, or death. Cellular uptake of the nanoparticles was studied using inductively coupled plasma-atomic emission spectroscopy (ICP-AES) analysis to correlate ROS generation with cellular internalization of $nTiO_2$, followed by a commonly used cellular viability assay which showed insignificant difference in cell viability; the elevated uptake and increased ROS levels may have harmful effects on cell function of living cells.

Experimental Procedure:

Anatase titanium dioxide nanoparticles were made by a sol-gel synthesis using isopropyl alcohol and titanium isopropoxide that were stirred and chilled for 30 minutes while a nitric acid catalyst was added; then the mixture was refluxed for 24 hours. Samples were dialyzed over a 5-10 day period followed by aging in an acid digestion bomb for 48 hours in a 200°C oven. Finally, the aged nanoparticle suspension was washed with ethyl alcohol and dried [1]. Nanoparticles were characterized using x-ray diffraction to determine their crystalline structure, dynamic light scattering to determine particle aggregation, and transmission electron microscopy to determine particle size.

ICP-AES was performed to quantify the number of nanoparticles internalized by cells after incubation with $nTiO_2$ at a concentration of 100 μg/ml for 24, 48, and 72 hours. Cells were rinsed three times with PBS and removed from the Petri® dish using trypsin enzyme. The Petri dish was scraped and the trypsin-cell suspension was put in a centrifuge tube with 1 mL of 2:1 H_2SO_4:HNO_3 digest solution in 3 mL H_2O and sonicated for one hour.

For the fluorescent assays, 3T3 mouse fibroblasts were plated in a clear bottom 96-well plate at a density of 10^4-10^5 cells/well and exposed to the fluorescent probe. TEMPO detects superoxide and hydroxyl radical while H_2DCFDA detects superoxide, hydroxyl radical, peroxyl radical, and singlet oxygen. After a one hour incubation period with the fluorescent probe, the probe was removed and the cells were rinsed once with PBS. Cells were then exposed to $nTiO_2$ at various concentrations (12.5, 25, 50, 100, 200, and 400 μg/ml) for 24 and 48 hours. For the positive controls, malachite green—a superoxide and hydroxyl radical generator, and rose bengal—a singlet oxygen generator, were used. After incubation, the $nTiO_2$ and media were removed, cells rinsed twice with PBS, and a uniform volume of PBS added to each well. Fluorescence intensity was then measured with a fluorescent plate reader.

An MTT (3-(4,5-dimethylthiazol-2-yl)-2,5-diphenyltetrazolium bromide) assay was performed in 24 well plates to assess cell viability. 3T3 cells were again incubated with the various concentrations of $nTiO_2$ listed above, for 24, 48, and 72 hours. Following incubation, the media and $nTiO_2$ were removed, cells rinsed three times with PBS, and incubated with MTT in cell media for two hours. The MTT was removed and DMSO was added to each well to dissolve the formazan crystals. After 20 minutes, optical density was measured at λ = 570 nm, and the absorbance was correlated to the percentage of viable cells.

Results and Conclusions:

Results from ICP analysis (Figure 1) show that the longer the cells were exposed to $nTiO_2$, the more nanoparticles the cells internalized. We hypothesized that longer incubation time, and more cellular internalization of $nTiO_2$, would lead to more ROS generation.

Linear regression analysis of our fluorescent probe assays (Figures 2 and 3) showed that there was a significant

increase in ROS as the concentration of $nTiO_2$ increased, leading us to assume greater oxidative stress on the cell and to hypothesize that this would lead to a decrease in cellular viability. However, statistical analysis (by student t-testing) shows that there is no significant difference between 24 and 48 hour incubation times, meaning that our previous hypothesis about longer incubation correlating to increased ROS production is false. In the future, we would like to extend incubation times past 48 hours, as this might show a more obvious trend.

Results from the cell viability assay (Figure 4) show statistically insignificant change in cell viability. This means that the increased concentration of $nTiO_2$, as well as varying exposure times, is not killing the cells, negating our hypothesis.

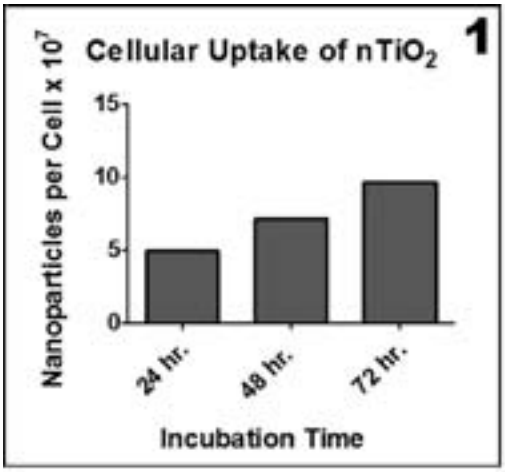

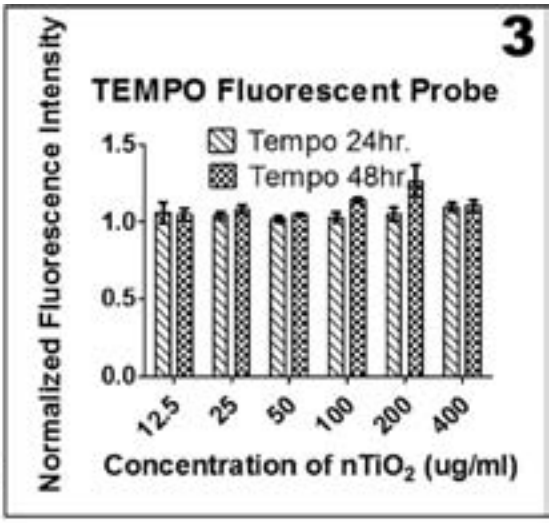

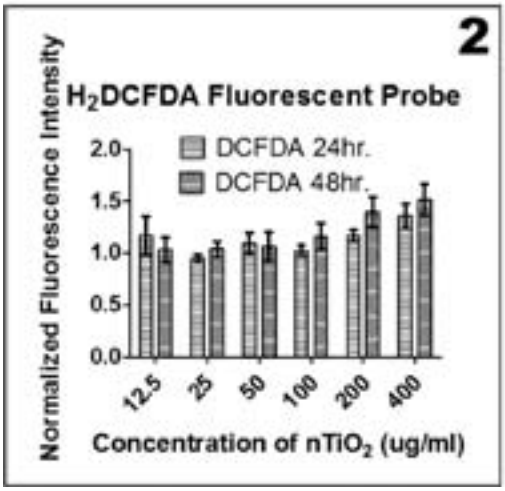

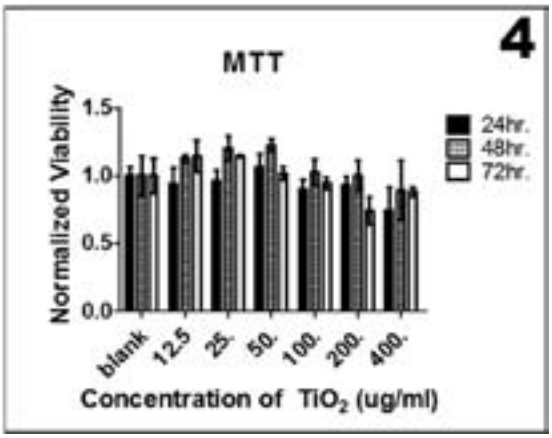

Figure 1: Cellular internalization of $nTiO_2$ increases with incubation time.

Figure 2: Increase in fluorescence intensity indicates an increase in ROS production as $nTiO_2$ concentration increases.

Figure 3: Linear regression analysis shows significant increase in fluorescence intensity as $nTiO_2$ concentration increases.

Figure 4: There is no significant decrease in cell viability over time or as concentration of $nTiO_2$ increases.

Future Work:

We would like to compare these results to those of similar assays performed on the immortalized mast cell line rat basophilic leukemia (RBL) cells. Mast cells play a critical role in immune response, and thus are an interesting, relevant cell for nanotoxicity studies.

Amperometry studies are currently underway to determine the effects of ROS on cell exocytosis. The results of these experiments will allow us to make predictions about overall cell health and function due to the internalization of $nTiO_2$ and increased amounts of ROS generated.

Acknowledgements:

I would like to thank Dr. Christy Haynes, Melissa Maurer-Jones, and the Haynes Research Group for kindly sharing their lab with me and patiently mentoring me. Also, I would like to thank Dr. Doug Ernie, Dr. Bruce Wollenberg, Becky von Dissen, Brooke Myhre, and Melanie-Claire Mallison for their time spent organizing this REU program. Finally, I would like to thank the National Nanotechnology Infrastructure Network Research Experience for Undergraduates Program for this opportunity and the National Science Foundation for funding.

References:

[1] Titanium Dioxide Nanoparticles: Effect of Sol-Gel pH on Phase Composition, Particle Size, and Particle Growth Mechanism, S. L. Isley and R. L. Penn (2008), Journal of Physical Chemistry C, 112, 4469-4474.

Microfluidic Single-Cell Assay Chip for Drug Efficacy Test

Nicolas Andrew Shillingford-Cordero
Microbiology, Cornell University

NNIN REU Site: Lurie Nanofabrication Facility, University of Michigan, Ann Arbor, MI
NNIN REU Principal Investigator(s): Euisik Yoon, Electrical Engineering, University of Michigan
NNIN REU Mentor(s): Xia Lou, Electrical Engineering, University of Michigan
Contact: nac56@cornell.edu, esyoon@umich.edu, xialou@umich.edu

Abstract:

Single-cell resolution assays incomparably increase the power of drug screens over conventional colorimetric assays by providing quantitative data. Assays of this class avoid cell-to-cell interactions present in traditional bulk sampling procedures; these interactions can mask nuances where individual cells are concerned, invariably causing rich amounts of information to be overlooked. Advances in microfluidic technology have allowed high throughput single-cell drug screens to be performed while exercising precise control over cell loading and culturing conditions with relatively insignificant amounts of expensive samples and reagents used. This project focused on optimizing the design and operation of our drug screening platform for single-cells and neurospheres. Microfluidic chips were fabricated via polydimethylsiloxane (PDMS) replication and bonding. Glioblastoma multiforme (GBM) cells—stained with green fluorescent protein (GFP)—were then introduced to the devices and, upon their capture within individual microwells, cultured to the neurosphere stage while being subjected to drug screens alongside control groups. Significant statistical data of cell viability can be obtained when the starting single-cell number in the chip is greater than 100 and after these cells have been cultured in the chip for at least five days.

Introduction:

Cell-based biological assays, such as drug screens, are notorious for frequently providing the mean data across an entire population of cells, despite the now ubiquitous knowledge that isolated cells, even those belonging to related cell lines, portray extremely diverse properties [1]. Advancements in microfluidic single-cell assay technologies provide biologists with a media through which they can tackle the most adamant challenges.

The quest for finding the cure to cancer is as much a race against time as it is against money, but by utilizing the properties of microfluidic PDMS chips the burden on humanity and on its coffers can be significantly reduced. These inexpensive chips can be used to segregate cells into discrete compartments, allowing many types of quantitative assays to be performed. This project focuses on optimizing the design and operation of a microfluidic single-cell drug screening platform for GBM cells.

Currently, GBM is the most common type of primary brain tumor and only palliative treatments exist. With this design, it is possible to culture single GBM cells to the neurosphere stage, allowing drug screens to account for the aging of cells, something previously unaccomplished. This design further prevents cell-to-cell interactions by providing a constant flow of fresh medium over the cells.

Microfluidic Chip Fabrication and Preparation. Photolithography of SU-8 on silicon wafers was used to create

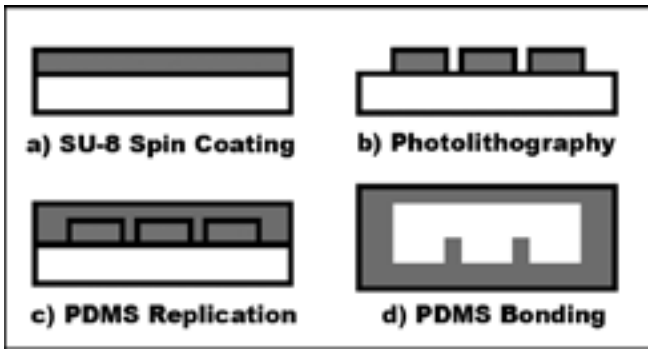

Figure 1, top: Microfluidic PDMS chip fabrication.
Figure 2, bottom: Microfluidic PDMS chip.

master molds for the channel (top) and microwell (bottom) halves of the PDMS chips (Figure 1). Input and output holes were punched into the channel half of a PDMS chip and then the two halves were treated with oxygen plasma and bonded (Figure 2). Cell-free medium was inserted at the input (80 μL) and output (40 μL) wells of the chip which was then degassed in a vacuum chamber to flush air bubbles from the channels.

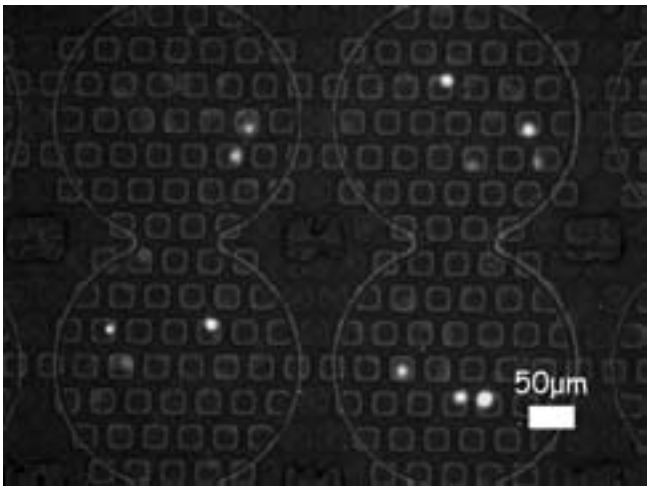

Figure 3: GBM single-cells.

Cell-Loading Procedure. The GBM neurospheres in the cell-containing medium were then manually disassociated to single-cells using a micropipette. The cell-free medium was removed from the input and output wells of the chip; cell-containing medium (80 μL) was then inserted at the input well. The medium was allowed to flow for 10 minutes before being removed from both wells; the cells in the microfluidic chip were allowed to settle for three minutes. The chip was then inspected with ultraviolet light (10X magnification) for neurospheres stuck in the channels, which were removed by providing negative pressure at the output well via pipette bubble suction. The single-cell captures were then counted manually (Figure 3). If the chip contained less than 100 single-cell captures, more cell-containing medium (80 μL) was inserted at the input well and the process was repeated until at least 100 cells were captured.

Drug Screening. Once 100 cells were captured, the cells were subjected to drug screens. For the control group, cell-free medium (80 μL) was injected into the inlets and the cells were cultured for more than five days while being subjected to a continuous flow of fresh medium from inlet to outlet via gravity difference. Chips were kept in an incubator set at 37°C, 5% CO_2 and 90% RH; fresh medium was replaced and cell viability recorded via GFP staining every 12 hours. For the treatment group, cell-free medium containing the drug (GSI) was used instead. Statistics were obtained for cell viability.

Results and Discussion:

The cell-loading procedure was first optimized using microbeads (15 μm) of similar size to GBM cells (Figure 4). The microbeads were most efficiently captured with the following: channel height, 22 μm; microwell diameter, 20 μm, microwell depth, 26 μm; bead concentration, 2.75 × 10^6 beads/mL. For the GBM cells, slight dimensional tweaking was required to compensate for the cells' affinity to each other: channel height, 37 μm; microwell diameter, 30 μm; microwell depth, 26 μm. As in the microbead experiments, the cell-loading procedure was most efficient when a high concentration of cells (greater than 10^6 cells/mL) was used, with which capturing over 100 cells became trivial. Preliminary drug screenings were unsuccessful at distinguishing a significant difference between viability in control (34.74%) and treatment group cells (34.84%). More frequent medium changes may be necessary for future screenings.

Acknowledgements:

Infinite gratitude goes to Professor Euisik Yoon and his research group for taking me as an intern and to Xia Lou for the fantastic mentoring that will be forever useful in future endeavors. Great thanks to Dr. Tom Bersano for his assistance with the cell-loading procedure. Much appreciation to the National Nanotechnology Infrastructure Network Research Undergraduate Experience Program, the National Science Foundation, and the wonderful staff at the Lurie Nanofabrication Facility for giving this biologist a taste of engineering.

References:

[1] Sims, C. E., and N. L. Allbritton. "Analysis of single mammalian cells on-chip". Lab on a Chip, 7, 423-440 (2007).

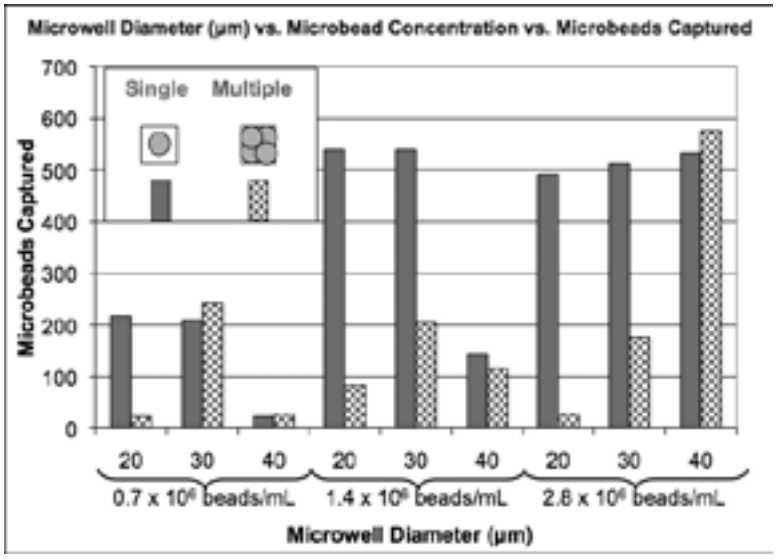

Figure 4: Optimization of microbead capture.

Nanotextured Surfaces: New Generation Bioelectronic Interfaces for Nanomedicine

Ericka Cottman

Electrical Engineering, Virginia Commonwealth University

NNIN REU Site: ASU NanoFab, Arizona State University, Tempe, AZ

NNIN REU Principal Investigator(s): Dr. Jennifer Blain Christen, Electrical Engineering, Arizona State University

NNIN REU Mentor(s): David Welch, BioEngineering, Arizona State University

Contact: cottmaner@vcu.edu, jennifer.blainchristen@asu.edu, djwelch1@asu.edu

Abstract:

Bioelectronics is a field of study that contributes to a growing intersection between nanostructures and nanomedicine. One application is using nanostructures for interfacing cells. This can help improve standard signal measurements from cells on a two-dimensional electrode array by using a nanotextured electrode surface instead. Nanotexturing increases the surface area to improve the adhesion of cells to electrodes and provides a more efficient electrical interface. We used a porous alumina membrane as a template to provide uniform nano-scale pores for electrodeposition of gold onto two-dimensional arrays of gold electrodes. We performed extensive characterization of electrodeposition parameters including, current density, deposition rate, nanorod uniformity, and experimental repeatability. Finally, we cultured HL-1 cardiomyocytes on the nanotextured gold arrays and characterized morphology, adhesion, and proliferation rate. These experiments confirmed our ability to culture electrically active cells on nanotextured gold electrodes.

Experimental Procedure:

We fabricated two-dimensional electrode arrays for nanotexturing using standard microfabrication techniques. The lithography was performed on glass substrates using a mask with electrodes and wires leading to bond pads. A 10 nm adhesion layer of chrome was deposited on the glass followed by a 100 nm layer of gold with the Edwards #2 thermal evaporator. Lift-off, agitating the substrate in acetone, patterned the chrome and gold.

The gold electrode array was modified using electro-deposition. Our experimental setup is illustrated in Figure 2. The electrical parameters for the deposition were controlled using a potentiostat. We built this circuit on a proto-board using two operational amplifiers, a resistor, and three electrodes operated using a power supply and a computer-controlled source measurement unit [1]. The potentiostat is used to monitor and control electrochemical reactions utilizing three electrodes. The counter electrode (CE) is used to apply a current, the reference electrode (RE) gives the solution a "chemical ground" and the working electrode (WE) allows for current flow. The counter and reference electrodes go into the solution, but they can be shorted together since they are at the same potential. The working electrode makes electrical contact with the bond pads on the patterned gold substrate. The glass slide patterned with gold was placed in between the two Teflon® cylinders, the top one containing CE, RE, and the ionic solution; this completes the circuit allowing current to flow. The electrodeposition performed with this setup is an electrochemical method for driving gold cations toward an electrode in solution. Potassium aurocyanide ($KAu(CN)_2$) was the gold ion solution placed in the electrochemical cell. Within the solution, the current

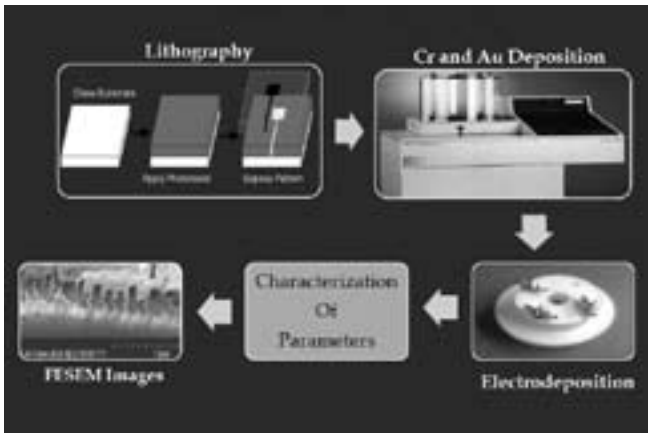

Figure 1, above: Process overview: lithography, deposition, electrodeposition, parameters characterized, and FESEM images.

Figure 2, below: Electrodeposition experimental setup includes: potentiostat circuit, three electrodes, membrane on patterned gold substrate, and potassium aurocyanide.

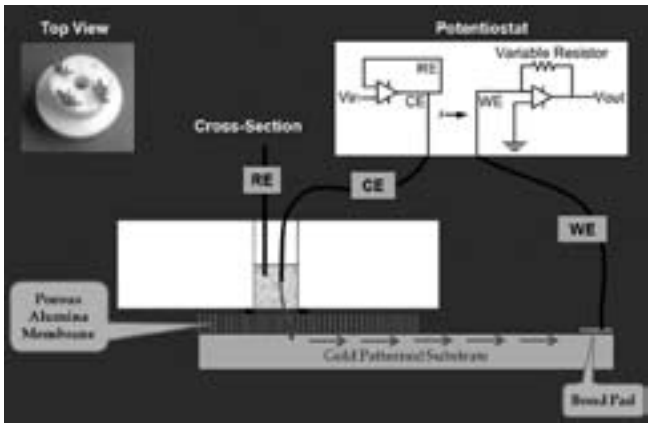

flow described is the movement of gold cations toward the patterned gold electrodes forming the deposited gold.

A porous alumina membrane was used as a template for the nanorod growth. The membrane is 40 μm thick and has pores with a 200 nanometer diameter. When placed above the electrode array as shown in the Figure 2, the flow of cations was restricted to the pore interior. Current flows through the pores of membrane then to the electrodes, resulting in the precipitation of gold within the pores. This results in the deposition of the 200 nm diameter gold rods with thickness depending on experimental parameters. This creates free-standing gold rods once the membrane is dissolved with sodium hydroxide.

Results and Conclusion:

One of our goals for this research was to correlate many experimental parameters with the resulting nanorod growth characteristics. We were able to use a MATLAB program for controlling the potentiostat to systematically vary the following experimental parameters: voltage, time, sampling rate, gain, and experimental run number using our potentiostat control function. All of the experiments were monitored in real-time using MATLAB plots of voltage vs. time, current vs. time, and total charge vs. time.

A wide array of experiments were performed, and we used an Excel spreadsheet to record the parameters described above, the substrate patterning and membrane use. Our experimental runs included deposition onto a gold surface with and without the membrane and gold electrodes with and without a membrane. Initial experiments allowed us to verify the complete experimental setup and determine the appropriate values for experimental parameters. We performed a total of 32 experiments, each with a different set of experimental conditions.

We used a Dektak II profilometer and a field emission scanning electron microscope (FESEM) to verify nanorod thickness and appearance. The profilometer allowed us to measure the film thicknesses. The FESEM allowed us to obtain high magnification images of our nanorods. A single row of nanorods is shown in Figure 3; the top image has a wide view of the sample at 35,000X and the bottom image focuses on the nanorods at an increased magnification of 50,000X. These images verify that the nanorods have dimensions consistent with the pore geometry in the membranes. Since we had to break the substrate to obtain a sample small enough for the FESEM, the nanorods were damaged in the process.

Ultimately we were able to culture HL-1 cardiomyocytes on the gold nanorod arrays. HL-1 cells are an electrically active cardiac cell line derived from rats. A transmitted light image was taken of the cells on the gold electrodes as seen in Figure 4. We were able to demonstrate the growth and viability of the cells on the nanorod electrodes surface. In addition we verified excellent cell adhesion, normal morphology and standard proliferation rate. Further testing will be required for a comparative study of the adhesion characteristics.

Acknowledgments:

This would not have been possible without the funding of National Science Foundation and National Nanotechnology Infrastructure Network. Melanie-Claire Mallison and Trevor Thornton were very helpful and did an awesome job. Dr. Jennifer Blain Christen, my Principal Investigator, was wonderful and her level of involvement enhanced my experience. My mentors David Welch and Steve Herman were dedicated to helping me with my research. I will never forget this experience because I learned a lot about research and graduate school from the perspective of professors and students. Thanks again!!!

References:

[1] Choi, E; "The Silicon Chip: A Versatile Micro-Scale Platform for Micro and Nano-Scale Systems"; John Hopkins University, Thesis, 1-177(2008).

[2] Moon, J and Wei, A; "Uniform Gold Nanorod Arrays from Polyethylenimine-coated Alumina Templates"; J Phys Chem B, 109(49), 23336-23341 (2005).

[3] Evan P, Hendren W, Atkinson R , Wurtz G, Dickson W, Zayats and Pollard R; "Growth and Properties of gold and nickel nanorods in thin film alumina"; Nanotechnology, 17(2006), 5746-5753 (2006).

[4] Martin, C; "Nanomaterials: A Membrane-Based Synthetic Approach"; Science, 266, 1961-1965 (1994).

[5] Lu, G and Zhao; "Nanoporous Materials: An Overview"; Science and Engineering, Chapter 1, 1-12 (2004).

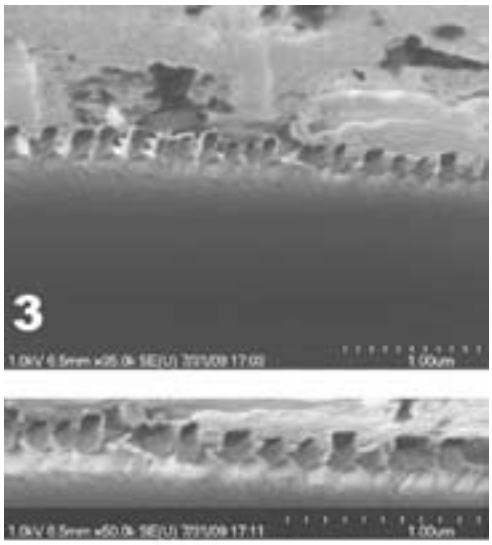

Figure 3: FESEM images; single line of gold nanorods at 35,000X and 50,000X magnification.

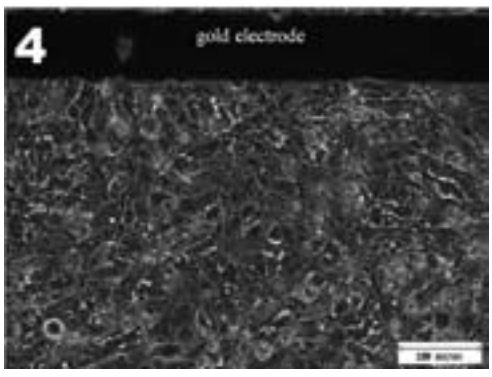

Figure 4: Phase contrast image of cultured HL-1 cardiomyocytes on Au nanorods.

Nanoporous Surfaces: Bioelectric Interfaces for Pathogen Detection

Lilian Gong

Biochemistry, Wellesley College

NNIN REU Site: ASU NanoFab, Arizona State University, Tempe, AZ

NNIN REU Principal Investigator(s): Shalini Prasad, Electrical, Computer, & Energy Engr, Arizona State University

NNIN REU Mentor(s): Gaurav Chatterjee, Srivatsa Aithal, ECEE, Arizona State University

Contact: lgong@wellesely.edu, shalini.prasad.1@asu.edu, gaurav.chatterjee@asu.edu, srivatsa.aithal@asu.edu

Abstract:

The goal of this project was to build a biosensor to detect low concentrations of pathogens [1]. The purity of a liquid depends on the pathogens that contaminate it. We used a label free technique, which uses electrochemical impedance spectroscopy (EIS). By keeping our methods label free, detecting pathogens is cheaper and less time consuming, as compared to conventional methods. We used a printed circuit board (PCB) based-device and an alumina membrane to generate a nanoporous surface. By overlaying the membrane on top of the interdigitated electrodes of the PCB, a high-density array of nanowells was formed, which facilitated nano-confinement and allowed for size based trapping of the pathogens. We used layer-by-layer chemistry. The membrane was functionalized such that the cationic polymer attached to the membrane. The endotoxin, being anionic, bound to the cationic polymer, forming an electrical double layer. The variations in the impedance of the electrical double layer due to the changes in the concentrations of the pathogen were characterized using EIS. We have identified the performance parameters of the biosensor for pathogen detection.

Introduction:

Testing the quality of drinking water for bacterial contamination is important because by testing for low concentrations of pathogens, many illnesses that are contracted via polluted water, such as cholera, can be avoided [2].

This summer we embarked on the first steps of building the said biosensor that would be portable, fast, and cost efficient. This was accomplished by using a label free technique, electrochemical impedance spectroscopy (EIS). In order to use EIS to characterize the impedance changes that occurred for different concentrations of endotoxins, layer-by-layer chemistry was used to modulate the charge in the electrical double layer at the solid/liquid interface, which allowed us to detect specific stepwise changes in impedance, that occur for the different dose concentrations of the endotoxin.

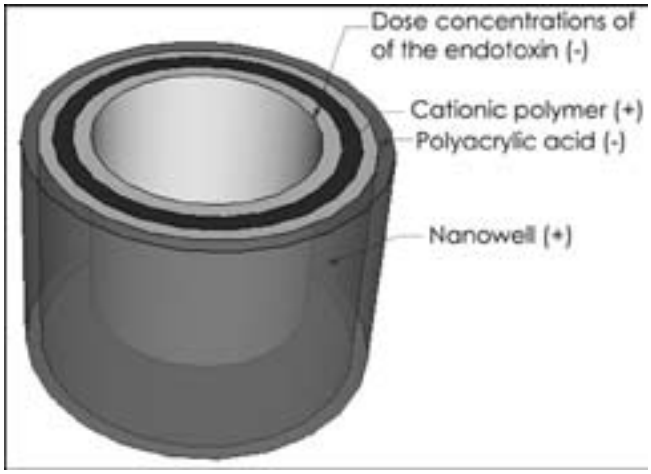

Figure 1: Layer-by-layer chemistry.

Materials/Methods:

The materials used include an alumina membrane with a nanoporous surface, polyacrylic acid (PAA), a cationic polymer, and an endotoxin (Lipopolysaccaride, LPS). Having an alumina membrane with pores that have an upper diameter of 200 nm and a lower diameter is 20 nm was crucial because when the membrane is placed on top of the interdigitated electrodes, it forms a high-density array of nanowells, which facilitate nano-confinement of the cationic polymer and allow for size based trapping of the endotoxin. Size matching is important because it allows for an increase in the binding efficacy of the endotoxin, which amplifies the signal. Layer-by-layer chemistry [3], which was used to create an electrical double layer, was accomplished by first functionalizing the nanoporous membrane with PAA. PAA was used as an adhesion layer between the alumina membrane and the cationic polymer. The endotoxin was the final layer added. This is illustrated in Figure 1.

When all the species bind together, they create an electrical double layer. The electrical double layer acts like capacitance. As the capacitance changes, so does the impedance of the system. Electrochemical impedance spectroscopy (EIS) [4] was used to characterize the system by measuring the change in impedance that occurred at different frequencies. This was accomplished by applying a voltage across a range of frequencies, measuring current, and calculating

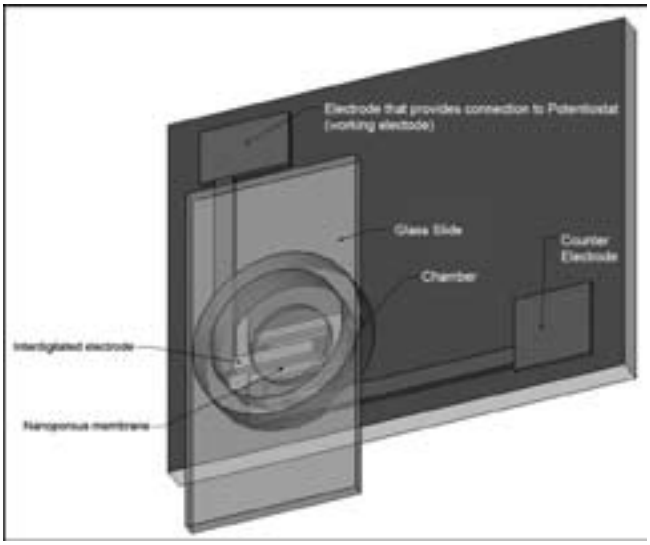

Figure 2: Experimental set-up.

the impedance at each frequency. This is called frequency response. When the frequency response is obtained for different doses, it is called the dose response. Figure 2 shows the experimental setup.

Results:

There were two experiments conducted, one with PEI-25, and the other with NPGDE 1,5 BIS. PEI-25 is a commercially available polymer, which was used to establish the concept. NPGDE is a polymer that was synthesized specifically for our experiment.

Experiment 1: As seen in Figure 3 (dose response), the impedance normalized to a phosphate buffered saline (PBS) baseline was plotted across dose concentrations in micrograms per milliliter (μg/ml). We took measurements for seven concentrations from 1-100 μg/ml. Higher concentrations are not applicable for future applications as they are not clinically relevant.

Experiment 2: After the establishment of concept with PEI-25, NPGDE was used. Data was plotted in the same way as PEI-25, as shown in Figure 4. This time there were 11 LPS concentrations from 1-500 μg/ml. Higher concentrations were tested for this run because less information is known about how this polymer interacts, and thus, performance parameters could be determined.

Conclusion:

The device was shown to be capable of detecting endotoxins in the lower μg/ml regime. An increase in the measured impedance was observed for increasing concentrations of the endotoxin. There also appeared to be a significant increase in the impedance changes associated with endotoxin binding with the polymer NPGDE which indicated that NPGDE was more effective than PEI-25 at detecting endotoxins.

Future Work:

Future plans involve screening a library of polymers to identify the polymer that will be the best match for endotoxin detection. Eventually this will lead to the development of a portable water quality monitoring device.

Acknowledgements:

I would like to thank Shalini Prasad, Gaurav Chatterjee, Srivatsa Aithal, Trevor Thornton, Center for Sold State Electronics Research, and Rege lab at Department of Chemical Engineering, at Arizona State University. And the National Nanotechnology Infrastructure Network Research Experience for Undergraduates and National Science Foundation for funding.

References:

[1] Ivnitski, D, Abdel-Hamid, I, Atanasov, P, and Wilkins, E (1998). Biosensors for detection of pathogenic bacteria. Biosensors and Bioelectronics, 14, 599-624.

[2] Oram, Brian; Water Testing Bacteria, Coliform, Nuisance Bacteria, Viruses, and Pathogens in Drinking Water. Retrieved August 6, 2009, from Wilkes University Center for Environmental Quality Environmental Engineering and Earth Sciences Web site: http://www.water-research.net/bacteria.htm.

[3] Bothara, M, Venkatraman, V, Reddy, R, Barrett, T, Carruthers, J, and Prasad, S (2008). Nanomonitors: electrical immunoassays for protein biomarker profiling. Nanomedicine, 4, 423-436.

[4] D. Shinn-Jyh, Chang, B-W, Wu, C-C, Chen, C-J, and Chang, H-C (2007). A new method for detection of endotoxin on polymyxin B-immobilized gold electrodes. ScienceDirect, 9, 1206-1211.

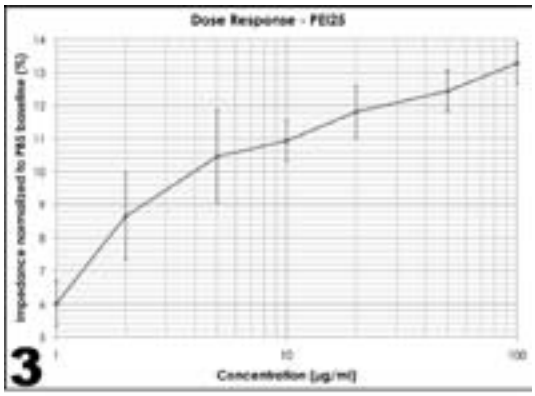

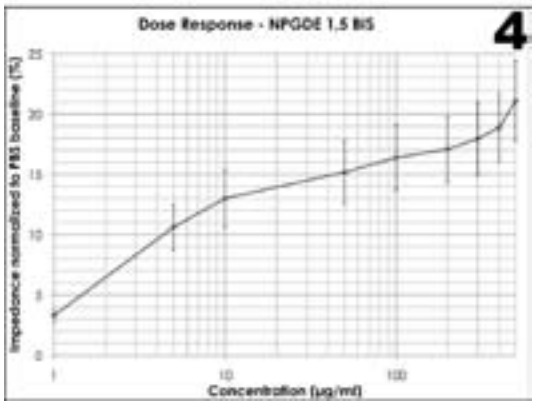

Figure 3: Dose response of PEI-25.
Figure 4: Dose response of NPGDE 1,5 BIS.

Nanostructured Scaffolds for Tissue Engineering Applications

Nathaniel Hogrebe

Chemical Engineering, University of Dayton

NNIN REU Site: Nano Research Facility, Washington University in St. Louis, St. Louis, MO

NNIN REU Principal Investigator(s): Dr. Younan Xia, Biomedical Engineering, Washington University in St. Louis

NNIN REU Mentor(s): Dr. Jingwei Xie, Biomedical Engineering, Washington University in St. Louis

Contact: hogrebnj@notes.udayton.edu, xia@biomed.wustl.edu, xiej@seas.wustl.edu

Abstract:

Polymeric nanofiber scaffolds with both random and aligned fiber orientations were fabricated through the process of electrospinning. A linear gradient of the bone mineral hydroxyapatite was successfully deposited onto the surface, and the bone mesenchymal stem cells of rats were then cultured onto the scaffolds. Preliminary results illustrate that a higher cell density was found on areas of low mineral content.

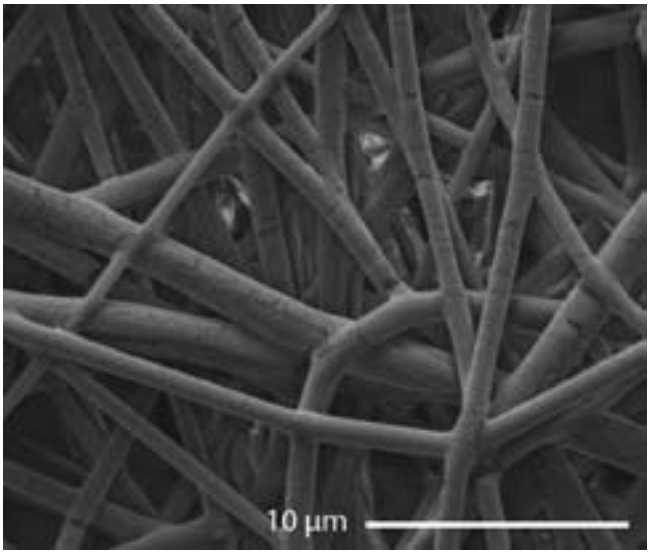

Figure 1: Scanning electron microscope (SEM) image of an unimineralized scaffold with random nanofiber orientation.

Introduction:

One of the current challenges to successful implementation of tissue regeneration techniques into mainstream modern medical practice is the lack of the essential extracellular structure that promotes proper cell attachment, migration, proliferation, and differentiation. Nanofibers fabricated through the process of electrospinning the synthetic biodegradable polymer poly(lactic-co-glycolic acid) (PLGA) offer a promising prospect for this necessary scaffold in repairing damaged tissue because of their high porosity and large surface area [1].

In particular, when coated with a gradient of the bone mineral hydroxyapatite, these nanofibers can potentially mimic the tendon-to-bone attachment site, which is a place of much localized stress due to its non-uniform tissue composition as it changes from soft tendon to hard bone. The objectives of this project, therefore, were to fabricate PLGA nanofiber scaffolds with both random and aligned orientations of the fibers, deposit hydroxyapatite onto the surface of the scaffolds in a gradient-like fashion, culture bone mesenchymal stem cells of rats onto these scaffolds, and finally characterize the cell activity in response to both varying concentrations of hydroxyapatite and orientations of the nanofibers in an effort to determine if these biomineralized scaffolds will be useful in the regeneration of damaged tendon-to-bone attachment sites.

Experimental Procedure:

Electrospinning, the process by which a solution of dissolved polymer is turned into nanofibers, was used to fabricate the scaffolds. An electric current was applied to the tip of a syringe in order to induce a charge on the outgoing droplet, creating an electric field that stretched the dissolved PLGA into thin nanofibers as the solvent evaporated. The fibers were deposited on a uniform piece of aluminum foil to obtain a random orientation but were collected in the empty space between two pieces of metal to achieve a parallel formation of the nanofibers.

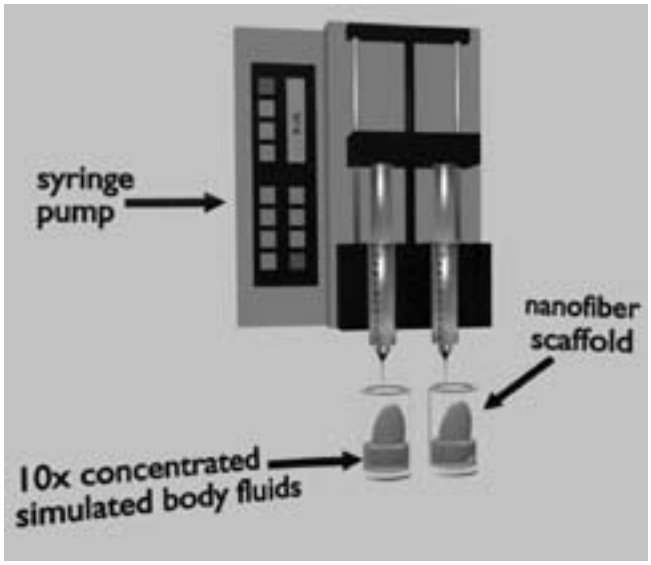

Figure 2: Schematic of the biomineralization process.

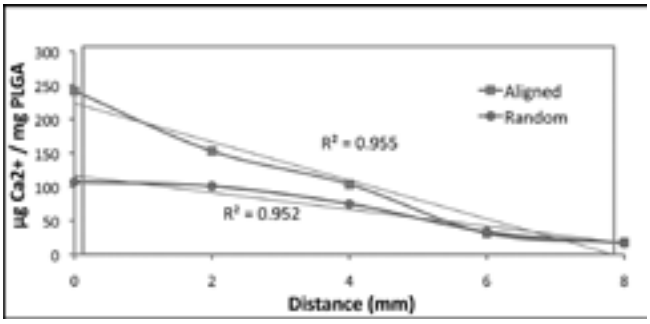

Figure 3: Graph of the mineral gradient.

Once the nanofibers were fabricated, the scaffolds were mounted onto copper wire frames and placed into glass vials. A gradient of hydroxyapatite was created by dripping 8 mL of a solution of ten times concentrated simulated body fluids and sodium bicarbonate over the course of an hour into the vials via a syringe pump. Since deposition is directly related to immersion time, the bottom of the scaffold obtained a higher concentration of mineral than the top, resulting in a linear gradient.

Once dried, the nanofiber scaffolds were mounted onto glass slides and prepared for cell culture. The bone mesenchymal stem cells (BMSC) of rats were grown onto the scaffolds using standard cell culture techniques using both proliferating and differentiating media. The scaffolds were monitored throughout the growth period for their attachment, proliferation, and differentiation characteristics in response to varying mineral content and nanofiber orientation.

Results and Conclusions:

The calcium ion concentration was measured with both inductively coupled plasma mass spectroscopy (ICP-MS) and energy dispersive x-ray spectroscopy (EDX) to determine hydroxyapatite content. The results indicate a relatively linear deposition pattern corresponding to immersion time. After seven days of cell culture on the scaffolds with gradations in mineral content, preliminary results suggest that cell proliferation was greater in areas of lower mineral content.

This outcome can possibly be attributed to the fact that the scaffolds retain a higher porosity in regions of lower mineral content, and thus there are more sites to which the cells can attach. This result was surprising, however, because of its apparent contradiction with previous work, but it could be due to variations in the cell culture process, such as the use of different cell types [2]. Rat bone mesenchymal stem cells, for example, could possibly retain a fibroblast phenotype and thus tend to attach on a site with lower mineral content.

Alkaline phosphatase staining was used to determine the differentiation characteristics of the bone mesenchymal stem cells in differentiating media. Fluorescence micrographs indicate that there was a higher concentration of osteoblasts in areas of low mineral content, which can be attributed to the fact that there was an overall higher cell concentration in these regions.

The result of immunohistochemistry tests indicate that bone mesenchymal stem cells secreted type I collagen on both the high and low mineral content regions, while they secreted very little type II collagen anywhere on the scaffolds. This outcome indicates the development of cells with characteristics of tendon and bone cells. If type II collagen secretion was desired to mimic the fibrocartilage found between tendon and bone, alterations in the cell culture process could be performed.

Future Work:

The preliminary results indicate that nanofiber scaffolds coated with a non-uniform layer of hydroxyapatite hold much promise for the regeneration of the tendon-to-bone interface due to their ability to yield a gradient of cell proliferation and behavior, which is critical to the structural integrity of the attachment site. Further research includes current in vivo experimentation of rat rotator cuffs that will attempt to determine the full extent of nanofiber scaffold utility in modern regenerative medicine.

Acknowledgments:

This research was made possible through the National Science Foundation and the National Nanotechnology Infrastructure Network Research Experience for Undergraduates Program. I would also like to thank Amy Sears and everyone at the Nano Research Facility at Washington University in St. Louis, my mentor Jingwei Xie, and Principal Investigator Younan Xia.

References:

[1] Xie, J., X. Li, X. Xia. Putting electrospun nanofibers to work for biomedical research. Macromolecular Rapid Communications 2008; 29:1775-1792.

[2] Li, X., et al. Nanofiber scaffolds with gradations in mineral content for mimicking the tendon-to-bone insertion site. Nano Letters 2009; 9:2763-2768.

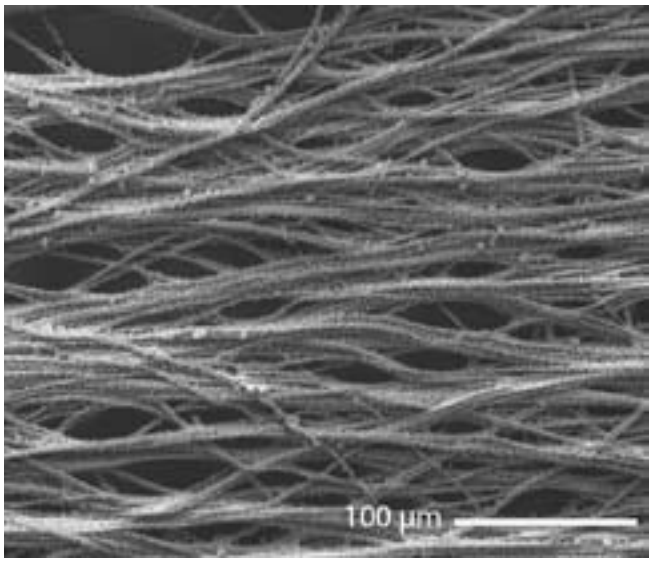

Figure 4: SEM of aligned nanofibers coated with mineral.

Antimicrobial Effects of Metal Oxide Nanoparticles

Angela K. Horst

Biochemistry, Clarke College

NNIN REU Site: Nano Research Facility, Washington University in St. Louis, St. Louis, MO

NNIN REU Principal Investigator(s): Dr. Yinjie Tang, Department of Environmental and Chemical Engineering, Washington University in Saint Louis

NNIN REU Mentor(s): Dr. Bing Wu, Environmental and Chemical Engr., Washington University in Saint Louis

Contact: angela.horst@clarke.edu, yinjie.tang@seas.wustl.edu

Abstract and Introduction:

In a world of emerging nanotechnology, one of the primary concerns is the potential environmental impact of nanoparticles (NPs). An efficient way to estimate nanotoxicity is to monitor the response of bacteria exposed to these particles [1]. This experiment explored the antimicrobial properties of nickel oxide, cobalt (II,III) oxide, zinc oxide, copper (II) oxide, iron (III) oxide, titanium dioxide, and iron (II,III) oxide against a model microorganism, *Escherichia coli*. The toxicity of these metal oxide NPs was tested using two methods: culturing in liquid media containing NPs, and electrospraying the NPs directly onto bacterial surface.

Aqueous exposure mimics the natural interaction between microbial species as NPs diffuse in the environment [2]. During these tests, there was noticeable aggregation, preventing effective interaction between the particles and the bacteria. The limited growth inhibition observed from this form of exposure to metal oxide NPs was therefore attributed to their ionic species.

On the other hand, the electrospray technique allows direct interaction between the NPs and cells. This exposure method grants insight into how "nano" associated properties from metal NPs affect the environment [2]. This method observed a higher death rate when the bacteria were exposed to oxidized nickel, zinc, and cobalt species; but no antimicrobial properties from titanium or iron. The disparity in the results of the two exposure techniques indicates that toxicity is dependant both upon the exposure method and the size of the particle.

NP	Aqueous	Electrospray	Ionic
CuO	NT	N/A	T>2µg
NiO	NT	T	T>2µg
Co3O4	NT	T	T>2µg
ZnO	NT	T	NT
Fe2O3	NT	NT	NT
Fe3O4	NT	NT	NT
TiO2	NT	NT	NT

Table 1: Summary of results. T= toxic, NT = non-toxic.

Experimental Procedure:

Escherichia coli (*E. coli)* were cultivated in M9 minimal media at 37°C. Optical density was measured at 600 nm (OD_{600}) using a UV spectrometer (Genesys, Thermo -Scientific, USA). Experiments began with a 5 mL *E. coli* culture with $OD_{600} = 0.05$ in M9 minimal media. The aqueous exposure method tracked the growth rate of *E. coli* with 2, 20, and 100 mg/L NPs. OD_{600} was recorded at 3, 6, 9, 21, 24 hours. The experiment was also performed using equivalent amounts of soluble chloride salt of the metals to test ionic toxicity.

For electrospray exposure experiments, the aliquot of *E. coli* was first filtered onto a polyvinylidene fluoride (PVDF) membrane (0.22 μm pore size, 1.25 cm × 1.25 cm, Millipore, US) to form a biofilm, which was then electrosprayed with NPs. The electrospray system was kept at a flow rate of 5 μL/min and a current of ~ 7 kV to maintain a cone shaped spray; the particles were suspended in 1.0 M sodium phosphate (Na_2HPO_4, pH 7) buffer. Then the biofilm was washed from membrane using minimal medium and the total living cells after electrospray exposure was measured based on the colony forming unit (CFU) using LB agar plates. Colonies were counted after the plates were incubated in 37°C for ~ 24 hours. Meanwhile, the cells from biofilm will be resuspended in the M9 minimal media and the recovery of growth was monitored by OD_{600}. Scanning electron microscopy (SEM) was used to observe changes in cell morphology after exposure to NPs.

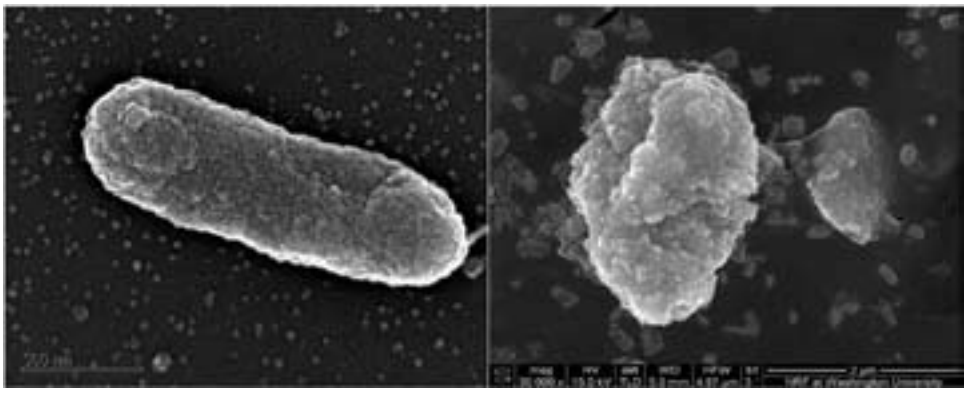

Figure 1: Comparison of an undamaged E. coli cell with one that has been electrosprayed with nickel oxide.

electrical field, ionic zinc, and buffer were nontoxic. The next two bars show the inhibition when electrosprayed with 4 μg/L and 20 μg/L zinc oxide NPs. This confirmed concentration has direct effect on toxicity. Next, the CFU after electrospraying with 4 μg/L zinc oxide microparticles (480 nm diameter) confirms toxicity increases as particle size decreases. Finally, the CFU of *E. coli* exposed to titanium dioxide was used as a reference between zinc oxide and a nontoxic metal oxide.

Results and Conclusions:

The growth curves from the aqueous exposure method displayed no growth inhibition from NPs, because all NPs aggregated. All ionic species, excluding iron and titanium, were inhibitory above 2 μg/L. Growth curves show that the electrospray exposure method was able to cause significant cell death when *E. coli* was exposed directly to nickel oxide, cobalt (II, III) oxide, and zinc oxide (nickel oxide shows highest toxicity). The *E. coli* grew more efficiently and consistently when electrosprayed with iron oxide NPs, were unaffected by titanium dioxide NPs, and copper (II) oxide was unclear. These results are summarized in Table 1. Figure 1 compares an undamaged *E. coli* cell with one that has been electrosprayed with nickel oxide.

Zinc oxide exposure was tested more thoroughly than the other metal oxides and the inhibition from electrospray exposure was clearly observed as function of doses and sizes. Figure 2 shows the increase in recovery time after electrospraying (solid square), as opposed to recovery from aqueous exposure (diamond), and uninhibited growth (open square). The complete results from zinc oxide testing can be seen in Figure 3. From left to right, the non-sprayed bacteria show a similar CFU to those electrosprayed with water, zinc chloride, and sodium phosphate buffer. This confirmed the

Future Work:

The CFU data collected from some metal oxide NPs was too inconsistent for conclusions. We will repeat these experiments and collect CFU data after electrospraying. Tunneling electron microscopy (TEM) images have been suggested to identify whether NPs entered into cells after electrospraying.

Acknowledgements:

Dr. Yinjie Tang and Dr. Bing Wu, for support, mentorship, and time. Dr. Yi-Shuan Lee for electrospraying. Washington University in St. Louis for use of their facilities, and National Nanotechnology Infrastructure Network Research Experience for Undergraduates Program and National Science Foundation for funding and making this all possible.

References:

[1] Brayner, R. "The toxilogical impact of nanoparticles." Nanotoday 3, 48-55 (2008).

[2] Wu, B. "New investigation of nano-ZnO antimicrobial activity." Submitted to Environmental Science and Technology (2009).

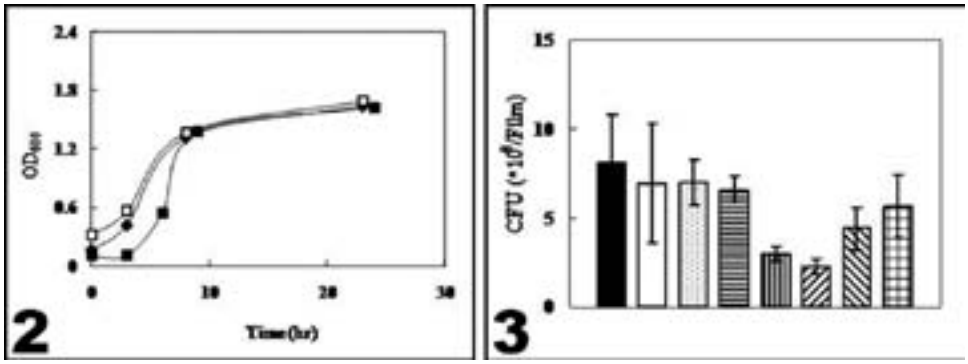

Figure 2: Increase in recovery time after electrospraying (solid square), as opposed to recovery from aqueous exposure (diamond), and uninhibited growth (open square).

Figure 3: Complete results from zinc oxide testing.

Optical Detection of Thrombus Formation within a Microfluidic Device using a Helium-Neon Laser as a Radiation Source

Adam Kozak

Biomedical Engineering, University of Rochester

NNIN REU Site: Nanotechnology Research Center, Georgia Institute of Technology, Atlanta, GA
NNIN REU Principal Investigator(s): Craig Forest, Assistant Professor of Mechanical Engineering, Georgia Tech
NNIN REU Mentor(s): Melissa Li, Biomedical Engineering, Georgia Institute of Technology
Contact: akozak2@u.rochester.edu, cforest@gatech.edu, melissa_li@gatech.edu

Abstract:

Understanding the dynamics of blood clotting, or thrombosis, is critically important to clinical evaluations of patients and to research laboratories studying diseases and drug effects. Particularly, the necessary conditions for late-stage acute thrombus formation are not well understood, and instrumentation has been limited in this context. The emerging field of microfluidics has led to significant advances in examining thrombus formation *in vitro*, allowing biologically relevant geometries and the measurement of volumetric growth rates in real time. However, current techniques (antibody binding, microscopic imaging) produce data with poor temporal and spatial resolution for accurate rate measurements. We present a method for detecting thrombus formation within a microfluidic device using a helium-neon laser, taking advantage of the low optical absorbance of platelets relative to erythrocytes. This method provides sub-second time resolution and a smaller instrument footprint compared to existing art. Our method is also capable of measuring the hematocrit of the blood being tested, as established in previous art [1], and which has been shown to affect thrombus growth in the past [2].

Introduction:

The optical properties of blood have been well defined in existing literature. The most pertinent of these in our efforts is the transmissive properties of erythrocytes and platelets within the visible spectrum, since these are the primary constituents of thrombi. In the red portion of the spectrum, erythrocytes exhibit minimal transmittance, while platelets exhibit significant transmittance [3]. Under high blood shear conditions, which are analogous to those present within mammalian hearts, thrombus forms primarily composed of platelets. Thus as the thrombus grows, its transmittance increases measurably in relation to the surrounding blood.

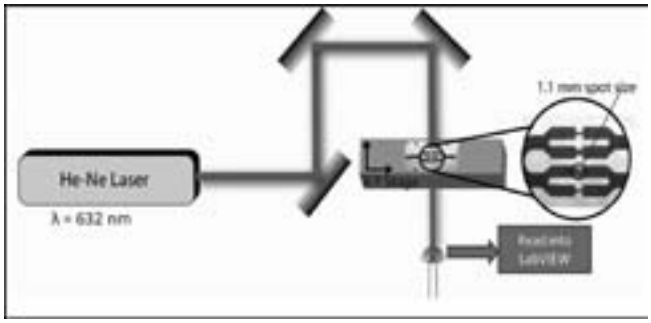

Figure 1: Schematic of the instrumentation for the single channel thrombosis measurement.

Construction:

Our research group had previously designed and manufactured a low-volume, high-throughput microfluidic device with several stenoses that exhibited shear rates between $4000s^{-1}$ and $7500s^{-1}$ (modeled through Poisuelle Flow and Particle Image Velocimetry). Porcine blood of known hematocrit (determined through centrifugation) was delivered via gravity pump into the microfluidic device which was placed upon an x-y stage for positioning.

Light from a 0.7 mW 632.8 nm helium-neon laser was passed through a series of mirrors and illuminated a single stenosis as shown in Figure 1. The transmitted light was measured by a photodiode and accompanying circuit, which provided a variable gain between 3E+5 and 1E+7. The output was read by a National Instruments Data Acquisition Device into LabVIEW where a butterworth bandpass filter was applied and a moving average was taken.

However, the aforementioned construction was only able to measure a transmittance function within a single channel. Desiring to measure thrombus formation within multiple stenoses simultaneously, our construction was modified accordingly. To accomplish this, the incident light was diverged in one dimension utilizing a BK7 uncoated cylindrical lens. This light was then passed through an acrylic aperture plate placed on top of the microfluidic device, which contained four 1000 μm apertures separated to match the channel spacing. The transmitted light was

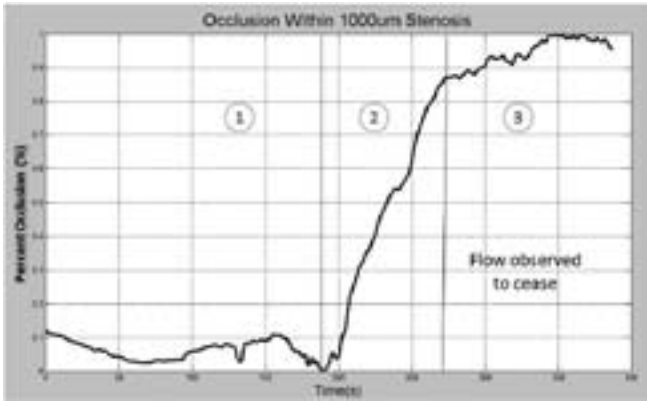

Figure 2: Photodiode output with three stage of thrombus formation labeled.

measured by a line CCD camera and read into LabVIEW for post-processing, as shown in Figure 2.

Results:

Thrombus growth was successfully measured in individual channels of the microfluidic device and was verified by comparison with microscopic imaging methods using identical blood samples and measuring at equivalent shear rates, as shown in Figure 3. Our method was able to measure the three distinct phases of thrombus formation: adhesion, acute growth, and occlusion, as shown in Figure 4. Volumetric thrombus growth could be measured with a sampling rate of up to 10 kHz, compared to microscopic imaging which operates at sub-hertz acquisition speeds.

Our method also provided a method of determining the hematocrit of the blood being measured. The initial intensity of the transmitted light is proportional to the concentration of erythrocytes, and thus can be related to the blood hematocrit with an error of approximately 2%.

Utilizing the high-throughput construction, growth has been observed in four stenoses simultaneously in addition to spatial localization of the growth within each stenosis.

Discussion:

Utilizing this method, differential thrombus formation has been observed under various blood parameters, such as

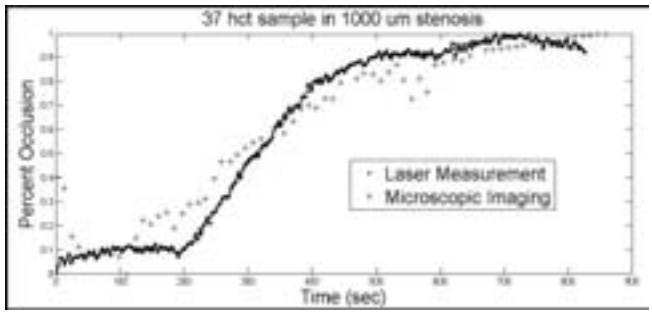

Figure 3: Comparison of laser detection with existing microscopic imaging (high frequency data corresponds to laser output).

Figure 4: Schematic of the instrumentation for multi-channel thrombosis measurement.

varying hematocrit, shear rate, and dosage of acetylsalicylic acid, an anti-thrombotic drug. However, more data is required before definitive analysis can be performed from a biological viewpoint.

The methods described above provide a superior method of detection over current art that can be expanded to perform large numbers of trials simultaneously. Additional tests are being conducted to validate the accuracy of the high-throughput instrumentation in comparison to the single-channel measurements. However, initial data indicates that it will be as accurate, in addition to providing previously unavailable spatial resolution.

Conclusion:

Described is a method of quantitatively analyzing acute volumetric thrombus growth. The method described provides not only a high time resolution, but also a smaller laboratory footprint and data load than existing art. The presented method is multifunctional, allowing an assessment of acute thrombus growth rate, time to occlusion, and the hematocrit of the blood being analyzed. Additional functionality can be added such as measuring hemoglobin concentration by observing the blood's optical scattering. Utilizing the presented method, the effects of drugs such as acetylsalicylic acid can be examined under different conditions, such as varied shear rates that simulate individuals with various stages of heart disease.

Acknowledgements:

The National Science Foundation, National Nanotechnology Infrastructure Network Research Experience for Undergraduates (NNIN REU) Program, and Georgia Institute of Technology.

References:

[1] Cullis, H.M., Method and Apparatus for Making a Rapid Measurement of the Hematocrit of Blood, U.S. Patent 4 303 336, 1981.

[2] Ross, J. M., L. V. Mcintire, et al. (1995). "Platelet-Adhesion and Aggregation on Human Type-Vi Collagen Surfaces under Physiological Flow Conditions." Blood 85(7): 1826-1835.

[3] Optical Properties of Circulating Human Blood in the Wavelength Range 400-2500 nm; Andre Roggan, Moritz Friebel, Klaus Dorschel, Andreas Hahn, and Gerhard Muller, J. Biomed. Opt. 4, 36 (1999), DOI:10.1117/1.429919.

Modeling Intermediates in Prion Protein Fibril Formation

Sin Ying Stephanie Lau
Chemistry, Wellesley College

NNIN REU Site: Center for Nanotechnology, University of Washington, Seattle, WA
NNIN REU Principal Investigator(s): Prof. Valerie Daggett, Bioengineering, University of Washington
NNIN REU Mentor(s): Dr. Marc van der Kamp, Bioengineering, University of Washington
Contact: slau@wellesley.edu, daggett@u.washington.edu, mwvdk@u.washington.edu

Abstract:

The misfolding and aggregation of the prion protein have been implicated in several fatal neurodegenerative diseases. Misfolded prion proteins first aggregate into toxic, infectious protofibrils before forming fibrils. We constructed different protofibril models from molecular dynamics simulations of the human prion protein under misfolding conditions. These protofibril models were compared with experimental data to assess if they are reasonable models for the toxic intermediates.

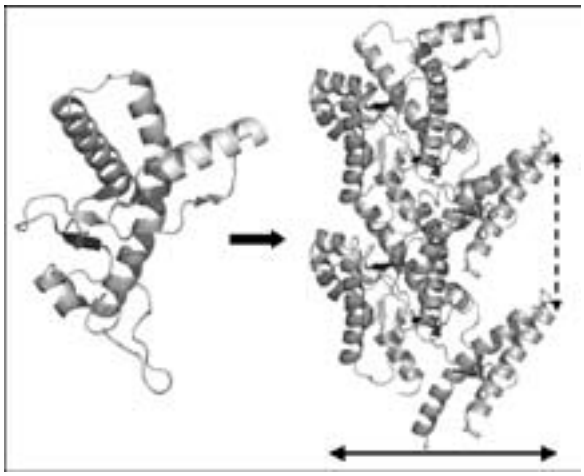

Figure 1: Left: Misfolded human PrP at pH 5. Right: Side view of a protofibril model. The dotted line indicates the rise per turn, while the solid line indicates the diameter of the model.

Introduction:

Aggregates of an abnormal form of the prion protein (PrP) are responsible for a group of fatal neurodegenerative conditions known as prion diseases, which include bovine spongiform encephalopathy (mad cow disease) and Creutzfeldt-Jakob disease. Prion diseases are caused by the misfolding and aggregation of PrP, which may be triggered by low pH or mutations. The structures of misfolded PrP cannot be determined experimentally, so our group used molecular dynamics to simulate the misfolding of PrP at various pH levels and with different mutations.

Misfolded prion proteins first assemble into soluble protofibrils before forming insoluble fibrils (Figure 1). There is evidence that protofibrils are toxic and infectious, and knowing the structure of these protofibrils can help us understand and combat prion diseases. Currently there is no high-resolution experimental data on protofibril structure, but experiments have shown that misfolded PrP aggregates have significantly more β-structure and less α-helical content compared with the natively-folded PrP. Experiments also indicated that residues 98-110 and 136-140 are important for aggregation and are likely on the binding interface between monomers [1].

Building on previous work [2], this project aimed to construct alternative human protofibril models with increased β-sheet content. We have built several models that are consistent with many available experimental data. (See Figure 1)

Methods. Misfolded conformations were selected from molecular dynamics simulations of PrP under misfolding conditions and docked manually to create models with cross-monomer β-sheets [2]. All models were constructed using PyMOL [3].

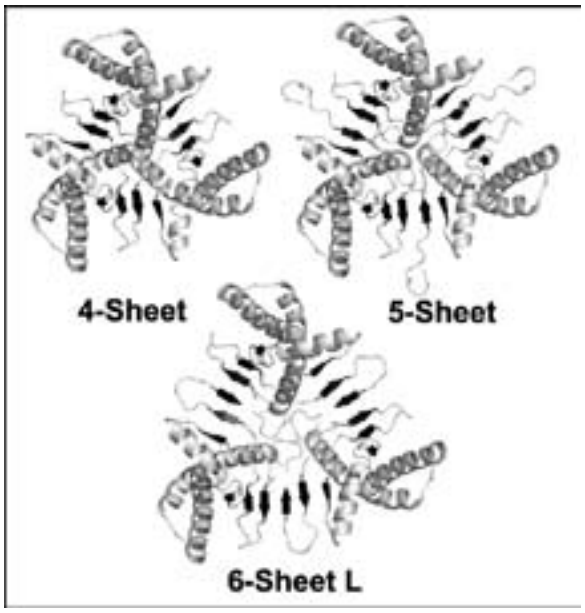

Figure 2: Top views of the left-handed spiral models.

Prion Protofibril Models. The human protofibril models we constructed are named according to the number of strands in the cross-monomer β-sheets. 4-sheet, 5-sheet, and 6-sheet L are left-handed spiral models built from misfolded wild-type PrP at pH 5 (Figure 2). All models have a repeating unit of three monomers. 4-sheet is similar to the previous protofibril models because each β-sheet has four strands. We were interested in building models with more β-structure, so we modeled one and two extra strands in the N-terminus to get 5-sheet and 6-sheet L, respectively.

While 6-sheet L has more β-structure, it also has more gaps in between monomers, which may make the model unstable. To make the model more compact while maintaining β-structure, we adjusted the 6-sheet conformations and fitted them into a right-handed spiral model, 6-sheet R, which has fewer gaps than its left-handed counterpart.

5-sheet D178N, whose cross-monomer β-sheet consists of five strands, was built from misfolded PrP conformations with the disease-causing mutation D178N. The mutated conformations only fit into a right-handed spiral, whereas the wild-type conformations fit readily into left-handed spirals.

To compare the different models, we measured the diameter and the rise per turn (Figure 1). The diameter increased with the increasing number of β-strands, but the rise per turn does not show a clear trend (Figure 3).

	4-Sheet	5-Sheet D178N	5-Sheet	6-Sheet R	6-Sheet L
# β-strands	4	5	5	6	6
Handedness	Left	Right	Left	Right	Left
Diameter (Å)	67.1	72.7	74.3	79.4	81.1
Rise (Å)	37.5	37.5	40.5	34.5	40.5

Figure 3: Comparison of protofibril models.

Comparison with Experimental Data:

To check if known antibody binding sites are accessible in our models, mapped epitopes were projected onto them (Figure 4). All models are accessible to the ICSM18 and H3:2 antibodies and, after some adjustments, also to R1. These three antibodies can bind to both native PrP and misfolded aggregates.

I5B3 and H3:3 bind selectively to misfolded PrP aggregates, and most of our models are accessible to them. Since I5B3 binds to three separate regions at once, the three regions must neighbor one another. This is indeed the case in our models (Figure 4). Furthermore, H3:3 binds to a region that is significantly altered during the misfolding simulations of PrP. The differences in the H3:3 binding region in native and misfolded PrP may explain the selectivity of H3:3 for PrP aggregates.

Finally, all our models can accommodate glycans at the known glycosylation sites, Asn-181 and Asn-197, and all have exposed proteinase K digestion sites at Gly-127.

Conclusions and Future Work:

Structures representing misfolded PrP can be fitted into continuous spiral models with 4, 5, or 6 β-strands. Two spiral conformations, left-handed or right-handed, are possible with 6 β-strands. However, the models with 6 β-strands show significant gaps, which may mean that these structures are unstable. Misfolded PrP with disease-related mutation D178N resulted in a different spiral model than wild-type misfolded PrP. Most of our models agree with available experimental data, indicating that the models are reasonable. More experimental data is needed to further assess if our models are representative of prion protofibrils.

Acknowledgements:

I thank my PI Prof. Valerie Daggett, mentor Dr. Marc van der Kamp, and site coordinator Dr. Ethan Allen, for their assistance. I also thank the National Nanotechnology Infrastructure Network Research Experience for Undergraduates (NNIN REU) Program and National Science Foundation for funding.

References:

[1] Abalos G.C., Cruite J.T., Bellon A., Hemmers S., Akagi J., Mastrianni J.A., Williamson R.A., Solforosi L. (2008) Identifying key components of the PrP^{C}-PrP^{Sc} replicative interface, J. Biol. Chem. 283, 34021-34028.

[2] DeMarco M.L. and Daggett V. (2004) From Conversion to Aggregation: Protofibril Formation of the Prion Protein, Proc. Natl. Acad. Sci. 101, 2293-2298; Scouras A.D. and Daggett V. (2008) Species variation in PrPSc protofibril models, J. Mater. Sci. 43, 3625-3637.

[3] DeLano, W.L. (2002) The PyMOL Molecular Graphics System (Palo Alto, CA, USA, DeLano Scientific).

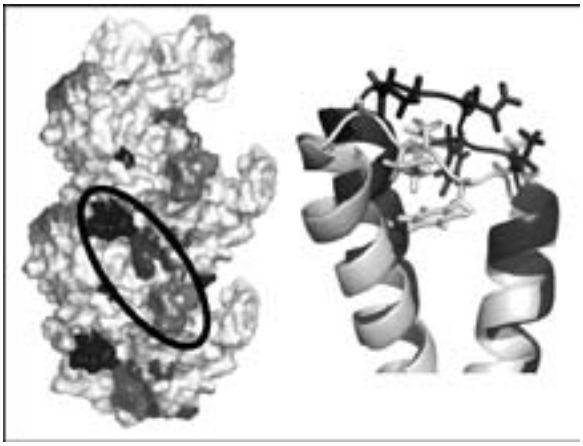

Figure 4: Left: I5B3 binding regions in the 4-sheet model. Right: Changes in the H3:3 binding region in native PrP (light gray) and misfolded PrP (dark gray).

Characterization of Gold Nanoparticles Functionalized with Thiolated Single-Stranded DNA

Alexandra J. Machen

Chemical Engineering, University of Kansas

NNIN REU Site: Center for Nanotechnology, University of Washington, Seattle, WA

NNIN REU Principal Investigator(s): Sirnegada Techane, Chemical Engineering, University of Washington

NNIN REU Mentor(s): Lara J. Gamble, Ph.D., David G. Castner, Ph.D., Bioengineering and Chemical Engineering, University of Washington

Contact: jaymac@ku.edu, castner@nb.engr.washington.edu, gamble@nb.engr.washington.edu, sdt5@u.washington.edu

Introduction:

Gold surfaces functionalized with deoxyribonucleic acid (DNA) are used in biomedical applications such as biosensing. When biosensors and other biomedical devices are placed in a biological environment, various reactions (analyte sensing, protein adsorption, etc.) will occur at their surface. For nanoparticles, where the surface-to-volume ratio is high, these surface properties are crucial and often unique from their larger scale counterparts [1].

Our work included functionalizing and characterizing gold nanoparticles (AuNPs) with thiolated single-stranded DNA (SH-ssDNA) in various buffers with different salt concentrations. We performed detailed surface analysis of the functionalized AuNPs using x-ray photoelectron spectroscopy (XPS). The SH-ssDNA functionalized AuNPs were then backfilled for varying amounts of time with hydroxyl-terminated alkylthiols to hinder DNA base-gold binding. Control flat Au surfaces were also functionalized with SH-ssDNA for comparison to the functionalized AuNPs.

Experimental Methods:

Materials. The 40-mer SH-ssDNA [5'(C5-Thiol) AGC TGC CCT GGT AGG TT TCT GGG AAG GGA CAG ATG ACA G 3'] was purchased from Trilink Biotechnologies (lot U17-0209-AC1A-A). Ultrapure water (resistivity >18.0 M Ω cm) used for preparing all aqueous solutions was purified by a Modulab Analytical research grade water system. Spectra/Por molecular porous membrane dialysis tubing was purchased from Sigma-Aldrich. Tubing-type 1 had a molecular weight cut off of 12-14,000 and tubing-type 2 had a molecular weight cut off 50,000 (wet in 0.1% sodium azide). All other chemicals were also purchased from Sigma-Aldrich.

Gold Nanoparticle Stability. UV/VIS measurements were performed to determine which buffer and salt conditions provided a stable environment for the AuNPs. A stable environment was considered one that did not cause the AuNPs to aggregate as identified by a change in color.

Thiol-DNA Assembly. Water, buffer, and SH-ssDNA were combined at the desired concentrations in a glass scintillation vial and mixed for 30 seconds. AuNPs were added, and when relevant, solution was mixed for 30 minutes before adding salt. The AuNPs were functionalized for 24 hrs before purification. Samples were dialyzed 2x in tubing-type 1 and 10x in tubing-type 2 (see materials) in 3500 mL water.

Backfilling Procedure. 97.55 μL of 9.0M hydroxyl-terminated alkythiol were added to 4 ml purified functionalized AuNPs. Samples were backfilled for varying amounts of time before being dialyzed 10x in tubing-type 2.

XPS Analysis. XPS measurements were performed on Surface Science Instrument S-Probe spectrometer with a monochromated Al-Kα x-ray source. Compositional survey, detailed scans (Au4f, C1s, O1s, P2p, S2p and N1s) and high resolution scans (C1s and N1s) were acquired. All measurements were taken at a 55° photoelectron takeoff angle. The computational data are averages of values from two samples, three spots per sample. Data analysis was performed on the Service Physics ESCA 2000 Graphics Viewer data reduction software.

Results and Discussion:

Stability of AuNPs. Adding SH-ssDNA to buffer before adding AuNPs helped decrease aggregation. Using this procedure, the highest stable salt concentrations in 1× Tris and 1× PBS were 1 mM NaCl and 100 mM NaCl, respectively. In both buffer systems, adding NaCl last allowed for a higher final salt concentration.

UV/VIS Absorbance of AuNPs (Graph 1). SH-ssDNA peaks appeared at 260 nm and gold peaks appeared around 525 nm. There was no SH-ssDNA peak in the AuNP solution before functionalization, as expected. The broadening of the gold peak in the functionalized samples indicated particle growth. This combined with the noticeable SH-ssDNA peaks suggested that SH-ssDNA had been attached to the AuNPs.

Surface Chemical Composition of AuNPs (Graph 2). Increasing the salt concentration of a sample was previously shown to increase the SH-ssDNA loading onto the surface by

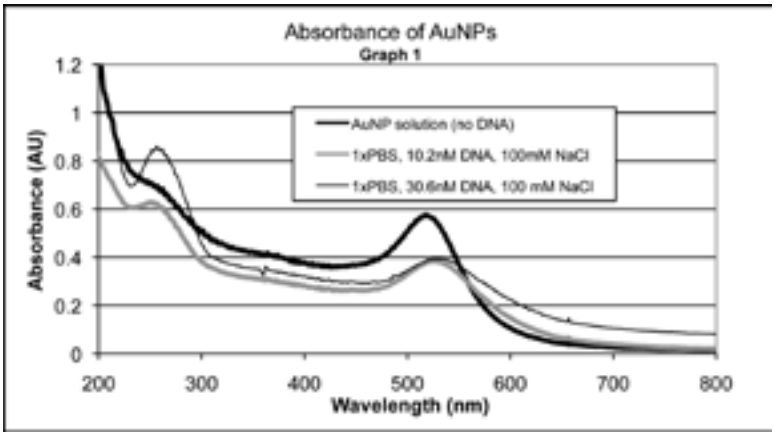

Graph 1

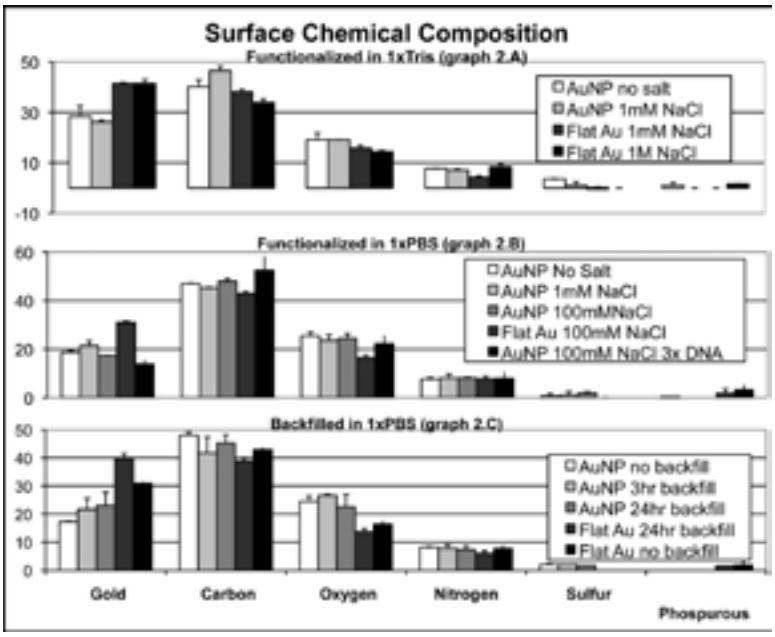

Graph 2

shielding the DNA-DNA repulsion forces [2]. However, SH-ssDNA loading on the AuNPs was not significantly affected by the salt concentration. An increase in loading would result in a lower percentage of gold seen on the surface [3]. This was not the case in Tris buffer (Graph 2.A) or PBS (Graph 2.B).

It is possible the SH-ssDNA concentration was too low to be affected by the repulsion forces. However, increasing the SH-ssDNA concentration by 3x (Graph 2.B) did not significantly change surface composition. In PBS, AuNPS exhibited similar nitrogen composition compared to flat surface. In Tris, there were similar phosphorus compositions. Some samples also had high amounts of sulfur. This was most likely due to minor contamination.

Graph 2.C shows the chemical surface composition of functionalized AuNPs backfilled with 6-mercapto-1-hexanol for 0, 3, and 24 hrs. The time allowed to backfill had little effect on alkythiol coverage on AuNPs. That is, the 3 hrs time range was long enough for the backfilling to be equilibrated; therefore, shorter times (< 3 hrs) are recommended for future studies. The flat surface comparison is also shown on Graph 2.C. Both the AuNPs and flat gold exhibited an increase in percentage of gold on the surface as backfilling occurred. This seems counter intuitive, but the hydroxyl-terminated alkylthiols being added were significantly shorter than the 40mer SH-ssDNA. Hence, the alkylthiols attenuated the gold signal less than the SH-ssDNA [3].

Conclusions:

To develop understanding of the structure-function relationship for biomedical devices and optimize their performance, their surface properties must be characterized. In this study, 14 nm diameter AuNPs were functionalized with SH-ssDNA in Tris and PBS buffer in varying salt concentrations. Using surface analysis techniques for characterization, we determined adding salt did not enhance SH-ssDNA assembly for the DNA concentration used in this study. Control flat gold surfaces were subjected to similar conditions. All AuNP samples had lower percentages of gold than the flat surface samples. The curved surface of AuNP may have enabled higher SH-ssDNA loading. Also, compared to flat surfaces, the XPS organic overlayer signals are enhanced relative the underlying gold signals for AuNPs [4].

Further characterization and optimization of the DNA coated AuNPs is currently underway.

Acknowledgements:

This research was supported by National Nanotechnology Infrastructure Network (grant ECS-0335765) Research Experience for Undergraduates Program (grant EEC-0649215), NESAC/BIO (NIH grant EB-002027), and the National Science Foundation.

References:

[1] Grainger D.W; Castner, D.G. Adv. Mater. 2008, 20, 867-877.

[2] Hurst, S.J.; Lytton-Jean, A.K.R.; Mirkin, C.A. Anal. Chem. 2006, 78, 8313-8318.

[3] Lee, C.; Gong, P; Harbers, G.M; Grainger D.W; Castner, D.G.; Gamble, L.J. Anal. Chem. 2006, 78, 3316-3325.

[4] Lee, C.; Harbers, G. M.; Grainger, D.W.; Gamble, L.J.; Castner, D.G. J. Am. Chem. Soc. 2007, 129, 9429-9438.

Development and Fabrication of a Micro-Microbial Fuel Cell

Isaac Markus

Chemical Engineering, The Cooper Union for the Advancement of Science and Art

NNIN REU Site: Cornell NanoScale Science and Technology Facility, Cornell University, Ithaca, NY
NNIN REU Principal Investigator(s): Dr. Largus T. Angenent, Biological and Environmental Engineering, Cornell
NNIN REU Mentor(s): Arvind Venkataraman, Biological and Environmental Engineering, Cornell University
Contact: markus@cooper.edu, la249@cornell.edu, av299@cornell.edu

Figure 1: Mask for channels.

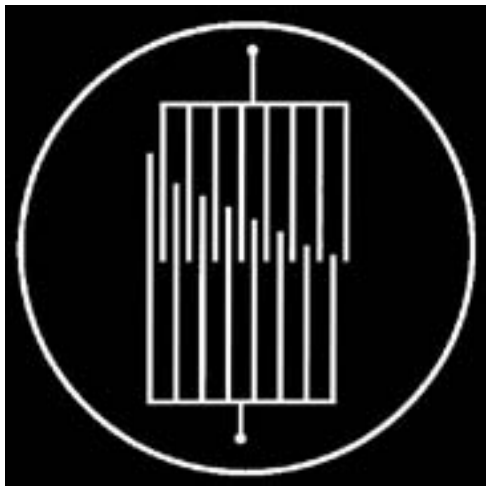

Figure 2: Mask for electrodes.

Introduction:

Bioelectrochemical systems (BESs) have gathered attention in recent years because they convert organic material in wastewater into electricity and chemicals, and are applied as biosensors. Microbial fuel cells (MFCs) are one example of a BES in which anaerobic bacteria oxidize carbon sources using the anode as a terminal electron acceptor thereby generating a current. The bacteria grow planktonic as well as an anodic biofilm employing direct electron transfer and/or mediators for current generation. The biofilm density and composition are determining factors for the efficiency and power generation of MFCs. This project focuses on developing and fabricating a micro-microbial fuel cell (μMFC). We believe that by reducing the overall surface to volume ratio the Coulombic efficiency can be increased subsequently leading to higher power densities. Additionally, the μMFC can be used as a tool to study real time biofilm growth and development [1].

Experimental Procedure:

Mask Design. The mask for the silicon (Si) masters and electrodes were design by Dr. Benjamin Steinhaus. The masks were printed through emulsion on transparent paper and the design is shown in Figures 1 and 2.

Master Fabrication. Masters were fabricated on 100 mm silicon wafers. The wafers were coated with P20 primer (2000 RPM at 1000 RPM/s) and then S1827 resist (2000 RPM at 500 RPM/s). Wafers were soft baked at 115°C for 90 sec, exposed for 16 sec placed in an ammonia image reversal oven, hard baked at 115°C for 90 sec and developed using MF321. Masters were etched using a Unaxis 770 Si etcher to a depth of 100 μm. Remaining resist was removed using a resist hot strip bath. Wafers were finally coated with an inert layer of 1H,1H,2H,2H-perfluorooctyl trichlorosilane (FOTS) using molecular vapor deposition.

Electrode Fabrication. Electrodes were fabricated on 100 mm borofloat wafers. Wafers were cleaned using isopropyl alcohol and acetone. The wafers were coated with P20 primer (2000 RPM at 1000 RPM/s) and then S1827 resist (2000 RPM at 500 RPM/s), soft baked at 115°C for 5 min, exposed for 16 sec, hard baked at 115°C for 5 min and developed using MF321. A titanium and gold layer (100/200 nm) was deposited using an SC4500 evaporator. Excess metal was removed by lifting off remaining resist using 1165 stripper.

Microfluidic Device Fabrication. The first device was cast with polydimethylsiloxane (PDMS), mixed in a 10:1 weight ratio with curing agent. The solution was degassed and poured over the Si master and cured for 2 hr at 90°C. PDMS was peeled away, and inlet and outlet holes were punched using 18G blunt needles. The second device was cast with a mixture of PDMS and zirconium n-butoxide. The latter chemical addition rendered the polymeric structure as a proton exchange membrane (PEM) [2]. Zirconium n-butoxide and ethyl acetoacetate were mixed in a molar ratio 1:1. This solution was then mixed with PDMS (95% PDMS by weight). The mixture was degassed and poured over the Si master. Solution was cured at 60°C for 2 hr and

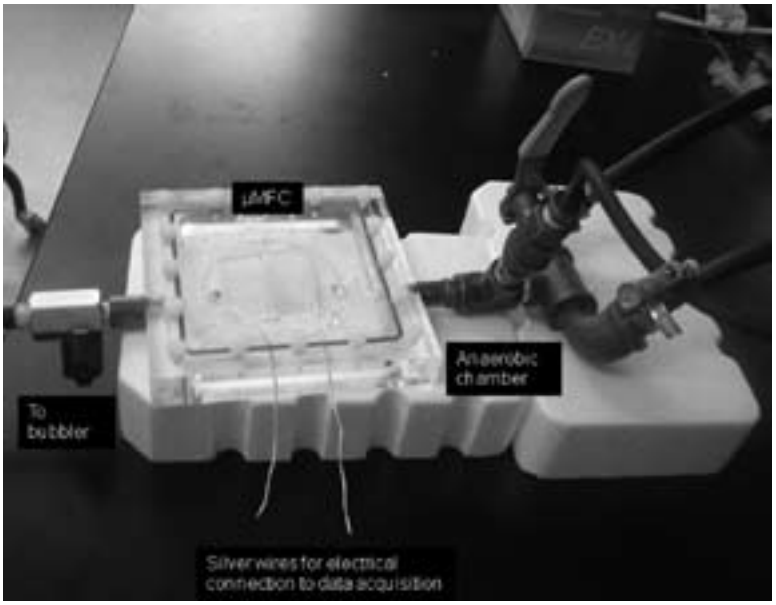

Figure 3: Experimental Setup. μMFC lies inside anaerobic chamber connected to syringe pump through tygon tubing. Electrodes are connected to data acquisition system with silver wires.

annealed at 120°C for two days. The PEM remained opaque, rendering it unsuitable for application.

Experimental Setup. The PDMS and the electrodes were exposed to plasma for 1 min and attached. Tygon tubing was connected to the inlets and outlets and sealed with epoxy. The electrodes were connected with silver wires to a Keithley voltmeter, which recorded the open circuit potential. The μMFC was operated under micro-aerobic conditions continuously for six days at a flow rate of 0.001 ml/min. The experiment setup is shown in Figure 3. A baseline was established by using 100 mM potassium ferricyanide in phosphate buffer as the catholyte and M4 media as the anolyte. The system was inoculated with 0.5 ml *Shewanella oneidensis* MR-I solution (grown overnight in Luria-Bertani) after 12 hours.

Results and Discussion:

The open circuit voltage (OCV) prior to inoculation was 61 mV. Post-inoculation the potential increased to 255 mV after five days (Figure 4). The potential suggests that the μMFC still has a high internal resistance since theoretical values of 850 mV have been reported [3] for MFCs using the same catholyte and anolyte. This can be attributed to the device being made from PDMS, a low ionic conductor. The OCV was also reduced due to the device being operated under micro-aerobic conditions, since oxygen is a better electron acceptor than the anode.

Conclusions and Future Work:

We successfully constructed a μMFC capable of operating at 255 mV. This initial prototype shows much promise and in the future can be improved by using a material with higher ionic conductivity such as a ZrO-PDMS mixture. Additionally, this potential can be increased by operating under anaerobic conditions, preventing the drain of electrons by oxygen.

Acknowledgements:

This work was supported by National Science Foundation, National Nanotechnology Infrastructure Network Research Experience for Undergraduates (NNIN REU) Program and CNF. Additionally, it was possible thanks to Largus T. Angenent and Arvind Venkataraman.

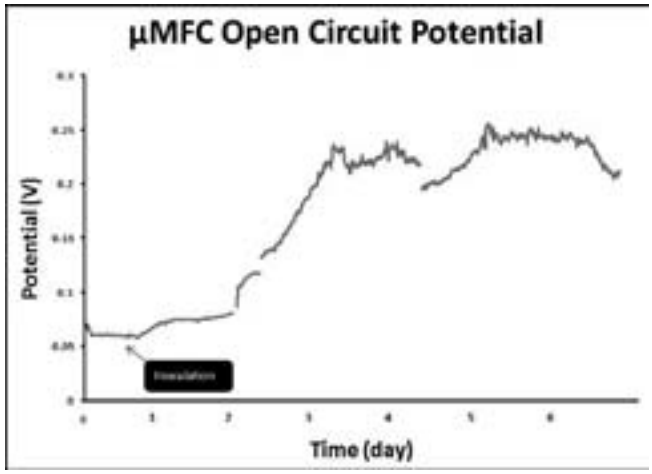

Figure 4: Open circuit potential results. The μMFC had a baseline OCV of 61 mV. The potential increased to 255 mV post-inoculation and stabilized at 235 mV.

References:

[1] Fornero J. J., Rosenbaum M., Cotta M. A. and Angenent L. T. "Microbial fuel cell performance with a pressurized cathode," Environmental Science and Tech Vol. 42, 22, 8578–8584 (2008).

[2] Katayama, S. Kubo, Y. Yamada, N. "Characterization and Mechanical Properties of Flexible Dimethylsiloxane-Based Inorganic/Organic Hybrid Sheets," Journal of the American Ceramic Society, 85 [5] 1157-1163 (2002).

[3] Rosenbaum, M. Zhao, F Schroder, U. Scholz, F. "Interfacing Electrocatalysis and Biocatalysis with Tungsten Carbide: A High-Performance, Noble-Metal-Free Microbial Fuel Cell," Angewandte Chemie, 118, 1-4 (2006).

[4] Du, Z. Li, H. Gu, T. "A state of the art review on microbial fuel cells: A promising technology for wastewater treatment and bioenergy," Biotechnology Advances, 25 [5] 464-482 (2007).

Single Walled Carbon Nanotubes as Nanopores for DNA Translocation

Claire McLellan

Physics, Wake Forest University

NNIN REU Site: ASU NanoFab, Arizona State University, Tempe, AZ

NNIN REU Principal Investigator(s): Dr. Stuart Lindsay, Biodesign Institute, Arizona State University

NNIN REU Mentor(s): Dr. Jin He, Biodesign Institute, Arizona State University

Contact: mcleca8@wfu.edu, stuart.lindsay@asu.edu, jinhe@asu.edu

Introduction:

Single molecule deoxyribonucleic acid (DNA) sequencing through nanopores is potentially a fast cost effective way to sequence long strands of DNA. Nanopores have a similar diameter to DNA, so DNA has to unravel itself when it is translocated through the nanopore, about 10 nm for double stranded DNA (dsDNA) and about 2 nm for single stranded DNA (ssDNA). The individual DNA bases can pass the nanopore in a sequential manner [1].

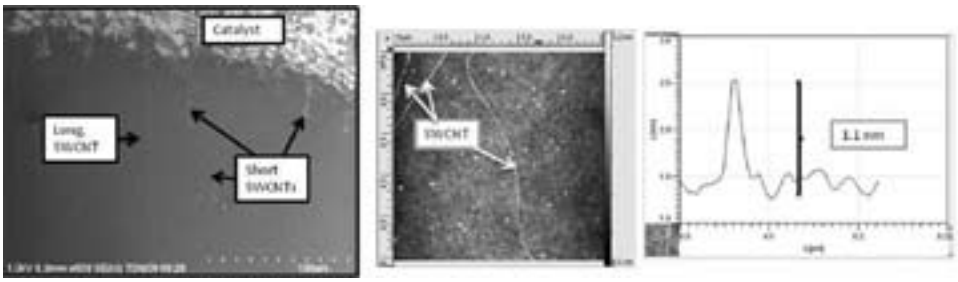

Figure 1: FESEM and AFM with height displacement graph for marker.

To translocate DNA, a voltage is applied across a nanopore that separates two reservoirs of aqueous electrolyte solution. The nanopore essentially becomes a Coulter counter. The ions in the electrolytes move through the nanopore and create an ionic current. DNA, which is a negatively charged molecule, is translocated through the pore by electrophoresis. DNA inside the SWCNT block the ion flow so a change in the ionic current is detected during translocation. Ionic current, as well as tunneling current and optical signal may be used as readout signals for nanopore DNA sequencing. Nanopore sequencing does not include all the complicated and time consuming processes of cloning, polymerase chain reaction, and capillary electrophoresis, potentially sequencing a diploid mammalian genome in 24 hours for about ~$1000 [2].

Currently nanopores have been created that can discriminate dsDNA and ssDNA by the different pore sizes used for the translocation. Ribonucleic acid (RNA) and DNA are discriminated by differences in the amplitude of the ionic current and the translocation duration time. The length of the DNA is discriminated by a change in the time length when the ionic current is blocked [3].

Single walled carbon nanotubes (SWCNTs) are well structured, long, and natural nanopores with atomically flat inner walls. SWCNTs are about ~ 1-4 nm in diameter and can reach the millimeter scale in length although usually the micron scale. The channel form of the SWCNT provides a way to contain DNA and potentially control the speed of the DNA when translocated past a base reader. In order to create a SWCNT translocation device, SWCNTs need to be well calibrated.

This summer we investigated SWCNT calibration by growing SWCNTs using a chemical vapor deposition (CVD) method and characterizing SWCNTs using atomic force microscopy (AFM) and field emission scanning electron microscopy (FESEM). We investigated the translocation capabilities of the SWCNTs by measuring the ionic current through the SWCNT based nanofluidic device.

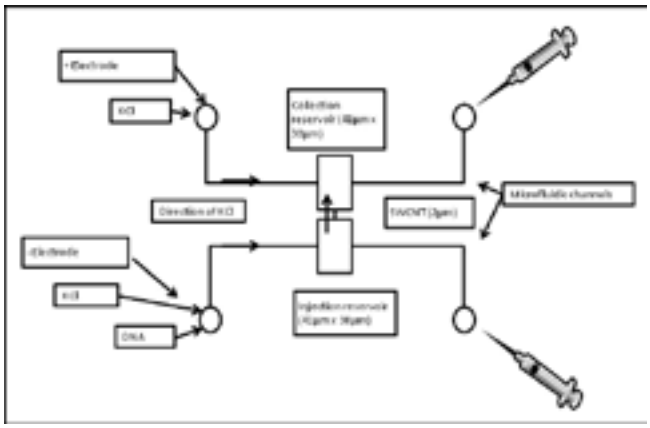

Figure 2: Schematic of DNA translocation device.

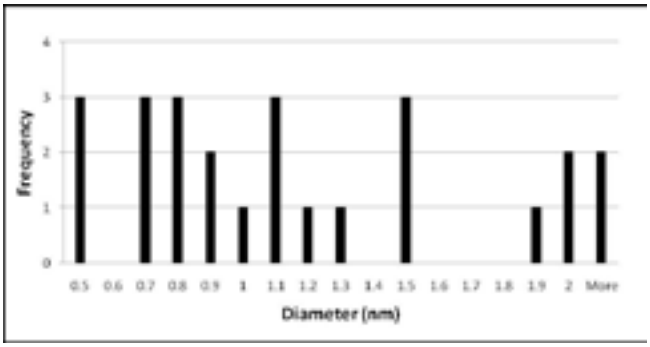

Figure 3: Histogram for SWCNT diameters.

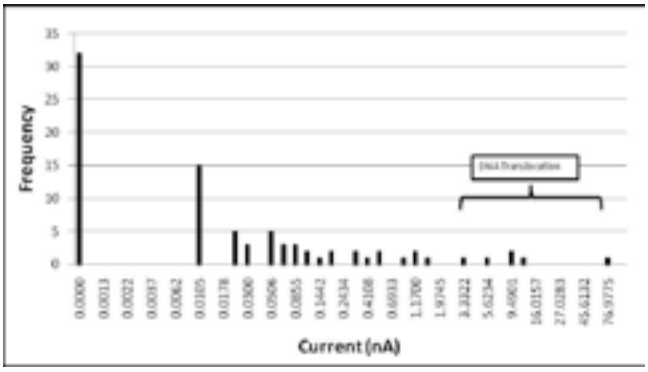

Figure 4: Histogram for SWCNT ionic currents.

Methods and Materials:

The CVD method gives control over SWCNT's orientation, horizontal alignment, length, and diameter. CVD-grown SWCNTs have been shown to have less defects than other methods. The catalyst was produced by a mixture of diblock polymer and cobalt salt. Argon and hydrogen were the gas carriers for the carbon source, ethanol. Ethanol was chosen because the OH group effectively removes any amorphous carbon that would cover and deactivate the cobalt nanoparticles. AFM and FESEM images were used to characterize the grown SWCNTs (Figure 1). A polydimethylsiloxane (PDMS) microfluidic system was prepared and used to introduce solution to SWCNTs. Electron beam lithography (EBL) was used to create reservoirs in the PMMA resist layer that covered on top of the SWCNTs. Oxygen plasma was used to remove the exposed SWCNT in reservoirs and open both ends of the SWCNT that connected two reservoirs. The SWCNT was soaked with an aqueous potassium chloride (KCl) solution. A voltage was applied across the SWCNT for ionic current (Figure 2).

Results and Discussion:

The diameters of the SWCNTs found using AFM are illustrated in Figure 3. The spatial distribution was found using FESEM. The distribution distances were taken 100 μm from the catalyst on four silicon dioxide (SiO_2) substrates. Usually surface density is used when studying distribution, but the SWCNTs were parallel so distances were found. The mean was 111 μm ± 98 μm. It was common to find many SWCNTs close to one another and then have hundreds of microns before another SWCNT was found. More SWCNT were found in the area closer to the catalyst. The CVD method of growing SWCNTs was successful in respect to growing many SWCNTs that were long and straight, well dispersed, with usable diameters. If a diameter was too small, the DNA could not translocate and if it was too large, the ionic current change was not obvious. The optimal diameter was 2 nm.

We tested the ionic current of the SWCNTs that had been etched by oxygen plasma and placed in a translocation device; the results are shown in Figure 4. Most, 67%, of the devices made were successful at transferring ionic current. Those devices that did not transfer current could have been contaminated, contained defects, or not opened entirely on each side. The SWCNTs that had successful ionic currents could be used for DNA translocation testing.

DNA translocation favors high ionic current. The distribution of currents may be caused by the distribution in diameter. It would be useful to study how to increase the yield of SWCNTs with high currents. Research in efficient DNA sequencing will help the understanding of the genome and its applications in medical research.

Acknowledgements:

I would like to acknowledge the National Science Foundation and the National Nanotechnology Infrastructure Network Research Experience for Undergraduates (NNIN REU) Program for providing the funding for this internship, Arizona State University for providing the facilities, Trevor Thornton for organizing the program, and Dr. Stuart Lindsay, Dr. Jin He and his graduate students for sharing their knowledge and laboratory.

References:

[1] Austin, R. (2003). Nanopores: The art of sucking spaghetti. Nature Materials, 2, 567-568.

[2] Branton, D., Deamer, D., Marziali, A., et al. (2008). The potential and challenges of nanopore sequencing. Nature Biotechnology, 26(10), 1146-1153.

[3] Rhee, M. and Burns, M. A. (2006). Nanopore sequencing technology: nanopore preparations. TRENDS in Biotechnology, 25(4), 174-181.

Nanomechanical Properties of Motor Proteins

Margaret Merritt

Biomedical Engineering, Brown University

NNIN REU Site: Nanotech @ UCSB, University of California, Santa Barbara, CA
NNIN REU Principal Investigator(s): Megan T. Valentine, Mechanical Engineering, UCSB
NNIN REU Mentor(s): Dezhi Yu, Materials Science, University of California at Santa Barbara
Contact: Margaret_Merritt@brown.edu, valentine@engineering.ucsb.edu, dezhi0622@umail.ucsb.edu

Abstract:

Motor proteins drive essential processes in the body, including muscle movement and cell division, by converting chemical energy to mechanical work. Yet, the relationship between the structure and function of these molecular motors is not well understood. Acquiring comprehensive knowledge of these interactions could ultimately lead to the creation of nanoscale proteins with tunable properties. Such proteins could vastly improve cancer and disease research as well as provide fundamental insight into cell biology. The present study aims to further investigate nanomechanical properties of kinesin, a motor protein responsible for intracellular transport. To accomplish this, we successfully generated a recombinant human kinesin construct, labeled with green fluorescent protein and a histidine epitope tag, and used high-resolution imaging to characterize its velocity and photostability *in vitro*.

Introduction:

Kinesins are one group of motor proteins that transport cargo and play a critical role in cell division [1]. In cells, kinesin molecules attach to, "walk" along, and detach from microtubules, one type of cytoskeletal polymer, by a series of chemical reactions involving adenosine triphosphate (ATP) [2,3]. Kinesin proteins can be expressed in bacteria cells and characterized *in vitro*. Observing this walking process in reconstituted systems can help to better understand the relationship between kinesin and microtubules, and will provide insight into the motor mechanism of kinesin.

One challenge for *in vitro* measurements of motor proteins is collecting sufficiently high signals to allow for visualization. Total internal reflection fluorescence microscopy (TIRFM) provides a useful solution. In TIRFM, a laser beam is steered into a microscope objective at a high incident angle. Above a critical angle, the majority of the incident light is reflected, but a small portion propagates into the sample, parallel to the surface, as an evanescent wavefront that excites fluorophores on and near the surface [4]. This decreases the fluorescence emission from within the sample and increases the signal to noise ratio. By using two lasers of distinct wavelengths, kinesin and microtubules can be distinguished if labeled with two different fluorescent dyes that possess excellent photostability characteristics. The present study used an electron-multiplying charged coupled device (EMCCD) camera with the TIRFM system to provide fast, high-resolution data acquisition in order to characterize the velocity and photo-properties of fluorescent kinesin proteins.

Experimental Procedure:

A protein expression protocol was developed and used to generate recombinant kinesin proteins. *Escherichia coli* bacteria, containing a plasmid with the *kif5b* kinesin gene fused to green fluorescent protein (GFP) for visualization and a histidine tag for purification, were obtained and replicated. This multi day procedure required sterility and ideal temperature and chemical conditions. After growth, cells were lysed by sonication, releasing cellular contents into solution. Kinesin was column purified using a type of nickel resin, which had high affinity for the histidine-tagged kinesin. Expression products were analyzed with gel electrophoresis.

Gliding filament assays were used to characterize the recombinant kinesin. Coverglasses were coated with GFP antibodies to bind kinesin to the surface. Because the GFP is located at the tail, each motor head pointed up into solution and attached and detached to microtubules in solution, thus causing them to glide. A 532 nm laser and a custom TIRFM system were used to visualize microtubules labeled with rhodamine dye.

For each microtubule, 200 frames were collected at a frequency of 10 frames per second with an EMCCD camera. Analysis software was implemented to locate the coordinates of the tip of each microtubule in the first and last frame (Figure 1). The distance between these points was calculated and divided by the elapsed time (20 seconds) to obtain velocity data. To assess photostability, single kinesin-GFP molecules were observed using a 473 nm laser.

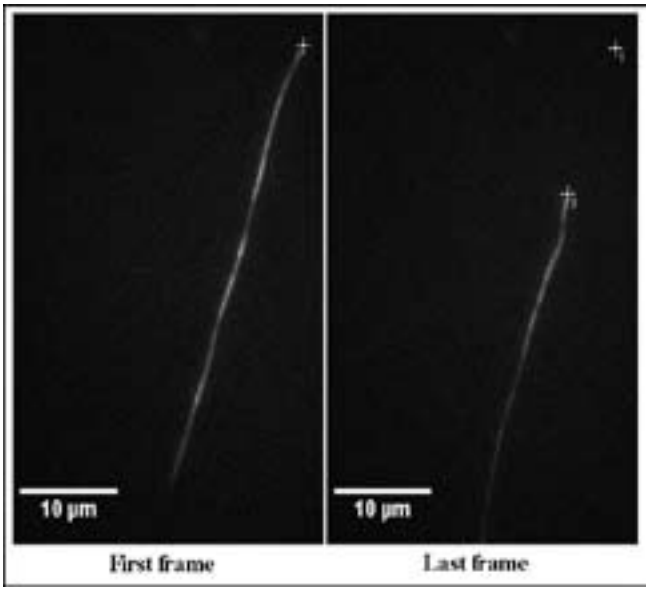

Figure 1: Analysis of a microtubule gliding assay video.

Results and Conclusions:

Green protein fractions and gel electrophoresis confirmed that GFP-fused kinesin was successfully made. To assess the functionality, microtubule velocities were calculated via gliding assays. The velocities of 160 microtubules were measured to be 650 ± 80 nm/s, consistent with earlier reports [5,6]. The distribution (Figure 2) was slightly skewed toward lower velocities, perhaps indicating the presence of non-or partly-functional motor proteins or imperfect surface immobilization.

Kinesin motors were also visualized at the single molecule level, and the fluorescence intensity was measured as a function of time to assess dye lifetime and brightness. The lifetime of a single GFP molecule was found to be ~ 10 seconds, as indicated by the steep vertical drop in mean intensity (Figure 3). This singular drop confirmed that single molecule signal detection had been achieved.

Future Work:

The robust protocol for the expression and characterization of kinesin motors that was developed will enable future analysis of a wide variety of motor proteins. In order to further improve the procedure, optimal conditions for single molecule imaging to reduce photobleaching, without impairing kinesin's functionality, should be investigated. Significant insight into the biology of motor proteins will be gained, which will help develop the promising concept of making proteins with desirable properties for cancer and disease applications.

Acknowledgements:

Thank you to the National Nanotechnology Infrastructure Network Research Experience for Undergraduates Program and the National Science Foundation for funding my summer research. Special thanks to Dr. Megan T. Valentine, Dezhi Yu, Nikki Lapointe, Claudia Gottstein, Angela Berenstein, the members of the Valentine lab, and my friends and family for their guidance and support.

References:

[1] Mazumdar, M and Misteli, T; Trends Cell Biol. 15, 349-355 (2005).
[2] Valentine, M and Gilbert, S; Curr. Opin. Cell. Biol. 19, 75-81 (2007).
[3] Asbury, C; Curr. Opin. Cell. Biol. 17, 89-97 (2005).
[4] Axelrod, D. et al; Ann. Rev. Biophys. Bioeng. 13, 247-368 (1984).
[5] Rosenfeld, S. et al; J. Biol. Chem. 278, 18550-18556 (2003).
[6] Romberg, L. et al; J. Cell Biol. 140, 1407-1416 (1998).

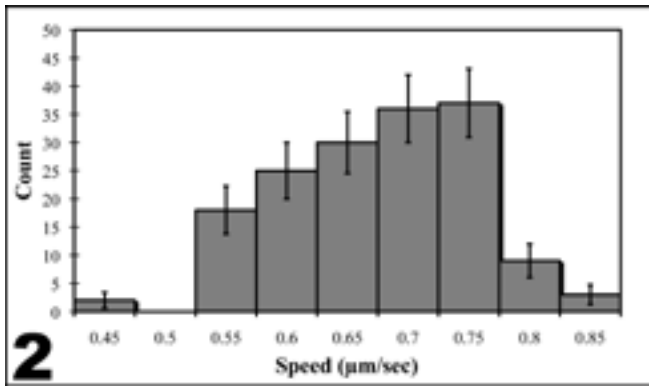

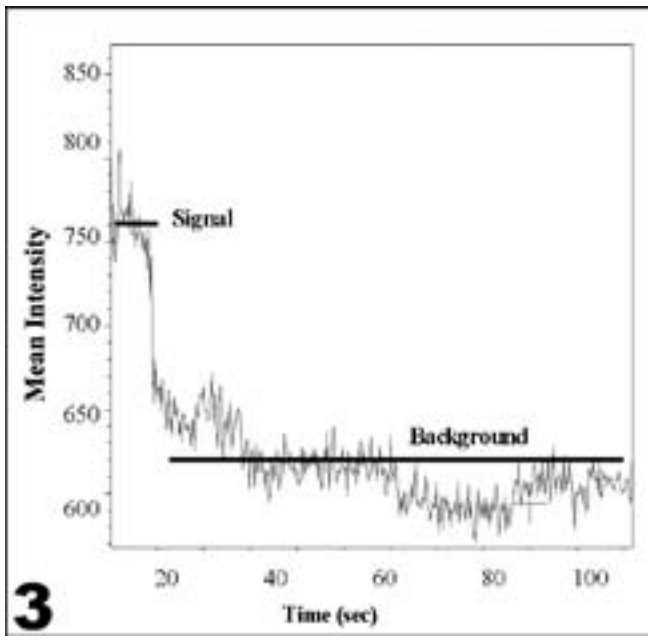

Figure 2, top: Distribution of microtubule speeds on kinesin-coated surfaces.

Figure 3, bottom: Photobleaching trace of a single GFP kinesin.

Microfluidics Guided Self-Assembly of Magnetoliposomes

Tiffany Moeller

Chemical Engineering, University of Nebraska

NNIN REU Site: Cornell NanoScale Science and Technology Facility, Cornell University, Ithaca, NY
NNIN REU Principal Investigator(s): Carl Batt, Department of Food Science, Cornell University
NNIN REU Mentor(s): Matthew Kennedy, Dickson Kirui, Department of Food Science, Cornell University
Contact: tiffanymoeller@msn.com, cab10@cornell.edu, mjk67@cornell.edu, dk322@cornell.edu

Abstract:

Liposomes in the range of 100 to 500 nm were created using a microfluidic flow-focusing device by varying composition and flow rates of the lipid and sheath fluids. Due to their amphiphilic structure, liposomes can be engineered to encapsulate magnetic nanoparticles, forming magnetoliposomes. The project aims were to (1) optimize reagent parameters to modify liposome size and (2) encapsulate nanoparticles. A three-dimensional microfluidic focusing manifold was employed to enhance the liposomes' monodispersity to improve *in vivo* pharmacokinetics. At flow rate ratios (FRRs)—sheath to lipid solution—from 10 to 25, increasing phospholipid concentration from 0.10 to 10.0 mM decreased liposome size from 215 to 120 nm. At the same FRRs, increasing the concentration of potassium chloride from 0.10 to 10.0 mM in the sheath fluid increased the liposomes' size from 120 to 470 nm; liposomes aggregated at FRRs less than 10.0. Magnetoliposomes were formed via an *in situ* precipitation of magnetite in the interior compartment of the liposomes.

Background:

Monodisperse liposomes are more desirable for *in vivo* applications because they display more uniform pharmacokinetics [1,2]. Additionally, liposomes with diameters of 150 to 200 nm demonstrate prolonged circulation half-lives and more efficient extravasation of tumor microvasculature compared to liposomes of other sizes [3,4]. Therefore, microfluidic-directed formation of liposomes is very useful as it allows for controlled size and more monodisperse liposomes over other synthesis methods [4].

Magnetoliposomes have been engineered to encapsulate magnetic nanoparticles to concentrate therapeutics at the delivery site [4]. An alternating magnetic field can induce hyperthermia, allowing a burst-release of the encapsulated therapeutic [2]. Magnetoliposomes have been synthesized using other methods [5], but we employed the microfluidic platform to produce more monodisperse product of controlled size.

Experimental Procedure:

Microfluidic Device. The microfluidic device was fabricated using general photolithography techniques. Polydimethylsiloxane (PDMS) was spun onto SU-8 patterned wafers, and the two pieces of PDMS were aligned. The cross-sectional dimensions of the square microchannel were 125 μm; the channel was 2.0 cm in length.

Liposomes for Size Experiments. The phospholipids 1,2-dipalmitoyl-*sn*-glycero-3-phosphocholine (DPPC) and 1,2-distearoyl-*sn*-glycero-3-phosphoethanolamine-N-[amino(polyethylene glycol)-2000] (DSPE-PEG) were dissolved with cholesterol (Chol) in ethanol in a 10.1:1.0:9.9 (DPPC/DSPE-PEG/Chol) molar ratio. The sheath fluid was deionized water or a potassium chloride solution. A syringe pump flowed the lipid solution through the center input of the device and the sheath fluid in the remaining four inputs. Product was collected at varying flow rate ratios (FRRs)—sheath to lipid solution—with a constant bulk flow rate of 20.39 μL/min and a Reynolds number of 2.72.

***In situ* Synthesis of Magnetoliposomes (MLs).** The sheath fluid was 5.0 mM $FeCl_3$ and $FeCl_2 \cdot 4H_2O$ (2:1 molar ratio). The lipid solution (10.1:1.0:8.1; DPPC/DSPE-PEG/Chol) was pumped at 1.3 μL/min and the sheath at 4.8 μL/min (FRR = 14.7). NH_4OH solution was added to the liposomes to precipitate magnetite (Fe_3O_4) according to the following chemical reaction:

$$2FeCl_3 + FeCl_2 + 8NH_3 + 4H_2O \rightarrow Fe_3O_4 + 8NH_4Cl$$

Size Determination. Hydrodynamic radii were determined with dynamic light scattering (DLS) at 0.010 mM phospholipid concentrations. Measurements were taken at 90° with a Melles Griot HeNe 632.8 nm laser.

Characterization by Transmission Electron Microscopy (TEM). A 5.0 μL aliquot of sample was pipetted onto a carbon-coated 200 nm mesh copper grid and stained with 5.0 μL of sodium phosphotungstate negative stain. Images were taken with a Philips Tecnai T-12 scope at 120kV.

Results and Discussion:

Monodispersity of Liposomes. The microfluidic device was based upon Kennedy et al. [6]. The three-dimensional design focused the lipid solution to the microchannel's

center. Diffusion of the lipids into the surrounding aqueous sheath fluid directed liposome self-assembly. Doing so narrowed the velocity distribution of the molecules, potentially narrowing the size distribution of the liposomes as well.

Effect of FRR on Liposomes. At FRRs below 10.0, there was no trend in liposome size (Figure 1). An insufficient volume of sheath fluid in the microchannel prevented complete diffusion of the lipids, resulting in incomplete liposome assembly. At FRRs of 10.0 and above, increasing the phospholipid concentration from 0.10 to 10.0 mM decreased liposome diameter from 215 to 130 nm. At the higher concentration, lipids had a shorter diffusion time before reaching the critical aqueous concentration at which liposomes self-assemble, resulting in smaller liposomes.

Increasing the sheath's salt concentration from 0.10 to 10.0 mM increased the liposomes from 150 to 470 nm. At the lower salt concentration, the solvating action of the water molecules stabilized the liposomes thereby minimizing their size. With increasing ionic strength, water molecules increasingly solvated salt ions. The instability created by decreased solvation resulted in larger liposomes which are prone to aggregation (Figure 2). Characterization by TEM showed all liposomes to be generally spherical; however, lipid aggregates predominated most samples (Figure 3).

Characterization of Magnetoliposomes (MLs). TEM images before and after addition of NH_4OH verified encapsulation of magnetite. Before NH_4OH addition, the liposomes were spherical with an average mean diameter of 160 nm. Precipitated magnetite appeared as black spots in the liposomes' interior (Figure 4). TEM verified DLS size measurements.

Acknowledgments:

The author thanks the National Nanotechnology Infrastructure Network Research Experience for Undergraduates (NNIN REU) Program and the National Science Foundation (NSF), the Cornell NanoScale Science and Technology Facility (CNF) and program coordinators Melanie-Claire Mallison and Rob Ilic, as well as the Batt Group—especially Matthew Kennedy, Dickson Kirui, and Carl Batt—for their assistance and support.

References:

[1] Xu, Q., et al.; Small Journal, 5.13, 1575-1581 (2009).

[2] Arruebo, M., et al.; Nanotoday, 2.3, 22-32 (2007).

[3] Litzinger, D., et al.; Biochimica et Biophysica Acta, 1190, 99-107 (1994).

[4] Gu, F., et al.; Nanotoday, 2.3, 14-21 (2007).

[5] Sabaté, R., et al.; International Journal of Pharmaceutics, 347, 156-162 (2008).

[6] Kennedy, M., et al.; "A Microfluidic Hydrodynamic Diffusion Mixer with Reduced Taylor Dispersion"; (2009).

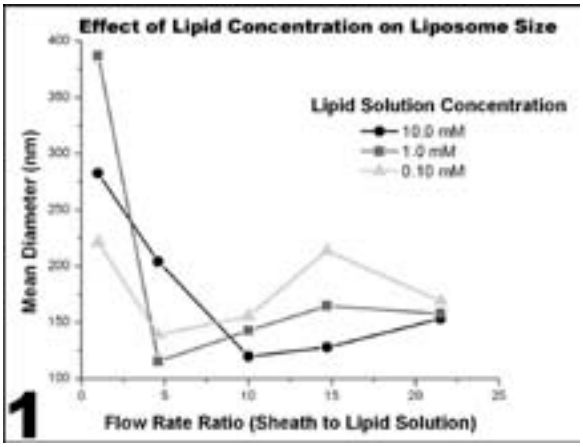

Figure 1: Increasing phospholipid concentration resulted in smaller liposomes.

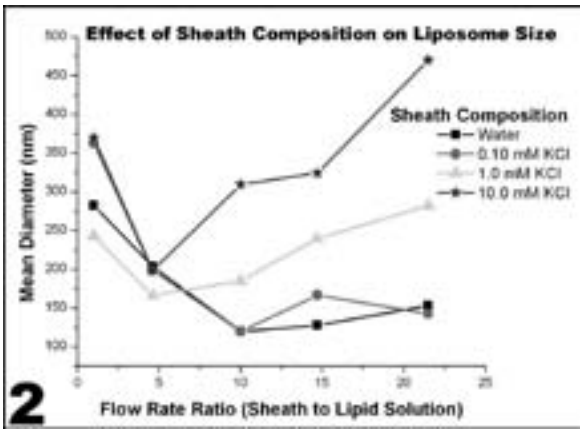

Figure 2: Increasing ionic strength of the sheath fluid resulted in larger liposomes.

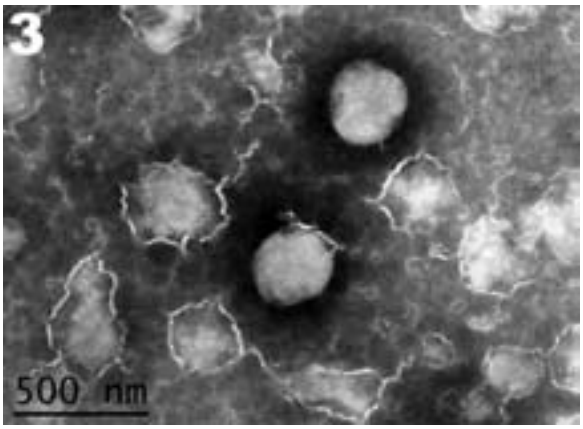

Figure 3: TEM image of liposomes with a mean diameter of 240 nm.

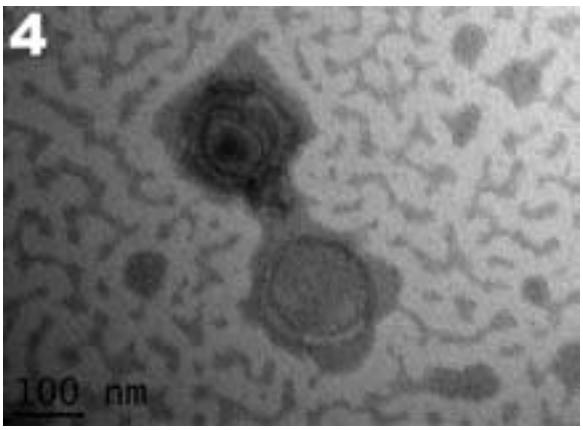

Figure 4: TEM image of a magnetoliposome. The top liposome is encapsulating magnetite while the bottom liposome is not.

Using Molecular Self-Assembly for Surface Charged Monolayers to Control Bio-Assembly

Theresia Monikang

Chemistry Department, Hampton University

NNIN REU Site: Howard Nanoscale Science and Engineering Facility, Howard University, Washington, DC
NNIN REU Principal Investigator(s): Dr. James Mitchell, Materials Chemistry and Engineering, Howard University
NNIN REU Mentor(s): Dr. Tina Thomas Brower, Chemistry, Howard University
Contact: Chemdance@yahoo.com, Theraneh@yahoo.com

Abstract/Introduction:

Self-assembled biological molecules are being utilized in many ways to include forming hydrogel networks and nanoscale tubles. The goal of this project is to develop a method to preferential assembly biomaterial on surfaces using ionic interactions. We employ photolithography and prepare a simple pattern—an array of gold (Au (111)) on mica. We form a monolayer of 4, 4'-dimercaptobiphenyl on the Au (111) surface. The monolayer is then treated with a photoresist, followed by selective exposure leaving part of the monolayer inaccessible. The monolayer is exposed to a solution of mercury (II) per chlorate hydrate. The mercury (II) per chlorate provides a positive charge to exposed area of the patterned surface. Finally the array is introduced to various biomaterials with the expectation that localized ionic interactions will result in preferential assembly of biomaterial. The array is examined by Kelvin force microscopy (KFM) before and after their introduction to the biomaterial.

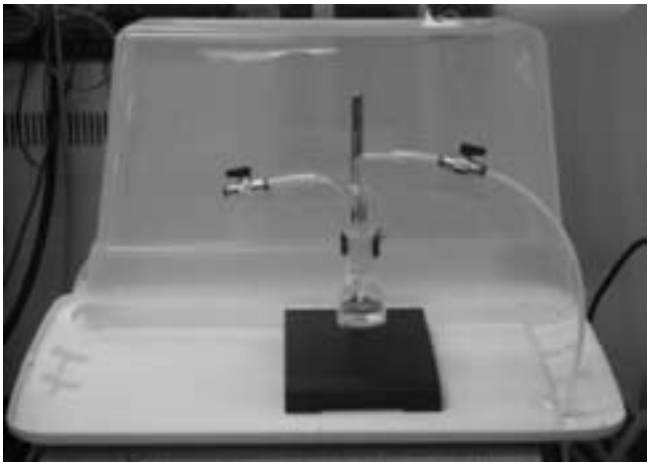

Figure 1: Homemade vented box. The bubbler flask is connected to a nitrogen gas tank allowing the self-assembly to occur in a nitrogen atmosphere.

Experimental Procedure:

The experiment was performed under a homemade vented box (Figure 1). The box contained a bubbler flask that was connected to a nitrogen tank. It was important for the solutions to be in a nitrogen atmosphere in order to prevent the formation of dual mechanism bifunctional polymer (DMBP) via disulfide bonds. Therefore, all the glassware were cleaned using a piranha solution. Cleanliness was important because impurities could interfere with the formation of a monolayer.

A 1 μm solution of DMBP was prepared and introduced to the bubbler flask. A gold sample was obtained and cleaned using an argon plasma. After cleaning the substrate, the optical constants were obtained using ellipsometry. These optical constants were later used to find the thickness of the monolayer. After measuring the optical constants, the substrate was put into the bubbler flask containing DMBP and left to self-assemble for four hours (Figure 2). After self-assembly, the gold substrate was rinsed with 200 proof ethanol and dried with a stream nitrogen gas. The monolayer thickness was obtained using ellipsometry.

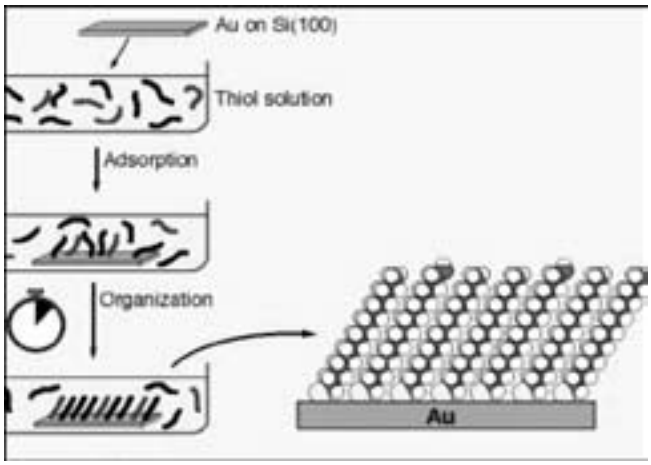

Figure 2: Gold substrate is put into a DMBT solution, DMBT self-assembles onto Au (111) substrate in a four hour period, to form a monolayer. Ref. http://www.ifm.liu.se/applphys/ftir/sams.html.

A pattern of 103 μm squares was created on a gold substrate using photolithography. A small area was covered with photoresist and left un-etched, leaving that part of the substrate available for measuring the thickness of the monolayer. The previous procedure was repeated to make the monolayer, then positive charges were partially introduced to the monolayer surface using mercury (II) per chlorate. In order to have a partially charged monolayer surface, half of the gold substrate was covered with photoresist. The photoresist was meant to keep the positive charges absent from certain areas. The charges were exposed in areas with no photoresist. The bubbler flask contained 50 μM of mercury (II) per chlorate in 50/50 200 proof ethanol in distilled H_2O. It seemed the photoresist adhered to the substrate well with 50/50 ethanol in distilled H_2O. After the two hour duration, the partially charged monolayer was taken out of the flask and analyzed using an atomic force microscopy—Kelvin force microscopy method, AFM/ KFM.

The maximum scan range for the AFM/KFM is 100 × 100 μm while our Au substrate was 1 × 1 cm. Therefore we double-masked the substrate so that each 103 μm square on the pattern had one half with a DMBP monolayer and the other half with a DMBP monolayer that had been exposed to mercury (II) percholorate hydrate. This procedure rendered the sample a useful size for measuring by AFM. Biomaterial with inherent negative charges was then introduced to the partially charged monolayer surface.

Results:

After cleaning with the argon plasma, the optical constants obtained were Ns = 0.186 and ks =3.400. The average thickness of the monolayer was 14.90Å. After the two hour time duration of creating the partially charged monolayer, the substrate no longer had photoresist on certain areas. Using a different approach, 50/50 ethanol in distilled H_2O was used. It seemed the photoresist adhered to the substrate well with 50/50 ethanol in distilled H_2O. Photolithography was used to double mask the substrate. The size of the substrate was initially too big to measure by AFM/KFM. For this reason, a partially charged monolayer was made on each of the patterned squares as an alternative to using the entire substrate (Figure 3). The biomaterials exposed to the partially charged monolayer included red blood cells, cellulose, and sulfuric acid in cellulose. Unfortunately the biomaterials did not preferentially adhere to the positive charges on the monolayer (Figure 4). The biomaterials covered the entire surface of the substrate.

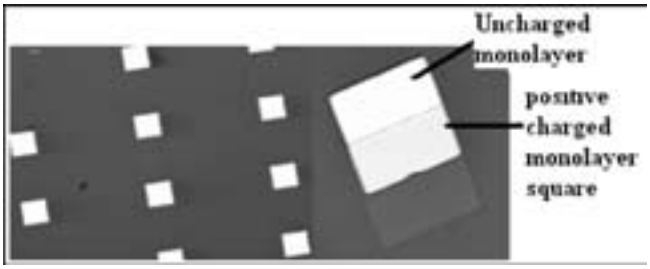

Figure 3: Patterned monolayer substrate (on left). Double patterned partially charged square (on right).

Conclusion:

We successfully created a patterned surface of 102 μm gold squares using photolithography. We were also successfully in preparing a single monolayer of DMBP on Au (111). In addition, we developed a method to selectively place charges on a monolayer. However, we did not show preferential adhesion of biomaterials to the positively charged areas of the monolayer.

Future work will include using other biomaterials in proving preferential assembly to charged surfaces. Finally, the continued study of the surfaces by AFM/KFM will be pursued in an effort to improve the patterning of the surfaces.

Acknowledgments:

I would like to thank the National Science Foundation, the NNIN REU Program, and HNF staff for the internship opportunity this summer. A special thanks to my principal investigator Dr. James Mitchell and my mentor Dr. Tina Thomas Brower for guiding me and making my first research experience enjoyable. I also wish to thank site coordinator Mr. James Griffin for his guidance and support.

References:

[1] Brower, L.T. "SA Multilayer of 4, 4'-Dimercaptobiphenyl Formed by CU (II)-Catalyzed Oxidation." 18-16 Nov. 2002: 6207-6216.

[2] Jordon, R., A. Ulman, J.F. Kang, S. Liao. "Mixed Self-assembled Monolayers of Rigid Biphenyl Thiols: Impact of Solvent and Dipole Moment." 120-8 April 1998: 9662-9667.

[3] Dickie, D.A., Chan, A.Y.C., Jalali, H., Jenkins, H.A., Yu, H.-Z., Clyburne, J.A.C. "*m*-Terphenyl thiols: rigid and bulky molecules for the formation of bioactive SA monolayers on gold"; Chem. Commim., 2004 2432-2433.

[4] Kane RS, Takayama S, Ostuni E, Ingber DE, Whitesides GM., "Patterning proteins and cells using soft lithography"; Biomats 20 (1999)2363-2376.

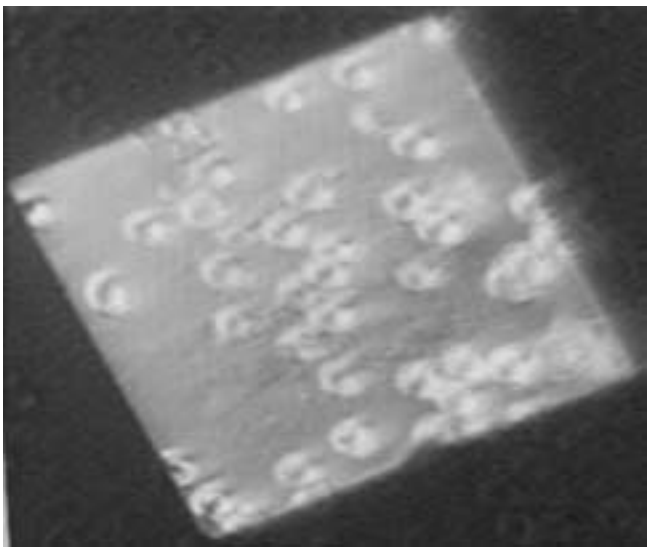

Figure 4: Blood cells did not seem to have a preference on the partially charged monolayer when exposed to the squares on the surface. In the picture above, the cells adhere to the whole square.

Engineering Hcp1 to Bind DNA

Keith Olson

Biochemistry and Psychology, Beloit College

NNIN REU Site: Center for Nanotechnology, University of Washington, Seattle, WA

NNIN REU Principal Investigator(s): Dr. Joseph Mougous, Microbiology, University of Washington-Seattle

NNIN REU Mentor(s): Julie Silverman, Department of Microbiology, University of Washington-Seattle

Contact: olsonk@stu.beloit, mougous@u.washington.edu, silverjm@u.washington.edu

Introduction:

Proteins are appealing building blocks for nanoscale systems because they are inexpensive, biocompatible, and have self-assembling properties. Specifically, protein nanotubes, such as viral capsids, microtubules, and tobacco mosaic viruses have been engineered for nanotechnological applications including nanowire synthesis, drug delivery, and gene delivery [1-3].

Current deoxyribonucleic acid (DNA) processing methods used for DNA sequencing and microarray analysis rely on restriction enzymes that produce oligonucleotides of heterogeneous lengths. Homogenous length DNA would be an advantage to chip based DNA analysis technologies as a way to reduce false positives (incorrect matches of complementary DNA). Nanotubes of discrete lengths could serve as a template for length specific DNA processing.

Our lab has previously demonstrated that Heme Carrier Protein 1 (Hcp1), a homohexameric ring protein secreted by *Pseudomonas aeruginosa*, forms stable nanotubes [4]. Currently, our lab is focused on optimizing Hcp1 to form tubes of discrete length. The potential to control nanotube length makes Hcp1 an ideal candidate for DNA scaffolding applications.

In this study we report progress toward DNA encapsulation with Hcp1. The work presented here, shows that the introduction of positively charged lysines to the interior of Hcp1 can mediate non-specific interactions between Hcp1 and the negatively charged backbone of DNA.

Materials and Methods:

Lysine Mutant Production and Purification. We produced two lysine modified Hcp1 mutants—Asp55Lys and Ser31Lys Asp55Lys—via site-directed mutagenesis. Hcp1 mutants were expressed in *E. coli* and purified over a His-Trap column with an increasing concentration gradient of imidazole buffer and were further purified on a size exclusion column.

Hcp1-DNA Electrophoretic Mobility Shift Assay. 1 μM of 40 base pair (bp) DNA and various protein concentrations of Hcp1 wild type Hcp1 (WT), Hcp1 (Asp55Lys) and Hcp1 (Ser31Lys Asp55Lys) mutants were mixed and incubated for one hour on ice. Next, the reactions were run on a 2% TBE agarose gel at 50 V for two hours, stained with ethidium bromide, rinsed and photographed using UV imaging. The second electrophoretic mobility shift assay (EMSA) incubated 100 nM plasmid DNA with various concentrations of Hcp1 WT, Hcp1 Asp55Lys and Hcp1 Ser31Lys Asp55Lys for 1 hour on ice. The mixtures were run on a 1.5% gel for 4 hours at 50 V, stained with ethidium bromide, rinsed and visualized by UV transillumination using a gel documentation system.

TEM Analysis of Hcp1 Asp55Lys with Cysteine Modifications. Hcp1 lysine mutants with engineered cysteine residues were produced and proteins purified as previously described. Protein samples were stained with uranyl formate and imaged by transmission electron microscopy (TEM).

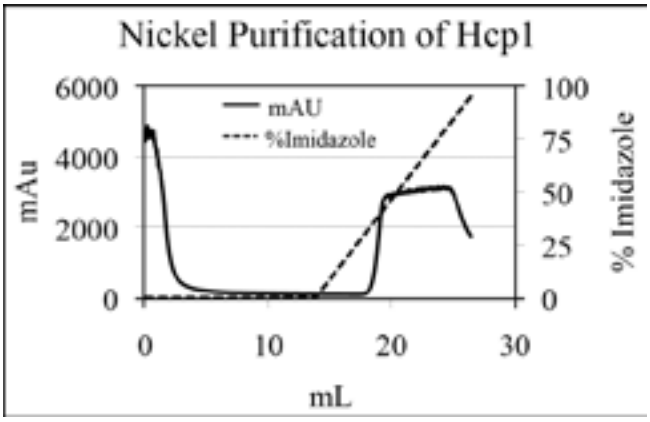

Figure 1: Representative elution profile of Hcp1 lysine mutants.

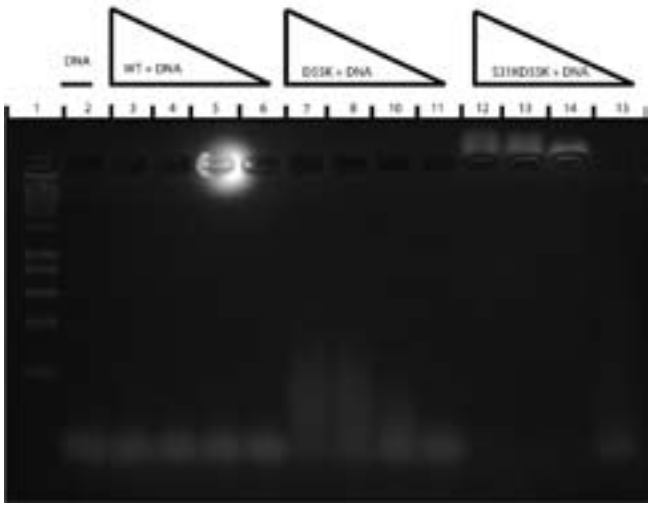

Figure 2: EMSA of DNA in the presence of Hcp1.

Results:

Hcp1-DNA EMSA. We performed electrophoretic mobility shift assays (EMSA) to determine if Hcp1 mutants would bind DNA with greater affinity than the WT. Figure 2 shows varied concentrations of Asp55Lys and Ser31Lys Asp55Lys in the presence of a 1 μM 40 base pair (bp) DNA strand. (Lane 1, DNA Ladder; lane 2, DNA control, lanes 3-6, lanes 7-11 and lanes 12-15 contained WT, Asp55Lys and Ser31Lys Asp55Lys respectively) (10 μM, 7 μM, 4 μM and 1 μM). At high concentrations of Asp55Lys and low concentrations of Ser31Lys Asp55Lys, a smear of DNA is observed, which is not seen with the WT. At high protein concentrations, Ser31Lys Asp55Lys shifts in the slightly positive direction. Additionally, low concentrations of Ser31Lys Asp55Lys weaken the DNA band compared to the DNA control.

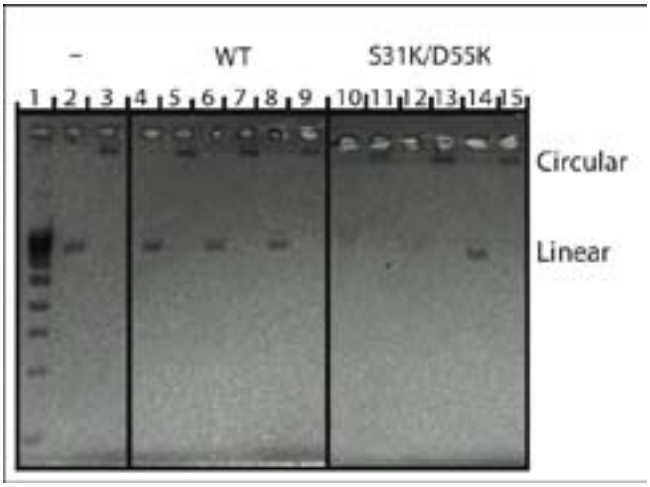

Figure 3: EMSA of circular vs. linear plasmid DNA.

Linear vs. Plasmid DNA EMSA. We utilized an EMSA with circular and linear plasmids to determine if DNA was binding to the interior of the protein. Figure 3 shows Ser31Lys Asp55Lys altered DNA migration patterns of the linear plasmid but not the circular plasmid. Protein concentration decreased left to right; 8 μM, 4 μM, 1 μM in lanes 1 and 2, 3 and 4, and lanes 5 and 6 respectively. The linear DNA shifted at high concentrations of Ser31Lys Asp55Lys.

TEM Hcp1 Asp55Lys with Cysteine Modifications. Transmission electron microscopy (TEM) visually confirmed Hcp1 Asp55Lys tube formation as previously described by Ballister et. al. [4] (Figure 4).

Discussion:

This work demonstrates the preliminary steps towards producing DNA encapsulating tubes. We show the introduction of positively charged lysine to the interior of Hcp1 promotes a non-specific DNA-protein interaction. At high concentrations of Ser31Lys Asp55Lys, an upward shift indicates a positively charged and possibly large DNA-protein complex. However, these results may suggest an aggregated complex of DNA and misfolded protein. Similarly, DNA smears can stem from a variety of possibilities including DNA being released during electrophoresis, numerous complexes forming and the presence of various charged species. Therefore, this experiment is inconclusive.

Preliminary evidence suggests DNA is binding to the interior of Hcp1. First, the protein eluted at the volume expected for the hexamer (data not shown). The linear plasmid migration pattern was altered in the presence of Ser31Lys Asp55Lys whereas the circular plasmid did not appear to show shift (Figure 3). This suggests DNA is binding to the interior of the protein because the linear DNA has exposed ends to allow for binding to the interior of Hcp1. This evidence depends on stable ring formation, which has not been conclusively determined yet. Although clear evidence of stable ring formation is not available for the Ser31Lys Asp55Lys mutant, we did observe intact ring conformation and tube formation for Asp55Lys (Figure 4).

Future steps include imaging the interaction between Hcp1 mutants and DNA encapsulation for tubes. The introduction of a di-copper complex at the top and bottom of an Hcp1 tube could cut DNA based on tube length. Di-metal complexes have shown to non-specifically cut the backbone of DNA5. This system would serve as an excellent scaffold to synthesize homogenous length DNA strands.

Acknowledgements:

I would like to thank Julie Silverman, Dr. Joseph Mougous, the Nanotechnology Infrastructure Network Research Experience for Undergraduates Program and National Science Foundation for funding.

References:

[1] Lamber, O, Letellier L, Gelbart WM, Riguad JL; "DNA delivery by phage as a strategy for encapsulating toroidal condensates of arbitrary size into liposomes"; J Gen Virol 81, 2531-2543 (2000).

[2] Cooper, A., Shaul, Y; "HBV viral capsid"; Biophysical and Biochemical Research Communications, 327, 1094-1099 (2005).

[3] Wang, Y, Schwedes, J, Mann, K, Tegtmeyer, P; "Interaction of p53 with its consensus DNA-binding site"; MolCellBio, 15, 1094-99 (2000).

[4] Ballister, E., et al.; "In vitro self-assembly of tailorable nanotubes from a simple protein building block"; Proc Natl Acad Sci USA, 105, 3733-3738 (2008).

[5] Rey, N., et al.; "Catalytic Promiscuity in Biomimetic Systems: Catecholase-like Activity, Phosphatase-like Activity, and Hydrolytic DNA Cleavage Promoted by a New Dicopper(II) Hydroxo-Bridged Complex"; Inorg. Chem., 46, 348-350 (2007).

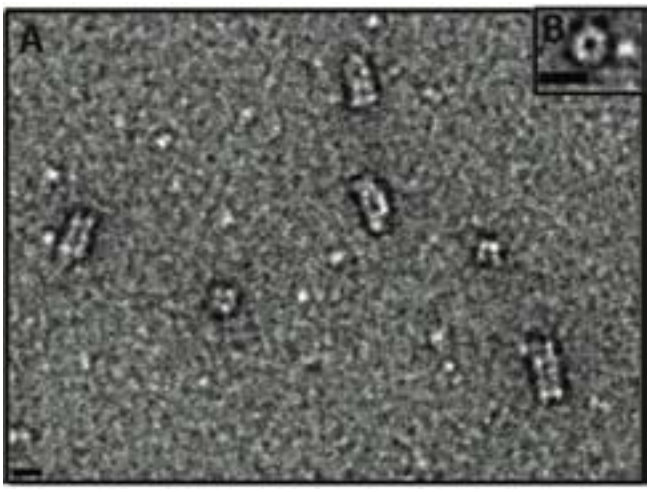

Figure 4: TEM of Hcp1 D55K with cystiene modifications.

Nano-Magnetic Particles for Cancer Diagnostics

Barbara D. Raynal

Electrical Engineering, University of Notre Dame

NNIN REU Site: Stanford Nanofabrication Facility, Stanford University, Stanford, CA

NNIN REU Principal Investigator(s): Prof. Shan X. Wang, Materials Science and Electrical Engr, Stanford University

NNIN REU Mentor(s): Mingliang Zhang, Robert Wilson, Materials Science, Stanford University; Dr. Mary Tang, Stanford Nanofabrication Facility, Stanford University

Contact: braynal.at.nd.edu, sxwang.at.stanford.edu, mzhang2@stanford.edu, bobmse@stanford.edu, mtang@stanford.edu

Abstract:

Nano-magnetic particles can be used to detect cancer cell markers in biological fluids. Cancer proteins are tagged with magnetic particles to identify cancer proteins since magnetism is rare in biological systems. The objective of this work was to create nano-magnetic particles of varying sizes that could be used to study the detection of different kinds of cancer cells. First, a monolayer of polymer nanospheres was spincoated onto a silicon wafer. The nanospheres were then etched and used as a mask to create a template consisting of tiny pillars. A second silicon wafer was then coated with polymethylglutarimide (PMGI) and polymethylmethacrylate (PMMA). The template was imprinted onto the PMMA layer of the second wafer to create many holes the size of the pillars. Next, the PMGI layer was etched with LDD26W to create deeper holes, followed by metal deposition. The metal fell into the holes and nanoparticles the size of the etched nanospheres were created. By varying the etching parameters it was possible to create templates with different pillar size, and by using one of the templates it was possible to create nanoparticles with the purpose of facilitating the detection of different kinds of cancer cells.

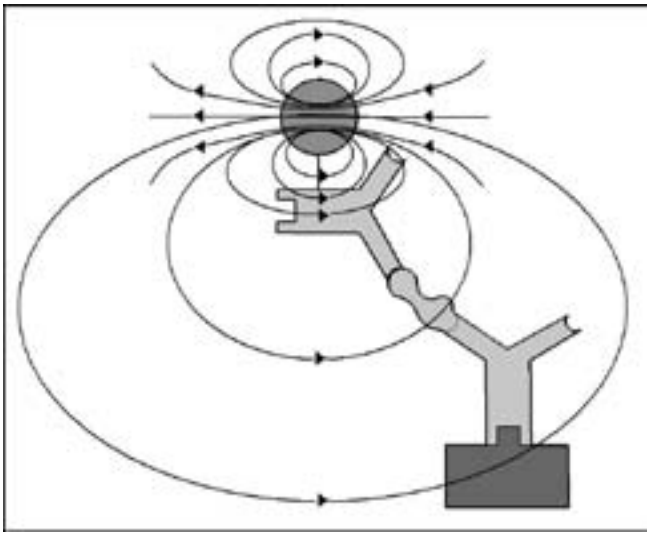

Figure 1: Sensor detecting the magnetic field of the nano-particle.

Introduction:

A silicon chip was embedded with sensors that were coated with different kinds of antibodies. When the blood sample was added, the antibodies grabbed specific cancer related proteins. A solution of nano-magnetic particles attached to antibodies was then added. The added antibodies attached to the captured proteins and a large external magnetic field was applied, which caused the nano-particles to create a stronger magnetic field. If the magnetic field created by the particles was detected by the sensor, it meant cancer related proteins had been found. Figure 1 is a good representation of how the device worked.

The nano-particle was made of five alternated layers of titanium and iron. The purpose of the surface layers of titanium was to prevent the iron layers from oxidizing. The iron layers created magnetic moments which pointed in opposite directions when no external magnetic field was applied so that the net magnetic field was zero. Because iron is a ferromagnetic element, the two layers could act as magnets when an external field was applied. The external field caused the opposing magnetic moments to gradually rotate until they were completely aligned with the external magnetic field, creating an even stronger one which was then detected by the sensor.

A self-assembly process was used rather than electron-beam lithography because the cost per unit area is about a thousand times less expensive for the self-assembly process.

Experimental Procedure:

The first step was to create a mask. First, a silicon wafer was coated with a monolayer of polymer beads that were originally 320 nm in diameter. A mixture of chlorine and oxygen gas was then used for plasma etching on the polymer beads with a resulting diameter ranging from 50 to 200 nm.

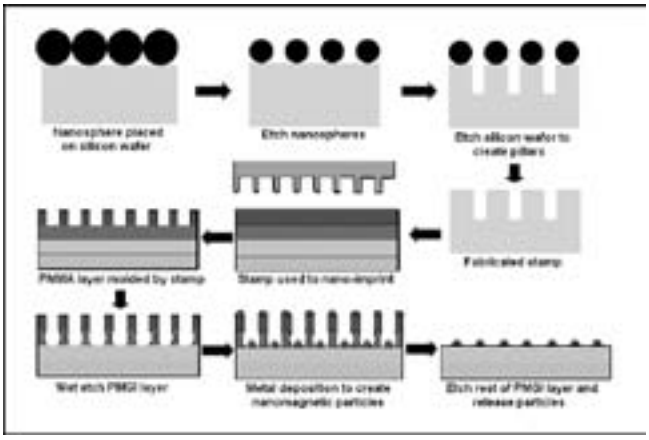

Figure 2: Nano-magnetic particle fabrication process.

The beads acted as a mask so that when the silicon was etched with a mixture of chlorine, hydrobromic acid, helium and oxygen gas, tiny pillars the size of the etched nanospheres were created. After the mask had been created, a second silicon wafer was coated with three polymer layers for the nano-imprinting step: the release layer, PMGI which was the undercut layer, and PMMA. The nano-imprinting was done at a temperature of 180°C. At this temperature, the PMMA layer became soft but the PMGI and release layers remained solid so that when pressure was applied on the wafers, only the PMMA layer was molded by the mask.

Once the mask was removed, tiny holes the size of the etched nano-spheres were left on the PMMA layer. LDD 26W was then used to wet etch the PMGI layer to create a deeper hole where the nano particle had deposited. Layers of iron and titanium were deposited into the holes through metal deposition. The rest of the PMGI layer was then etched and the nano-particles were left on the release layer, which was then dissolved in order to release the nano-particles. The fabrication process is represented in Figure 2.

Results and Conclusions:

Masks of different pillar size were created by varying the etching time. The polymer sphere etching was first done starting at 10 seconds up to 30 seconds with 5 second intervals in between. All of the samples turned out to be under etched except the 30 second etched sample. A few more masks were then made with different etching times centered at 30 seconds. Through this process of varying etching times, it was possible to successfully create two masks with optimal pillar dimensions for the creation of nano-magnetic particles at 27 and 29 seconds etching times for the polymer spheres, and a 35 second etch for the silicon wafer. The 27 second etched mask is shown in Figure 3. The diameter of the pillars is 120 nm and their height is 212 nm. A previously made mask using 390 nm polymer spheres was used to create nano particles through the nano-imprinting process. The particles are shown in Figure 4.

Future Work:

In the future, nano-particles will be created using the 27 and 29 second etched masks as well as working on finding ways by which the nano-magnetic particles can be attached to the antibodies.

Acknowledgements:

I would like to thank my mentors Mingliang Zhang, Dr. Mary Tang, Dr. Robert Wilson, my PI Prof. Shan X. Wang, our site coordinator Dr. Michael Deal, Maureen Baran and the SNF staff, the National Nanotechnology Infrastructure Network Research Experience for Undergraduates Program and the National Science Foundation.

References:

[1] S.J. Osterfeld, H. Yu, R.S. Gasataer, S. Caramuta, L. Xu, S.-J. Han, D.A. Hall, R.J. Wilson, S. Sun, R.L. White, R.W. Davis, N. Pourmand, and S.X. Wang. "Multiplex protein assays based on real-time magnetic nanotag sensing." PNAS vol. 105 no. 52 (2008): 20637-20640.

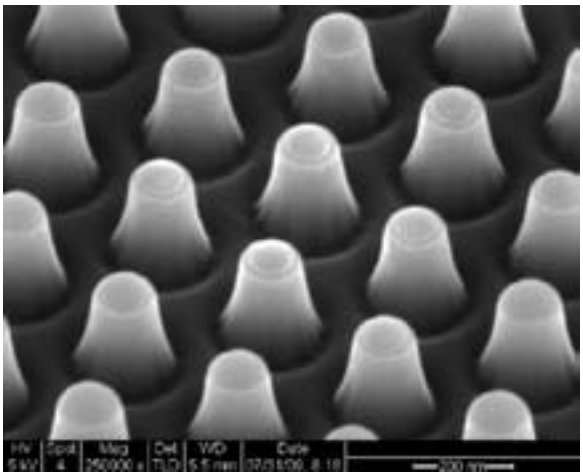

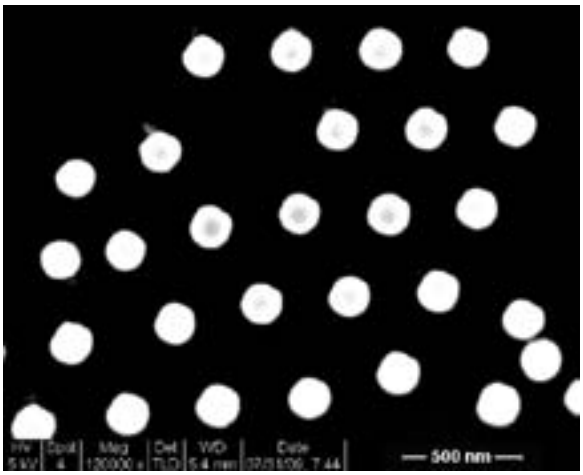

Figure 3, top: Resulting mask after a 27 second etch of the polymer nano-spheres.

Figure 4, bottom: Nano-magnetic particles created by nano-imprinting.

Optimization and Bioconjugation of Silicon Nanowire Biosensors for Cancer Marker Detection

Jacob Sadie

Electrical Engineering, Clemson University

NNIN REU Site: Nanotechnology Research Center, Georgia Institute of Technology, Atlanta, GA
NNIN REU Principal Investigator(s): Dr. James Meindl, Electrical Engineering, Georgia Institute of Technology
NNIN REU Mentor(s): Ramasamy Ravindran, Electrical Engineering, Georgia Institute of Technology
Contact: jake.sadie@gmail.com, james.meindl@mirc.gatech.edu, rravindran@gatech.edu

Introduction:

Silicon nanowire (SiNW) biosensors are highly sensitive nanoscale field-effect transistors. Because the channel width and height are on the nanometer scale, minor environmental alterations elicit obvious changes in the transistor's conductivity [1].With proper bioconjugation techniques, the presence of bound molecules in buffer solutions will alter the surface charge on the nanowires, changing the conductivity of the wire and indicating the sensing event [2]. Label-free methods are more cost and time-effective than labeled procedures, so we will focus our work on successful label-free procedures for ultimately detecting cancer markers [1]. Our process is a top-down fabrication technique including electron-beam lithography for the patterning of silicon nanowires. This project focused on optimizing the fabrication process by (a) adjusting the electron-beam resist application and etching procedures, (b) modifying the annealing procedures before and after electrode deposition, and (c) determining optimal conditions for pH sensing and protein bioconjugation.

Procedure:

Fabrication. The fabrication process began with electron-beam lithography (EBL) using negative resist hydrogen silsesquioxane (HSQ) spun on a silicon-on-insulator (SOI) wafer. The pattern was an array of sixteen nanowires. After lithography, we developed the resist with resist developer MF-319. Next, dry plasma etching with a standard oxide etcher (SOE) removed both silicon and HSQ to expose the silicon nanowires (SiNW) and buried oxide layer (BOX). To optimize the resist procedure, the initial thickness of HSQ was found using an automated film thickness measuring system. By varying the initial thickness (~ 30-40 nm) and etch time (14-20 sec) and then using a profilometer to measure the final thickness, the etch rates of HSQ, silicon, and the BOX could be found. Next, an oxygen anneal in a rapid thermal processor (RTP) reduced damage caused by the etching process and grew an oxide layer on the SiNWs. Our wafers underwent optical lithography (NR9-1500PY resist) and electron-beam evaporation to pattern the aluminum electrode contacts. A final forming gas anneal was performed in the RTP to ensure contact between the SiNWs and aluminum contacts. The time for this anneal was varied to determine the most effective procedure. A final passivation step exposed the tips of the aluminum electrodes and a small rectangular region around the nanowire array to prepare for wet testing.

Testing. Dry testing involved a three-point probe, where the source and drain were two electrodes on either end of the SiNW and the chuck acted as a back-gate. We used a semiconductor parameter analyzer to measure the drain current versus source drain voltage at varying gate voltages as well as the transconductance of the nanowires. To perform wet testing we attached glass wells around the exposed nanowire array using crystal bond. Then, buffer solutions at different pH levels were transferred in and out with a micropipetter. A third test was also performed, which plotted the transient drain current as buffer solutions in the well were changed.

Functionalization. The final procedure for protein conjugation required silicon nanowire functionalization with 3-aminopropyltriethoxysilane (3-APTES) [3]. We then bonded fluorophore-tagged (FITC) proteins to the 3-APTES molecules using a 2-(*N*-morpholino) ethanesulfonic acid (MES) buffer solution, a cross linker, and an activator.

Results:

Resist Optimization. We were able to characterize the etch rates of HSQ, silicon, and BOX in our given plasma process (Figure 1). The most important etch rate determined was the HSQ etch rate. Previously, the initial HSQ thickness of the process was approximately 80 nm, which meant that even after a buffered oxide etch (BOE) dip, HSQ may have remained

Spin	Average HSQ Height After EBL (nm)	Standard Deviation (nm)
1	41.6	0.9
2	33.1	1.4

Spin	Average Etch Rates (nm/s)			Standard Deviation (nm/s)		
	Si	BOX	HSQ	Si	BOX	HSQ
1	5.9	0.9	1.6	0.0	0.1	0.1
2	5.9	1.0	1.5	0.0	0.3	0.3
Cumulative	5.9	1.0	1.6	0.0	0.2	0.2

Figure 1: Silicon, buried oxide, and HSQ etch rates.

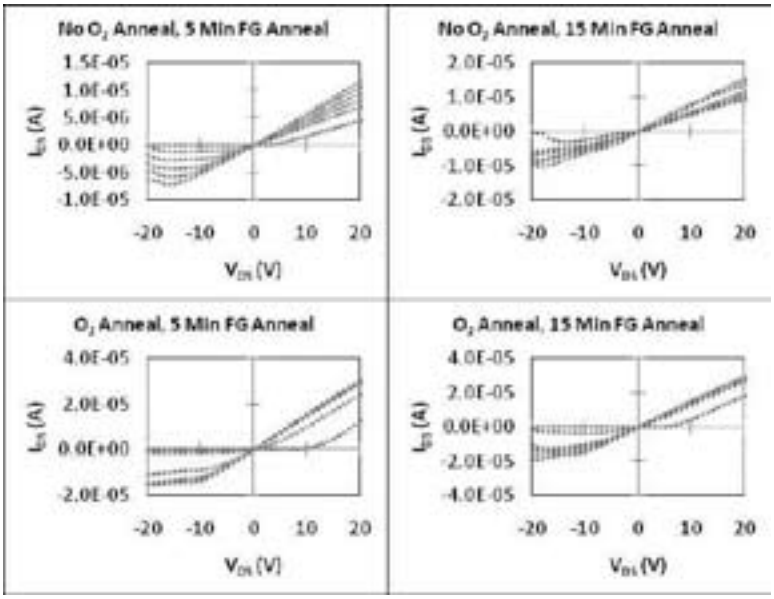

Figure 2, above: Anneal optimization results.

Figure 3, below: Transient pH test results.

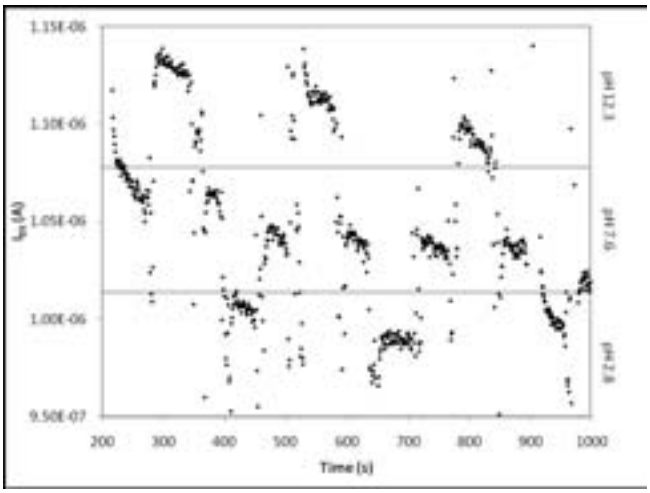

on the SiNW and prevented bioconjugation. Now, we have optimized initial HSQ thickness to be approximately 40 nm, allowing the plasma etch to nearly remove all of the HSQ and ensuring complete removal after a short dip in BOE.

Anneal Optimization. Our tests altered the two anneal procedures to determine the most effective process before and after metallization. Results seen in Figure 2 reveal that the initial oxygen anneals prior to metallization proved necessary, as the drain current range was doubled as a result of this anneal. In addition, we determined that there is no significant difference between a five or fifteen minute post-metallization anneal with FG. Finally, energy dispersive spectroscopy (EDS) indicated that thirty minute FG anneals would sometimes cause the aluminum to diffuse the length of the SiNW, effectively creating short circuits.

Potential of Hydrogen (pH) and Bioconjugation. Figure 3 indicates that our chips can sense and function over a range of pH levels. However, there was only an approximately 15% change in current over our large pH range rather than reported current changes of about 50% over similar pH ranges [3]. Finally, our bioconjugation techniques proved successful as seen in Figure 4. When performing a photobleaching process with confocal microscopy, we confirmed the binding of proteins to a silicon dioxide substrate.

Future Work:

The next steps will be to apply the bioconjugation techniques we have begun to the SiNW array in order to begin protein sensing experiments. Finally, because label-free methods are the ultimate goal, we will begin researching methods for label-free bioconjugation and testing.

Acknowledgements:

I would like to acknowledge Dr. James Meindl and Ramasamy Ravindran for granting me the opportunity to work on this project. In addition, I would like to thank the members of the GSI group for being so welcoming and the MiRC staff for providing a hospitable work environment. Finally, thanks to the National Science Foundation and the National Nanotechnology Infrastructure Network Research Experience for Undergraduates (NNIN REU) Program for funding.

References:

[1] Stern E, "Label-free sensing with semiconducting nanowires" (PhD dissertation, Yale University, 2007) pp. 39-93.

[2] Stern E, Vacic A, Reed MA, "Semiconducting Nanowire Field-Effect Transistor Biomolecular Sensors," IEEE Transactions On Electron Devices, vol. 55, pp. 3119-3130, Nov. 2008.

[3] Cui Y, Wei QQ, Park HK, Lieber CM, (2001) "Nanowire nanosensors for highly sensitive and selective detection of biological and chemical species," Science 293:1289–1292.

Figure 4: Bioconjugated and photobleached SiO_2 substrate.

Development of an Intravessel Xylem Probe for Viniculture and Forest Ecology

Ellen Sedlack

Microelectronic Engineering, Rochester Institute of Technology

NNIN REU Site: Cornell NanoScale Science and Technology Facility, Cornell University, Ithaca, NY
NNIN REU Principal Investigator(s): Abraham Stroock, Chemical and Biomolecular Engineering, Cornell University
NNIN REU Mentor(s): Amit Pharkya, Chemical and Biomolecular Engineering, Cornell University
Contact: exs2093@rit.edu, ads10@cornell.edu

Abstract:

This research project presents the design, fabrication and testing of a single, hollow microneedle whose purpose was to be integrated with a water pressure sensor to form a microelectromechanical systems (MEMS) intravessel xylem probe (IVXP). The intent of this IVXP would be to continuously extract a fluid sample from plant xylem to monitor water content. Double polished silicon wafers were coated with photoresist, patterned via photolithography, and deep reactive ion-etched. The resultant matrix of various needle dimensions was diced to create individual needles, which then were characterized with grape vine xylem. Successful xylem insertion was observed for needles of 200 μm in length.

Introduction/Background:

Botanical research demands improved technology to measure water transport in the xylem tissue of plants. Initial methods were indirect as they measured, in surrogate, the water content of air and soil. Current lab-confined probes [1] yield a single measurement per puncture, are destructive to the plant tissue and suffer from a pressure limit of minus 10 atmospheres (atm).

As plant fluids function at relatively high negative pressures, this sap is metastable and defies easy extraction; this liquid readily changes phase from liquid to gas, which sabotages analysis. The design of this project's *in situ* probe, inserted into xylem, would continuously read water flow in a growing plant and would provide readings down to minus 80 atm. A micro-proportioned needle could traverse the short distance into the xylem but without causing plant mortality.

The smaller needles feature a 20 μm inner diameter and a 30 μm outer diameter. The largest needles feature a 40 μm inner diameter and a 100 μm outer diameter. Recent micro-needle research and development [2] has etched needles as arrays, because, due to strength in numbers, these needles are less submissive to fracture. However, this project required a single needle strong enough to survive xylem probing. A successful microneedle should both penetrate grape leaf xylem without fracture and enable sufficient fluid transport of plant sap through its bore, without clogging. Nitrite sensors for plant nutrition logically could follow. Parallel fabrication and low device maintenance would ensure effective cost control.

Fabrication:

After furnace deposition of silicon nitride (Si_3N_4), the Si_3N_4 on the backside of the wafer was patterned using contact lithography and etched to create an etch mask. The exposed silicon was then etched using 33% potassium hydroxide at 90°C for 35 minutes. This created a backside trench of 68 μm deep (Figure 1). The presence of this trench reduced the time necessary to create a through hole in later inside-diameter etching. The trench also created a site for future pressure sensor placement. The next few steps in the process are shown in Figure 2. First, the annulus was patterned; 3 μm of oxide was first deposited on the front side of the wafer using plasma enhanced chemical vapor deposition (PECVD).

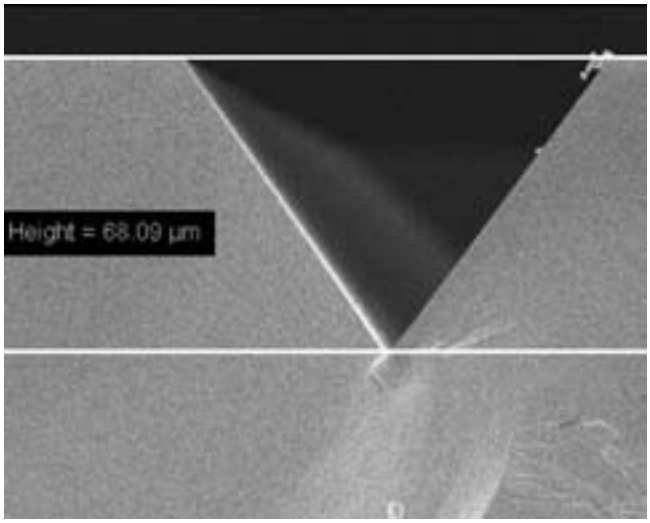

Figure 1: SEM of backside trench.

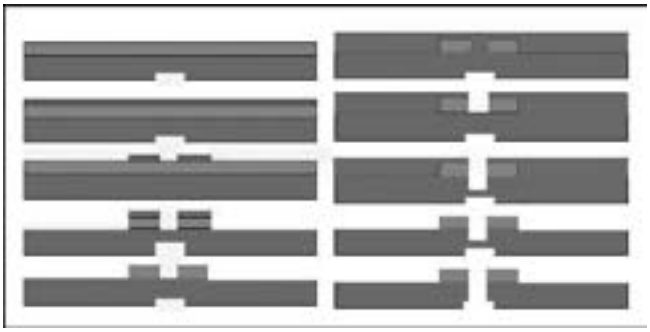

Figure 2: Process flow for needle fabrication.

This oxide was then patterned with contact lithography and etched using a 6:1 buffered oxide etch (BOE) for 35 minutes. The remaining oxide, after resist removal, served as silicon etch mask for the purpose of etching the annulus. Since only the inside diameter of the needle needed to be etched completely through the wafer (a longer etch time as opposed to the outside diameter etch duration), photoresist was applied and patterned in a manner such that only the inner diameter silicon was etched away. An initial 125 μm was etched using the Oerlikon deep silicon etcher. Then, after removing the resist, etching was continued so that the entire wafer (except the annulus, masked with oxide) was etched. This process created the sidewalls and allowed for further inner diameter etching. Upon etch completion, needle lengths of 150 to 200 μm were measured (Figure 3).

Results and Discussion:

Difficulties in boring completely through to the other side of the wafer were experienced. Further, in cases of sidewall thicknesses of less than 15 μm, the elongated episodes of linear etching down the length of the needle shaft partially eroded through these sidewalls (Figure 4). This resulted in needle breakage. Thicker sidewalls did survive etching and their strength was tested.

For initial testing of these needles, in lab methods were used. A grape vine leaf was removed from the plant and pressurized to mimic the vacuum existing in plants. Microneedle insertion into the xylem was monitored via microscope. Insertion was successful with needles of 200 μm length. Shorter needles drifted off location which resulted in breakage. The development of a single hollow microneedle requires further research and development. Longer etch times prior to resist removal could ensure through-hole success, and longer etches after resist removal (for needles with larger wall thicknesses) could generate longer needles. The fabrication of tapered versus parallel-walled needles should be explored. Ultimately, successful needle manufacture should be followed up with the installation of the water pressure sensor and nitrate sensor.

Acknowledgements:

I would like to thank the following organizations and people: National Nanotechnology Infrastructure Network Research Experience for Undergraduates (NNIN REU) Program; National Science Foundation; Cornell NanoScale Science & Technology Facility; CNF Staff especially Melanie-Claire Mallison; my PI: Abraham Stroock; my mentor: Amit Pharkya; Vinay Pagay, Peter J. Melcher, and CNF users: Stephen Jones and Nicolás Sherwood Droz.

References:

[1] "Comparative measurements of xylem pressure in transpiring and non-transpiring leaves by means of the pressure chamber and the xylem pressure probe", P.J. Melcher et al., Journal of Experimental Botany, Vol.49, n°327, pp.1757-1760, October 1998.

[2] "Microneedle array for transdermal biological fluid extraction and *in situ* analysis", E.V. Mukerjee et al., Sensors and actuators A, Physical, 2004, vol. 114, no2-3, pp. 267-275.

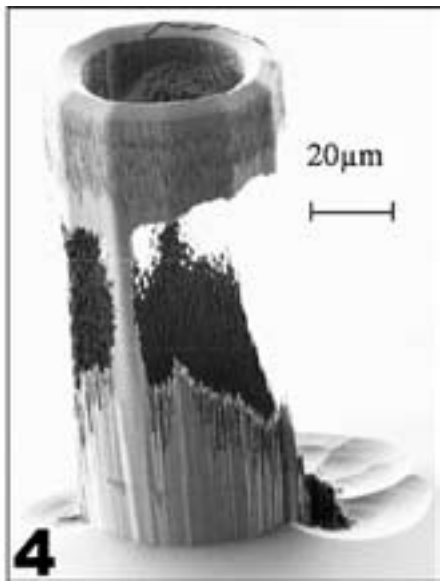

Figure 3: SEM of needle after etch completion.

Figure 4: Sidewall damage on needles with sidewall thicknesses of less than 15 µm.

Artificially-Manufactured Surface-Enhanced Raman Scattering-Active Nanoparticles for Cancer Diagnostics

Sweta Sengupta

Biology and Computer Science, Emory University

NNIN REU Site: Stanford Nanofabrication Facility, Stanford University, Stanford, CA

NNIN REU Principal Investigator(s): Dr. Shan Wang, Material Science and Electrical Engineering, Stanford Nanofabrication Facility, Stanford University, Stanford, CA

NNIN REU Mentor(s): Dr. Jung-Sub Wi, MSE, Stanford University; Dr. Robert Wilson, MSE, Stanford University; Dr. Mary Tang, Stanford Nanofabrication Facility, Stanford University

Contact: ssengu2@emory.edu, sxwang@stanford.edu

Abstract:

Surface-enhanced Raman scattering (SERS) is a powerful method for examining biological samples. Antibody marked SERS-active nanoparticles can be used in human serum bioassays to detect cancer cells. In this report, we show preliminary results on artificially engineered SERS nanoparticles. These nanoparticles are designed for enhancing a local electromagnetic field and are fabricated by nanoimprint lithography, thin film deposition, and release of nanoparticles from substrate. Uniformly created nanoparticles and their enhanced Raman signals are confirmed by scanning electron microscope and Raman spectroscopy.

Introduction:

Raman scattering, which is based on the energy shift by inelastic scattering between incident photons and molecules, has long been considered to have possible diagnostic advantages. Raman scattering produces a sharp spectrum, not susceptible to photobleaching, and maintains multiplexing capabilities.

Despite the advantages, Raman scattering is weak and nearly indistinguishable from background noise. However, with the advent of surface-enhanced Raman scattering (SERS), created from the adsorption of textured, aggregate, and/or structured nanometer sized metal nanoparticles to Raman dye, signal intensity of Raman scattering can be increased several folds, making Raman dyes a feasible option as labels in immunoassays.

For achieving this benefit, many research groups have been studying the enhanced Raman scattering from clustering of nanoparticles. However, reliability and controllability of aggregated nanoparticles with rough and irregular surfaces are still under investigation [1].

Here, we performed preliminary fabrication and assessments of the validity of artificially designed SERS nanoparticles and their potential to amplify Raman scattering. Our research idea was to create SERS nanoparticles with uniform size and shape by using nanoimprint lithography. These nanoparticles also could be functionalized with antibodies for bioassay purposes.

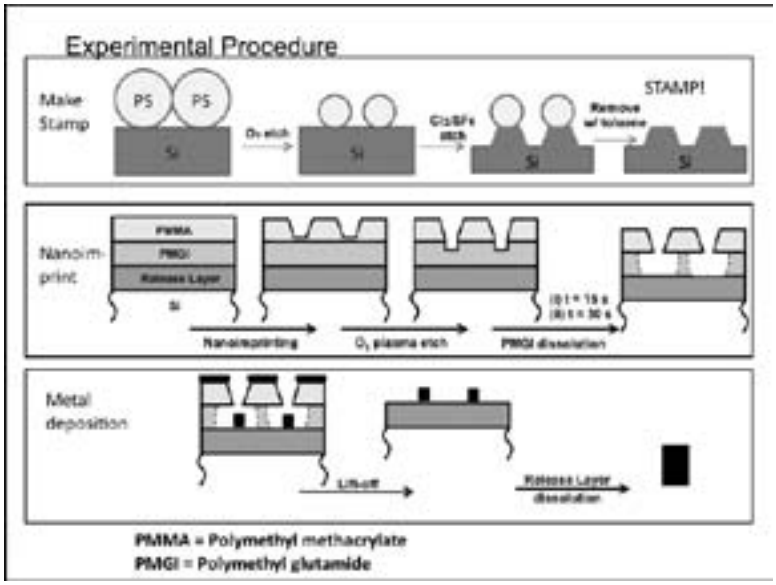

Figure 1: Nanoparticles were created using three steps: make a stamp, nanoimprint, and then metal deposition.

Experimental Procedure:

At first, a nanoimprint stamp was created by selective plasma etching of a silicon (Si) substrate with spin coated polystyrene beads as an etching hard mask. Using the anisotropic oxygen (O_2) plasma condition for reducing a size of polystyrene bead and anisotropic chlorine sulfur hexafluoride (Cl_2/SF_6) plasma condition for vertical etching of Si substrate, the

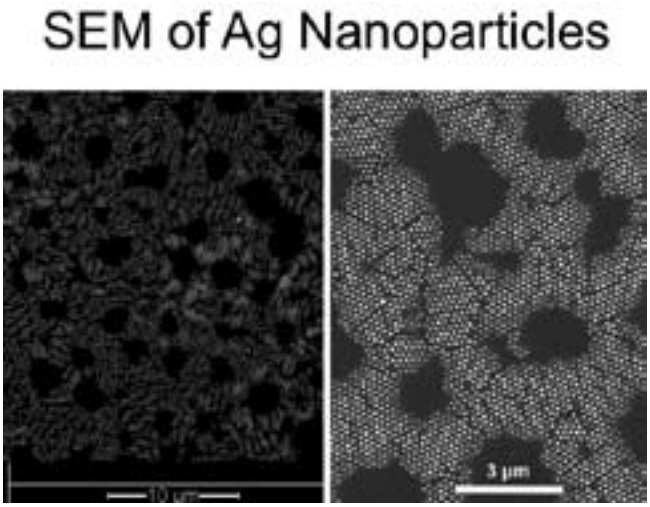

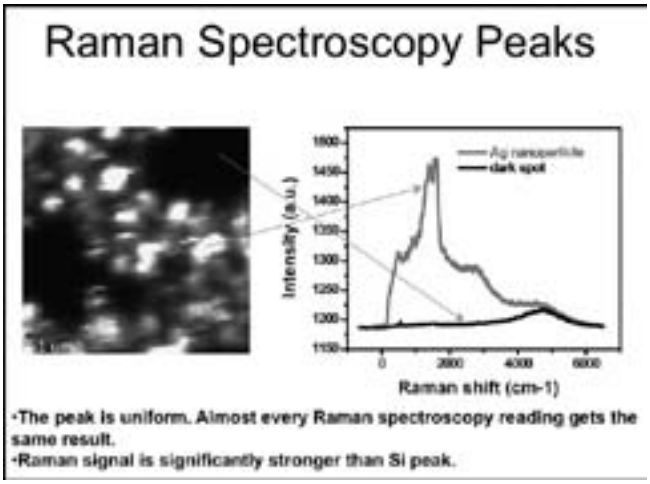

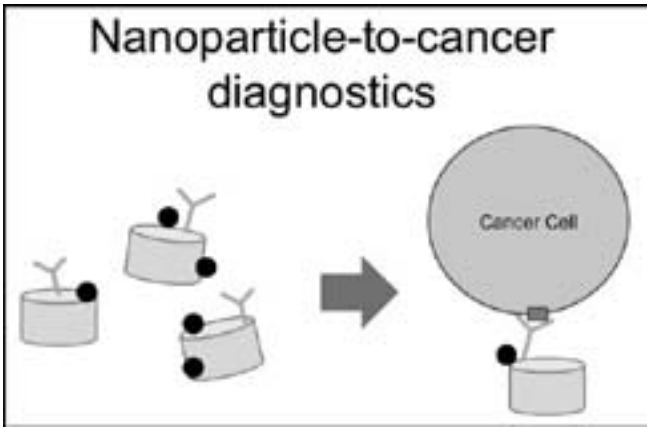

Figure 2, top: Plan view SEM images of unreleased 70 nm diameter Ag nanoparticles.

Figure 3, middle: The above Raman spectroscopy data demonstrates that the bright regions from the Raman intensity map (left) corresponds to the 1600~1700 cm^{-1} Raman peak (right), which is characteristic of methylene blue. The Raman peak reading was also uniform and reproducible.

Figure 4, bottom: The diagram demonstrates how Ag nanoparticles with Raman dye (small circles) and antibodies (y-shaped structures) can localize to cancer cell markers.

nanoimprint stamp was fabricated. Once the stamp was created, nanoimprint lithography, O_2 plasma etching, PMGI dissolution, and silver (Ag) film deposition were carried out sequentially for creating Ag nanoparticles, as depicted in Figure 1. Ag nanoparticles were then submerged overnight in a methylene blue (Raman dye) solution. Scanning electron microscopy (SEM) and Raman spectroscopy were used to characterize the particles and assess the SERS, respectively.

Results and Conclusions:

We were able to create a nanoimprint stamp with a 70 nm sized nano-dot array by studying and optimizing etching conditions for polystyrene and Si substrates. With this stamp, uniform Ag nanoparticles with 70 nm diameter and 30 nm thicknesses were successfully created (Figure 2). The preliminary Raman spectroscopy analysis demonstrated the presence of a huge Raman signal enhancing from the Ag nanoparticles. In addition, the Raman signal peak was uniform and reproducible (Figure 3).

Future Work:

The next step will be to functionalize the SERS nanoparticle surface with various antibodies and examine biological samples (Figure 4). We will also investigate more techniques to enhance Raman scattering, including creating surface roughness and irregularities.

Acknowledgements:

I would like to thank Jung-sub Wi, Bob Wilson, Maureen Baran, Edward Barnard, Mingliang Zhang, Mary Tang, Mike Deal, Shan Wang, and the National Nanotechnology Infrastructure Network Research Experience for Undergraduates (NNIN REU) Program.

References:

[1] K.Kneipp, M. Moskovits, H. Kneipp (Eds): Surface-Enhanced Raman Scattering- Physics and Applications. Topics Appl. Phys. 103, 409-426 (2006) Springer-Verlag Berlin Heidelberg. 409-424.

Development of a Multiplex CARS Flow Cytometer for Label-Free, Real-Time Classification

Hamsa Sridhar

Physics and Mathematics, Harvard College

NNIN REU Site: Nanotechnology Research Center, Georgia Institute of Technology, Atlanta, GA
NNIN REU Principal Investigator(s): Prof. Ali Adibi, Electrical and Computer Engineering, Georgia Tech
NNIN REU Mentor(s): Dr. Siva Yegnanarayanan, Charles Camp, Electrical and Computer Engr, Georgia Tech
Contact: hsridhar@fas.harvard.edu, adibi@ece.gatech.edu, sivay@ece.gatech.edu, ccampjr@ece.gatech.edu

Abstract:

An effective, label-free method of identifying unknown particles in a flow cytometer is presented through the application of multiplex coherent anti-Stokes Raman spectroscopy (MCARS) to a microfluidic chip. Various designs for microfluidic channels were theoretically modeled using COMSOL Multiphysics and fabricated using photolithography. A program was written in MATLAB to perform principal component analysis in order to determine the spectra of unknown substances and to classify them in real-time. As proof of principle, chemically specific differentiation of polystyrene microbeads and oil was experimentally demonstrated.

Introduction:

Flow cytometers are used to observe and characterize individual microscopic particles, such as cells, in a stream of fluid. The major advantage of using these devices, as opposed to examining single droplets in a microscope, is the high throughput of sample in a given time frame. Current cytometers use laser scattering to classify cell size and shape, and fluorophores, which bind to specific proteins on the surface of a cell, for chemical identification. However, such endogenous fluorophores can disrupt the physiological systems of living samples. Moreover, it requires advance knowledge of the substances present. Additionally, the large fluorescence bandwidth renders multiplexing of multiple fluorophores challenging; it also requires hardware-intensive structures, including the use of several pump lasers at different wavelengths and unique sets of excitation/emission filters and photomultipliers (PMTs) for each multiplex channel. Hence, there is a need for chemically specific, label-free classification in a flow cytometer.

In this work, MCARS was applied to cytometric analysis on a microfluidic chip. Multiplex coherent anti-Stokes Raman scattering (MCARS) is a label-free method of optical imaging that uses the vibrational chemical signature of molecules to uniquely identify and visualize them. As a result, it eliminates the need for fluorophores. Moreover, the coherent pumping of Raman bands and multiplex detection allow for high sensitivity and full spectrum measurements (Figure 1). This new addition to flow cytometry complements traditional sizing and morphological information with fluorophore-free chemical information. Moreover, the narrow Raman spectral peaks, compared to the broad emissions from fluorophores, further facilitate multiplexing.

The aim of this project was to fabricate a MCARS cytometer that could effectively flow a mixture of various cells in a stream of fluid, and analyze their chemical signatures in real-time, thereby allowing for down-stream sorting of the sample. (See Figure 1.)

Microfluidic Design. Fluid flow is governed by the Navier-Stoke equation. In microfluidics, flow speeds are approximately quartically proportional to the channel diameter. Therefore, microfluidic channels were designed to perform hydrodynamic focusing, a method of maintaining fast and thin sample flows by means of adding a sheath fluid. Such focusing was theoretically modeled in COMSOL Multiphysics through the Navier-Stokes incompressible flow and convection / diffusion modules (Figure 2). It was found through this form of analysis that for a 1000 psi pressure drop across the sample microfluidic channel, a volumetric flow rate of approximately 3 microliters per second could be achieved. This would allow the system to analyze approximately 30 to 3×10^5 cells per second, depending on sample concentration

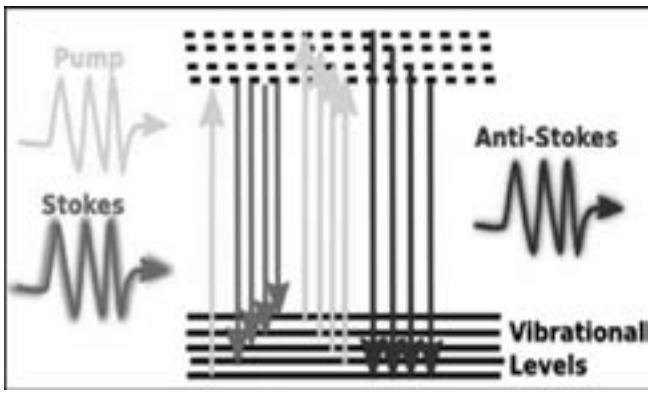

Figure 1: The energy-level diagram for MCARS is shown. The use of white light as the Stokes beam allows gathering of information about all the vibrational energy states of the molecule.

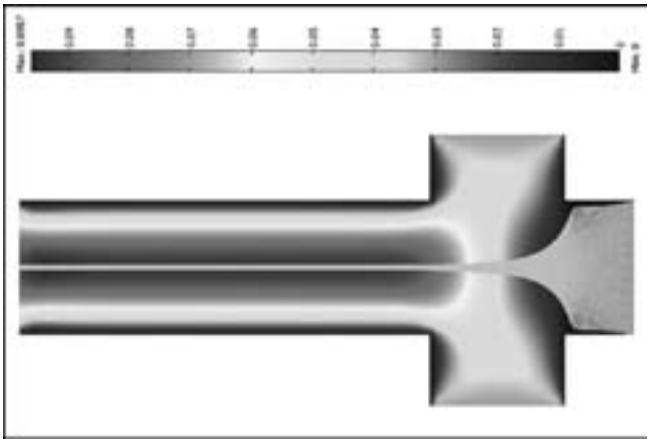

Figure 2: A COMSOL velocity field plot of hydrodynamic focusing is shown. The three inlet channels are all 150 μm wide and the sample particles (represented by the grey streamlines) from the center inlet are focused into a thin stream by the sheath fluid.

and the CCD frame rates, which is comparable to current industry standards. Such a microfluidic channel design was chosen and drawn in Auto CAD, as shown in Figure 2.

Fabrication. Fabrication of the microfluidic channels was done through photolithography. A chrome mask of the channel designs was purchased from Photosciences, Inc. First, a 30 μm layer of SU-8 (negative photoresist) was spun on a silicon wafer. A two-step bake was performed to cure the resist. Then, it was exposed to 365 nm UV light for 13 seconds and developed for 5 minutes. The prepared wafer was then coated with 100 nm of chrome and 200 nm of gold using electron-beam evaporation. Next, polydimethysiloxane (PDMS) was prepared by mixing Sylgard 184 with its curing agent in a 10:1 ratio. The mixture was degassed under vacuum, poured uniformly onto the wafer, and cured for 4 hours at 70°C. Then, the PDMS layer was peeled off and holes were punched in it for attaching nanoports. Finally, the PDMS was treated with oxygen plasma for 10 seconds at 50W before sealing it to a glass slide, completing the fabrication process.

Analysis. In order to analyze the MCARS spectral data collected from these microfluidic devices, a chemometric tool called principal component analysis (PCA) was used. PCA is a mathematical method that decomposes data into an alternative basis, maximizing variance between subsequent principal components, or basis vectors. Each substance's spectrum can then be easily identified as linear combinations of the first few principal components.

A GUI was written in MATLAB to perform this analysis. First, it applied a Savitsky-Golay filter and normalized the data. Next, PCA was performed. Then, the projection of each spectra onto the first few principal components was graphed. This caused clustering which allowed one to differentiate and identify various substances. This method was used successfully to differentiate polystyrene beads in oil although the MCARS spectra of both substances are very similar (Figure 3).

Figure 3: An image of polystyrene beads (black) in oil (grey) is shown. It was reconstructed in MATLAB by performing PCA on the MCARS spectral data collected.

Once the spectrum of each substance is determined through a training set, real-time identification can be implemented by grabbing one spectrum of a particle flowing by and matching it to the various spectra collected beforehand through the training set.

Conclusions:

Microfluidic channels with the capacity for hydrodynamic focusing were modeled theoretically, designed, and fabricated. A program in MATLAB was written to differentiate and identify various substances flowing through the microfluidic devices by applying PCA to the spectral data collected. In this manner, chemically specific differentiation of polystyrene and oil was experimentally demonstrated. This sets the groundwork for the implementation of a flow cytometer chip that will perform real-time identification of particles using MCARS.

Future Work:

Once real-time particle identification is accomplished, it will be useful to introduce a sorting device to classify the particles into bins accordingly. Common methods of doing this include the use of micro-actuators, magnetic coatings, or electric potentials. It is also beneficial to introduce cameras in order to determine the size of particles through scattered light.

Acknowledgments:

I would like to thank the National Science Foundation (NSF), the NNIN REU Program, and the Georgia Institute of Technology for funding and providing facilities for conducting this research. Furthermore, I would like to extend my gratitude to Prof. Ali Adibi, Dr. Siva Yegnanarayanan, and Charles Camp for including me in their research and guiding me through this work.

Magnetron Sputtering and Characterization of Ag-Si for Infrared Photodetectors

John Abrahams

Electrical Engineering and Physics, University of Maryland at College Park

NNIN REU Site: Howard Nanoscale Science and Engineering Facility, Howard University, Washington, DC
NNIN REU Principal Investigator(s): Dr. Clayton Bates, Electrical Engineering, Howard University
NNIN REU Mentor(s): Dr. Chichang Zhang, Electrical Engineering, Howard University
Contact: jabrah23@umd.edu, bates@msrce.howard.edu

Abstract:

Silver and silicon (Ag-Si) composite films are the first metal-semiconductor composite system to demonstrate a response to radiation over the 1-14 μm wavelength range from liquid nitrogen to room temperature. Magnetron co-sputtering at 550°C was used to deposit 1 μm thick Ag/n-Si films with Ag concentrations ranging from 13%-23% onto highly resistive n-Si (111) substrates. The Van der Pauw method was used to characterize the transport properties of these films. Room temperature resistivity measurements on the order of 10-1Ω·cm are higher than expected of only highly doped n-Si. Lower resistivity was recorded with higher Ag concentration. Measured mobility of around 1 cm^2/V·s was observed at room temperature. This low mobility is due to the high dopant concentration in the silicon. Resistivity and mobility measurements are different from values of only highly doped n-Si. Carrier concentration at room temperature is consistent with highly doped n-Si for lower Ag concentration, but generally increased with Ag concentration. While the behavior of carrier concentration is not currently fully understood for Ag/n-Si systems, the above results were verified at the National Institute of Standards and Technology in Gaithersburg, MD.

Introduction:

Ag/n-Si composite films are the first metal-semiconductor composite system to demonstrate a response to radiation over the 1-14 μm wavelength range from liquid nitrogen to room temperature. With an electric field of 2×10^6 V/cm applied to a sample with the composite film, previous studies have shown efficiencies of up to 35% depending on incident wavelength [1]. Magnetron co-sputtering was used to deposit silver and highly doped n-type silicon simultaneously. A deposition temperature of 550°C was high enough to ensure that the deposited silicon was crystallized [2]. This method of deposition allows the silver to form small nanoparticles that are embedded within the silicon crystal lattice. Before devices can be made using this technique, the transport properties must be measured. Hall effect measurements were used to characterize these properties.

Experimental Procedure:

A Kurt J. Lesker CMS-18 Magnetron Plasma co-sputtering system was used with one silver target and one highly doped n-type silicon target. High resistivity (2000-3000 Ω·cm) n-type Si (111) wafer was used as the substrate. To grow each sample, a constant temperature of 550°C and with 3.5 mTorr argon pressure was used for the 50 minute deposition. The sample was rotated at 20 rpm to help ensure a uniform film. A power of 330W was applied to the silicon target for all runs. The power applied to the silver target was changed for each run depending on the desired concentration of silver and can be seen in Figure 1.

Sample	power to Ag target	Ag concentration
74a	12 W	22% - 23%
74b	9 W	16% - 17%
75a	7 W	13% - 14%

Figure 1

Hall measurements were made using the MMR Technologies, Inc., Hall measurement system. This system uses the Van der Pauw technique to measure resistivity, Hall coefficient, carrier mobility, and carrier density [3]. The system was used to take measurements at temperatures from 80K up to 500K with a magnetic field of 10kG. Chromium and gold were deposited to form the ohmic contacts.

Results and Discussion:

Using the given sputtering parameters, the resulting deposition had a thickness of 1 μm. The results of varying the power to the silver target on the concentration of silver can be seen in Figure 1. These concentrations were measured using electron dispersive spectroscopy (EDS). Each sample appeared to have low resistivity of less than 10 Ω·cm at liquid nitrogen temperature. The general decreasing trend of

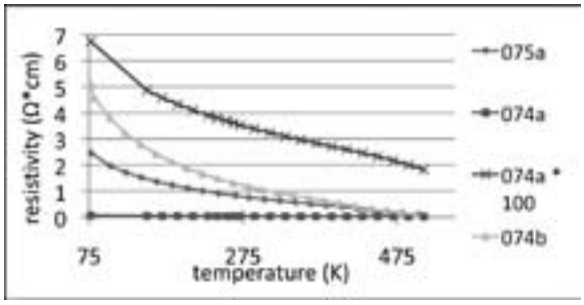

Figure 2

the resistivity with increasing temperature, as seen in Figure 2, is similar to the behavior of silicon and was expected due to the separation of silver nanoparticles by silicon crystal. It should be noted that sample 74a, which had the highest silver concentration displayed the lowest resistivity. The magnitude of the carrier mobility generally increased with temperature as seen in Figure 3.

All samples were measured to have very low carrier mobility of much less than 1 $cm^2/V{\cdot}s$ at temperatures around liquid nitrogen temperature. This mobility increased slowly to about 1 $cm^2/V{\cdot}s$ at room temperature. This was expected due to overlapping depletion regions at the silver-silicon interfaces.

Samples 74b and 75a, with lower concentrations of silver, displayed carrier densities consistent with the highly doped n-type silicon used in deposition over temperature ranges from liquid nitrogen to room temperature. Sample 74a had a higher silver concentration and showed a significantly higher carrier density. For each sample, the carrier density decreased with increasing temperature as seen in Figure 4.

While the behavior of the carrier density and mobility in this composite film is not fully understood, measurements made at the National Institute of Standards and Technology (NIST) agreed with the data found in this study.

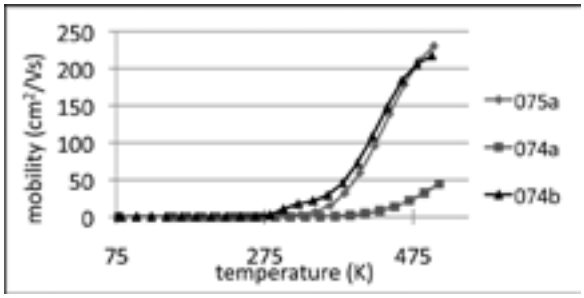

Figure 3

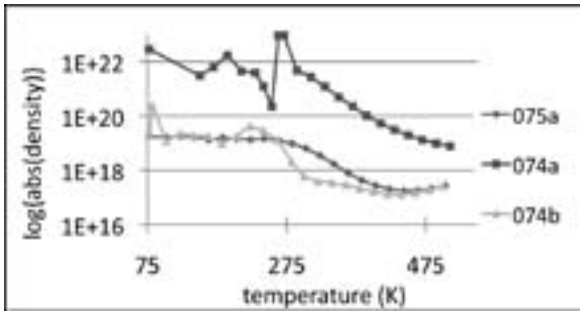

Figure 4

Future Work:

Future work will include the measurement of responsivity of this silver-silicon composite film for different wavelengths of incident radiation. Further analysis of the data found in this study may help find the optimal conditions under at which future devices may operate.

Acknowledgements:

I would like to thank the National Nanotechnology Infrastructure Network Research Experience for Undergraduates Program for a great research experience, and the National Science Foundation for providing funding for the program, my advisor Dr. Clayton Bates and my mentor Dr. Chichang Zhang for all the help they provided throughout the program, the staff at the Howard Nanoscale Science and Engineering Facility and at the University of Maryland Nanocenter for providing assistance on this project, and Dr. Robert Thurber of the National Institute of Standards and Technology for providing Hall measurement equipment.

References:

[1] "Electric field dependence of quantum efficiencies of Ag/n-Si composites in the infrared at room temperature." J. Appl. Phys. 104, No.7 (Oct 2008): 076101. Clayton W Bates and Chichang Zhang.

[2] Zhang, Chichang, and Clayton Bates, Jr. "Metal-mediated crystallization in Si-Ag systems." Thin Solid Films 517 (2009): 5783-5785.

[3] "Hall Effect Measurement System." MMR Technologies, Inc. http://mmr.com/PDFs/hall_PPT.pdf. Retrieved on 07-06-2009.

The Cyclic Charging of Reduction-Oxidation Markers in Metal-Oxide-Semiconductor Capacitors

Julie Bellfy

Chemical Engineering, Villanova University

NNIN REU Site: Cornell NanoScale Science and Technology Facility, Cornell University, Ithaca, NY
NNIN REU Principal Investigator(s): Prof. Edwin Kan, Electrical and Computer Engineering, Cornell University
NNIN REU Mentor(s): Jonathan Shaw, Electrical and Computer Engineering, Cornell University
Contact: Julie.Bellfy@villanova.edu, kan@ece.cornell.edu, jts57@cornell.edu

Abstract:

The study of the cyclic charging of reduction-oxidation (Redox) markers in metal-oxide-semiconductor (MOS) capacitors would allow for the eventual creation of a memory device that contains a molecular component. This molecular component would be a redox organometallic compound such as ferrocene. Redox molecules have naturally occurring discrete energy levels that can store charge. The creation of a device that utilizes the charge-storing capability of these molecules would allow for the creation of a multi-bit memory. The memory created would be able to function at low potentials and be able to undergo trillions of read-write cycles [1].

Experimental Procedure:

For this research project, a functional molecular memory was not obtained. The ultimate goal of this project was to create device that exhibited "Coulomb Staircase" behavior, an indication that the molecule is storing the charge on its discrete energy levels [2,3]. Although a device that exhibits this behavior was not obtained, a great deal of knowledge about the mechanism of molecular memory was obtained.

A basic MOS capacitor with the integration of a redox molecule was fabricated. (See Figure 1.)

First, a 2 nm tunneling oxide of silicon dioxide (SiO_2) was grown on a silicon substrate. Then a self-assembled monolayer (SAM) of benzoic acid and ferrocene was formed. Next a 25 nm control oxide of aluminum oxide (Al_2O_3) was deposited using atomic layer deposition (ALD). A gate metal of 100 nm of chromium (Cr) and 50 nm of aluminum (Al) was deposited. The gate metal was patterned using lithography and etching techniques. The device was annealed to rid the control oxide of interface traps. Finally the device was tested using a capacitance-voltage (CV) meter.

For this experiment, three sets of complete devices were fabricated. The first set was used to determine if the molecule was indeed storing a charge. The second set was used to determine whether a thermal or plasma method of deposition of the control oxide would produce better results. The third and final set was used to determine what annealing temperature would produce the best results.

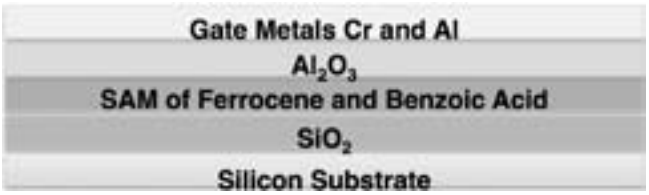

Figure 1: A depiction of the cross-section of the fabricated device.

For trial one, three samples were created: a control sample without a SAM, a benzoic acid only sample with just benzoic acid in the SAM, and a ferrocene/benzoic acid mixture sample with a mixture in the SAM. This experiment was designed to test whether or not a charge was indeed being stored by the molecule and not interface traps. In the control sample, there was no charge storage site because no molecule or intentional dielectric trap was inserted in the gate stack. Both the benzoic acid only and ferrocene/benzoic acid samples exhibited charge storage. The charge storage in the benzoic acid only sample was unexpected because a redox molecule was not present, indicating interface traps in the control oxide. This rendered the data inconclusive as to whether or not the molecule alone was storing a charge since a sample without a molecule was storing a charge. To improve upon this data, it was decided to test whether a thermal or plasma method of deposition for the control oxide would produce better results by reducing interface traps in the control oxide.

For trial two, several process splits were employed to test whether a thermal or plasma method of deposition of the control oxide would produce better results. For this trial, each method of deposition was tested using a control sample against a ferrocene and benzoic acid mixture. In comparing the control samples of this trial, one was able to see that, before annealing, the plasma method of deposition exhibited did not exhibit charge storage (see Figure 3), while the thermal

method did exhibit charge storage. The charge storage of the thermal method sample indicated interface traps. From this data, it was determined that the plasma method of deposition produced the best and most consistent results across devices. However, after annealing, the heat sensitive molecules decomposed, resulting in inconsistent charge storage across devices.

For trial three, it was decided to test different annealing temperatures to determine which would produce the best control oxide, but maintain the integrity of the molecules. Three different annealing times and temperatures were tested, 400°C for 30 minutes, 200°C for 60 minutes, and 100°C for 90 minutes. It was determined that annealing at 200°C produced the best results. The electron injection test after annealing at 200°C produced the most consistent charge storage. (See Figure 3.) Annealing at 400°C destroyed the heat sensitive molecules resulting in no charge storage. Annealing at 100°C created more interface traps in the oxide, resulting in inconsistent charge storage. Different ratios of ferrocene to benzoic acid were also tested, but did not result in a significant difference in charge storage.

Results and Future Work:

Although "Coulomb Staircase" behavior was not exhibited by any of the samples, a great deal about the application of redox molecules to a memory device has been learned. The redox molecule can indeed store a charge; however, interface traps in the control oxide layer prevented one from conclusively stating whether or not the molecule alone was storing the charge. To improve the oxide layer, different methods of deposition were tested. It was determined that a plasma method of deposition created a better oxide. Finally, different annealing temperatures were tested to determine how much heat could eliminate the interface traps and leave the molecules intact. It was determined that an annealing temperature of 200°C would produce the best device.

From this information one can perform further testing to try and obtain a working memory device with the integration of a redox molecule. Perhaps adjusting the annealing temperature into finer increments would produce a better device that would exhibit staircase behavior but have no traps. For this research only one type of molecule was used, perhaps a different molecule could withstand the high annealing temperatures. Creating this device would result in a smaller, cheaper, multi-bit memory that can undergo trillions of read-write cycles.

Acknowledgements:

I would like to thank the National Science Foundation, National Nanotechnology Infrastructure Network Research Experience for Undergraduates (NNIN REU) Program, and the Cornell NanoScale Science and Technology Facility. I would like to thank the CNF staff especially Phil Infante, and other CNF users. Thank you to my PI Edwin Kan and his research group. Finally I would like to thank my mentor Jonathan Shaw.

References:

[1] Hou, Tuo-Hung. "Nanocrystal Memory Scaling: From Material Selection to Performance Improvement." Diss. Cornell University, 2008.

[2] Hou, Tuo-Hung. "Programable molecular orbital states of C60 from integrated circuits." Diss. Cornell University, 2006.

[3] Park, Jiwoong. "Electron Transport in Single Molecule Transistors." Diss. University of California, Berkeley, 2003.

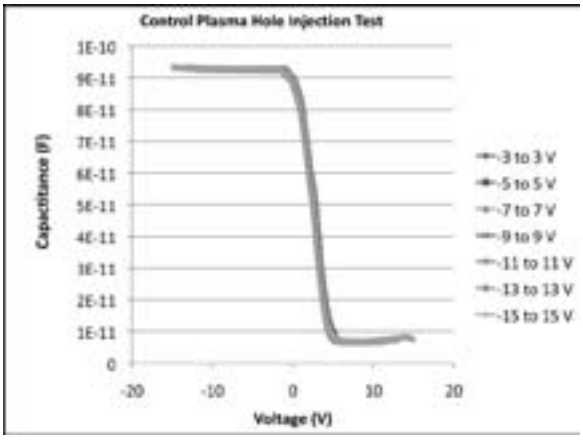

Figure 2: As the testing voltage increases there is no shift, indicative of no charge storage and no interface traps.

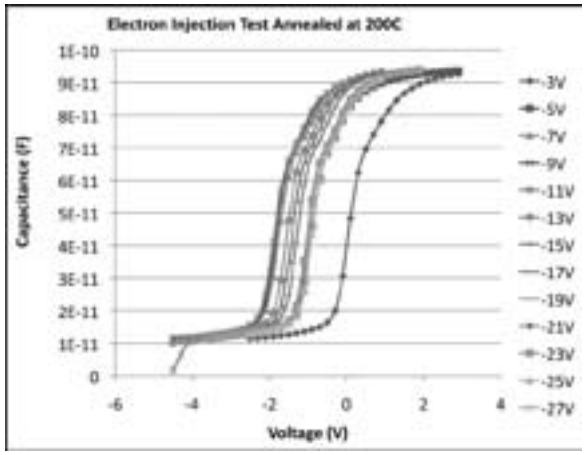

Figure 3: As the testing voltage increases, there is a consistent shift, indicating a stored charge.

Fabrication and Design of Nanowire Transistors

Gabrielle Castillo

Materials Science and Engineering, Arizona State University

NNIN REU Site: Howard Nanoscale Science & Engineering Facility (HNF), Howard University
NNIN REU Principal Investigator(s): Dr. Gary L. Harris, Director of HNF, Howard University, Washington, DC
NNIN REU Mentor(s): Dr. William Rose, HNF, Howard University, Washington, DC
Contact: keroppiqueen8@yahoo.com, gharris@msrce.howard.edu, wbullrose@gmail.com

Abstract and Introduction:

Modern society continues to crave smaller and energy saving electronics. For years, scientists have depended on the use of complementary metal-oxide semiconductor technology. However, with the year 2020 quickly approaching, devices are predicted to scale down to less than 45 nm in size, which exceeds the minimum dimensions of the current technology. Researchers have intensely labored to find solutions for this dilemma and one possible solution is III-V metal-oxide semiconductor field effect transistors (MOSFETs). These transistors specifically use nanowires as a bridge between electrodes. The wires are grown using elements from groups IIIA and VA of the periodic table, which together exhibit high mobilities making them more efficient for electron transport. The goal of this project was to fabricate and test a gallium nitride (GaN) MOSFET nanowire transistor.

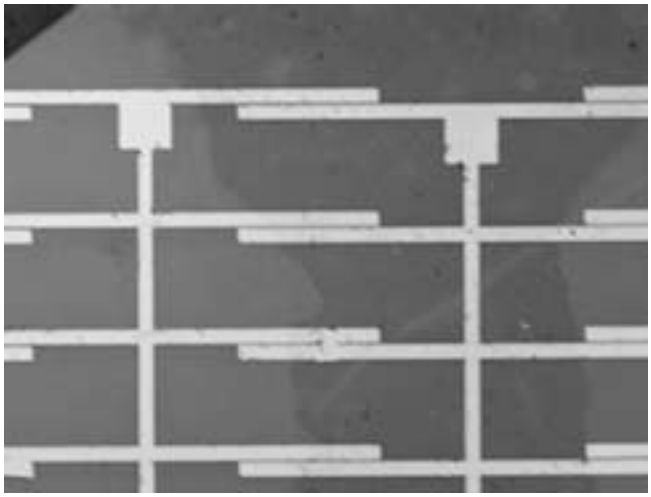

Figure 1: Mask #2 using photolithography, with source-drain metal contact fingers.

Procedure:

To begin the process, we obtained a p-type silicon substrate which is a silicon wafer heavily doped with boron in order to decrease resistivity. Next, a silicon dioxide layer was grown on the silicon substrate to be used as the gate insulator for the device. The oxide layer was grown by the process called thermal oxidation to a required thickness of 50-100 nm. Thermal oxidation is defined as the formation of an oxide layer on the surface of a semiconductor. Before device oxidation, a series of trial runs was performed to calibrate the oxidation growth rate. The thickness of these layers was then measured by ellipsometry and 700 nm was determined best for the fabrication of this device.

An ohmic contact was formed on the backside of the silicon substrate which operated as the gate of the transistor. An ohmic contact is a metal-semiconductor junction allowing carriers to flow in and out of the semiconductor [1]. In order to form the contact, 100 nm of silicon-aluminum eutectic solution was thermally evaporated onto the backside of the substrate. Under high vacuum, the solution condensed and evaporated onto the back of our silicon substrate as a current was applied to the crucible—in turn heating up the source material. The substrate was then annealed at 500°C for 1 minute in order to reduce any barriers at the interface.

Photolithography was used to pattern the top surface for metal deposition of the source and drain contacts. The first mask used comprised of an array of 100 μm × 100 μm squares, which were double-exposed to create the source and drain and to manipulate the distance between them. The average length of a nanowire was about 50 μm, so it was ideal to have distances less than 50 μm. This mask did not work so well because the nanowires seemed to land in open areas instead of across the source and drain. A second mask that had fingers branching off from the center was employed to increase the probability of landing a nanowire across the source and drain pads. This mask was also doubly-exposed to manipulate the distance between the source and drain fingers. This design proved to be much better as more nanowires landed across the source and drain pads (Figure 1). After photolithography, gold contacts were thermally evaporated onto the patterns. About 10 nm of chrome was evaporated onto our substrate as a primer and 100 nm of gold was evaporated as our metal contacts.

Lastly, we used a microgripper with a very fine tip and carefully collected gallium nitride nanowires from a gallium nitride sample. The nanowires attached to the tip by means of Van der Waals dipole-dipole attraction. After attaching

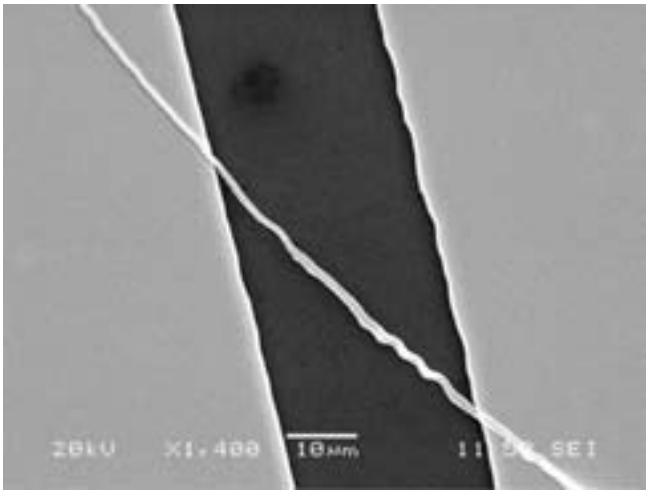

Figure 2: SEM micrograph of a nanowire transistor.

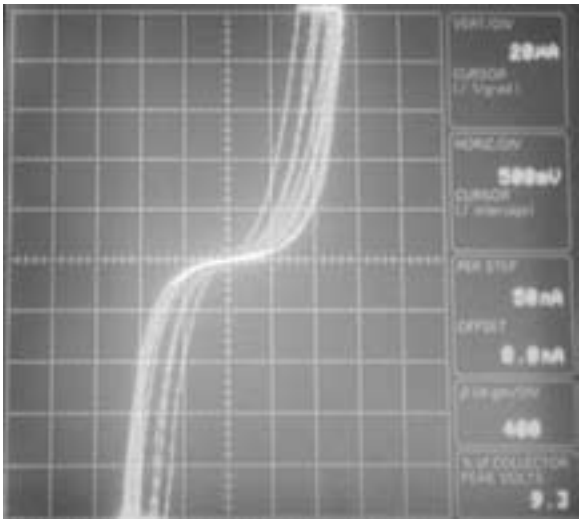

Figure 4: Current-voltage (I-V) curve of nanowire device.

the nanowires, we carefully placed our substrate underneath the tip, avoideing vibrations, and applied methanol to the tip using a syringe. The methanol forced the nanowires off the tip and disbursed them onto the surface of the substrate.

Next, we used an optical and scanning electron microscope to view our samples and determined whether or not a nanowire was successfully deposited between two electrodes to complete the transistor. (Figure 2.)

Results and Conclusion:

After conducting current-voltage testing on these devices, it was concluded that the nanowires did not make full contact across the source and drain. We tested other devices and found operating devices when two test probes were applied (Figure 3). One probe was applied to one gold contact as the source and the second gold contact as the drain, which resulted in a linear graph. Lastly, we tested our annealed sample that was heated at 500°C for 1 minute.

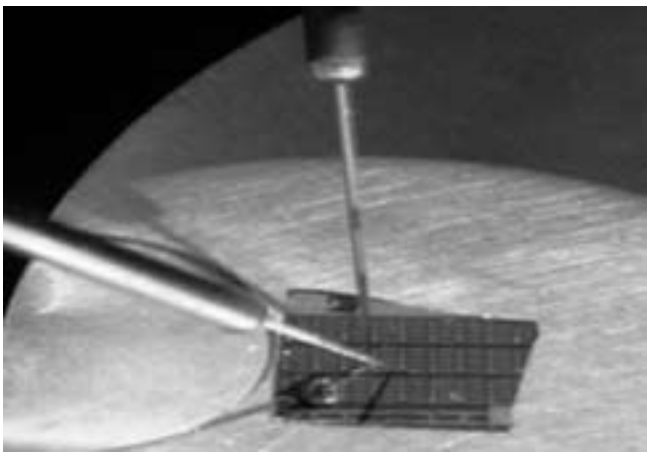

Figure 3: Nanowire transistor under test using probes.

As we tested this final sample, a third probe was applied to the back gate of the device. This was done by touching the probe onto the metal stage, which was in contact with the backside of the substrate [2]. This resulted in a back-to-back diode current-voltage curve of this device (Figure 4). The figure also shows the effect of point probe contacts via the noisy I-V current.

Future Work:

Since it was sometimes difficult to land nanowires across the electrodes, the ability to move them around on the surface using a micro-tipped cantilever would be immensely helpful. A second option would be to use e-beam lithography to pattern the samples after the nanowires were deposited. This technique would allow for the precise placement of the source and drain over the nanowires.

Acknowledgements:

This has been an incredible experience and I would like to thank Dr. Gary L. Harris, Mr. James Griffin, and Dr. William Rose for guiding me through this internship. I would also like to thank the entire Howard Nanoscale Science and Engineering Facility (HNF) staff. This work was supported by the National Science Foundation and the National Nanotechnology Infrastructure Network Research Experience for Undergraduates (NNIN REU) Program. All of my research was conducted in the HNF facility.

References:

[1] Ohmic Contact Technologies. 2004. 14 July 2009. http://www.SiliconFarEast.com.

[2] Wenzel, R.; Fischer, G.G.; Schmid-Fetzer, R. "Ohmic contacts on p-GaN (Part I): Investigation of different contact metals and their thermal treatment." 2001. 28 July 2009. http://www.sciencedirect.com/.

Design and Fabrication of Aluminum Nanoelectromechanical Switches

Vivian Feig

Chemical Engineering, Columbia University

NNIN REU Site: Stanford Nanofabrication Facility, Stanford University, Stanford, CA

NNIN REU Principal Investigator(s): Prof. Roger T. Howe, Electrical Engineering, Stanford University; Prof. H.-S. Philip Wong, Electrical Engineering, Stanford University

NNIN REU Mentor(s): Dr. J. Provine, Electrical Engineering, Stanford University; Roozbeh Parsa, Electrical Engineering, Stanford University

Contact: vrf2103@columbia.edu, rthowe@stanford.edu, hspwong@stanford.edu, jprovine@stanford.edu, rparsa@stanford.edu

Abstract:

In integrated circuits, nanoelectromechanical (NEM) switches are advantageous because they have nearly zero power dissipation in their off state. An energy recoverable design that stores elastic energy in the mechanical switch can further lower operating voltage. In this project, we constructed a lateral cantilever beam that switches between two symmetric sense electrodes (drains) when voltage is applied to two symmetric drive electrodes (gates). To avoid conductivity issues of silicon beams, we used aluminum to construct our device on a quartz substrate. Silicon was used as a sacrificial release layer for the aluminum. Though we were not able to finish fabricating a device, we ultimately aim to use our design to achieve a significant decrease in switching voltage as compared to a traditional NEM switch.

Introduction and Background:

Currently, most logic operations in electronic devices are performed by transistors, which dissipate power in their off state. As transistors have gotten smaller, this power leakage problem has resulted in large amounts of wasted energy [1]. Nanoelectromechanical (NEM) switches provide lower power alternatives to transistors by taking advantage of mechanical properties to reduce the two main components of standby power dissipation: I_{off} (off-state current) and V_{DD} (operating voltage).

Figure 1 shows our NEM switch design, consisting of a cantilever beam, a source electrode, and two sets of gate and drain electrodes. The beam switches to a drain due to an electrostatic force once a sufficiently high voltage, $V_{pull\text{-}in}$, is applied to the corresponding gate. When the gate voltage is lowered, the beam stays attached to the drain due to attractive surface forces until it releases at some lower $V_{pull\text{-}out}$. Because the beam is physically detached from the drain when it is not pulled in, I_{off} is zero.

Figure 1: Generalized design for a lateral cantilever beam switch, with a source electrode and two gates (G) and drains (D).

To further reduce power dissipation, parallel electrode designs take advantage of energy recoverable operation (ER) [2]. To understand ER, consider a swing set (Figure 2): initializing a swing from rest requires pulling it with a certain force F1. After release, one can hold it at the other side using a greatly

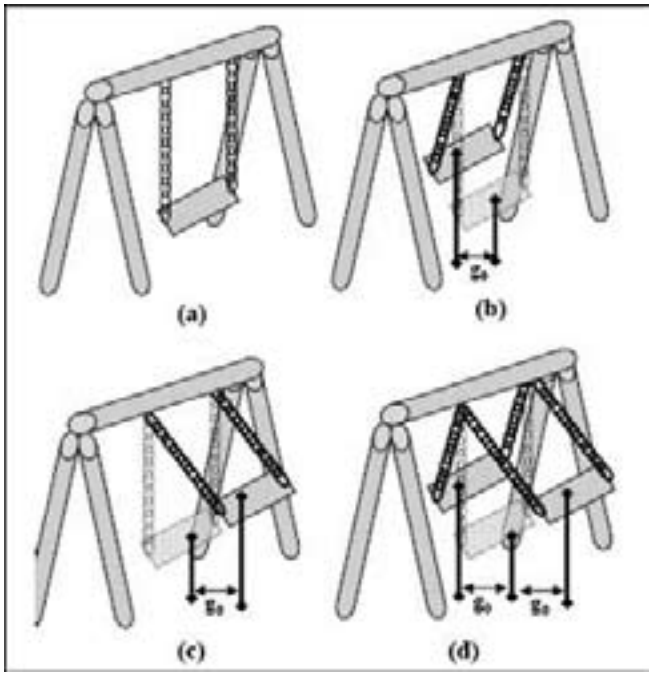

Figure 2: Swing set analogy for energy recoverable operation of lateral NEM switches.

reduced force F2 << F1. Similarly, a parallel electrode switch is initialized to one drain at a relatively high $V_{pull\text{-}in}$. Stored elastic energy switches the beam to the opposite drain at $V_{pull\text{-}out}$, where the beam can be held at a lower V_{hold} << $V_{pull\text{-}in}$. In other words, after initialization, our switch operates at significantly reduced V_{DD}.

Previous switches fabricated with this design used silicon as the structural layer. However, silicon forms a layer of insulating oxide when exposed to air, whose thickness requires significantly higher drain biases, decreasing energy efficiency. We used aluminum, which forms thinner, self-limiting native oxide layers. Aluminum is also a metal, whose conductivity makes it easier to pass current. Further, aluminum processes are low-temperature and back-end-of-line (BEOL) compatible, broadening the range of applications for these devices.

Procedure:

We first designed a lithography mask of an array of devices that varied beam-to-gate overlap (12 to 19.5 μm) and beam-gate gap (500 or 600 nm). Simulation of our standard device using a parallel plate model showed that as beam-to-gate overlap increases, switching time increases, whereas pull-in voltage decreases.

To fabricate, we deposited a sacrificial polysilicon layer on top of a quartz substrate. We used metal sputtering to deposit 0.7 μm of aluminium, which we patterned with photolithography and etched using a chlorine-based reactive ion etch. Photoresist was removed with a piranha clean and our devices were released dry using xenon difluoride.

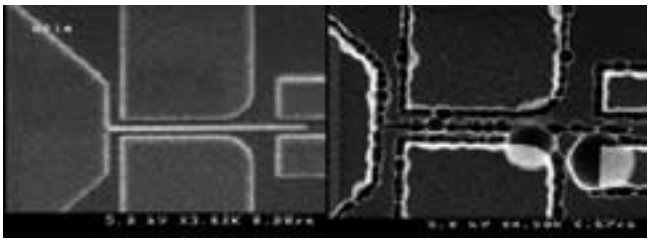

Figure 3: SEM image of unreleased device (left) versus device after 72 seconds of xenon difluoride release (right).

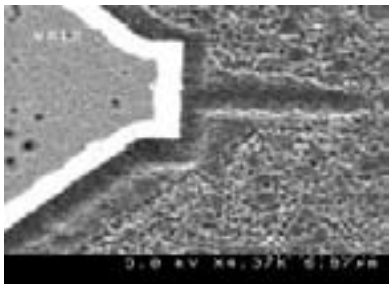

Figure 4: SEM image of device without beam after 90 seconds of xenon difluoride release.

Results:

We were unable to successfully release an aluminum device because our structural layer was etched away after exposure to xenon difluoride. Scanning electron microscope (SEM) images of two devices show that the aluminum layer begins being eaten away at 72 seconds of release (Figure 3) and the beam disappears completely after 90 seconds (Figure 4).

Discussion and Future Work:

Our results were unexpected because xenon difluoride should not attack aluminum. We initially suspected that the release step, which is highly exothermic, melted away the aluminum. However, running the release with less heat by adding nitrogen flow and delays between etching cycles yielded the same results. The most plausible explanation is that the structural layer deposited was not 100% aluminum, but a mixture of aluminum and silicon.

Once we fabricate successfully released devices, we will test them by ramping gate voltage and looking for the voltage ($V_{pull\text{-}in}$) at which current starts to flow between the beam and the corresponding drain. We will then sweep the voltage in the other direction to see when the drain current returns to zero, indicating pull-out.

Conclusion:

Aluminum NEM switches with cantilever beams laterally situated between parallel electrodes can greatly reduce both active and standby power dissipation. We modeled, designed, and fabricated such devices. However, we were unable to release a device; future work will involve determining why the xenon difluoride release step was unsuccessful. Ultimately, we hope these devices can use energy recoverable operation to run on significantly reduced voltages.

Acknowledgements:

Thank you to the National Nanotechnology Infrastructure Network Research Experience for Undergraduates; the Stanford Nanofabrication Facility and Center for Integrated Systems; Prof. Roger T. Howe and Prof. Philip Wong; Dr. J Provine, Roozbeh Parsa, and Soogine Chong; and the National Science Foundation.

References:

[1] Markovic, D. et al.; "Methods for true energy-performance optimization"; IEEE J. Solid-State Circuits, vol. 39, no. 8, pp. 1282-1293 (2004).

[2] Akarvardar, K., D. Elata, R. T. Howe, and H. S. P. Wong; "Energy-reversible complementary NEM logic gates"; Device Research Conference, pp. 69-70 (2008).

Plasmonic Focusing of Light

Chelsea Frid

Material Science and Engineering, Michigan State University

NNIN REU Site: Lurie Nanofabrication Facility, University of Michigan, Ann Arbor, MI
NNIN REU Principal Investigator(s): Mona Jarrahi, Electrical Engineering, University of Michigan
NNIN REU Mentor(s): Christopher Berry, Electrical Engineering, University of Michigan
Contact: fridchel@msu.edu, mjarrahi@umich.edu, berryc@umich.edu

Abstract:

The goal of this project is to develop a terahertz detector. Terahertz is a portion of the electromagnetic spectrum that lies between the microwave and optical ranges. The device consisted of a periodic array of Schottky diodes with interdigitated comb fingers on a low-resistivity gallium arsenide (GaAs) substrate. Schottky diodes are used for terahertz detection because their nonlinear current-voltage characteristic aid in the detection of high frequency signals. In operation, the alternating electrodes are connected to a voltage source through a bias resistance. The sinusoidal electric field of the terahertz radiation modifies the average voltage difference between the electrodes, due to the nonlinear characteristics of the diode. The periodic arrangement of the Schottky diodes assists collecting a large portion of the incident terahertz radiation. Due to the time constraints, testing of the final device was not fully completed. In this paper, we present the fabrication process and the initial electrical characterization results.

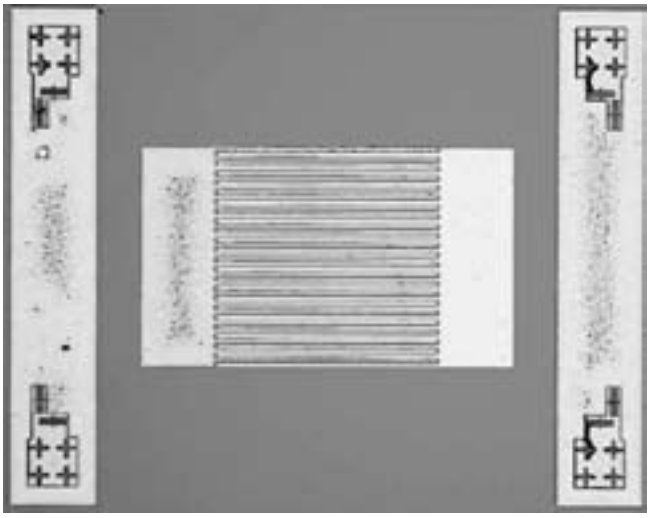

Figure 1: Completed device consisting of alternating ohmic and Schottky contacts.

Introduction:

Terahertz (THz) radiation is an electromagnetic radiation in 0.1-10 THz frequency range. This radiation lies between the optical and microwave regions of the electromagnetic spectrum. Some applications of terahertz technology include medical imaging and surveillance. For medical imaging, terahertz radiation is desirable because unlike x-rays it is not damaging to the tissue or deoxyribonucleic acid (DNA). Terahertz radiation is highly absorbed by water. Therefore, the waves can only penetrate into the body a few millimeters. This allows changes in water content to be imaged near the surface of the body, which can be used to identify tumors. For surveillance, the radiation is transmitted through fabric, plastic and several packaging materials but is highly absorbed and/or reflected by metals. This allows concealed weapons to be seen.

This paper presents a terahertz detector. The fabricated device was composed of alternating ohmic and Schottky, interdigitated comb fingers on a highly doped n-type gallium arsenide (GaAs) substrate, as seen in Figure 1. The alternating fingers formed an array of Schottky diodes. Applying a positive voltage to the Schottky contact placed the device in forward bias mode. This decreased the potential barrier resulting in an increase in the output current. The incident terahertz field between the fingers effectively added a small sinusoidal voltage to the applied bias voltage. Since Schottky diodes exhibit an exponential current gain with respect to the applied voltage, the average output current would be larger when illuminated with a terahertz radiation.

Purpose:

The size of a terahertz detector plays an important role in the total absorbed terahertz power. By choosing the geometry of the device to excite plasmonic resonances in the metal fingers, the wave can be channeled around the fingers to cause the radiation to be more intense in the active region. This allows the gap between the electrodes to be reduced, increasing the speed of the device, while using a large device size. Therefore, the presented terahertz detector is expected to provide greater sensitivity than the prior art.

Experimental Procedure:

To fabricate the terahertz detector, we first patterned the ohmic contact followed by the Schottky contact. The process consisted of two photolithography steps using Shipley 1827 photoresist spun on the GaAs wafer at 4000 rpm for 30 seconds. Using photolithography we defined the first set of fingers and one contact pad using a SUSS MA/BA6 mask aligner. The sample was exposed to an ultra violet light for twelve seconds followed by development in Microposit MF-319 for fifty seconds. The ohmic contact was formed using a SJ-20 metal evaporator to deposit nickel/germanium/gold/titanium/gold (250/325/650/200/3000 Å). For liftoff, the sample was soaked in heated acetone for approximately twenty-four hours. Cleanroom tape was applied to the sample to peel off excess metals. After liftoff, the metal was annealed at 385ºC for 60 seconds to alloy the metals. The photolithography step was then repeated to pattern the Schottky contacts. The Schottky contact of platinum/gold (1500/3425 Å) was then deposited by an EnerJet evaporator. The same liftoff procedure was followed, completing the fabrication.

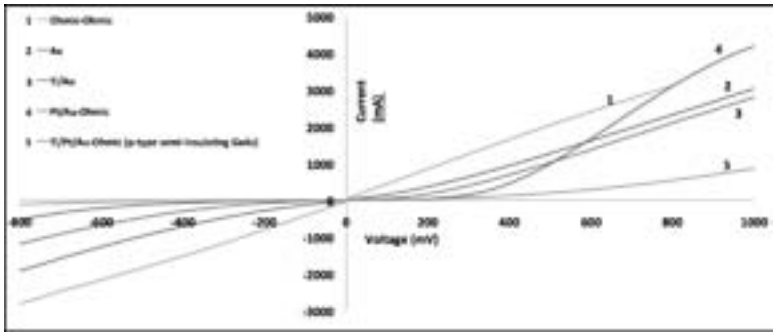

Figure 2: Schottky contact tests.

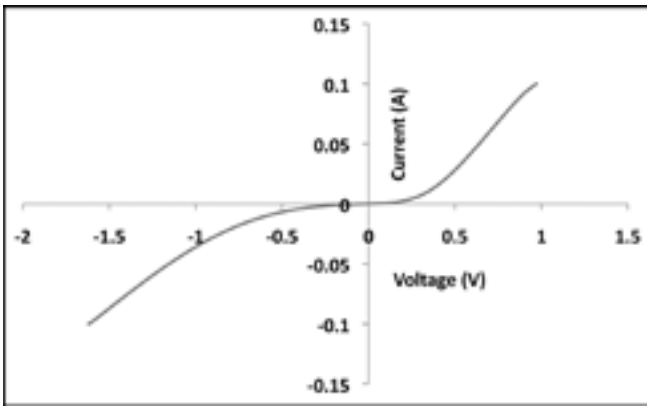

Figure 3: Current-Voltage characteristics of the final tested device.

Results:

To identify the best Schottky contact, we tested a couple of different metals on our substrate. The current-voltage results are shown in Figure 2. The platinum/gold contact responded the best, with an exponential growth with increasing voltage as is characteristic of a Schottky diode. Using the platinum/gold Schottky contact, several devices were fabricated. The current-voltage characteristics of a representative device can be seen in Figure 3. The device exhibited exponential current gain from 0 to 0.5 V. In Figure 3, the graph is not symmetrical, meaning that the diode allowed less reverse current than in the forward direction. The exponential current gain with applied voltage suggests that this device may be able to detect terahertz radiation. Due to time constraints, we were not able to obtain all of the needed equipment to fully test the terahertz radiation detection during the project.

Conclusion and Future Work:

The fabrication of a terahertz detector was optimized to create a functioning Schottky diode consisting of interdigitated fingers on a highly-doped GaAs substrate. Future work includes testing the detectors with a terahertz source and optimizing the device geometry to respond to different frequencies of terahertz radiation.

Acknowledgements:

I would like to thank my mentor Chris Berry and Professor Jarrahi for helping me to understand the background knowledge of the project, along with the project itself. Thank you to Brandon Lucas and Sandrine Martin for making my stay at the University of Michigan so comfortable. Lastly, thank you to the National Nanotechnology Infrastructure Network Research Experience for Undergraduates Program for this opportunity.

Innovative Imprint Lithography for Chip-to-Chip Connections

Laura Gaskins

Chemical Engineering, Rice University

NNIN REU Site: Nanotechnology Research Center, Georgia Institute of Technology, Atlanta, GA
NNIN REU Principal Investigator(s): Dr. Paul Kohl, Chemical Engineering, Georgia Institute of Technology
NNIN REU Mentor(s): Venmathy Rajarathinam, Chemical Engineering, Georgia Institute of Technology
Contact: laura.e.gaskins@rice.edu, paul.kohl@chbe.gatech.edu, venmathy.rajarathinam@chbe.gatech.edu

Abstract:

Transmission lines on printed circuit boards are currently fabricated with copper and an insulating glass dielectric, but this structure is not viable for high frequencies, long transmission lengths or high density. To reduce power loss, increase signal propagation and minimize noise, an innovative structure has been fabricated with an encapsulated air dielectric and copper shielding. This structure was fabricated with only one alignment step through the use of imprint lithography, chemical-mechanical polishing, and a sacrificial polymer. Production of these coaxial transmission lines could enable high frequency chip-to-chip communication with low power loss and low manufacturing cost.

Introduction:

Routing high frequency signals off-chip is a challenging task with current transmission line technology. Since loss in the dielectric scales linearly with frequency and loss in the conductor scales with the square root of frequency, at operating frequencies above 10 Ghz, the loss in the dielectric becomes the dominant loss contribution [1]. The power dissipated limits the maximum distance the signal can be routed at the necessary signal to noise ratio. Furthermore, crosstalk limits the proximity of lines to each other.

Imprint lithography's three-dimensional patterning capabilities were used to fabricate the halfcoaxial structure shown in Figure 1. The air dielectric layer can lower power loss from both the conductor and dielectric, allowing signals to be routed over longer lengths with increased signal propagation velocities, and the copper shielding could minimize crosstalk noise and radiation losses [1]. The imprint process minimized registration steps increasing attainable densities, and planarized surfaces improving line definition.

Figure 1: Half-coaxial schematic.

Experimental:

To create the semicircular stamp, tin/lead solder lines were electroplated and then reflowed to achieve the semi-circular geometry. The stamp, coated with Teflon®, was imprinted into a softbaked film of a polynorbornene polymer Avatrel 2000P (Promerus) at 110ºC and 45 bar for 60 seconds. The sample was then blanket exposed to ultra-violet (UV) light and then post-exposure baked. A seed layer of copper was then sputtered and electroplated to 1.5 μm. Chemical-mechanical polishing was used to remove copper from the field, leaving copper solely in the trench. A thick layer of polypropylene carbonate (PPC) was spin-coated on to the imprinted sample and then a Teflon-coated glass slide pressed the sacrificial material into the trench at 60ºC and 45 bar for 180 seconds. A polyhedral oligomeric silsesquioxane (POSS) (Hybrid Plastics Inc.) was spin-coated onto the sample, soft-baked, and blanket exposed to UV light. A seed layer of copper was sputtered and then photo-patterned with NR-9 (Futurexx). After the transmission line was electroplated, the seed layer was wet-etched back and the PPC was slowly decomposed in a nitrogen furnace.

Results and Discussion:

One of the primary objectives for patterning the half-coaxial structure was to minimize expensive or complex processing steps. To achieve this objective, photolithography masking and registration steps were minimized to reduce complexity and cost. The semi-circular geometry was transferred into Avatrel 2000P using only elevated temperature and pressure. The natural relief of the structure allowed the copper shielding in the trench to be patterned using simple chemical-mechanical polishing. Spin coating the sacrificial polymer, PPC, into the trench did not produce a planar sample surface and only partially filled the trench. This challenge was remedied by imprinting the sample with a Teflon-coated blank glass slide and thereby, pushing the polymer into the trench and planarizing the surface.

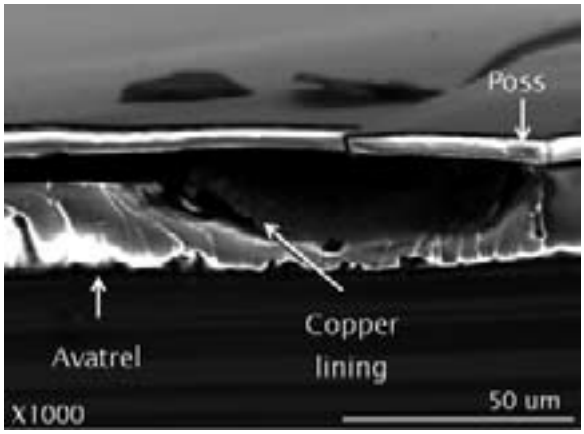

Figure 2: Inlayed air cavity.

The decomposition temperature of PPC on copper is greater than that of PPC on Avatrel 2000P, allowing thermal patterning of the sacrificial material. The primary volatile products of PPC decomposition are acetone and carbon dioxide and can permeate through many dielectrics at the decomposition temperature [2,3]. Decomposing PPC through the POSS overcoat initially resulted in damage to the POSS overcoat as shown in Figure 2. Thermo-gravimetric analysis of PPC allowed an improved decomposition recipe to be created eliminating overcoat damage. Patterning the transmission line was the only alignment recipe needed for the structure and x-ray tomography confirmed that the structure was successfully patterned. However obtaining cross sectional scanning electron microscope images (SEM) required breaking the sample, and the damage in Figures 3 and 4 are due to cross-sectioning.

Figure 3: SEM of smooth, planar, POSS overcoat.

Figure 3 shows that the field is planar and that the damage is only in the cleaved area. Figure 4 shows the transmission line extending from the air cavity and the crack in the overcoat is attributed likely due to dicing the sample.

Conclusions:

An ultra-low loss half-coaxial transmission line was fabricated using imprint lithography, chemical-mechanical polishing, and sacrificial polymers. Imprint lithography allowed the fabrication of a complex geometry and also planarized surfaces simplifying the buildup process. The use of chemical-mechanical polishing and sacrificial polymers eliminated costly masking and registration steps. Incorporation of an air insulation layer in the transmission line can lower power loss and increase signal propagation velocities enabling high frequency chip to chip communication.

Acknowledgements:

I would like to thank the National Nanotechnology Infrastructure Network Research Experience for Undergraduates and the National Science Foundation for funding this project, as well as Promerus LLC for providing materials. I would also like to thank Venmathy Rajarathinam, as well as Nathan Fritz for his guidance and dedication. Thanks also to the entirety of Dr. Paul Kohl's research group for their support.

References:

[1] Tummala, R., ed. Fundamentals of Microsystems Packaging. 2001, McGraw-Hill: New York.

[2] Cupta, M., Photoacid Generators for Catalytic Decomposition of Polycarbonate, in School of Chemical and Biomolecular Engineering. Master's Thesis. Georgia Institute of Technology.

[3] P. J. Joseph, H.A.K., S.A.B. Allen, P.A. Kohl, Journal of Micromechanics and Microengineering, 2005. 15.

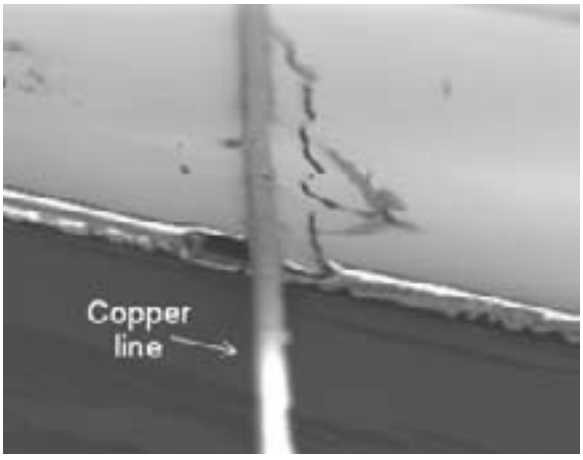

Figure 4: SEM cross-section of half-coaxial transmission line.

Integration of Gallium Nitride Nanowires with Silicon Circuits

Lydia Kisley

Chemistry, Wittenberg University

NNIN REU Site: Colorado Nanofabrication Laboratory, University of Colorado, Boulder, CO

NNIN REU Principal Investigator(s): Dr. Bart Van Zeghbroeck, Electrical Engineering, University of Colorado at Boulder; Dr. Kris A. Bertness, Optoelectronics Division, National Institute of Standards and Technology (NIST)

NNIN REU Mentor(s): Christopher Dodson, Optoelectronics Division, NIST

Contact: s10.lkisley@wittenberg.edu, bart@colorado.edu, bertness@boulder.nist.gov, cdodson@boulder.nist.gov

Abstract:

Gallium nitride (GaN) nanowires synthesized previously through catalyst-free molecular beam epitaxy [1] were integrated with silicon circuits containing p-type metal-oxide-semiconductor field-effect transistors (MOSFETs). Basic silicon circuits were designed and fabricated, containing specific contact areas where nanowires could be deposited. GaN nanowires were aligned to the contacts by dielectrophoresis and contacted with an additional metal layer. Optical and scanning electron microscope (SEM) images and current-voltage measurements were taken to image and test the devices.

Introduction:

GaN and its alloys with aluminum and indium have many potential applications due to the large range of their semiconductor band gap from the ultraviolet to infrared areas of the electromagnetic spectrum. Currently macroscale GaN is used in light emitting diodes and lasers found in cell phones, traffic lights, and DVD players [2]. GaN grown on the nanoscale as nanowires has benefits over its macroscale counterpart. Nanowires can be grown with a much lower defect density than macroscale GaN due to their small cross sectional area which avoids crystal lattice structure mismatch. GaN nanowires can also be grown directly on silicon substrates, commonly used in the electronics industry. Due to their high purity and convenient band gap, GaN nanowires have potential applications in quantum computing, biological sensing, and spectroscopy.

For any of these applications to become a real, marketable product, GaN nanowires must be integrated into circuitry. In this project, GaN nanowires were applied to integrated silicon circuits containing transistors and studied by current-voltage measurements and microscopy.

Experimental:

A basic device was designed for the nanofabrication of the circuits to contain a p-type MOSFET connected to an area for nanowire applicationa. Devices were fabricated on <100> n-type silicon wafers. A layer of silicon dioxide was formed through wet oxidation with an automatic ellipsometer measured thickness of 0.713 ± 0.036 μm. Field oxide areas were etched in the oxide using negative resist photolithography (Futurrex NR9-1000PY, 1000 nm) and buffered oxide etch (JTBaker, 6:1). Boron was diffused into the field oxide regions using solid source boron nitride wafers (PDS) to form source and drain regions. Regions for gate oxidation were etched and oxidation took place in a dry/wet/dry oxidation sequence for a total oxide thickness of 0.1061 ± 0.0005 μm. The oxide was annealed at 910°C in a nitrogen environment. Via holes were etched over the source and drain regions. A thickness of 0.300 ± 0.003 μm of aluminum (Alfa Aesar, 100%) was thermally evaporated on the wafers and etched using a positive resist photolithography (Clariant

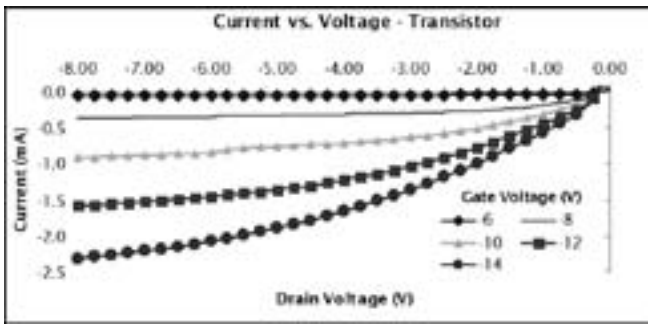

Figure 1, top: Typical current-voltage curve for a transistor.

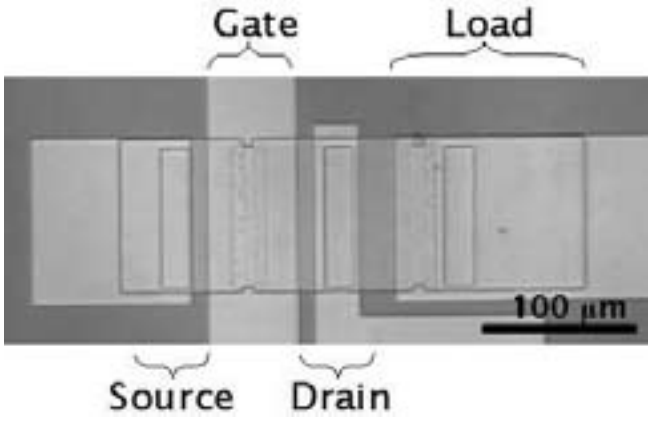

Figure 2, bottom: Optical microscope image of transistor with regions of the transistor labeled.

AZ4210) and aluminum etch at 40°C (Transene type A) to form areas for nanowire application and complete transistor fabrication.

GaN nanowires were synthesized by catalyst-free molecular beam epitaxy according to previous reports [1]. The n-type doping variation as a fraction of total length of the nanowires was 30/50/20% high/undoped/high. Using a micropipette, 3.5 μL of a suspension of the nanowires in isopropanol were applied and aligned by dielectrophoresis [3]. Metal to contact the nanowires to the devices was formed through negative resist liftoff photolithography (Futurrex NR7-1500PY) and electron beam evaporation of 20 nm of titanium and 200 nm of aluminum. The metal was annealed by rapid thermal anneal at 500°C for 60 seconds in a 5/95% hydrogen/argon environment.

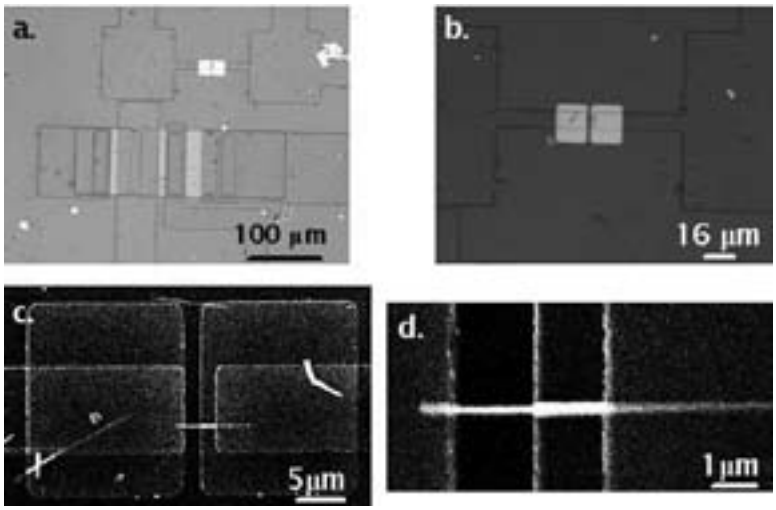

Figure 3: Optical (a, b) and SEM (c, d) images of a final device.

Results and Discussion:

After fabrication, current-voltage measurements were taken of the transistors. Of the devices fabricated, 85% of the transistors were working. Typical current-voltage curves for a transistor can be seen in Figure 1. An optical microscope image of a transistor is shown in Figure 2.

After nanowire application, 27% of the devices had nanowires across the metal leads designed for the application and 8% had a single nanowire. Optical and SEM images were taken of the devices (Figure 3).

Current-voltage measurements were taken across the single nanowires. The measurements are indicative of Schottky-like or insulating behavior (Figure 4) which does not agree with previous electrical characterizations of the wires on simpler substrates. A possible explanation for this discrepancy could be the metal contacts landed on the undoped regions of the wire, causing a non-ohmic contact. The metal contact process could be adjusted so better contact could be made.

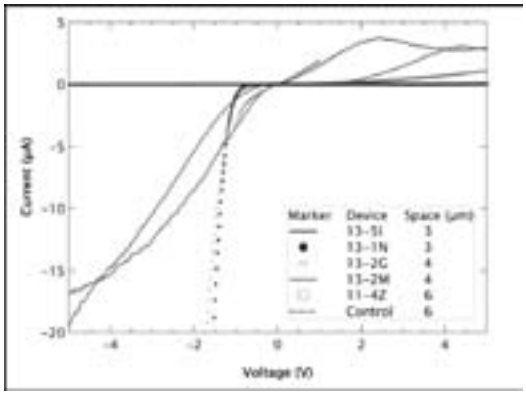

Figure 4: Current-voltage measurements on single nanowire devices.

Conclusions:

In this project, a basic device was designed for a circuit containing a transistor and an area for GaN nanowires to be applied. Transistors were fabricated with 85% of the transistors working. GaN nanowires were applied to the devices using dielectrophoresis, and shown to work with an insulator or diode behavior.

Previous research has shown GaN nanowires have a good photoconductive response and a high potential as an ultraviolet photoconductor [4]. Completely depleted wires are insulating when measurements are taken in the dark, but in light, photons are absorbed by the wire, reducing the depletion region so the wire becomes more conductive. With the circuits fabricated in this project which contain depleted nanowires, future studies will demonstrate their application as an ultraviolet photoconductor. The transistors will also be studied to see if they amplify the photoconductive signal of the nanowires.

This is one basic step in the application of GaN nanowires with silicon circuits. Future work can expand by applying GaN nanowires to more complex circuitry and studying many of the possible applications of GaN in silicon circuits.

Acknowledgements:

This work was financially supported by the National Science Foundation, National Nanotechnology Infrastructure Network Research Experience for Undergraduates (NNIN REU) Program, and University of Colorado at Boulder. The Colorado Nanofabrication Lab and NIST are also to thank for their support and facilities.

References:

[1] Bertness, K.A.; et. al. J. of Electronic Materials, 2006, 35, 576-580.
[2] Bertness, K.A.; et. al. J. of Defense Software Engr, 2006, 9-12.
[3] Motayed, A.; et. al. Journal of Applied Physics, 2006, 100, 114310.
[4] Mansfield, L. M.; et. al. J. of Electronic Materials, 2009, 38, 495-504.

Semiconductor Nanocrystal Inks for Printed Photovoltaics

James Mueller

Chemical Engineering, University of Michigan – Ann Arbor

NNIN REU Site: Microelectronics Research Center, University of Texas, Austin, TX
NNIN REU Principal Investigator(s): Brian A. Korgel, Chemical Engineering, University of Texas
NNIN REU Mentor(s): Matthew G. Panthani, Chemical Engineering, University of Texas
Contact: jamesmue@umich.edu, korgel@che.utexas.edu, mgp424@che.utexas.edu

Abstract:

In this study, photovoltaic solar cells were fabricated using a solution-processable route. These devices were comprised of several metallic or semiconducting layers, all of which were solution-processed from colloidal nanocrystals. Conventional copper indium gallium selenide (CIGS) solar cells (made through vapor deposition and sputtering of metal or semiconductor targets) typically have a stacked structure of an evaporated metal back electrode, co-evaporated semiconducting layers, and a sputtered transparent conductive oxide top contact such as indium- tin oxide (ITO). Rather than sputtering or evaporating these layers, we sprayed dispersions of nanocrystals using an airbrush purchased from a local art supply store. In this study, we used a back contact of gold (Au), semiconductor layers of zinc oxide (ZnO), cadmium sulfide (CdS), and CIGS, and an ITO top electrode. Devices were prepared on both glass and flexible plastic substrates, and annealed in a tube furnace or on a heating stage. The power conversion efficiency of the completed devices were tested to assess the feasibility of implementing devices made in this manner.

Introduction:

The world is in an energy crisis right now. We are using non-renewable resources to create energy, but now these resources are disappearing and energy prices are skyrocketing. Most of these non-renewable resources are carbon based products, such as coal and oil, and produce greenhouse gases (CO_2 and NO_x). These greenhouse gases lead to many negative environmental impacts such as acid rain and global warming.

Solar power is becoming a sought-after alternative to carbon based energy. Harnessing solar energy has been considered for a long time, but it was never thought of as a good alternative to fossil fuels because of the large price of solar panels. On average, a solar panel will cost around $20,000 for a typical home. Our goal is to reduce that number to $2000 per panel.

In this project, we will be using colloidal nanocrystal dispersions to create "inks" that can be used to spray coat all the layers needed for a photovoltaic cell. The light-absorbing semiconductor will be CIGS nanocrystals. CIGS is an attractive material because it has a bandgap suited well to the solar spectrum and has a high absorption coefficient [5], enabling it to absorb most of the incoming light with a very thin (~ 1 μm) layer. In laboratory scale-devices, it has shown power conversion efficiencies approaching 20% [6].

Experimental Procedure:

There were five layers to the solar cells we made. We used Au and indium tin oxide (ITO) as top and bottom electrodes, respectively. These would extract the charge carriers from the semiconductor layers. Copper indium gallium selenide (CIGS) was used as the p-type absorber layer. Lastly, cadmium sulfide (CdS) and zinc oxide (ZnO) was used as the n-type semiconductors. The CIGS – CdS, ZnO layers were used to make a p-n junction that would create a difference in electronic potential which would cause positive and negative charge carriers to separate, creating a current. Each of these materials were synthesized, expect ITO was bought from Sigma-Aldrich in a 20% wt dispersion in isopropyl alcohol. ZnO and ITO nanocrystals were dispersed in isopropyl alcohol (IPA), and CIGS, Au, and CdS nanocrystals were dispersed in toluene. The nanocrystals were synthesized using the following methods: Au via the Brust method [1], CIGS via the Panthani method [2], CdS with the Shieh procedure [3], and ZnO via the Greene method [4].

The nanocrystals were then dispersed to 5 w/v% (20 mg/mL) in the solvents described above. These were the "inks" we used. We used an artist's airbrush to spray this ink on a glass substrate.

To make the full device, we sprayed each layer, and then after each layer, we annealed in a vacuum oven at 100°C for 2 minutes. After the full device was sprayed and each layer was annealed, we annealed the completed device at 200°C for 5 minutes.

Results and Conclusions:

In Figure 1, you can see the full device as prepared. The Au contacts are the shapes that look like fingers that stretch the whole width of the device. Nickel paint was put on top of the contacts to protect them and those are the circular spots on the left of the figure. The stack of all the nanocrystals is located on the right of the figure.

Figure 2 shows a scanning electron microscope (SEM) micrograph of a completed device that was cracked in half. Different layers can be seen on the image and this suggests that we made device with all the layers intact.

A power conversion efficiency test was run to determine if any photocurrent would be produced from the device. No photocurrent was found. This could be from a few things, including nonuniformity of sprayed layers. It is important to have complete and discontinuity-free layers to prevent shorts.

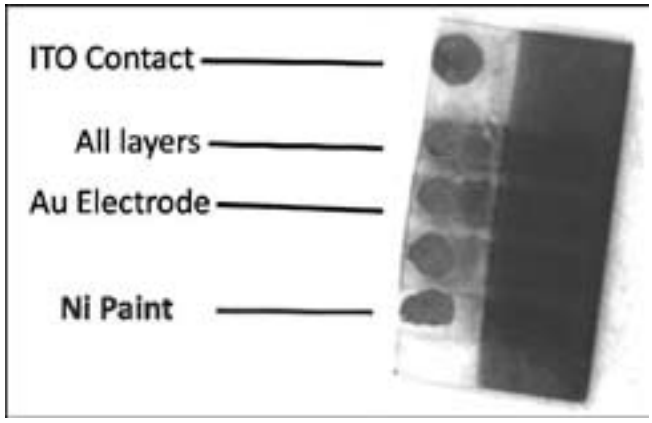

Figure 1: Fully prepared device.

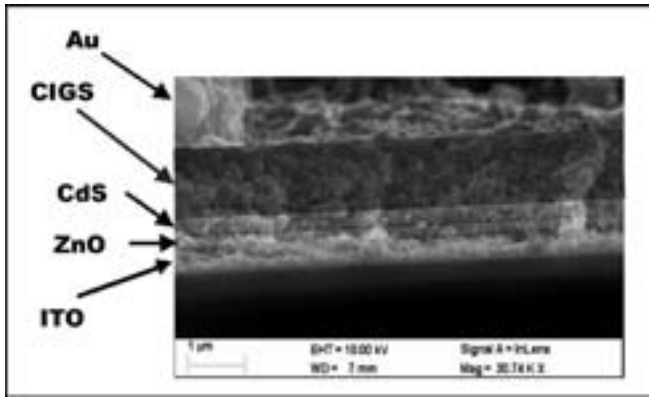

Figure 2: SEM of cracked device.

Future Work:

Different techniques of creating continuous films should be explored. Spraying continuous and complete layers are vital to create a current through the device. Other techniques should be explored to spray the nanocrystals onto the substrate. Our method for synthesizing ZnO caused discontinuous films to form. Other ways to deposit ZnO should be explored. Different annealing methods should also be explored.

Acknowledgements:

National Nanotechnology Infrastructure Network Research Experience for Undergraduates Program, the National Science Foundation, Dr. Brian A. Korgel, Matthew G. Panthani, Vahid Akhavan, Brian Goodfellow, the Korgel Group, Jean Toll, the University of Texas at Austin, and the University of Michigan.

References:

[1] Brust et al, J. Chem. Soc., Chem. Commun., 1994, 861.

[2] Panthani et al, J. Am. Chem. Soc., 2008, 130 (49), pp 16770-16777.

[3] Shieh et al, J. Phys. Chem. B, 2005, 109 (18), pp 8538-8542.

[4] Greene et al, Nano Lett., 2005, 5 (7), pp 1231-1236.

[5] Rockett et al, R. W. Journal of Applied Physics, 1991, 70, R81-R97.

[6] Repins et al, Progress in Photovoltaics: Research and Applications, 2008, 16, 235-239).

High-Aspect-Ratio Polyimide Pore Array Template for Thin Film Solar Cells

Travis Rosmus

Chemistry, Saint Francis University

NNIN REU Site: Penn State Nanofabrication Laboratory, Pennsylvania State University, State College, PA
NNIN REU Principal Investigator(s): Dr. Theresa Mayer, Electrical Engineering Department, Penn State University
NNIN REU Mentor(s): Heayoung Yoon, Electrical Engineering Department, Penn State University
Contact: txrst8@mail.francis.edu, tsm2@psu.edu, hxy148@psu.edu

Abstract:

A lightweight and flexible photovoltaic device can be created within high-aspect-ratio pores in a polymer sheet, where the geometry of radial junctions would offer a high carrier collection. By spinning and curing liquid polyimide (PI) on an oxidized silicon (Si) pillar array, a high-density PI pore array template (~ 10^5 pores) was fabricated. The features of the released polymer template were investigated using an optical microscope and a field-emission scanning electron microscopy (FE-SEM). Radial junctions of p-i-n can be achieved within the pores of the template using conformal thin-film deposition to create high-performance solar cells.

Introduction:

A conventional planar solar cell consists of n- and p-type Si layers. When the light illuminates on the top-most highly absorbing layer (e.g., p+ layer), the generated electron-hole pairs should travel through the bulk layer until they are separated at the depletion region to be harvested. While the carriers in a planar cell, whose thickness is much thicker than the minority carrier diffusion length ($L_{n,p}$), are largely lost due to the recombination, those generated in a radial junction of a diameter of < 2 $L_{n,p}$ can be separated and collected in a perpendicular direction of the illumination, resulting in higher efficiencies [1,2]. By taking advantage of this geometry, high-aspect-ratio pores created on a polymer sheet would provide desirable features including flexibility and being lightweight. In addition, the technique of a-Si thin-film deposition within the pores in the PI template can provide a much cheaper and efficient way to fabricate solar cells when compared to the cells made from a crystalline Si substrate. Using the spinning and curing methods of liquid PI on an oxidized Si pillar array, we fabricated 2.5 mm × 2.5 mm (~ 10^5 pores) high-aspect-ratio pore array PI templates. The flexible template substrate will be used for thin-film radial junction solar cells.

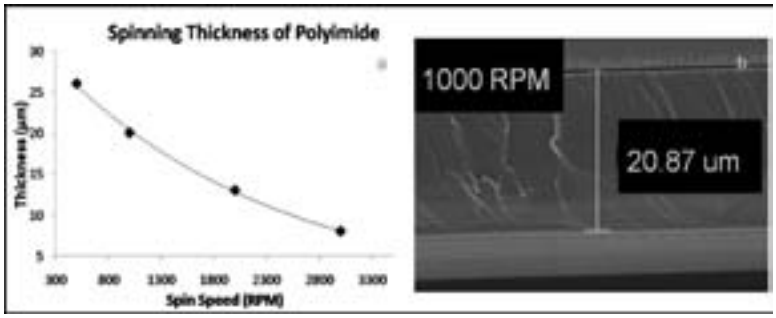

Figure 1: PI thickness vs. spin speed performed on Si planar substrates. Right shows FE-SEM image of the PI film after the spinning and curing processes.

Experimental Procedure:

A PI template was fabricated by spin-coating and curing the liquid PI [3] on an oxidized Si pillar. In order to determine the optimized condition for spin-coating, the liquid PI was spun on three planar samples with spin speeds of 500, 1,000, and 2,000 revolutions per minute (RPM), respectively, and cured in an oven at 250ºC for 3 hours. As shown in Figure 1, a thickness of 21 μm PI planar film could be achieved at the spin-speed of 1,000 RPM. Using this condition, we spun the liquid PI onto oxidized Si pillar arrays of a diameter of 20 μm, height of 25 μm, and the distance between the pillars of 5 μm (~ 10^5 pillars in 2.5 mm × 2.5 mm square) and cured the sample. The SEM image in Figure 2 (a) shows the side-view of the sample.

A reactive ion etching (RIE) process was performed for 10 minutes to etch away the PI on the tops of the pillars, exposing the oxide layer (Figure 2, b). The whole sample was then placed in a buffered oxide etchant (BOE 1:10) for two days to etch the oxide layer off the pillars, thus making it easy to release the PI pore template from the Si pillar arrays. Once the oxide was completely removed, the template was removed, using double-sided carbon tape, for the SEM analysis.

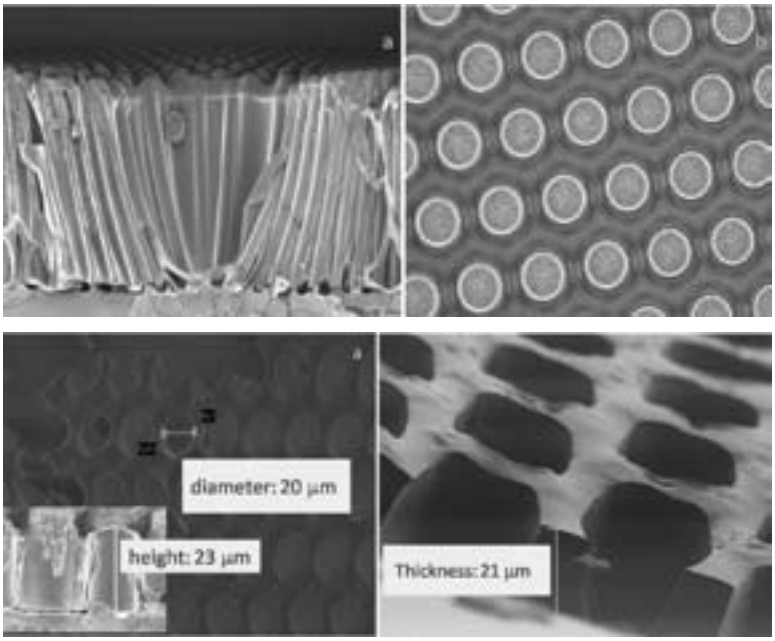

Figure 2, top: FE-SEM images of PI coated pillars (a) and RIE etched pillars (b). The pillar array of 2.5 mm × 2.5 mm that contained ~ 10^5 pillars of 20 μm-diameter, 25 μm-high and a distance of 5 μm between the pillars.

Figure 3, bottom: FE-SEM image of the top- and side-view of the released PI pore template of a diameter of 20 μm, height of ~ 21 μm, and the distance between the pillars of 5 μm in 2.5 mm × 2.5 mm square.

Results and Conclusion:

Figure 3 shows top- and side-view of the released PI pore template. Each pore had a diameter of ~ 20 μm and the distance between the pillars was 5 μm (Figure 3, b). The measured thickness was approximately 21 μm, indicating the RIE condition was just enough to open up the tops of the pillars and not etch the PI template further. In addition, the optimized fabrication process allowed us to release the whole PI template (2.5 mm × 2.5 mm) from the Si pillar array substrate. Through a series of samples, diameters of 8-32 μm PI pore array templates were obtained.

Future Work:

In this work, we developed a fabrication procedure to create a high-aspect-ratio PI pore template using spin-coating, curing, and releasing processes. Using a conformal thin-film deposition of a-Si, radial junction of p-i-n can be achieved within the pores of the template, creating thin film solar cells. The pore template can also be obtained by direct etching technique, such as using magnetically enhanced reactive ion etching on a metal patterned PI planar substrate.

Acknowledgements:

We would like to thank Yu Yuwen for all her assistance in helping to get the REU student trained and being there to answer all his questions. We would like to thank Seokho Yun for his assistance with the thin-film removal off the tops of the pillar array. All experimentation was performed in the Microfabrication Facility at Penn State at which the staff was crucial in the REU training and aideing the REU student in his processes. Finally, we thank the National Nanotechnology Infrastructure Network Research Experience for Undergraduates (NNIN REU) Program for funding.

References:

[1] Zhiyong, F. et al., "Three-dimensional nanopillar-array photovoltaics on low-cost and flexible substrates" (2009).

[2] Kayes, B., et al., "Comparison of the device physics principles of planar and radial p-n junction nanorod solar cells" (2005).

[3] HD MicroSystems Product Bulletin (http://www2.dupont.com/HDMicroSystems/en_US/pdf/PI-2525_2555_2556_2574_ProductBulletin.pdf).

Optimization of Tunnel Diodes in Multi-Junction Solar Cells

Alexander Sharenko

Materials Science and Engineering, Georgia Institute of Technology

NNIN REU Site: ASU NanoFab, Arizona State University, Tempe, AZ

NNIN REU Principal Investigator(s): Prof. Yong-Hang Zhang, Electrical Engineering, Arizona State University

NNIN REU Mentor(s): Dr. Kevin O'Brien, Electrical Engineering, Arizona State University

Contact: alexsharenko@gmail.com, yhzhang@asu.edu, kgobrie1@asu.edu

Abstract:

Tunnel diodes (TD) are highly doped p-n diodes which allow for quantum mechanical tunneling through their narrow depletion regions at relatively low forward bias voltages. Unfortunately, when incorporated into multi-junction (MJ) solar cells their comparatively low peak tunneling current densities (J_{PT}) often limit cell performance in terrestrial applications. The purpose of this research was to investigate whether the J_{PT} of gallium arsenide (GaAs) TDs could be improved via the simple introduction of impurity atom defects during epitaxial growth. Three TDs were grown by molecular beam epitaxy (MBE) with an interruption of 0, 1, or 10 minutes between growth of the n and p-doped layers. Current-voltage (I-V) measurements were used to determine device J_{PT} values, which were measured as 5.08, 4.82 and 3.29 mA/cm^2 respectively at 300 K. The introduction of a growth interruption period therefore resulted in a decline in J_{PT}, which suggests a more controlled means of defect introduction is required to improve TD performance.

Introduction:

MJ solar cells are monolithic devices consisting of several photovoltaic subcells stacked vertically with each subcell connected via a TD. TD junctions are of vital importance to MJ solar cells as they provide a relatively optically transparent, low resistance, lattice-matchable means of transferring current from one subcell to the next. There are two major tunneling mechanisms in TDs: band-to-band and defect-assisted. Band-to-band tunneling is depicted in Figure 1 and by itself usually results in relatively low (< 1 A/cm^2) J_{PT}. Defect-assisted tunneling is depicted in Figure 2 and is advantageous for producing large (< 10 A/cm^2) J_{PT} in TDs [1].

The main objective of this project was to investigate whether an interruption between epitaxial growth of n- and p-doped layers could introduce performance enhancing background impurity atoms into the depletion region of GaAs TDs. The incorporation of defects into the depletion region has been shown to improve J_{PT} in GaAs TDs via defect-assisted tunneling [2]. Improved J_{PT} values in TDs would allow MJ solar cells to be used in high concentration photovoltaic systems where sunlight is focused 1000 times or more on a cell. Such systems are of great interest because of their potential to produce cost-effective, environmentally benign energy.

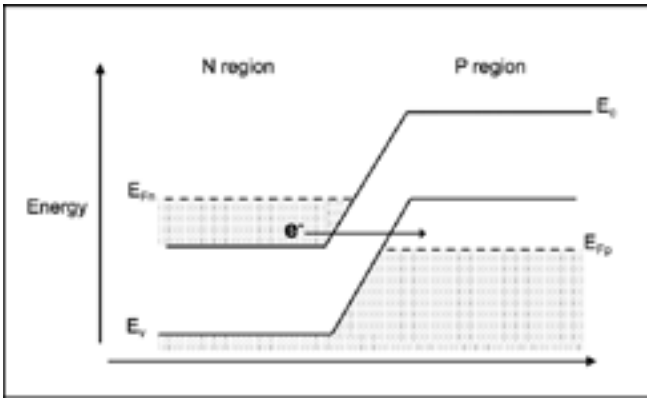

Figure 1: Energy band diagram of direct band-to-band tunneling in a tunnel diode.

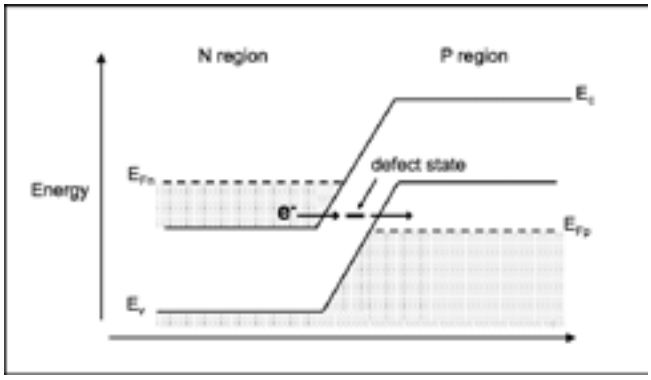

Figure 2: Energy band diagram of defect-assisted tunneling in a tunnel diode.

Procedure:

Three GaAs TD samples were grown using a VG V80H MBE system. N-type doping was achieved with silicon (Si) at a doping concentration of 5×10^{18} cm^{-3} and p-type doing was achieved with beryllium (Be) at a concentration of 3×10^{19} cm^{-3}. An interruption between the growth of the n and p-doped layers was introduced by closing all the elemental source shutters for 0, 1 or 10 minutes. I-V characterization was then performed on each TD from 80 to 300 K at 20 K intervals using a two wire Lake Shore Cryotonics low temperature probe station.

Results and Discussion:

At 300 K, J_{PT} values were measured to be 5.08, 4.82 and 3.29 mA/cm^2 for the 0.0, 1.0 and 10 minute growth interruption period samples respectively, as shown in Figure 3. These values are several orders of magnitude below that which is required for use in a high efficiency MJ solar cell under high concentration and indicate that the dominant tunneling mechanism was band-to-band tunneling. A strong linear correlation between the decline in JPT and increasing growth interruption period was observed with a coefficient of determination (R^2) value greater than 0.99 as shown in Figure 4. This relative trend held true at all investigated temperatures. A possible explanation for these results is that any impurities introduced into the TDs' depletion regions had the effect of freezing out free carriers introduced by Si and Be doping, thus widening the depletion region. A wider depletion region would decrease the probability of quantum mechanical tunneling and thus lead to lower J_{PT}.

Conclusion:

These results suggest the tested TDs predominantly exhibit band-to-band tunneling and that any incorporated impurity atoms only lowered J_{PT}. Also implied is that enabling defect-assisted tunneling in GaAs TDs requires a more controlled, tailored approach than the uninhibited inclusion of background impurity atoms during MBE growth.

As future work, the use of transmission electron microscopy to determine the extent of the incorporation of impurity atoms into the TDs' depletion regions would help confirm that defects played a role in device deterioration. Additionally, experimentally verifying the doping profile of the TD samples would help elucidate the specific mechanism of performance degradation as introduced defects may have led to deviations from the expected doping profile. This is significant because the doping of the device largely determines the band-to-band tunneling probability and therefore lower than expected doping levels could explain the observed decreases in J_{PT} associated with increases in the growth interruption period.

Acknowledgments:

I would like to thank Prof. Yong-Hang Zhang and Dr. Kevin O'Brien for their guidance through this research process. Additionally I would like to thank the National Science Foundation, the National Nanotechnology Infrastructure Network Research Experience for Undergraduates, and the Center for Solid State Electronics Research at Arizona State University for research support and funding.

References:

[1] K. Jandieri, S. D. Baranovskii, O. Rubel, W. Stolz, F. Gebhard, W. Guter, M. Hermle, and A. W. Bett, "Resonant electron tunneling through defects in GaAs tunnel diodes," Journal of Applied Physics, vol. 104, p. 094506, 2008.

[2] K. Jandieri, S. D. Baranovskii, O. Rubel, W. Stolz, F. Gebhard, W. Guter, M. Hermle, and A. W. Bett, "Resonant tunneling as a dominant transport mechanism in n-GaAs/p-GaAs tunnel diodes," Applied Physics Letters, vol. 92, p. 243504, 2008.

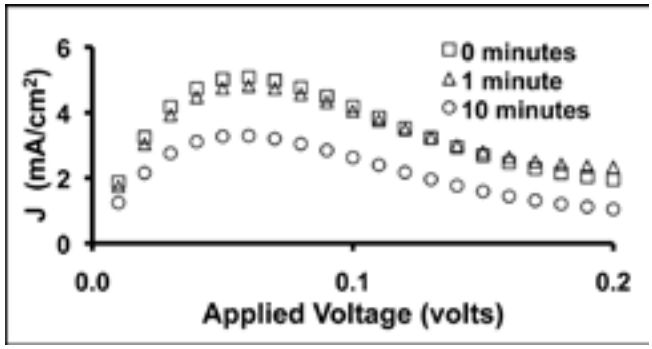

Figure 3: Tunnel diode I-V measurements at 300 K. Legend denotes time of growth interruption period.

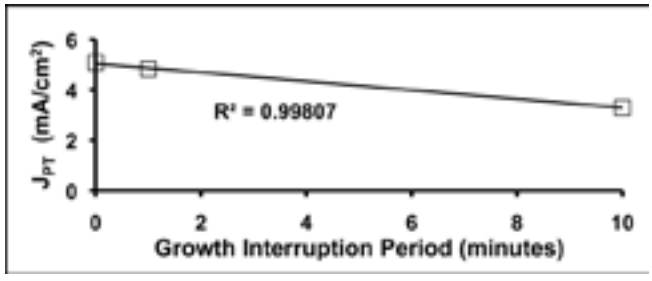

Figure 4: Relationship between growth interruption period and J^{PT} at 300 K.

Ohmic Contact Study for Gallium Nitride-Based High Electron Mobility Transistors and Ultra-Short N-Type THz Devices

Ian Walsh

Applied Physics, Rice University

NNIN REU Site: Cornell NanoScale Science and Technology Facility, Cornell University, Ithaca, NY

NNIN REU Principal Investigator(s): Prof. Lester F. Eastman, Electrical and Computer Engr, Cornell University

NNIN REU Mentor(s): Dr. Quentin Diduck, Electrical and Computer Engineering, Cornell University; Jonathan Felbinger, Electrical and Computer Engineering, Cornell University

Contact: iaw1@rice.edu, lfe2@cornell.edu, felbinger@cornell.edu

Abstract:

Gallium nitride (GaN) based high electron mobility transistors (HEMTs) and terahertz (THz) emission devices are promising technologies for high-speed, high-power applications [1]. The formation of reliable, low resistance, thermally stable ohmic contacts is a crucial part of improving device performance. In this study, we examined various metal layers for making contacts on both HEMT and THz type substrates with the goal of achieving lower transfer resistance and improved repeatability. We also tested the response of the contacts to rapid thermal annealing (RTA) to determine the optimal anneal conditions for each metal stack. Those using vanadium (V) in the first-deposited layer were the top performers for the HEMT material system, while niobium (Nb) in the first layer produced the best results for the THz material system.

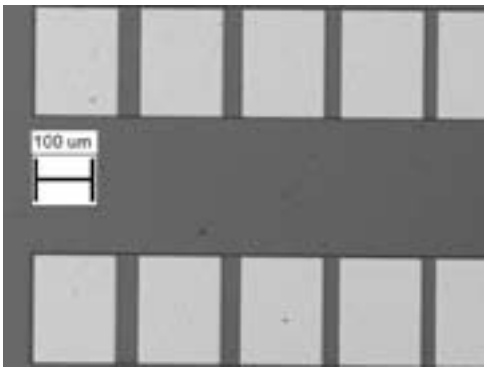

Figure 1: Overhead view of TLM structures.

Methods:

Ohmic contacts were studied for two different GaN material systems, corresponding to the two devices of interest. The HEMT material was an epitaxially-grown AlGaN/GaN hetero-junction on a silicon (Si) substrate, available commercially from Nitronex. The THz material was germanium-doped n+ type GaN ($N_D \approx 2 \times 10^{20}$ cm^{-3}), grown via molecular beam epitaxy at Cornell, prior to this experiment. Each wafer was patterned with 200 μm wide, 100 nm tall rectangular mesas using a reactive ion etcher with $Ar/Cl_2/BCl_3$ chemistry. Transfer length method (TLM) patterns were created with a contact spacing that varied linearly from 5 μm to 40 μm in increments of 5 μm. The HEMT and THz material wafers were cleaved into smaller samples (~ 5 mm × 5 mm) to analyze multiple metal configurations and anneal conditions.

All of the metals in this study were deposited using e-beam evaporation, except for gold (Au) and aluminum (Al), which were evaporated thermally. Immediately prior to being loaded into the evaporator, the samples were cleaned in an oxygen plasma for 60 seconds at 100 W power to remove any residual resist in the contact areas and then immersed for 30 seconds in a buffered oxide etch solution (BOE 30:1) to remove any native oxide. All of the metal layers for a given stack were deposited *in situ*. After evaporation, a standard liftoff was performed followed by a deionized water rinse. Figure 1 shows an overhead view of two of the finished mesas and metal arrays used in this study.

Using four-point-probe technique, we measured the resistance of each TLM gap; from the linear relationship between resistance and gap length, we were able to calculate the contact resistivity ρc (in ohm-mm), the sheet resistance R_{sh} (in ohms/sq), the transfer length L_t (in μm), and the specific contact resistance R_{sc} (in ohm-cm^2) [2]. For each sample, these values were averaged over the results from many mesas with a typical 85% uniformity.

To study the thermal dependence of ohmic contact formation, we used an AG HeatPulse rapid thermal annealer (RTA) to examine a range of temperatures and times. All of the anneals were performed in a nitrogen (N_2) ambient and the carrier wafer temperature was measured via thermocouple.

Terahertz Material Results:

A complete thermal profile of every metal configuration investigated was neither feasible nor necessary for our purposes, which were to find the lowest contact resistance. Table 1 summarizes the best contact resistances we were able to achieve from each metal stack and the associated anneal conditions.

Note that where marked with an asterisk, the anneal conditions shown were only the final temperatures used after previous, lower-temperature anneals on the same sample. In general,

Metal Stack	Layer Thicknesses (Å)	Rc (ohm-mm)	Rsh (ohms/sq)	Lt (μm)	Rsc (ohm-cm²)	Anneal Conditions
Sc	1100	0.943	25.7	39.3	1.50E-05	as deposited
Sc/Au	500 / 600	0.788	32.1	25.1	7.99E-06	30 sec at 350 °C
Ti/Sc/Mo/Au	100 / 600 / 400 / 450	0.750	36.6	20.6	6.25E-06	30 sec at 650 °C *
V/Al/V/Au	150 / 800 / 200 / 1000	0.141	39.5	3.63	2.09E-07	30 sec at 650 °C *
Nb/Al/Nb/Au	150 / 800 / 200 / 890	0.136	42.4	3.22	1.76E-07	30 sec at 700 °C *
Nb/Au	150 / 300	0.223	37.2	6.00	5.35E-07	30 sec at 600 °C *

Table 1: Optimal contact resistances for Terahertz material.

Metal Stack	Layer Thicknesses (Å)	ρc (ohm-mm)	Rsh (ohms/sq)	Lt (μm)	Rsc (ohm-cm²)	Anneal Conditions
Sc	1100	(not ohmic)	n/a	n/a	n/a	n/a
Sc/Au	500 / 600	(not ohmic)	n/a	n/a	n/a	n/a
Ti/Sc/Mo/Au	100 / 600 / 400 / 450	(not ohmic)	n/a	n/a	n/a	n/a
Ti/Al/Mo/Au	150 / 900 / 400 / 500	(not ohmic)	n/a	n/a	n/a	n/a
Ti/Al/Si/Au	125 / 700 / 350 / 1000	0.427	1170	0.362	7.17E-08	30 sec at 750 °C *
Ti/Al/Si/Cu	125 / 700 / 350 / 1000	1.24	1700	0.728	3.60E-07	30 sec at 800 °C *
Ta/Ti/Al/Mo/Au	75 / 150 / 900 / 400 / 500	2.01	899	2.28	1.87E-06	60 sec at 700 °C then 20 sec at 800 ° C
V/Ti/Al/Mo/Au	75 / 150 / 900 / 400 / 500	0.796	591	1.37	4.52E-07	60 sec at 700 °C then 20 sec at 800 ° C
V/Al/V/Au	150 / 800 / 200 / 1000	0.521	763	0.677	1.74E-07	40 sec at 775 °C
V/Al/Si/Au	150 / 800 / 350 / 1000	0.984	1230	0.788	3.31E-07	30 sec at 800 °C *
V/Al/Si/Cu	150 / 800 / 350 / 1000	0.176	1000	0.176	1.24E-06	30 sec at 800 °C *
V/Al/V/Cu	150 / 800 / 200 / 1000	(not ohmic)	n/a	n/a	n/a	n/a
Nb/Al/Nb/Au	150 / 800 / 200 / 890	0.851	926	1.02	5.53E-07	30 sec at 850 °C *
Nb/Au	150 / 300	(not ohmic)	n/a	n/a	n/a	n/a

Table 2: Optimal contact resistances for HEMT material.

the anneals were performed in steps of 50°C beginning at 350°C, annealing for 30s at each temperature, and letting the sample return to room temperature for measurement between successive anneals

HEMT Material Results:

The nature of the AlGaN barrier layer made forming good contacts to the undoped HEMT material more challenging. In contrast to the THz material, none of the as-deposited metal stacks exhibited a linear current/voltage relationship. Annealing, often beyond 500°C, was required before the contacts became ohmic. Several of the metal stacks exhibited nonlinear current/voltage relationships regardless of anneal condition. Table 2 summarizes the best results achieved for contacts to the HEMT material.

Summary:

The metal stack Nb/Al/Nb/Au exhibited the lowest contact resistance to the THz material, with good edge acuity and thermal stability. For the HEMT material system, V-based stacks demonstrated the best overall performance, but several exhibited high sheet resistances after annealing. The TLM model assumes uniform sheet resistance throughout the semiconductor, including under the contacts, and is not valid when this assumption is violated [2].

Acknowledgments:

The author wishes to thank: Prof. Lester F. Eastman and his group, esp. Dr. Quentin Diduck and Jonathan Felbinger; Rick Brown and Stephen Jones, CNF Users; The National Nanotechnology Infrastructure Network Research Experience for Undergraduates (NNIN REU) Program; The National Science Foundation; Cornell NanoScale Science & Technology Facility; All of the CNF staff, especially Melanie-Claire Mallison, Rob Ilic, and Aaron Windsor.

References:

[1] Quay, R. (2008). Gallium nitride electronics. Berlin: Springer.

[2] Y. Sun, X. Chen, and L. Eastman, J. Appl. Phys. 98, 053701 (2005).

Sidewall Process for III-V MOSFET Fabrication

Lorraine Weis

Engineering Physics, Franklin W. Olin College of Engineering

NNIN REU Site: Nanotech@UCSB, University of California, Santa Barbara, CA

NNIN REU Principal Investigator(s): Mark Rodwell, Electrical and Computer Engr, UC Santa Barbara

NNIN REU Mentor(s): Gregory Burek, Electrical and Computer Engr, University of California at Santa Barbara

Contact: lorraine.weis@students.olin.edu, rodwell@ece.ucsb.edu, burek@ece.ucsb.edu

Abstract:

Downsizing scalable transistor technology to increasingly smaller dimensions is necessary for more powerful electronics, as well as cheaper, more energy efficient devices, but *scaling* introduces new difficulties. While silicon technology may be reaching its limits, new materials, such as III-V semiconductor, are being developed for use in complementary metal-oxide semiconductor (CMOS) transistors with gates smaller than 15 nm. However, as gate lengths decrease, other features need to scale as well. Sidewalls, also called spacers, insulate the drain and source metal contacts from the gate of the transistor. Two techniques were investigated for producing thin, reliable sidewalls for use in metal-oxide semiconductor field effect transistors (MOSFETs).

Introduction:

As transistors continue to shrink, III-V semiconductor has a number of advantages over silicon. As a compound semiconductor, lattice spacing can be adjusted to allow very thin heterojunctions, and therefore, charge carriers may be closely confined in the channel, and offset the effects of scaling. Furthermore, with less affinity for oxygen, interfacial layers and native oxide formation are less of a problem. This material also has a lower electron effective mass, which should allow a higher drive current than in silicon transistors.

Metal-oxide semiconductor field effect transistors (MOSFETs) are widely used in digital and analog applications. Current between the source and drain is controlled by the gate voltage, which is electrically isolated by a thin insulating layer and sidewalls. Sidewalls, then, must support a large electric field without allowing large current leakage. They must also be as thin as possible, so that the gate has good control of the channel and can reduce the effect of interface traps on carrier population. In this project, over-etching of 30 nm sidewalls and slow deposition of thinner sidewalls were compared. The sidewalls of varying thickness were then electrically tested for their effectiveness as insulators.

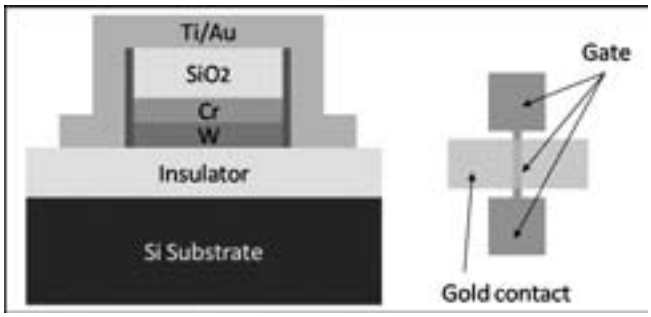

Figure 1: Structure used to test sidewall processes. Leakage current was measured by applying a voltage between the gold contact and the chromium of the gate.

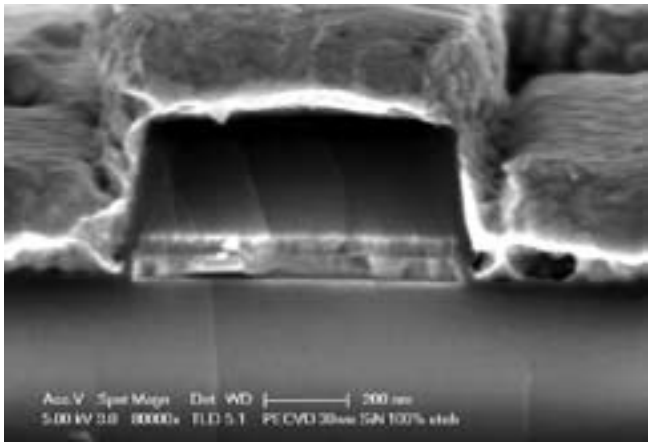

Figure 2: SEM of test structure. The sidewalls appear fairly thin, ~ 30 nm, and conformal to the gate metals.

Procedure:

To test the sidewalls, a gate stack similar to that intended for the full MOSFET was used; on silicon wafers, with a layer of either silicon dioxide or aluminum nitride, 50 nm of tungsten, 50 nm chromium, 150 nm of silicon dioxide, and another 50 nm of chromium as a hard mask. After depositing the gate stack, several etches are used to form the gate structure. SiN was then deposited in a thin film, and the horizontal regions were etched away with a low power anisotropic etch. Finally, gold contacts were sputtered on to allow close contact with the sidewall, and the gate contacts were exposed.

Results and Future Work:

The electrical properties of the sidewalls were measured by sweeping voltage across the gate and gold sidewall contacts. As expected, increased etching decreased the effectiveness and reliability of the sidewalls. Using plasma enhanced chemical vapor deposition produced conformal 30 nm sidewalls. However, over-etching on silicon dioxide did not result in significantly thinner sidewalls, as the reactants etched the field. Very slow deposition also formed thin, conformal sidewalls, although this technique was not been fully tested.

Very thin sidewalls can be made insulating on III-V semiconductor MOSFETs. This is encouraging for the development of these devices. Thinner sidewalls allow the gate to have greater control over the channel, and help increase the charge carrier concentration. Further experiments are needed to compare over-etching with slower deposition, using AlN instead of SiO_2. Because of the different chemical compositions of these insulators, over-etching should result in thinner sidewalls, while slower deposition may allow thinner sidewalls in the first place. The larger project is to make useful, small, high frequency MOSFETs out of III-V semiconductor. With gate lengths less than 15 nm, these materials should provide faster switching time, higher drive current and better drive control than other technologies.

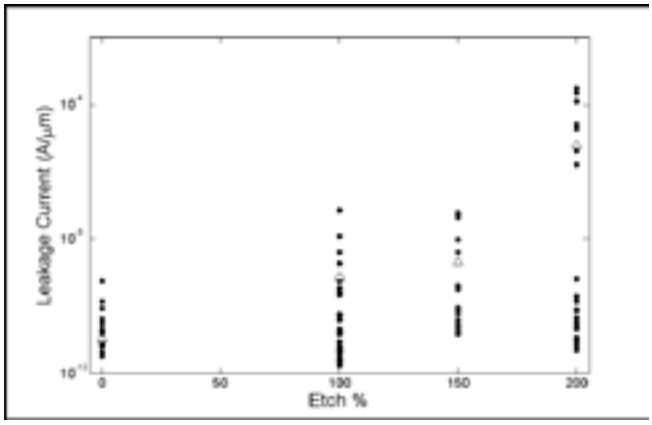

Figure 3: Plot of leakage currents for different etch amounts.

Acknowledgements:

Special thanks to Dr. Mark Rodwell and mentor Gregory Burek for excellent support in this project and to UCSB, the NNIN REU program, the NSF, and the SRC for funding and support.

Growth of CuIn(Ga)Se_2 Thin Film Solar Cells

Menooa Badalian

Computer Engineering, Glendale Community College

NNIN REU Site: Howard Nanoscale Science & Engineering Facility, Howard University, Washington, DC

NNIN REU Principal Investigator(s): Dr. Gary L. Harris, HNF, Howard University

NNIN REU Mentor(s): Mr. James Griffin, HNF, Howard University

Contact: menooa@hotmail.com, gharris@msrce.howard.edu, griffin@msrce.howard.edu

Abstract and Introduction:

Copper indium diselenide ($CuInSe_2$) and copper indium gallium diselenide ($CuInGaSe_2$) thin film solar cells deposited by spray pyrolysis are a low cost way to provide solar energy. Although they are relatively cheap to fabricate, they suffer from low efficiencies because of their small grain sizes. In this work, we investigated the conditions of growth rate and temperature in order to obtain stoichiometric layers of these materials. We also investigated the conditions necessary to grow cadmium sulfide (CdS) by chemical bath deposition, which was used as the n-type window layer for our solar cell structure. Employing cadmium sulfide also increased the photovoltaic solar efficiency of our tandem structure.

$CuInSe_2$ and $CuInGaSe_2$ films were grown on soda lime glass substrates coated with 150 nm of evaporated molybdenum at 350-400°C for 30-60 minutes. Energy dispersive spectroscopy (EDS) data for $CuInSe_2$ indicated the presence of all three elements. Cadmium sulfide (CdS) films were grown in a bath of cadmium chloride ($CdCl_2$), thiourea and aqueous ammonia at 70°C with a pH of 11. EDS on cadmium sulfide indicated the presence of both elements in equal abundance.

Scanning electron microscopy (SEM) and optical microscopy indicated uniform deposition of CdS and $CuInGaSe_2$ films but non-uniform films for copper indium diselenide.

Experimental Procedure:

Before deposition on the surface of the soda lime glass substrate, the glass was cleaned thoroughly. The glass was first put in a bath with soap and water followed by a 10 minutes acetone rinse and then a 5 minute methanol rinse. The glass was then cleaned in a 30% hydrochloric acid bath for about 30 minutes, and finally, in aqua regia [1].

The back contact layer, molybdenum (Mo), was deposited on soda lime glass by a technique called electron-beam evaporation. The thickness of the layer was set to 150 nm. The $CuInSe_2$ layer was deposited on the Mo-coated soda lime glass by spray pyrolysis as seen in Figure 1. The thickness of this layer had to be between 1000-2000 nm in order to make the solar cell work efficiently. Initial stock solutions of copper chloride ($CuCl_2$) and indium chloride ($InCl_3$) were prepared. The concentrations of the solutions were 25 mM for $CuCl_2$ and 62.5 mM for $InCl_3$. The dimethylselenide (DMSeu) had to be mixed two hours before each run and kept away from the light for about two hours until it was ready to be mixed. The concentration that was used was 165 mM [2]. To grow $CuInGaSe_2$, gallium was incorporated in the form of gallium trichloride ($GaCl_3$). The concentration of indium and gallium was 62.5 mM in order to adjust the total concentration to 125 mM, which was double the original concentration that was used.

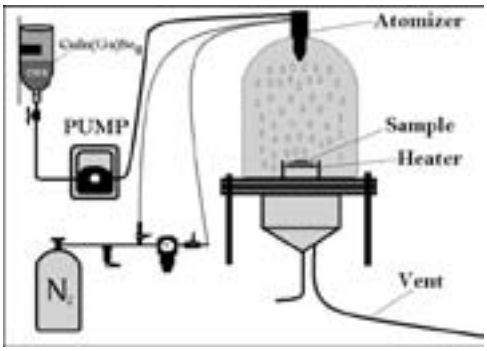

Figure 1: Spray pyrolysis system.

The growth temperature was kept between 350-400°C. The growth lasted between 30-60 minutes depending on spray rates, with 45 minutes being optimum. The spray rate was kept low to facilitate pyrolysis. In order to improve surface adhesion during pyrolysis, some glass surfaces were roughened with sand paper. The conditions for $CuInSe_2$ and $CuInGaSe_2$ growth can be seen in Table 1.

The CdS layer was deposited by chemical bath deposition and was the n-type contact for the cell. Initial stock solution of thiourea, $CdCl_2$, and ammonium hydroxide (NH_4OH) were made with solution concentrations of 10 mM for $CdCl_2$, 50 mM for thiourea and 1 M for NH_4OH. At first NH_4OH and $CdCl_2$ were mixed and heated in a water bath until the temperature reached 70°C. Thiourea was added to the bath and the pH was adjusted to 11 with 20% potassium hydroxide (KOH) and the substrate was then quickly immersed. The deposition time was 30 minutes [3].

Results and Conclusion:

The $CuInSe_2$ and CdS layers were deposited more uniformly when the concentrations of the solutions were doubled. EDS data for CdS indicated the presence of both elements as seen in Figure 2. The rate of deposition for the CdS layer was approximately 3 nm/min which produced an 80 nm thick layer. EDS on $CuInGaSe_2$ indicated the presence of all four elements as seen in Figure 3. When the concentration of Ga and In were split in half, we had a more uniform layer with the

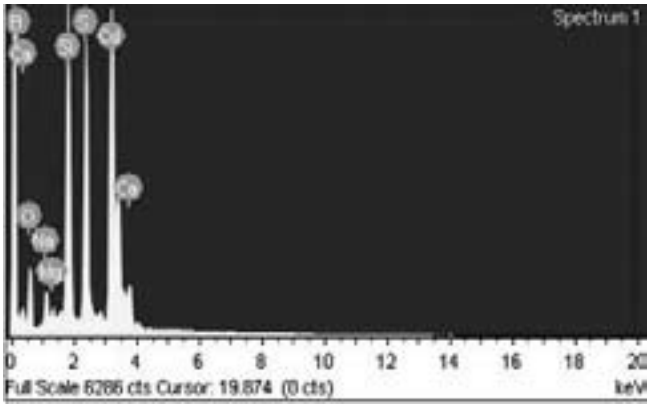

Figure 2: EDS data of CdS layer.

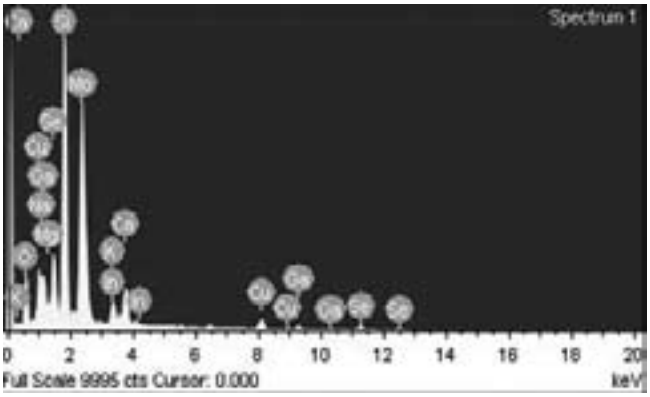

Figure 3 : EDS data of CIGS layer.

presence of all elements. We also had a better deposition rate when we roughened the surface of our sample. Uniform films of CdS were routinely obtained by chemical bath. Uniform films were more difficult to obtain by spray pyrolysis. Slower spray rates in general produced better films. CIGS films also appeared more uniform than CIS films.

Future Work:

Steps need to be taken to increase the growth rate for all layers. Efforts should also be undertaken to determine what parameters affect layer uniformity. Grain sizes need to be determined to see if they can be increase by rapid thermal annealing at high temperatures. Finally, solar cells should be fabricated so efficiency measurements can be performed.

Acknowledgements:

I would like to acknowledge the National Science Foundation, the National Nanotechnology Infrastructure Network Research Experience for Undergraduates (NNIN REU) program, and the Howard Nanoscale Science and Engineering Facility (HNF) for this great opportunity. I would also like to thank my principal investigator Dr. Gary L. Harris, my mentor Mr. James Griffin, and other staff and students at HNF including Ms. Bokani Mtengi and Ms. Mpho Musengua for their guidance and support.

References:

[1] Bachman, Mark. AMPEL Nanofabrication Facility. Fall 1999. 2 August 2009 <Mark Bachman>.

[2] Varner, E; "Factors Influencing the Performance of Copper Indium Diselenide/ Cadmium Sulfide Solar Cells Made by Chemical Spray Pyrolysis";45-54(1996).

[3] Hodes, G; "Chemical Solution Deposition of Semiconductor Films"; 50-55 (2003).

Experiment	Substrate	Concentration	Temp	Atomizer	Chamber Pressure	Flow Rate	Time	Special Pressidure	Results
1	soda lime glass	$2.5x10^{-2}$M $CuCl_2$ $6.25x10^{-2}$M $InCl_3$ 0.165M dimethylselenide	275C-350°C	5psi	40-60psi	High	1 hour	Roughened surface Cleaned with H_2SO_4, HNO_3, DI Water	Some traces of selenium
2	70nm of Moly on soda lime glass	$2.5x10^{-2}$M $CuCl_2$ $6.25x10^{-2}$M $InCl_3$ 0.165M dimethylselenide	300-350°C	5psi	40-60psi	constant	1 hour	Roughened glass Used a 4 step cleaning bath	Cu, In, Se present but in different areas so non-uniform
3	70nm of Moly on soda lime glass	$2.5x10^{-2}$M $CuCl_2$ $6.25x10^{-2}$M $InCl_3$ 0.165M dimethylselenide	350-400°C	10psi	50psi	Low	1 hour	Smooth surface Used a 4 step cleaning bath	Cu,In,Se present (non-uniform)
4	70nm of Moly on soda lime glass	$2.5x10^{-2}$M $CuCl_2$ $6.25x10^{-2}$M $InCl_3$ 0.165M dimethylselenide	350-400°C	10 psi	59 psi	constant	55 min	Used a 4 step cleaning bath	Cu,In,Se present (non-uniform)
5	70nm of Moly on soda lime glass	$2.5x10^{-2}$M $CuCl_2$ $6.25x10^{-2}$M $InCl_3$ 0.165M dimethylselenide	300-350°C	10psi	60psi	High	20 min	High spray rate Used a 4 step cleaning bath	Some traces of copper and selenium, no indium
6	cadmium sulfide on soda lime glass	$5x10^{-2}$M $CuCl_2$ $12.5x10^{-2}$M $InCl_3$ 0.330M dimethylselenide	350-400°C	5psi	59psi	constant	35 min	Doubled concentration and cadmium sulfide substrate Used a 4 step cleaning bath	Se, Cd and S present. Some traces of copper, no traces of Indium
7	85nm of Moly on soda lime glass + a top layer of cadmium sulfide	$5x10^{-2}$M $CuCl_2$ $12.5x10^{-2}$M $InCl_3$ 0.330M dimethylselenide	300-400°C	5 psi	59psi	constant	45 min	85 nm of Molybdenum and doubled concentration Used a 4 step cleaning bath	Layer came off because of molybdenum some traces of selenium, cadmium and sulfur
8	150nm of Moly on soda lime glass	$12.5x10^{-2}$M $CuCl_2$ $6.25x10^{-2}$M $InCl_3$ $6.25x10^{-2}$M $GaCl_3$ 0.330M dimethylselenide	350-400°C	5psi	59psi	constant	1 hour	Added gallium chloride to make it a $CuInGaSe_2$ cell Used a 4 step cleaning bath	Uniform layer of Cu,In,Ga,Se

Table 1: Spray pyrolysis growth conditions for $CuInSe_2$ and $CuInGaSe_2$.

Zn Diffusion for High Sensitivity InGaAsN Photodetectors

Jasmine Banks

Electrical Engineering, Virginia Commonwealth University

NNIN REU Site: Lurie Nanofabrication Facility, University of Michigan, Ann Arbor, MI

NNIN REU Principal Investigator(s): Rachel S. Goldman, Materials Science and Engineering, University of Michigan

NNIN REU Mentor(s): Yu Jin, Physics, Materials Science and Engineering, University of Michigan

Contact: banksjl@vcu.edu, rsgold@umich.edu, jinyu@umich.edu

Abstract:

The sensitivity of solid-state photodetectors is often limited by surface leakage current along the etched/cleaved side wall under reverse bias voltage, as shown in Figure 1 (a). A significant reduction in leakage current was recently reported for indium gallium arsenide nitride (InGaAsN), using epitaxial growth of an n-i-n structure, followed by spatially selective surface dopant type conversion during metal-organic chemical vapor deposition re-growth using dimethylzinc and diethylzinc [1-3]. The etched/cleaved surface is thus surrounded by the n-type layer and no longer under bias, as shown in Figure 1 (b). In this summer project, we proposed a novel *ex situ* zinc (Zn) diffusion approach to surface dopant type conversion of n-i-n diodes, using a commercially-available Zn-containing spin-on-glass (SOG). We investigated the influence of annealing time on the diffusion of Zn into gallium arsenide (GaAs). Specifically, we used Hall measurements to investigate the active Zn concentration profiles as a function of annealing time and etch depth. This Zn-SOG surface dopant type conversion approach will be used for the fabrication of low leakage InGaAsN based photodetectors, intended for operation in the 1.3 μm to 1.55 μm wavelength range [4,5].

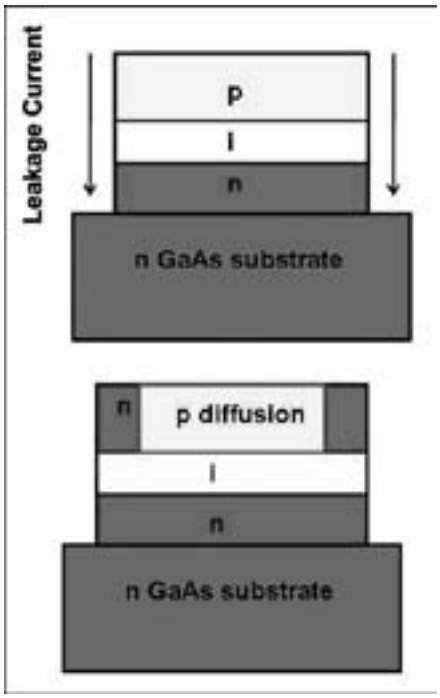

Figure 1: (a) p-i-n photodetector with sidewall leakage current, (b) selectively diffused n-i-n photodetector.

Procedure:

For GaAs:Zn-SOG diffusion studies, the GaAs wafer surface was first conditioned by heating at 350°C to 400°C for a few minutes in air. Zincsilicafilm 306 was then coated on the wafer surface by spin coating at 3000 rpm for 1 minute. After spinning, the wafer was cured by heating in air for 10-15 minutes at 100°C to 120°C [6]. Annealing was then carried out in a quartz furnace with N_2 overflow, with a GaAs proximity cap to prevent As out-diffusion. Following annealing, the Zincsilicafilm was removed by etching in 10% HF, and the surface was examined in an optical microscope. To identify the optimal annealing conditions for photodetector fabrication, the GaAs:Zn-SOG samples were annealed at 850°C for various durations: 15, 20, 23, 30, and 40 minutes.

To characterize the active Zn concentration depth profile, each ~ 1 × 1 cm^2 GaAs:Zn-SOG sample was cleaved into fourths, and one corner of each piece was then coated with photoresist as an etch stop. Following baking for 10 minutes at 130°C, wet etching in H_3PO_4:H_2O_2:H_2O (1:1:25) was carried out for 0, 38, 75, 113 s, resulting in depths of 0, 135 ± 1, 182 ±14, 325 ± 18 nm, as determined by Dektak profilometry. The etched pieces were then cut into ~ 4 × 4 mm^2 pieces, and Hall and resistivity measurements were carried out at room temperature.

Results and Analysis:

We assume that the active Zn concentration profile follows the so-called "finite source" Gaussian diffusion profile, as shown in Figure 2 (a), where x is the depth from the unetched surface, p_0 is the carrier concentration at the unetched

(a)
$$p(x) = p_0 \exp(-\frac{x^2}{2\sigma^2})$$

(b)
$$p_s(x_s) = \int_{x_s}^{\infty} p_0 \exp(-\frac{x'^2}{2\sigma^2})dx' = p_0\sqrt{\frac{\pi}{2}}\sigma(1 - erf(\frac{x_s}{\sqrt{2}\sigma}))$$

Figure 2: (a) "finite source" Gaussian profile assumed for Zn diffusion, (b) integration of the profile in (a) to fit the measured residual sheet carrier density as a function of etch depth.

Annealing Time (min)	Carrier Concentration at unetched surface p_0 (10^{20}cm^{-3})	Characteristic Diffusion Length σ (nm)
15	1.30	250
20	1.20	290
23	1.17	320
30	1.09	370
40	1.00	450

Figure 3: Summarizing Carrier concentrations at the unetched surface, p_0, and characteristic diffusion lengths, σ, for samples with various annealing times.

surface, *p(x)* is the carrier concentration at depth *x*, and σ is the characteristic diffusion length. The experimentally obtained data cannot be directly fit to the Gaussian profile since the measured sheet carrier density is the total residual carrier density in the film. Therefore, the Gaussian profile was integrated to fit the measured residual sheet carrier density, $p_s(x_s)$, as a function of etch depth, x_s, as shown in Figure 2 (b). For each annealing time, p_0 and σ were then obtained by fitting the measured data to the integrated Gaussian expression, as summarized in Figure 3. As shown in this table, annealing at 850°C for 15 min yields *p* (200 nm) ~ 9×10^{19} cm^{-3}, which is more than double the n-type dopant concentration in the top of the GaAs photodetector structure (5×10^{18} cm^{-3}), and therefore is sufficient to convert the top layer to p+. Figure 4 shows the best fit Gaussian curve for all of the annealing times, which indicates that as the annealing duration is increased, σ increases and p_0 decreases.

Since a localized active Zn profile is needed to limit the thickness of the i-layer which is converted to p-type, 850°C for 15 min is identified as the optimal annealing condition for the purpose of photodetector fabrication via surface dopant type conversion of n-i-n diodes.

Conclusions:

We proposed a novel *ex situ* Zn diffusion approach to surface dopant type conversion of n-i-n diodes, using a commercially available Zn-SOG. We characterized the Zn diffusion profile for GaAs:Zn-SOG samples and concluded that the 15 minute annealing time produces the optimum profile of electrically active Zn. In the future, this approach will be used to reduce leakage currents in InGaAsN-based photodetectors.

Acknowledgements:

I would to thank God, my family, and friends, Dr. Rachel Goldman, my principal investigator, Yu Jin, my mentor, the Goldman group, the National Nanotechnology Infrastructure Network Research Experience for Undergraduates (NNIN REU) Program, the National Science Foundation, Melanie-Claire Mallison, Trasa Burkhardt, Sandrine Martin, Brandon Lucas, and the LNF staff for all of their help.

References:

[1] Vanhollebeke K; "MOVPE based Zn diffusion into InP and InAsP/InP heterostructures"; Journal of Crystal Growth, 233, 132-140(2001).

[2] Otsuka N., Kito M., Ishino M., Matsui Y., Toujou F.; "Control of double diffusion front unintentionally penetrated from a Zn doped InP layer during metalorganic vapor phase epitaxy"; Journal of Applied Physics, 84, 4239-4247(1998).

[3] Hampel C., Blaauw C., Calder I.D., Glew R., Macquistan D., Bryskiewicz T., Guillon S.; "Metalorganic vapor phase diffusion using dimethylzinc. Part 1 : Analysis of the reproducibility of the resulting diffusion profile as measured by secondary ion mass spectrometry"; Journal of vacuum science and technology, 22, 912-915(2004).

[4] Touam, T., Wu, C., Gigase, Y., Belanger, M., Currie, J. F., Najafi, S. I..; "Fabrication, characterization, and analysis of zinc-diffused GaAs waveguides"; IEEE Journal of Quantum Electronics, 25, 850-853(1989).

[5] Rai S.; "Zinc Diffusion in GaAsSb from spin-on glass dopant sources"; Thesis (M.S.), University of Notre Dame (2004).

[6] http://www.emulsitone.com/znsif_306.html; "Zincsilicafilm 306" 11:06 am (September 30, 2009).

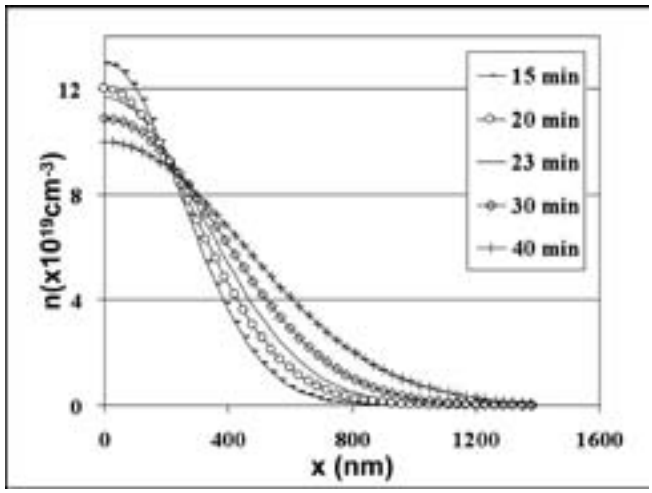

Figure 4: Carrier concentration, n vs. etch depth, x.

Graphene Synthesis by CVD on Copper Substrates

Mark Borysiak

Chemical Engineering, Ohio State

NNIN REU Site: Microelectronics Research Center, University of Texas, Austin, TX

NNIN REU Principal Investigator(s): Professor Rodney S. Ruoff, Department of Mechanical Engineering and the Texas Materials Institute, University of Texas at Austin

NNIN REU Mentor(s): Dr. Xuesong Li, Department of Mechanical Engineering and the Texas Materials Institute, University of Texas at Austin

Contact: Borysiak.1@osu.edu, r.ruoff@mail.utexas.edu, Xuesongli@mail.utexas.edu

Abstract and Introduction:

Graphene is an extremely interesting and potentially important material with unique and desirable physical characteristics. A few of the practical applications envisioned for graphene include semi-conductor applications, optoelectronics (solar cells, touch screens, liquid crystal displays), graphene based batteries/super-capacitors, and thermal management. To achieve some of these goals though, large, high-quality graphene is needed [1]. Our research focused on synthesis of monolayer graphene on 25 μm thick copper (Cu) substrates, which allowed for lateral growth on the scale of many centimeters; various measurements showed predominantly uniform, monolayer graphene. The graphene was grown using chemical vapor deposition (CVD) with methane and hydrogen gas in a tube furnace vacuum system. The as-grown graphene was characterized using a scanning electron microscope (SEM) to understand growth at different conditions and to find desired growth parameters. The graphene films were then transferred to SiO_2/Si wafers for further characterization by optical microscopy and micro Raman spectroscopy. To date, we have seen that higher temperature growth results in a faster growth rate with generally higher quality graphene coverage and that the growth mechanism is based on surface adsorption.

Experimental Procedure:

Graphene samples were grown on 25 μm thick copper foil in a quartz tube furnace system using a CVD method involving methane and hydrogen gases [2]. Under vacuum conditions of 10 mtorr, the furnace would be heated with a 2 sccm flow of H_2 present. Temperatures that were tested ranged from 800°C to 1050°C. After 40 minutes of heating to allow the copper foil to anneal, a flow of 35 sccm of methane would be introduced for a growth time ranging from 30 seconds to 15 minutes. A quick cooling method was used (~300°C/min) after growth, and the methane and hydrogen gas flows were continued throughout the cooling process. The graphene films on copper were then characterized using SEM images. After transferring the films to Si/SiO_2 wafers through polymethyl methacrylate (PMMA) coating and iron (III) nitrate etching [2,3], the films would be further analyzed by optical microscopy and Raman

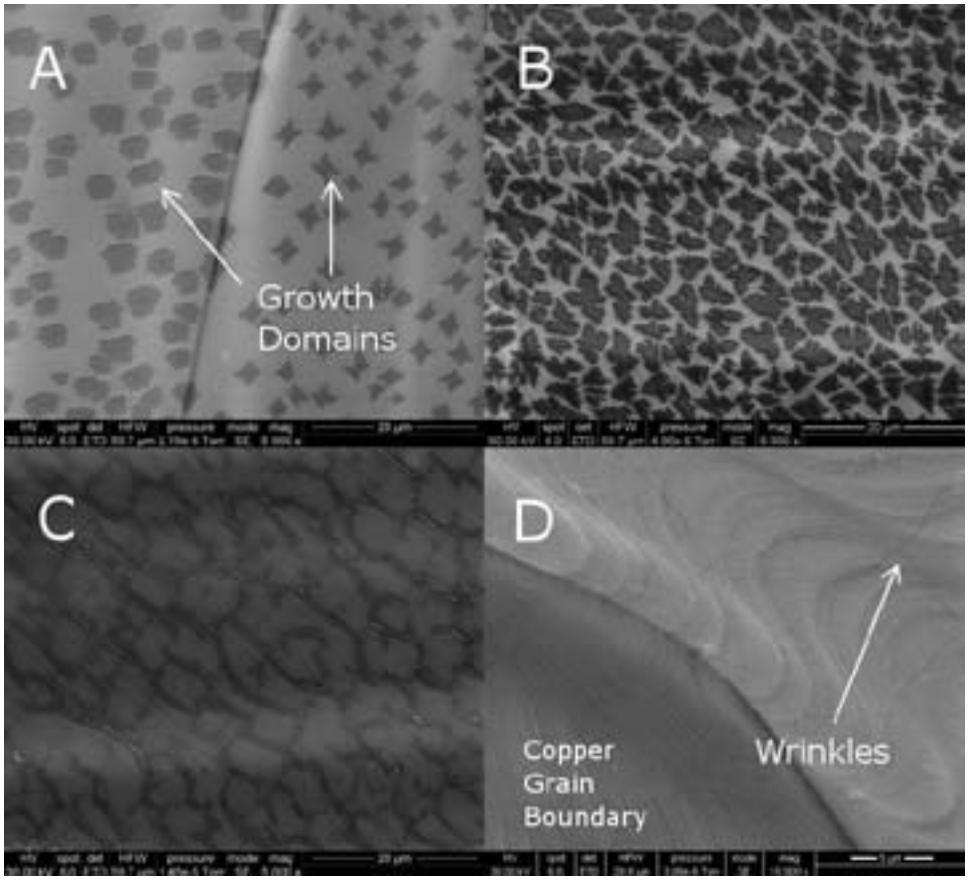

Figure 1: Growth for 10 minutes - clockwise starting with A, growth temperatures of 900, 950, 1000, and 1050°C, respectively.

spectroscopy.

Results and Discussion:

The graphene films that were grown on the copper substrates were predominantly uniform monolayer graphene; on the scale of many centimeters, with minimal defects/multilayer flakes. The uniform monolayer growth can be attributed to a surface adsorption growth mechanism due to carbon's low solubility in copper [4].

The growth mechanism consists of carbon nucleation sites adsorbing to the copper surface and then growing with addition of carbon to the edges of these growth domains. This growth mechanism, as opposed to a precipitation-based mechanism, allows for the monolayer growth, with very little of the multilayer growth that is seen for precipitation-based growth [4]. The growth domains can be seen in Figure 1, with the domains increasing in size from additional carbon atoms being adsorbed to the edges of the nucleation sites until the domains join, forming graphene (Figure 1d). These figures also display the temperature effect on the growth of the graphene sheets. The images show that increasing temperature (in the range we studied) while holding growth time constant results in significantly faster growth at the higher temperatures, with generally larger domains. This shows that the growth rate of the graphene is highly dependent on the temperature of growth and that full high-quality coverage is apparently more easily achieved at these higher temperatures.

Figure 2 shows Raman spectroscopy results obtained on a transferred graphene film. The spectrum has large, symmetrical G and 2D peaks indicating the presence of monolayer graphene [5]; additionally, the absence of the D peak suggests that defects are minimal [5]. The main defects found while characterizing the sheets were wrinkles (Figure 1d, which are due to the difference in the coefficients of thermal expansion between the graphene and copper [4]) but the full coverage and lack of multilayer flakes shows progress in the growth of high quality and monolayer growth.

Conclusion and Future Work:

Large, uniform monolayer graphene sheets can be grown on copper substrates by the thermal CVD method used, and these sheets are able to be transferred to other substrates. We also determined that higher temperatures allow for faster growth and large growth domains from observing samples with sub-full layer coverage; the data support growth by surface nucleation and surface adsorption at the edges of growing domains. At longer growth times, the monolayer graphene does not add layers to form multi-layer graphene sheets strongly arguing against precipitation-based growth.

Future research on CVD growth of graphene on metals such as Cu can hopefully lead to larger growth domains and improved physical characteristics. Improved electrical properties may also be able to be achieved through some form of doping to create n or p type films. Finally, achieving uniform bi-layer or other n-layer graphene with control of n, vs. only monolayer graphene, is an exciting challenge.

Acknowledgements:

I would like to thank Professor Rod Ruoff for the opportunity to participate in this program and allowing me to work on this project with his team members. I would also like to thank Dr. Xuesong Li, a postdoctoral fellow in the Ruoff group, for teaching and helping me immensely throughout the research. Additionally, I would like that thank the National Nanotechnology Infrastructure Network Research Experience for Undergraduates (NNIN REU) Program for organizing this program and the National Science Foundation for their contributions to the program and furthering my education.

References:

[1] A. K. Geim., Graphene: Status & Prospects. Sci.324: 1530-34 (2009).

[2] Li, X.S. et al., "Large-area synthesis of high-quality and uniform graphene films on copper foils." Science 324, 1312 (2009).

[3] Reina, A. et al., "Transferring and Identification of Single- and Few-layer Graphene on Arbitrary Substrates." J. Phys. Chem. C 112, 17741-17744 (2008).

[4] Li, X.S. et al., "Evolution of graphene growth on Cu and Ni studied by carbon isotope labeling." Mat.Science, arXiv:0907.1859v1 (2009).

[5] L.M. Malard, et al., Raman Spectroscopy in graphene. Physics Reports (2009).

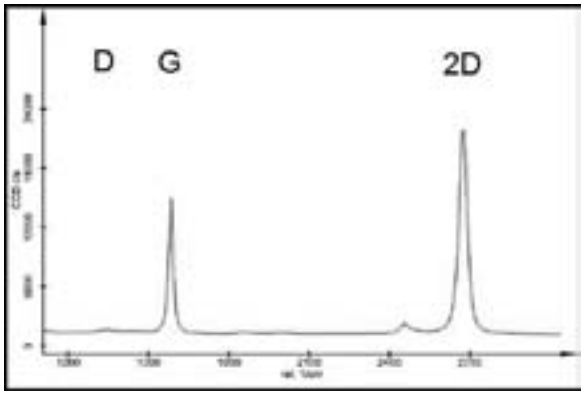

Figure 2: Raman spectrum of a graphene sample.

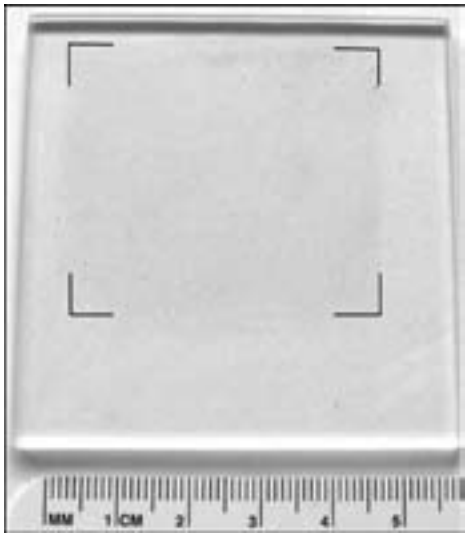

Figure 3: Transferred graphene, 4.5 × 4.5 cm^2.

Mechanical Properties of Atomic Layer Deposited Tungsten

Steven Brown

Physics and Mathematics, University of Minnesota

NNIN REU Site: Colorado Nanofabrication Laboratory, University of Colorado, Boulder, CO
NNIN REU Principal Investigator(s): Prof. Victor Bright, Mechanical Engineering, University of Colorado at Boulder
NNIN REU Mentor(s): Bradley Davidson, Mechanical Engineering, University of Colorado at Boulder
Contact: brow2178@umn.edu, victor.bright@colorado.edu, davidsob@gmail.com

Abstract:

Using passive test structures, the residual stress and through-thickness stress gradients for atomic layer deposition (ALD) tungsten on nickel were found to have a mean of 1555 pascals (Pa) and a standard deviation of 144 Pa and a mean of -77 Pa and a standard deviation of 572 Pa, respectively.

Introduction:

Because tungsten is a refractory metal, its use as a structural material in micro or nano-electromechanical devices allows the devices to operate at high temperatures. Atomic layer deposition tungsten (WALD) has the additional advantage of low deposition temperatures (120°C) in addition to the perfectly conformal coating of all surfaces—even those that have been undercut. In designing WALD devices, it is important to know the residual stress, which results from the mismatch between the thermal expansion coefficients of the deposited tungsten and the underlying material. Residual stress can cause cantilever structures to curl toward or away from the substrate, changing working distance and function of a device. In addition, residual stress can affect the resonant frequency, which is critical for sensor applications. Characterization of the residual stress should lead to better models and simulations of devices, allowing for the proper design of a functioning WALD device. Using passive test structures, the residual stress and through thickness stress of WALD deposited on nickel was measured.

Procedure:

First, a 10 nm thick layer of chromium, followed by 300 nm of nickel were deposited on a silicon substrate via thermal evaporation. Next, 32 nm of WALD was grown on the substrate at 120°C. Bridges and cantilevers were then patterned by optical lithography using spin-coated NR-9 negative resist. A hard-mask was developed by evaporation of a 35 nm thick layer of Ni followed by lift-off. The WALD structures were completed after reactive ion etching (RIE) for 45 seconds. The hard-mask and sacrificial layer were then removed via wet etching, releasing the WALD structures, and a critical point dryer used to avoid stiction caused by surface tension. Finally, a topographical map of the structures was obtained using a light interferometer, which could then be analyzed to find the displacements of the bridges and cantilevers.

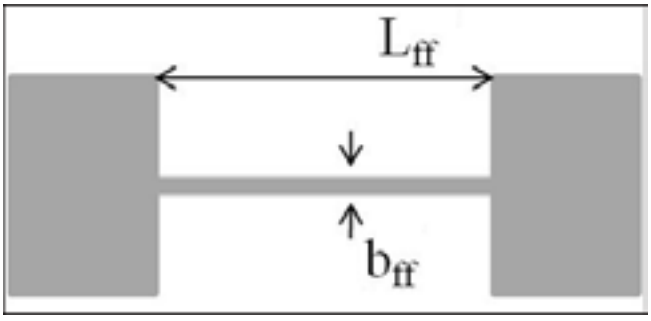

Figure 1: Schematic of bridge structure.

Results and Analysis:

The bridge structures allowed the compressive residual stress to be extracted, whereas the cantilevers allowed the through thickness stress to be measured. Residual stress can be calculated using Equation 1, where σ is the stress, L_{ff} is a geometrical constant from Figure 1, E is Young's modulus, v is Poisson's ratio, H is the maximum displacement of the beam, and h is the thickness [1].

$$\sigma = \frac{E\pi^2}{12(1-v)L_{ff}^2}(3H^2 + 4h^2)$$

Equation 1

The through thickness stress gradient is found using Equation 2, where Δσ is the through thickness stress gradient, E is Young's modulus, L_{cb} and h are geometrical constants from Figure 2, z is the deflection at the tip, K_0 is a constant in v and h, σ is the stress from Eq. 1, and K_1 is a constant in h [1].

$$\Delta\sigma = \frac{Ehz - K_0\sigma L_{cb}h}{K_1 L_{cb}h + L_{cb}^2}$$

Equation 2

$$K_0 = (1.33 + 0.45v)(1.022 - 0.014h)$$

Equation 3

$$K_1 = 0.0086h^2 - 0.047h + 0.81$$

Equation 4

Young's modulus was taken to be the same as for bulk tungsten. The mean and standard deviation of the residual stress and stress gradient was found since the unevenness due to the growth process (mainly from the evaporation of nickel) far outweighed the uncertainty in measurement from the light interferometer.

Conclusion:

The residual stress of atomic layer deposition tungsten on nickel was found have a mean of 1555 Pa and a standard deviation of 144 Pa. The through thickness stress gradient was found to have a mean of -77 Pa and a standard deviation of 572 Pa. The residual stress is quite small especially when compared to the expected thermal stress for the same thickness of bulk tungsten on nickel, which should be about 331 MPA. The majority of the stress is believed to be thermal stress, but it would seem that the thermal expansion coefficient of WALD is much higher than bulk tungsten. This would not be that surprising as WALD is thought to be a nano-crystalline in structure. It is important to find the thermal expansion of WALD on nickel as the devices utilizing WALD will be operated at high temperatures and therefore could only be properly modeled by taking into account thermal expansion. Since the structure of WALD is different than bulk tungsten, it would be expected to have a different Poisson ratio and Young's modulus as well.

Future Work:

There is much more work to be done to truly understand WALD. Some of these include: finding Young's modulus, finding the thermal expansion coefficient (that way the stress due to thermal mismatch can be calculated), finding Poisson's ratio, and seeing how the growth parameters (temperature and time) of WALD affect its properties.

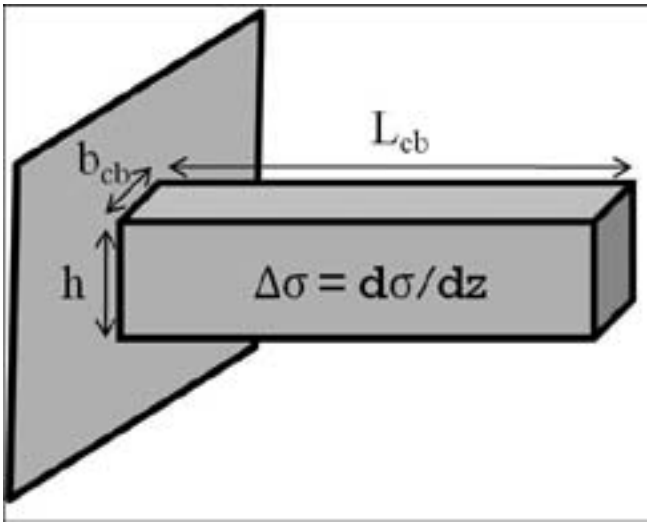

Figure 2: Schematic of cantilever structure.

Acknowledgements:

I would like to thank Dragos Seghete and Bradley Davidson. I would also like to thank the National Nanotechnology Infrastructure Network Research Experience for Undergraduates Program and National Science Foundation for the opportunity to carry out this research.

References:

[1] Marie Tripp, "Atomic layer deposited thin films for micro- and nano electromechanical systems with applications in short-wavelength adaptive optics," 2005.

[2] Peroulis, D.; Pacheco, S. P.; Sarabandi, K.; Katehi, L. P. B.; "Electromechanical Considerations in Developing Low-Voltage RF MEMS Switches," IEEE Transactions on Microwave Theory and Techniques, vol. 51, no. 1, pp. 259-270 (2003).

Photon-Enhanced Crystallization Kinetics and In Situ High Temperature Conductivity Studies in Ultra-Thin $La_{0.6}Sr_{0.4}Co_{0.8}Fe_{0.2}O_{3-\delta}$ Films

Tyler Cain

Materials Science and Engineering, University of Illinois at Urbana-Champaign

NNIN REU Site: Center for Nanoscale Systems, Harvard University, Cambridge, MA

NNIN REU Principal Investigator(s): Professor Shriram Ramanathan, School of Engineering and Applied Sciences, Harvard University

NNIN REU Mentor(s): Dr. Bo-Kuai Lai, School of Engineering and Applied Sciences, Harvard University

Contact: tcain2@illinois.edu, shriram@seas.harvard.edu, blai@seas.harvard.edu

Abstract and Introduction:

Solid oxide fuel cells (SOFCs) have drawn attention for electrical power generation because of their low emissions, high efficiency, and flexibility in fuel sources [1]. SOFCs typically operate at temperatures at or above 700°C, creating issues with thermal stress, material selection, and device packaging [2,3]. Efforts are being made to reduce SOFC operating temperatures to between 200°C and 600°C utilizing thin film device structures, reducing many of the impacts of the aforementioned factors [4]. However, reduced operating temperature may also decrease the ionic/electronic conductivity and decrease oxygen reduction reaction rate at the cathodes [5]. Thus, it is critical to advance synthesis routes for high performance cathodes with superior electrical conductivity [6,7].

$La_{1-x}Sr_xCo_yFe_yO_{3-\delta}$ has been explored as a possible cathode material for use in SOFCs [8]. LSCF exhibits mixed ionic and electronic conductivity and high electrocatalytic activity [9]. Synthesis of $La_{0.6}Sr_{0.4}Co_{0.8}Fe_{0.2}O_{3-\delta}$ by RF-sputtering has been shown to produce functional films with crystallization temperatures in the vicinity of 450°C without producing interfacial reaction products with yttria-stabilized zirconia (YSZ) [9,10].

La = Lanthanum
Sr = Strontium
Co = Cobalt
Fe = Iron
O = Oxygen

The interaction of energetic UV photons with oxygen can produce oxygen radicals or ozone, dramatically increasing oxygen reactivity on surfaces and enhancing oxygen incorporation into thin films [11]. In this paper, we demonstrate that photo-excitation during crystallization leads to enhanced oxygen incorporation into a prototypical perovksite oxide that in turn results in a significant improvement in the high temperature conductivity. Further, utilizing *in situ* conductivity measurements, we show an enhancement in crystallization kinetics arising from photo-excitation.

Experimental Procedure:

$La_{0.6}Sr_{0.4}Co_{0.8}Fe_{0.2}O_{3-\delta}$ thin films were RF-sputtered from a stoichiometric target (AJA International) onto single crystalline YSZ substrates. Sputtering was carried out in 5×10^{-3} Torr of argon plasma starting from a base pressure of 3 × 10-8 Torr with a gun power of 60 W. *In situ* high temperature conductivity studies were also performed on 60 nm thin LSCF films on similar substrates with platinum electrodes in air. Photon sources in-built into the probe station enable *in situ* exposure while heating experiments as well as electrical conductivity. The temperature was continuously monitored using thermocouples. LSCF films were characterized by x-ray diffraction (XRD).

Results and Discussion:

In order to examine the crystallinity of LSCF films annealed at 450°C, low angle XRD was performed at an incident angle of 1°. The results of the scans, seen in Figure 1, indicate that both the films annealed with and without UV are crystalline after annealing to 450°C. XRD peaks appear around two-theta 33°, 41°, and 47°, corresponding to the LSCF peaks (110) (104), (202), and (024) respectively [12]. No additional peaks are observed for the films annealed under UV irradiation, indicating that no un-desirable reactions between the LSCF and the YSZ substrate have occurred. The location of the 33°

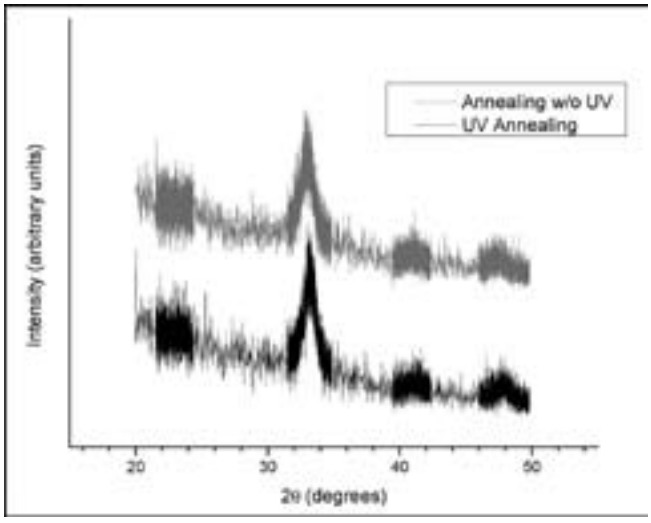

Figure 1: XRD profile of LSCF films annealed at 450°C.

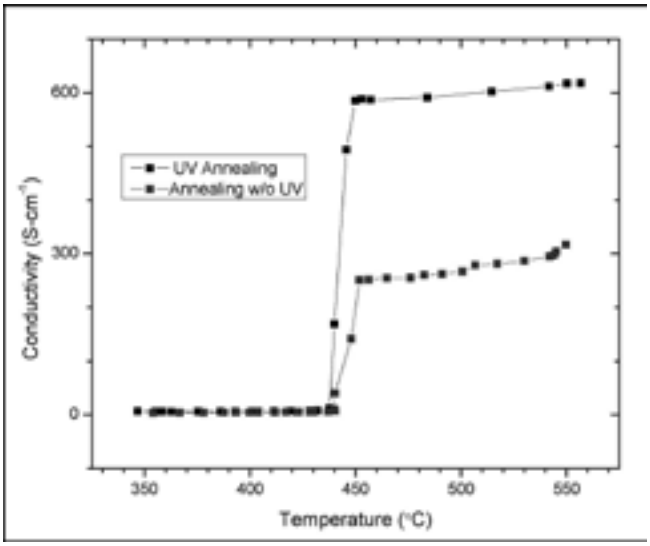

Figure 2: LSCF in-plane electrical conductivity vs. temperature.

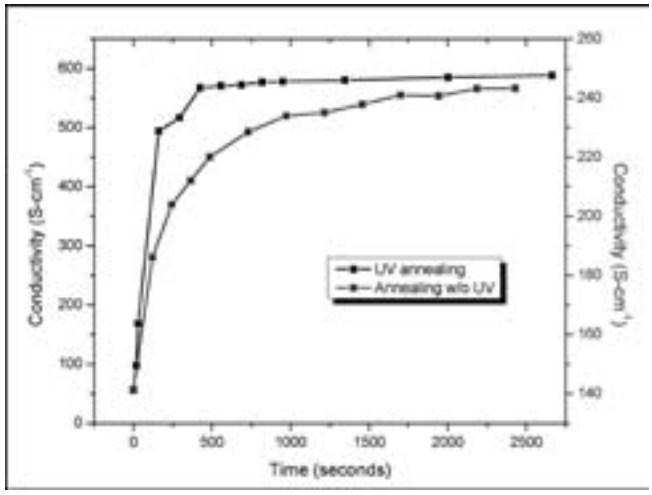

Figure 3: Conductivity vs. time during crystallization of LSCF films at T ~ 450°C.

two-theta peak is 0.1° higher for the film crystallized under UV irradiation compared to the film annealed without UV, indicating a slight decrease in the average lattice parameter of the LSCF thin film. Enhanced oxygen incorporation during annealing could possibly decrease the overall oxygen deficiency in the film, reducing the number of oxygen vacancies [11].

In situ conductivity studies were performed on LSCF thin films during and prior to the onset of crystallization. Sample temperature was held at 450°C for 40 minutes to observe LSCF conductivity changes with time. Film resistance was calculated via linear regression to tabulate in-plane LSCF conductivity. Upon crystallization, a conductivity increase of approximately 100x can be observed, serving as a suitable *in situ* probe of the structural evolution. The onset temperature for this change in conductivity is ~ 440°C in films crystallized both with and without UV assist as observed in Figure 2. The conductivity of the LSCF films measured 248 S-cm^{-1} and 588 S-cm^{-1} at 450°C after 50 minutes for samples annealed with and without UV irradiation respectively. Upon increasing temperature to 557°C, conductivities measured 320 S-cm^{-1} and 618 S-cm^{-1} in films annealed without UV irradiation and with UV irradiation respectively.

Figure 3 shows the evolution of in-plane conductivities for LSCF films annealed both with and without UV at 450°C. With time, the film conductivities annealed with and without UV approach a maximum asymptotically. The rate at which the films approach their maximum conductivity is differs. The LSCF film crystallized under UV approaches its maximum conductivity at 450°C faster than the film crystallized without. This suggests that the crystallization rate of LSCF thin films is influenced by oxygen incorporation.

Conclusion:

We have demonstrated that UV assisted crystallization of RF-sputtered $La_{0.6}Sr_{0.4}Co_{0.8}Fe_{0.2}O_{3-\delta}$ thin films leads to higher in-plane electronic conductivity and more rapid crystallization. A decrease in lattice parameter was observed in films annealed under UV irradiation, indicating increased oxygen concentration or decreased in oxygen vacancy concentration in the LSCF film due to the greater presence of oxygen radicals and ozone during crystallization. More rapid crystallization was also observed in films annealed under UV irradiation. The results indicate that UV enhanced crystallization of LSCF ultra-thin films could provide an increase in cathode performance.

Acknowledgements:

I would like to thank everyone that helped me during the 2009 NNIN REU, most notably my PI, Professor Shriram Ramanathan, my mentor, Dr. Bo-Kuai Lai, and our site coordinator Dr. Kathryn Hollar. This work was performed with the support of the Rowland Institute at Harvard. A special thanks to the Harvard Center for Nanoscale Systems staff. Finally, I would like to thank the National Nanotechnology Infrastructure Network Research Experience for Undergraduates Program and National Science Foundation for funding.

References:

[1] B.C.H. Steele, A. Heinzel, Nature 414 (2001) 345.
[2] J.W. Fergus, JOM December 59 (2007) 56-62.
[3] N.Q. Minh, Solid State Ionics 174 (2004) 271-277.
[4] S.M. Haile, Acta Mater. 51 (2003) 5981.
[5] S.Litzelman, J.Hertz, W.Jung, H.Tuller, Fuel Cells 5 (2008), 294-302.
[6] J. Fleig, Annu. Rev. Mater. Res. 33 (2003) 361-382.
[7] R. O'Hayre, S.W. Cha, W. Colella, F.B. Prinz, Fuel Cell Fundamentals, John Wiley & Sons, New York, USA, 2005.
[8] L.-W. Tai, M.M. Nasrallah, H.U. Anderson, D.M. Sparlin, S.R. Sehlin, Solid State Ionics 76 (1995) 259-271.
[9] B.-K. Lai, A.C. Johnson, H. Xiong, S. Ramanathan, Journal of Power Sources 186 (2009) 115-122.
[10] A.C. Johnson, B.-K. Lai, H. Xiong, S. Ramanathan, J. Power Sources 186 (2009) 252.
[11] M. Tsuchiya, S.K.R.S. Sankaranarayanan, S. Ramanathan, Progress in Materials Science 54 (2009) 981-1057.
[12] S. Wang, M. Katsuki, M. Dokiya, T. Hashimoto, Solid State Ionics 159 (2003) 71-78.

Annealing Thin-Film Block Copolymers to Achieve Ordered Morphologies

Kevin Donaher

Materials Science and Engineering, Simon's Rock College of Bard

NNIN REU Site: Penn State Nanofabrication Laboratory, Pennsylvania State University, State College, PA

NNIN REU Principal Investigator(s): Dr. Michael A. Hickner, Department of Materials Science and Engineering, The Pennsylvania State University

NNIN REU Mentor(s): Stephanie A. Petrina (2006 UCSB NNIN REU), Materials Science and Engineering, The Pennsylvania State University

Contact: kdonaher07@simons-rock.edu, hickner@matse.psu.edu, sap262@psu.edu

Abstract:

A proton exchange membrane fuel cell requires a membrane that selectively allows for the passage of protons. One way to accomplish proton conductivity is to use sulfonated self-assembling block copolymers. The negative charge of the sulfonic acid groups in one of the block copolymer phases imparts the desired cation or proton conductivity. It is likely that the morphology of the film affects the conductivity; however, before the conductivity-morphology connection can be quantified, there must first be an understanding of the morphologies of sulfonated films as well as a reliable way of inducing them. To accomplish morphological control of sulfonated block copolymers, annealing was conducted on unsulfonated and sulfonated systems. The process of annealing uses solvents or heat to allow the polymer to become mobile and the phases to separate and align in reference to each other. This work tests annealing on unsulfonated copolymers, as well as whether sulfonated copolymers can be successfully annealed, and what phases result.

Introduction:

Block copolymers form morphologies with domains on the order of 10-100 nm due to separation of the different chemical phases of the polymer chain. When the polymers are allowed to move, the different blocks will naturally self-assemble into distinct phases based on the composition and volume fractions of the polymer constituents. By heating a polymer past its glass transition temperature (T_g) or using solvent to depress the T_g, the polymer chains become mobile and rearrange towards an equilibrium structure.

This work is directed at testing various ways of arranging an unsulfonated block copolymer, and to determine if the behavior of sulfonated copolymer analog is at all similar. Experiments were conducted on poly(hexyl methacrylate)-*b*-polystyrene-*b*-poly(hexyl methacrylate) (PHMA-*b*-PS-*b*-PHMA). This triblock copolymer was chosen due to the low glass transition temperature of poly(hexyl methacrylate). The low T_g allows annealing to be conducted at lower temperatures, decreasing the chances of the copolymer decomposing.

Methods:

Unsulfonated PHMA-*b*-PS-*b*-PHMA in dioxane and 100% sulfonated PHMA-*b*-PS-*b*-PHMA in dimethylformamide were used. The films were spun cast onto silicon wafers coated with a poly(styrene) brush. After the wafers were rinsed with ethyl alcohol, the brush was made by casting 1% w/v polystyrene in THF, baking under vacuum at 195°C for 2.5 h, and then rinsing away the excess poly(styrene) with toluene. 15 μL of 0.1 wt % polymer solution were spin cast at 1000, 2000, and 3000 rpm to achieve varying film thicknesses on the order of 100 to 200 nm. The thickness of the spun cast films was measured using profilometry. Samples were subjected to thermal annealing or vapor annealing. Thermal annealing was conducted under vacuum at 180°C for 8 hours with cooling to room temperature under vacuum. Non-selective solvent vapor annealing was conducted under a saturated dioxane atmosphere for the unsulfonated samples and dimethylformamide for the sulfonated samples at 24°C for 24 hours. The samples were examined using atomic force microscopy and field emission scanning electron microscopy.

Results:

Figure 1 displays the disorganized mixed lamellar and cylindrical morphologies of unsulfonated PHMA-*b*-PS-*b*-PHMA. The morphological domains are 30 to 70 nm in width. Both thermal and vapor annealing increased the order of the unsulfonated PHMA-*b*-PS-*b*-PHMA domains. After annealing, the lamellar structures were aligned parallel to one another with less cylindrical domains.

While the morphologies of Figure 1 are disorganized, Figure 2, a 3000 rpm spin cast sample after vapor annealing, shows aligned morphologies.

Figure 3 shows an unannealed sulfonated PHMA-*b*-PS-*b*-PHMA spun cast at 1000 rpm. The sulfonated poly(styrene) midblock has aggregated, causing the film to be different than the unsulfonated sample. This morphology does not change with thermal or vapor annealing, which is displayed by Figure 4, a vapor annealed sulfonated PHMA-*b*-PS-*b*-PHMA.

Conclusions:

The unsulfonated PHMA-*b*-PS-*b*-PHMA triblock copolymer showed disordered morphologies in the as-cast state, but upon either thermal or vapor annealing showed a mixture of aligned lamellar and cylindrical morphology. These results indicate that temperatures of 180°C or the use of a non-selective solvent were sufficient to allow re-arrangement of the phases. Sulfonated PHMA-*b*-PS-*b*-PHMA did not show domain arrangement in the as-cast state and instead showed an aggregated structure that may be a result of the sulfonated polymer's solution behavior. The sulfonated copolymer does not seem to form the same morphologies as the unsulfonated copolymer. Neither thermal nor vapor annealing caused a significant difference in the phase behavior of the sulfonated PHMA-*b*-PS-*b*-PHMA. The aggregated sulfonated PS domains prevented annealing.

Future Work:

One reason that annealing could not be achieved in the sulfonated sample is that sulfonation has raised the glass transition temperature (T_g) of polystyrene such that 180°C is no longer sufficient for annealing. To test this increase in the T_g, annealing will be attempted at higher temperatures. Also, as this project only examined 0% and 100% sulfonated copolymer, research will be done on partially sulfonated copolymers to determine if their behavior is intermediate to the unsulfonated or fully sulfonated samples.

Acknowledgements:

I would like to thank Dr. Michael Hickner for his direction, Stephanie Petrina for her advice, Dr. Tomonori Saito for his skill with polymer preparation, and Dr. Jingling Yan for his assistance with drying and annealing. This work was supported by The Pennsylvania State University Materials Research Institute Nano Fabrication Network and the National Science Foundation Cooperative Agreement No. 0335765, National Nanotechnology Infrastructure Network Research Experience for Undergraduates (NNIN REU) Program, with Cornell University.

References:

[1] Bosworth, J.K., Paik, M.Y., Ruiz, R., Schwartz, E.L., Huang, J.Q., Ko, A.W., Smilgies, D.M., Black, C.T., Ober, C.K. "Control of self-assembly of lithographically patternable block copolymer films." ACS Nano 2. 7 (2008): 1396-1402.

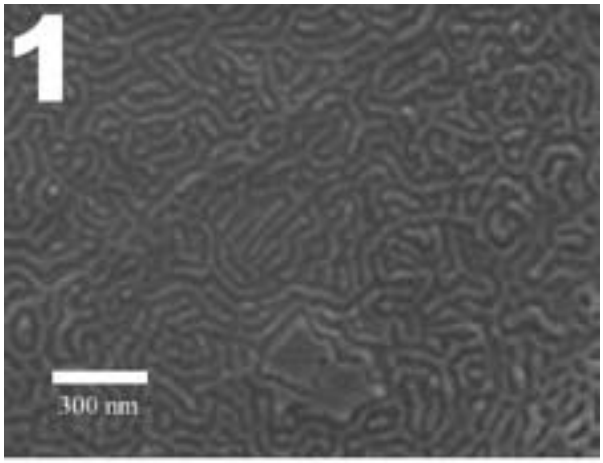

Figure 1: Unannealed unsulfonated PHMA spin cast.

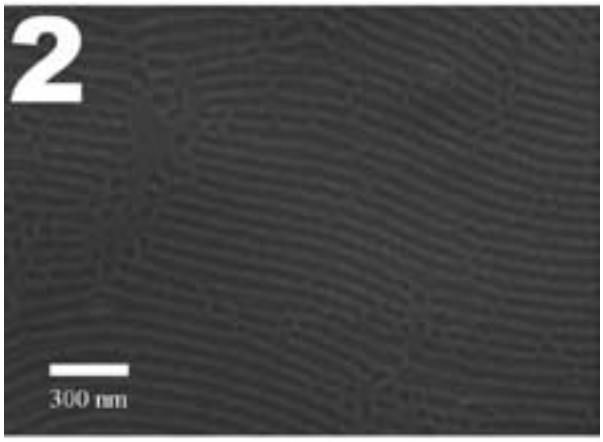

Figure 2: Vapor annealed sulfonated PHMA spin cast.

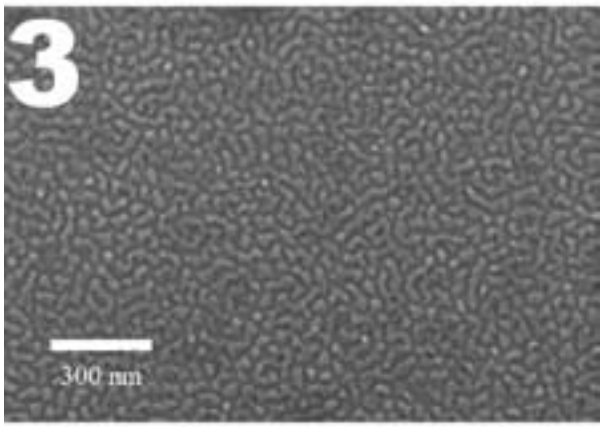

Figure 3: Unannealed sulfonated PHMA spin cast.

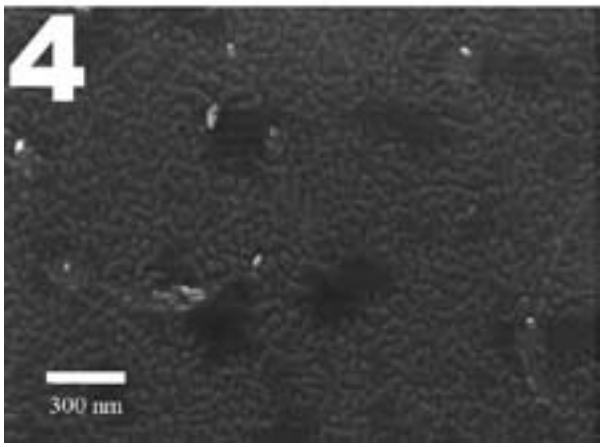

Figure 4: Vapor annealed sulfonated PHMA spin cast.

Pattern Deposition of Nanoparticles of Different Shapes by an Aerosol Route

Richard Frnka

Math, Physics and Computer Science, Eckerd College

NNIN REU Site: Nano Research Facility, Washington University in St. Louis, St. Louis, MO

NNIN REU Principal Investigator and Mentor: Dr. Da-Ren Chen, Department of Energy, Environmental, and Chemical Engineering, Washington University in St. Louis

Contact: frnkara@eckerd.edu, chen@wustl.edu

Introduction:

The electrospray system disperses highly-charged, monodisperse droplets which can be showered over a plate of large area. By varying the liquid feed flowrate and voltage of the system, nano-sized particles can be distributed over the area. Using the soft lithography technique of micro-contact molding, a certain pattern can be imprinted on a polymer coated plate. This molding reveals a silver substrate in the pattern outlined by the nonconductive polymer. The electrospray apparatus can be used to spray highly positively-charged nanoparticles that are then deposited on the surface in the respective pattern. An electric field is established between spray head and substrate, assisting the containment of the sprayed particles in the desired area. Before spraying particles the polymer-coated surface is charged by electrospraying a highly conductive solution. The gold nanoparticles used range in size from 10 to 20 nm and are generally conglomerated inside the desired pattern after spraying. Being able to control the positioning and patterning of nanoparticles by use of the electospray system will allow a much larger area to be covered in a much shorter time compared to existed deposition experiments.

There has been much research done in the field of controlling the size, shape and phases of nanoparticles, but controlling the placement of these particles has presented itself as a challenge [1]. A precise patterning of nanoparticles would be greatly beneficial in some areas of interest, and even a loose patterning of a large amount of these particles would prove to be practical in some applications.

This experiment attempted to find an efficient way to quickly and accurately deposit nanoparticles in a given pattern. An electrospray device developed in our lab was used to shower highly charged nanoparticles onto an opposite charged patterned substrate outlined with nonconductive polymer, consequently depositing them in the desired pattern.

Experimental Procedure:

An elastomer stamp was created from a master with our micron-sized pattern on it (in this case, 10 μm holes). This stamp was used for micro-contact molding to imprint the pattern on our photoresist, which was a silicon wafer coated with silver. This left a pattern on the highly conductive silver that was outlined by a nonconductive polymer (see Figure 1). This process was set up so we could mass produce our patterned plates in a quick and efficient manner. In one hour, as many as 15 plates could be patterned and ready for spraying.

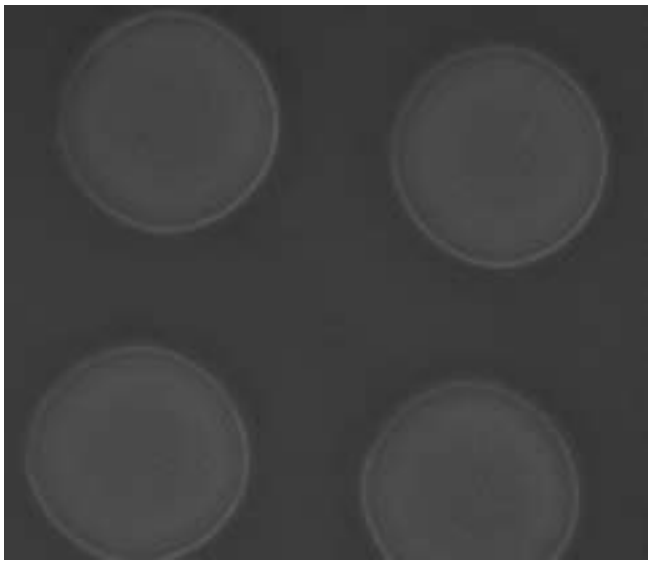

Figure 1: 10 μm hole pattern in the substrate.

After the plates had been patterned, they were ready to be sprayed by the electrospray device. This device is a particle generation/dispersion system used to shower monodisperse droplets over a large area. In this experiment, we were able to use it to shower individual nanoparticles over the prepared patterns. The particles being used were 10-20 nm gold colloid nanoparticles. The liquid in which the nanoparticles were suspended was fed into the system by a syringe pump so the flow rate could easily be controlled. As the suspension flowed through a capillary towards a very sharp tip, the particles were subjected to an divergent electrical field established by applying a high voltage between the capillary and plate. The established electric field was also used to help contain the particles and keep them focused in the desired area [2].

Before the gold particles were sprayed, we introduced a highly conductive pre-spray solution of nitric acid and ethanol to charge the surface of our plates. The plate charging helped to target the spray particles towards the highly conductive silver patterns and away from the non-conductive polymer. After 30 minutes of the pre-spray and 30 minutes of electrospray by the nanoparticles, the process was complete.

Results were then obtained by use of the scanning electron microscope (SEM) to inspect deposited particles on the plates, and to obtain data of the distribution of deposited nanoparticles.

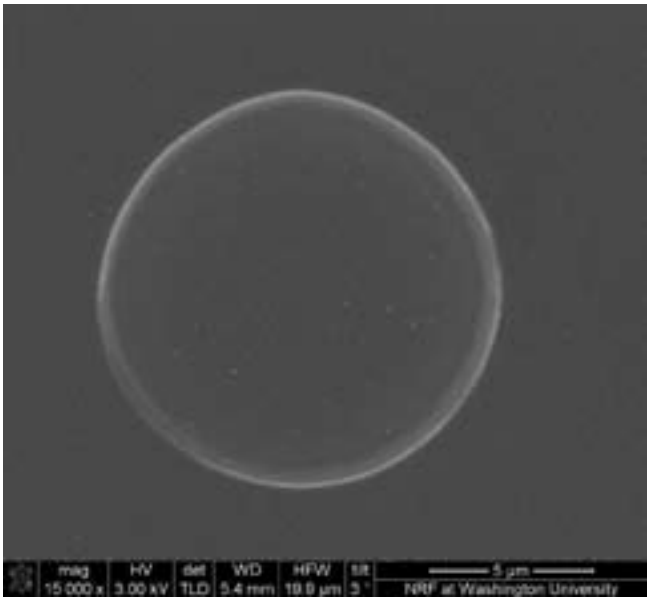

Figure 2: Nanoparticles mainly located in the holes.

Results and Discussion:

After many trials, our experiment eventually led to a 75% successful rate of nanoparticles in the holes, compared to being outside of the holes. Figure 2 shows a close up of the holes with the particles enhanced in size for better viewing. This success was mainly attributed to the correct combination of our lithography method for producing the patterns, the use of the unipolar charger, and the introduction of the pre-spray solution to help charge our surface before the shower of nanoparticles. Micro-contact molding replaced micro-contact printing which had produced silver holes with a silicon outline, which didn't work because the silicon provided a semi-conductive surface that attracted particles. The unipolar charger resulted in a successful but random distribution of particles on our molded plates, compared to using no charger and a bipolar charger, which had yielded no particles on the surface. After the success of the unipolar charger, the pre-spray solution allowed a much more accurate focusing of particles into the patterned holes. Increasing the conductivity of this solution produced even better results.

Future Work:

This experiment demonstrated that a large percentage of the particles could be conglomerated inside the target holes compared to being outside on the nonconductive surface. We weren't able to achieve full accuracy, but future experiments will be geared toward reaching that goal. Also, new patterns and different types of particles will be used to conduct the experiment.

Acknowledgements:

I'd like to thank Dr. Daren Chen and everyone working in his lab, especially Dr. Fan Mei, the entire Nano Research Facility at Washington University in St. Louis, especially Dr. Dong Qin, Kristy Wendt, Brent Riggs, and Yujie Xiong, and also my site coordinator, Amy Sears. I'd also like to acknowledge the National Science Foundation and the National Nanotechnology Infrastructure Network Research Experience for Undergraduates Program for their funding and support.

References:

[1] H. Kim, J. Kim, H. Yang, J. Suh, T. Kim, B. Han, S. Kim, D. S. Kim, P. Pikhitsa, M. Choi. "Parallel patterning of nanoparticles via electrodynamic focusing of charged aerosols." Nature. Vol. 1, November 2006.

[2] Chen, Pui, and Kaufman. "Electrospraying of Conducting Liquids for Monodisperse Aerosol Generation in the 4 nm to 1.8um Diameter Range." Journal of Aerosol Science. Vol. 26, No. 6, pp. 963-977, 1995.

Growth of Silicon, Germanium, Si_xGe_{1-x} and Various Polytypes of Silicon Carbide Nanowires

Keara Harris

Electrical Engineering, Hampton University

NNIN REU Site: Howard Nanoscale Science and Engineering Facility, Howard University, Washington, DC
NNIN REU Principal Investigator(s): Dr. Gary L. Harris, Electrical Engineering, Howard University
NNIN REU Mentor(s): Mr. Crawford Taylor, Electrical Engineering, Howard University
Contact: keara.harris@pipeline.hamptonu.edu, gharris@msrce.howard.edu, crawford@msrce.howard.edu

Abstract:

The silicon-germanium (SiGe) alloy has played an important role in the semiconductor industry because of its inexpensive production and high power capabilities [1]. Silicon carbide (SiC) has also played an important role due to its high thermal conductivity and wide energy band gap [2]. In this study, silicon, germanium, Si_xGe_{1-x} and various polytypes of SiC nanowires were grown via a chemical vapor deposition (CVD) reactor. Nanowires are 1-dimensional nanostructures with very interesting properties such as a high electron mobilities, several times higher than conventional structures. Polytypes of SiC were grown on silicon substrates using silane and propane with nickel (Ni) as a catalyst. The polytypes were achieved by varying the temperature of the CVD reactor during growth. In doing this, we changed the phase of the nanowires from cubic SiC (3C) to hexagonal SiC (6H). The silicon, germanium, and Si_xGe_{1-x} structures were grown using silane and germane. X-ray and other characterization techniques were used to examine the structure and nature of the 1-dimensional system.

Introduction:

With its low energy band gap, high mobility, and ability to synthesize nanowires at low temperatures, germanium has become one of the key players in the semiconductor industry [3]. Silicon-germanium's high power capabilities make it ideal for wireless communications devices [1]. Silicon carbide is another key player in the semiconductor industry because of its high thermal conductivity. Polytypes of silicon carbide refer to the stacking structure of the silicon and carbon atoms, with the basic crystalline structures being cubic (3C), hexagonal (6H), and rhombohedral (15R), with each structure having its own unique optical and electronic properties.

Experimental Procedure:

Silicon (100) substrates were cut into 1 cm × 1 cm sized pieces and cleaned using detergent, trichloroethylene, acetone, and methanol. Electron-beam evaporation was used for the deposition of a 10 nm film of nickel for silicon nanowire catalysis, and a 10 nm film of aluminum was deposited for SiC nanowire catalysis. A thin gold film of approximately 10 nm was required for germanium and silicon-germanium nanowires catalysis, and was deposited by thermal evaporation. Nanowire growth took place in a cold wall, temperature controlled, horizontal CVD reactor.

Germanium nanowires were grown with germane (GeH_4) as the precursor gas, while silicon-germanium nanowires required germane and silane (SiH_4). Silane and propane (C_3H_8) were the precursor gases used for silicon carbide nanowires. In each reaction, hydrogen was used as the carrier gas. Hydrogen created a laminar flow within the growth chamber and was also used as a carrier gas for the precusors.

Results and Conclusions:

Gold proved to be an effective catalyst for both the germanium [4] and silicon-germanium nanowires. Germanium nanowire growth was achieved at 800°C and a growth time of 30 minutes. Growth was sparse across the sample, but denser along the edge (Figure 1). The silicon-germanium wires, while technically not "nano" in size, were successfully grown at 900°C (Figure 2). Energy dispersive spectroscopy (EDS) was performed on the wires and it was determined that there was in fact the presence of both silicon and germanium along the wire. Silicon nanowire growth was attempted, but efforts were unsuccessful, even though silicon nanowires had been successfully grown previously in this reactor.

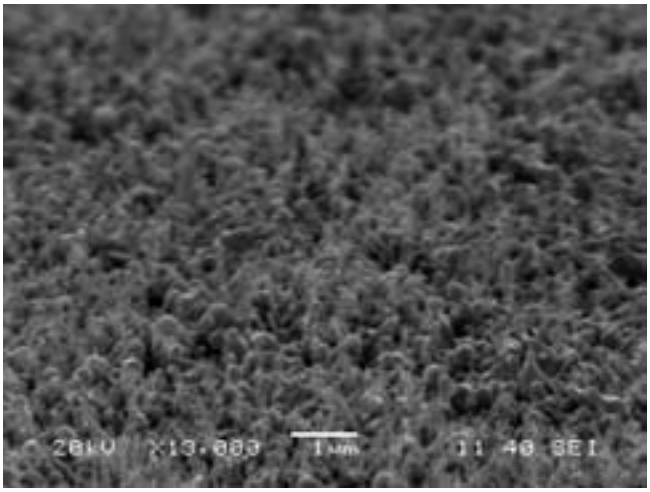

Figure 1: SEM micrograph of Ge nanowires.

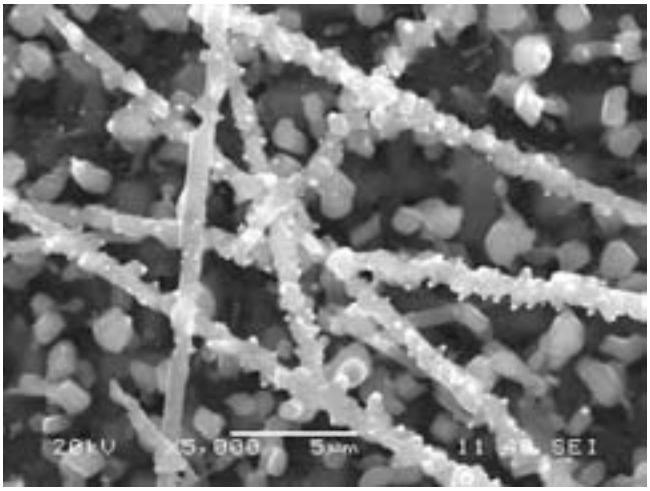

Figure 2: SEM micrograph of Si_xGe_{1-x} nanowires.

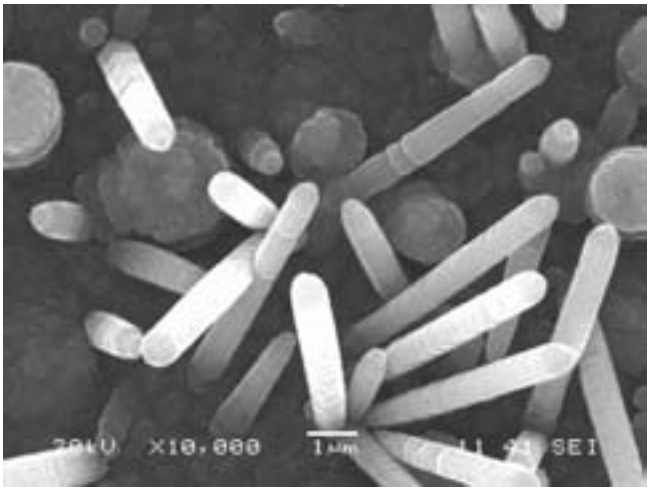

Figure 3: SEM micrograph of SiC nanowires.

Nickel proved to be an effective catalyst for various polytypes of silicon carbide nanowires. To grow different polytypes required changing the growth temperature at different times during the growth cycle. This was done to examine the temperature dependence on polytype formation. During the first growth cycle the temperature was ramped to 1050°C and held for 15 minutes, then ramped to 1336°C and held for another 15 minutes, and then ramped down to 1050°C and held for a final 15 minutes. SEM imaging showed that there were a plethora of wires of different lengths and diameters (Figure 3). The tips of these wires appeared to be hexagonal, which may indicate different polytypes were successfully formed. The second growth was done with only one temperature change, 1050°C to 1330°C. The wires appeared to have a hexagonal shape and may be evidence of a phase shift dependence on temperature, which would further proved that different polytypes of silicon carbide were obtained.

Future Work:

In the future, the nanowires should be probed to determine their electrical properties. Photoluminescence data should also be collected to determine the purity of the nanowires, along with transmission electron microscopy (TEM) to determine their exact crystalline structure along the length of the nanowires.

Acknowledgements:

I would like to thank Dr. Gary L. Harris, Mr. Crawford Taylor, Mr. James Griffin, and all the faculty and staff at the Howard Nanoscale Science and Engineering Facility. I would also like to thank the National Nanotechnology Infrastructure Network Research Experience for Undergraduates (NNIN REU) Program and the National Science Foundation for funding this project.

References:

[1] Ouellette, Jennifer. "Silicon-Germanium Gives Semiconductors The Edge." The Industrial Physicist 7 July 2009: 22-25. Print.

[2] Choyke, W.J and Devaty, Robert P. "SiC-The Power Semiconductor for the 21st Century: A materials Perspective." Naval Research Reviews 51.1:4-11.

[3] Wang, Dunwei, Ryan Tu, Li Zhang, and Hongjie Dai. "Deterministic One-to-One Synthesis of Germanium Nanowires and Individual Gold Nanoseed Patterning for Aligned Nanowire Arrays." Angewandte Chemie International Edition 44.19 (2005): 2925-929. Print.

[4] Wang, Dunwei. "Synthesis and Properties of Germanium Nanowires." Pure and Applied Chemistry 79.1 (2007): 55-65. Print.

Materials for CZTS Photovoltaic Devices

Rachel Hoffman

Chemical Engineering, Cornell University

NNIN REU Site: Nanofabrication Center, University of Minnesota-Twin Cities, Minneapolis, MN

NNIN REU Principal Investigator(s): Stephen Campbell, Electrical Engineering, University of Minnesota; Eray Aydil, Chemical Engineering and Materials Science, University of Minnesota

NNIN REU Mentor(s): Kushagra Nagaich, Electrical Engineering, University of Minnesota; Banu Selin Tosun, Chemical Engineering and Materials Science, University of Minnesota

Contact: rsh95@cornell.edu, campb001@umn.edu

Abstract and Introduction:

Thin film solar cells made of copper indium gallium selenide ($CuIn_{1-x}Ga_xSe_2$ or CIGS) combined with cadmium sulfide (CdS) to form a *pn* heterojunction are nearing the commercial production stage. However, indium and selenium are rare, and cadmium is toxic, so CIGS solar cells are not a good option for large scale energy production. Copper zinc tin sulfide (Cu_2ZnSnS_4 or CZTS) is modeled after CIGS, but uses abundant, environmentally friendly materials. CdS, which forms the heterojunction with CZTS, must be replaced with zinc sulfide (ZnS). Zinc is also useful in the compound CdZnS in CIGS solar cells to tune the band gap. In the first half of this project, deposition of ZnS and CdZnS was explored. ZnS deposition on glass slides looks promising and merits further investigation. CdZnS deposition on molybdenum coated glass slides was unsuccessful as x-ray diffraction (XRD) and energy-dispersive x-ray spectroscopy (EDX) revealed no Zn was present in the film. In the second part of this project, a method for depositing CZTS was developed. Zinc, copper and tin were deposited using thermal evaporation on molybdenum coated quartz slides. The CZT stack was annealed with sulfur powder in a Petri® dish. The CZTS films were analyzed using XRD and scanning electron microscopy (SEM).

Methods and Results:

Cadmium and zinc sulfide films were deposited using chemical bath deposition. CdS films are easily deposited in a chemical bath consisting of deionized water (DI water), $CdSO_4$, thiourea, and NH_4OH at temperatures between 50°C and 90°C in under an hour. Replacing some or all of the $CdSO_4$ in the CdS bath with $ZnSO_4$ did not lead to ZnS or CdZnS deposition. O'Brien and McAleese [1] suggest adding hydrazine, triethanolamine, or ethanolamine to promote ZnS deposition. ZnS films were deposited on scratched glass slides using the bath described above, with the addition of triethanolamine at 70°C for 1.5 to 4.5 hours. The transmission measurements are shown in Figure 1. It was found that a deposition time of at least 2.5 hours was needed for an appreciable film thickness.

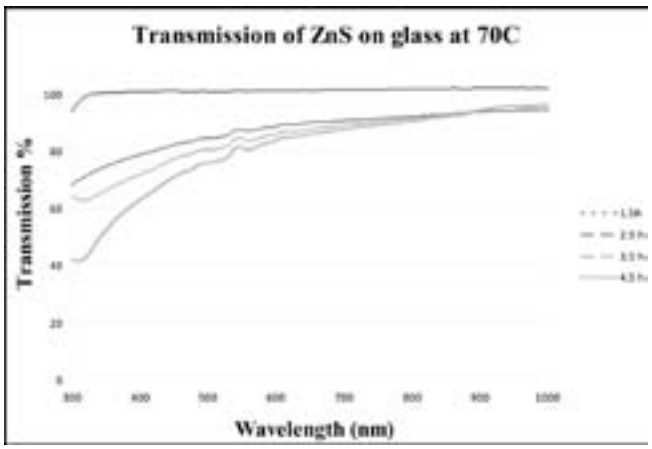

Figure 1: Transmission through ZnS deposition on glass slides.

Next, the deposition of CdZnS was attempted using the bath composition described above for ZnS. The ratio of 3:7 for Cd:Zn was chosen because Dona and Herrero [2] determined that ratio yields the highest stability CdZnS compound. Deposition was first done on scratched glass slides, then on molybdenum coated glass slides. The transmission measurements on the glass slides suggested some Zn may have deposited, but XRD and EDX on the molybdenum coated slides showed the film contained only CdS.

CZTS films were deposited on quartz slides coated with molybdenum, using e-beam evaporation or sputtering. Sputtered films were found to be better quality than e-beam evaporated films. Layers of zinc, copper, and tin were deposited using thermal evaporation. The order Zn/Cu/Sn was used because Araki et al. [3] showed it produced the most efficient solar cell. Ratios of Cu/(Zn+Sn) between 0.85 and 0.96 and Zn/Sn between 1.05 and 1.3 were used.

The CZT stack was placed in a fused silica Petri® dish with sulfur powder and annealed at 560°C, so the film was exposed to a sulfur vapor environment. Previously, the annealing step had been done in an atmosphere of hydrogen

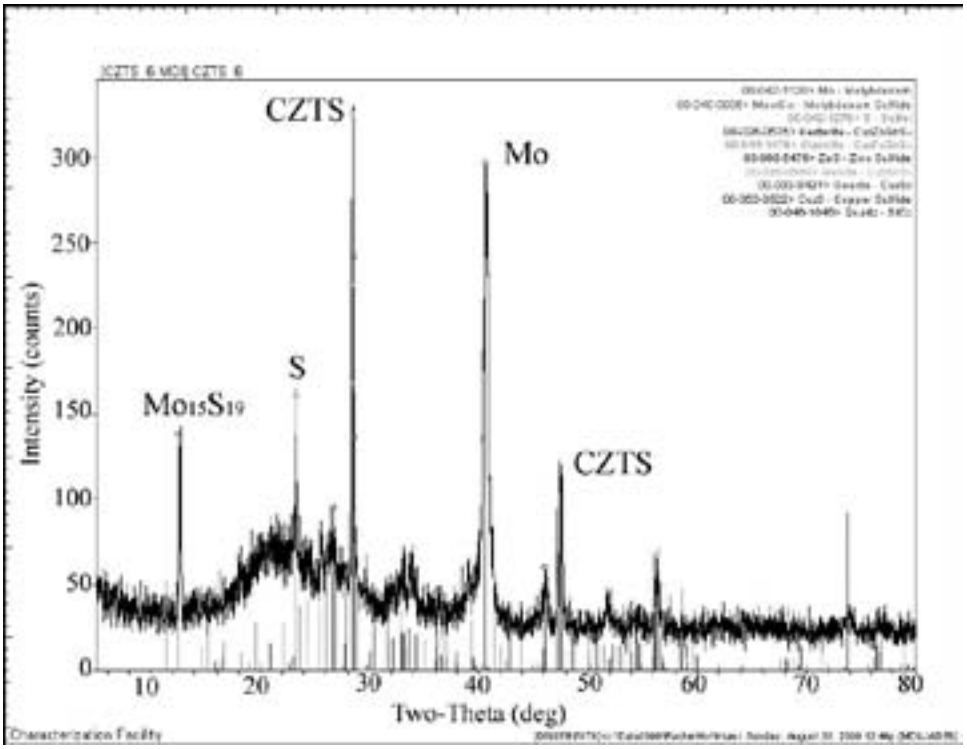

Figure 2: XRD: 30 mg sulfur anneal CZTS peaks show stannite structure so S was incorporated. The existence of S and MoS peaks suggest too much sulfur was added.

sulfide and nitrogen gases, but this project elected to use the sulfur powder method because of the toxicity of H_2S. Sulfur amounts between 4 mg and 20 mg were tested. XRD of the resulting films showed remaining copper and zinc suggesting that sulfur was not being incorporated into the film. SEM images showed that the crystalline CZTS structure was not obtained.

A weight, of approximately 470g, was obtained to hold down the lid of the Petri dish so that the increasing pressure from the evaporating sulfur would not lift the lid, allowing the sulfur vapor to escape. The amount of sulfur added was increased to 30 mg, resulting in higher CZTS peaks. XRD of this film is shown in Figure 2. Part of the CZTS film was scratched off after deposition to obtain a molybdenum contact.

Complete solar cells are formed by depositing CdS in a chemical bath followed by sputtering zinc oxide and aluminum doped zinc oxide.

Conclusions and Future Work:

Zinc sulfide deposition on glass slides looks promising and merits further investigation. Deposition on molybdenum coated slides will allow verification that it is ZnS, and then deposition on CZTS films can be attempted. The addition of a weight during the sulfur anneal step led to CZTS formation. This process will be used to characterize CZTS films and relate deposition parameters to solar cell efficiencies.

Acknowledgements:

NNIN Research Experience for Undergraduates Program and NSF for their support of this research. Parts of this work were carried out in the Nanofabrication Center which receives partial support from NSF through the NNIN program. Parts of this work were carried out in the Institute of Technology Characterization Facility, University of Minnesota, a member of the NSF-funded Materials Research Facilities Network (www.mrfn.org). I would like to thank Professor Campbell, Professor Aydil, Banu Selin Tosun, SeongHo Jeong, Min Woo Jang, Maryam Jalali, Rick Liptak, Gagan Aggarwal, Maria Torija, and the NFC staff, particularly Lage Matzke and Terry Brough for their assistance.

References:

[1] O'Brien, P., J. McAleese; "Developing an understanding of the processes controlling the chemical bath deposition of ZnS and CdS"; Journal of Materials Chemistry, 8, 2309-2314 (1998).

[2] Doña, J.M., J. Herrero; "Chemical bath codeposited CdS-ZnS film characterization"; Thin Solid Films, 268, 5-12 (1995).

[3] Araki, H., A. Mikaduki, Y. Kubo, T. Sato, K. Jimbo, W. S. Maw, H. Katagiri, M. Yamazaki, K. Oishi, A. Takeuchi; "Preparation of Cu2ZnSnS4 thin films by sulfurization of stacked metallic layers"; Thin Solid Films, 517, 1457-1460 (2008).

Metallization for High Temperature Electronics

Katherine C. Kragh

Engineering Physics, Rose-Hulman Institute of Technology

NNIN REU Site: Penn State Nanofabrication Laboratory, Pennsylvania State University, State College, PA

NNIN REU Principal Investigator(s): Dr. Suzanne E. Mohney, Materials Science and Engineering, The Pennsylvania State University

NNIN REU Mentor(s): Brian Downey, Materials Science and Engineering, The Pennsylvania State University

Contact: kraghkc@rose-hulman.edu, mohney@ems.psu.edu, bpd126@psu.edu

Abstract:

With its wide band gap and large thermal conductivity, silicon carbide can replace silicon as the semiconductor for high temperature and high power electronics. This study investigated metallic capping materials that could withstand elevated temperatures, while maintaining a low sheet resistance. Sputtered gold and ruthenium films were monitored for agglomeration through microscopy and for sheet resistance through the van der Pauw technique. Low resistance, pure gold films demonstrated significant agglomeration upon annealing at 600°C. Pure ruthenium, however, withstood agglomeration through 50 hours of annealing while sustaining an acceptably low sheet resistance. Despite the popularity of gold, a capping layer of 150 nm of ruthenium provides high-quality adhesion and low resistance through continued annealing at 600°C.

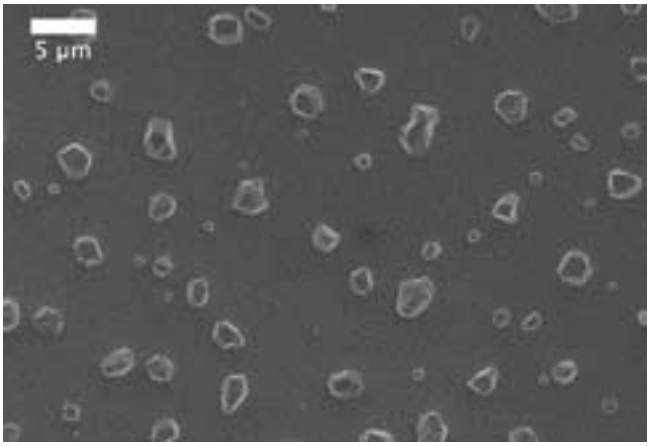

Figure 1: FESEM micrograph of gold agglomeration after annealing.

Introduction:

Wide band gap semiconductors such as silicon carbide can be utilized for high temperature devices. In comparing silicon carbide to silicon electronics, the power to size ratio increases, in addition to an efficiency improvement and a reduction in physical size [1]. With the wide band gap, thermal electrons remain unlikely to surmount the energy barrier and contribute leakage current. In order to realize the full potential of these wide band gap semiconductors, robust metal contact layers must be implemented that can also withstand the high temperatures resulting from significant power operation. As a capping material for electronics, gold has been a popular metal choice due to its low resistivity and limited oxidation. However, gold-based films agglomerated into mounds as shown in Figure 1 during annealing at 600°C. This research aimed to discern a capping metal or gold alloy with strong adhesion to titanium nitride and low resistance after prolonged annealing in air.

Experimental Procedure:

For economical reasons, silicon pieces were used with a diffusion barrier of grown oxide. A 100 nm titanium layer was sputtered onto the substrate before annealing in nitrogen to produce a titanium nitride thin film. The capping metal film was sputtered onto the titanium nitride contact layer. Various thicknesses of gold, ruthenium, and different co-sputtered gold-ruthenium films were investigated as capping metals. Samples were cycled through annealing in air at 600°C and measuring the sheet resistance. The sheet resistance, or resistance over film thickness, was measured with a four point probe van der Pauw technique. This technique obtained voltages and currents along each pair of the sample's sides to calculate sheet resistance, correcting for shape irregularities [2]. Adhesion was tested with tape. Both an optical microscope and a field emission scanning electron microscope (FESEM) were employed for detecting agglomerations.

Results:

Although possessing a lower sheet resistance upon deposition, the gold films agglomerated rapidly during the annealing process. When the film pulls itself into mounds, the gold minimizes its surface energy. However, the agglomeration increases the sheet resistance and permits oxygen diffusion.

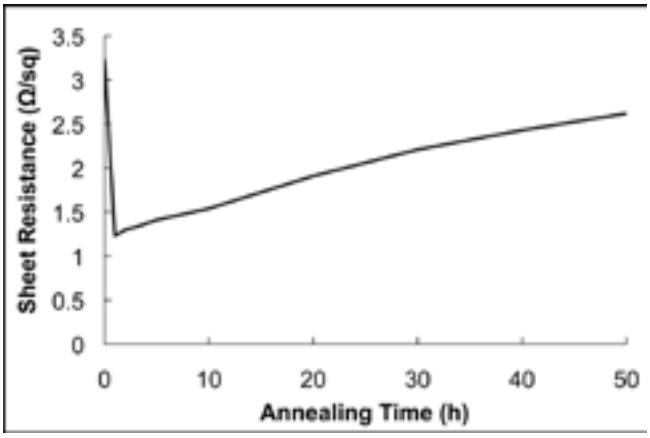

Figure 2: 150 nm ruthenium retained a low sheet resistance after annealing at 600°C in air.

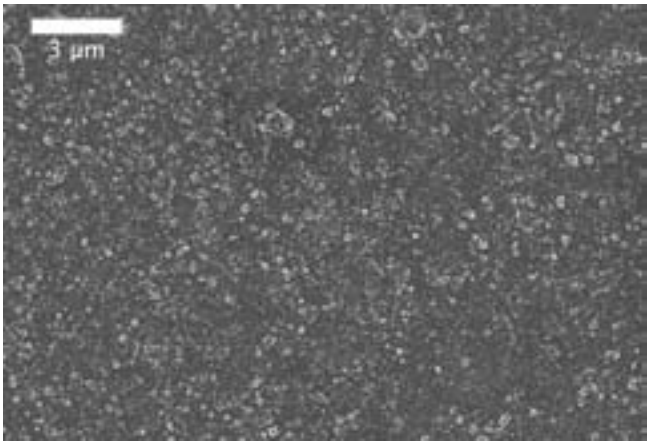

Figure 3: FESEM micrograph of the ruthenium surface after prolonged annealing.

Possibly caused by stress in the films, the agglomeration in gold films had a fractal appearance similar to that reported by Gadkari et al. [3]. Pure ruthenium demonstrated an initial drop in sheet resistance before rising slowly with prolonged annealing, as shown in Figure 2. The sheet resistance remained very low at 2.6 Ω/square, even after 50h of annealing. The ruthenium film was agglomeration-free at 44h, as shown in Figure 3. Co-sputtered alloys of ruthenium and gold showed an early onset of agglomeration and increased sheet resistance.

High-quality adhesion in a sample was valued for material compatibility in the device. Whereas the gold-based films had weak adhesion, ruthenium films showed strong adhesion to the titanium nitride layer. When layered, gold and ruthenium adhered considerably to each other as well.

With annealing time, the gold-based films darkened towards a brass color. Ruthenium experienced various color changes through the annealing process. Initially a shiny silver color, ruthenium passed from orange to red to purple by three hours of annealing. The purple hue continued deepening. After 20h of annealing, however, a dark blue color was prevalent. The color change may be constructive light interference of a surface oxide. The oxide composition likely would be ruthenium oxide or ruthenium-titanium oxide. Auger electron spectroscopy revealed only ruthenium and oxygen present at the surface. Notably, Rard and others mentioned that ruthenium (IV) oxide, RuO_2, was a dark blue color [4]. Further, RuO_2 has been noted as a conductive oxide, which would help retain the low sheet resistance [4].

Conclusions and Future Work:

Although gold initially had a lower sheet resistance, ruthenium maintained a lower sheet resistance throughout annealing compared to the gold-based films. Ruthenium also possessed better adhesion than gold to titanium nitride. A metal capping layer of 150 nm ruthenium has been recommended from this study for further inquiry. Ruthenium being less expensive than gold, the thin 150 nm requirement creates a financially viable solution. Future work will investigate the specific composition of the oxide and further evaluate ruthenium as a possible metallization layer for silicon carbide devices.

Acknowledgements:

The National Science Foundation, the National Nanotechnology Infrastructure Network Research Experience for Undergraduates (NNIN REU) Program, and the Materials Research Institute at Penn State University are greatly appreciated for sponsoring this research program. Bangzhi Liu is thanked for his tutelage and assistance. The authors are further grateful for the support of the Penn State University Nanofab staff and the Mohney Research Group members.

References:

[1] Neudeck, P.G.; "Silicon Carbide Electronic Devices"; Encyclopedia of Materials: Science and Technology, Vol. 9, 8508-8519 (2001).

[2] Schroder, D. K.; Semiconductor Material and Device Characterization, 3rd Ed., 2-20 (2006).

[3] Gadkari, P. R., A. P. Warren, R. M. Todi, R. V. Petrova, K. R. Coffey; "Comparison of the agglomeration behavior of thin metallic films on SiO_2"; J. Vac. Sci. Technol. A, Vol. 23(4), 1152-1161 (2005).

[4] Rard, J. A.; "Chemistry and Thermodynamics of Ruthenium and Some of Its Inorganic Compounds and Aqueous Species"; Chemical Reviews, Vol. 85(1), 18-20 (1985).

Characterization of Thermally Induced Bilayer Distortions

Arjunen Ryan Kutayiah

Physics, City University of New York Hunter College

NNIN REU Site: Nanotech@UCSB, University of California, Santa Barbara, CA

NNIN REU Principal Investigator(s): Prof. Deborah K. Fygenson, Physics Department, Biomolecular Science and Engineering Program, University of California Santa Barbara

NNIN REU Mentor(s): Kimberly L. Weirich, Biomolecular Science and Engineering Program, University of California Santa Barbara

Contact: arjunenryankutayiah@hotmail.com, deborah@physics.ucsb.edu, kweirich@physics.ucsb.edu

Abstract:

Supported lipid bilayer (SLB) is a promising biologically inspired surface coating and model system for reconstructing membrane processes. We apply thermal stress to SLB and report on the resulting structural distortions. Thermal stress induces long, thin, flexible protrusions (worms) in the SLB that are unstable and eventually collapse into giant vesicles. We examine the length distribution, and collapse of SLB worms as a means toward better understanding the material properties of SLB.

Introduction:

Lipids are molecules composed of a hydrophilic head and hydrophobic tail. In the presence of water these molecules self assemble into a bilayer structure. Supported lipid bilayer (SLB) is a lipid bilayer that has been deposited on a substrate such as glass [1,2]. SLB holds great promise as a biocompatible surface coating and a model for studying membrane processes such as membrane embedded proteins [3]. Understanding SLB mechanics could potentially lead to a more efficient membrane permeable drug delivery system. We studied the response of the SLB to thermal stress and the resulting structural distortions.

Experimental Procedure:

We prepared a vesicle solution of 97% 1, 2-dimyristoyl-sn-glycero-3-phosphocholine (DMPC) and 3% of the fluorescent phospholipid N-(7-nitrobenzoxa-2, 3-diazol-4-yl)-dimyristoyl-phosphatidyle ethanol-amine (NBD – DMPE). Our vesicle preparation followed a standard protocol [4]. Briefly, a lipid film was dried on the surface of a clean glass vial and placed under vacuum for 24 hrs. Then, the film was hydrated with 150 mM PBS (buffer), freeze/thawed, and extruded through a series of membranes with decreasing pore sizes (200 nm, 100 nm, 20 nm).

A clean piece of borosilicate glass was exposed to buffer for ~ 30 minutes in a temperature-controlled flowcell. After the temperature stabilized to 30ºC, the buffer was replaced by vesicle solution. The glass was exposed to 0.1 mg/mL vesicle solution for 15 min before rinsing with buffer to remove vesicles from the bulk solution. The glass surface was then imaged in epifluorescence using an inverted microscope and a CCD camera. A spot was bleached by reducing an aperture and increasing the current of the LED light source. An image was taken directly after the bleach and 30 minutes later to check for fluorescence recovery. The surface was imaged at 30 seconds intervals as the temperature was increased to 37ºC.

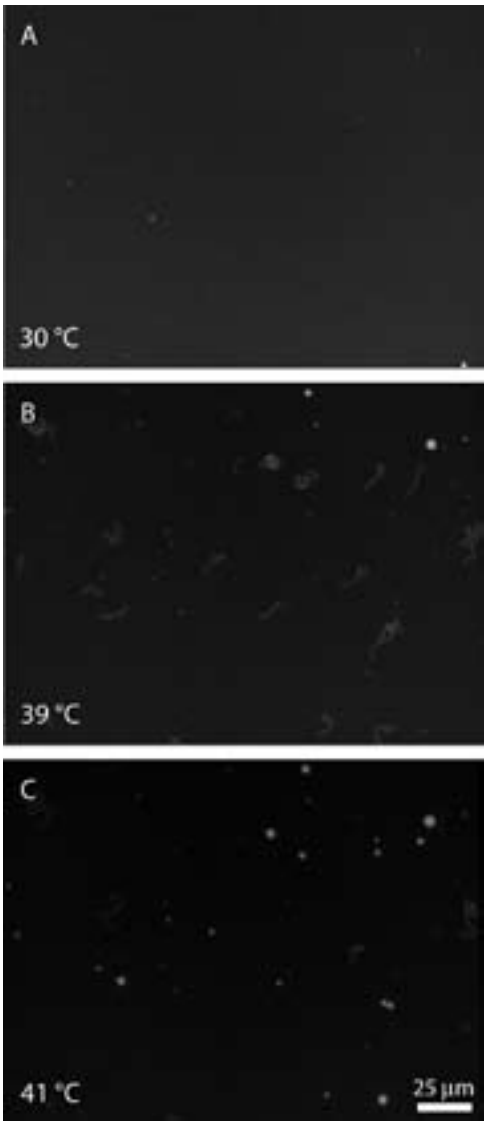

Figure 1: A. Bilayer at 30°C. B. Bilayer at 39°C worms grow. C. Worms at 41°C bilayer collapse.

Results and Conclusion:

We checked the bleached spot for recovery. Recovery indicated that the surface was covered in SLB. At 37ºC, we observed the appearance of bright round spots—as the temperature increased these spots elongated into varied-sized, floppy worm-like structures or simply "worms" (Figure 1). While the temperature continued its increase, some of the worms continued to grow; others remained constant, while others collapsed into bright round spots.

We hypothesized that the worms were a result of thermal expansion. Since the SLB was confined to a fixed area (i.e. borosilicate glass) and it expanded faster than the area it was confined to, it tended to protrude from that surface. However, these protrusions were unfavorable and thus collapsed to a more stable geometry, i.e. giant vesicles.

We analyzed the growth and collapse (Figure 2) of the worms and obtained a rate of growth and collapse. We analyzed the length distribution of the worms (Figure 3).

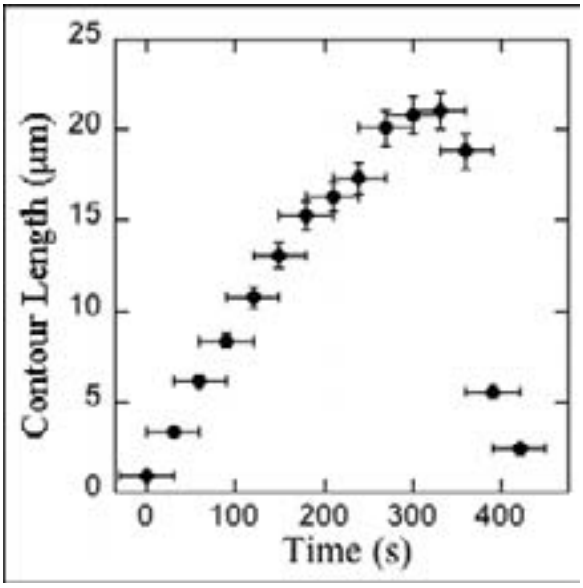

Figure 2: Growth and collapse of a worm.

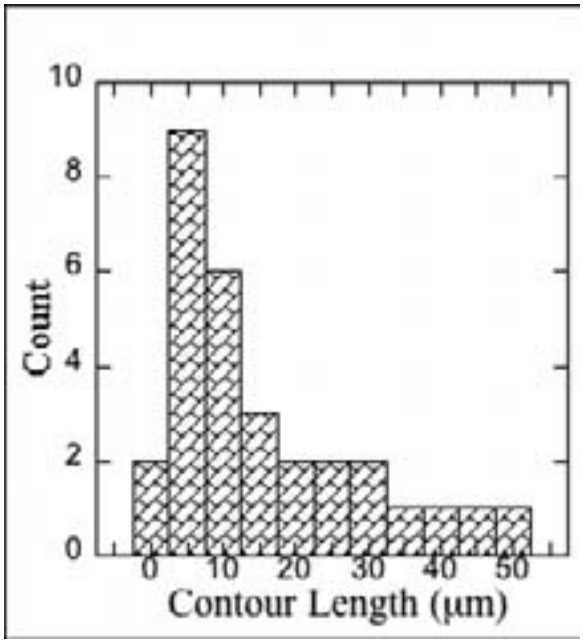

Figure 3: Length distribution of worms.

Acknowledgements:

The author gratefully acknowledges the Fygenson group, especially my mentor Kim Weirich, Daniel Schiffels and Prof. Deborah K. Fygenson. I would like to thank Angela Berenstein our NNIN REU site coordinator, the National Nanotechnology Infrastructure Network Research Experience for Undergraduates (NNIN REU) Program, National Science Foundation (NSF) and National Institutes of Health (NIH) for funding.

References:

[1] Brian, A. A., and H. M. McConnell. 1984. Allogenic stimulation of cytotoxic T-cells by supported planar membranes. Proceedings of the National Academy of Sciences of the United States of America-Biological Sciences 81:6159-6163.

[2] Tamm, L. K., and H. M. McConnell. 1985. Supported phospholipid bilayers. Biophysical Journal 47:105-113.

[3] Suzuki, H., and S. Takeuchi. 2008. Microtechnologies for membrane protein studies. Analytical and Bioanalytical Chemistry 391:2695-2702.

[4] Olson, F., C. A. Hunt, F. C. Szoka, W. J. Vail, and D. Papahadjopoulos. 1979. Preparation of liposomes of defined size distribution by extrusion through polycarbonate membranes. Biochimica Et Biophysica Acta 557:9-23.

Characterization of the Diffusivity of Conductive Polymers in Nanochannel Confinement

Jamal Lottier Molin

Computer Engineering, University of Maryland, Baltimore County

NNIN REU Site: Stanford Nanofabrication Facility, Stanford University, Stanford, CA

NNIN REU Principal Investigator(s): Prof. Reinhold Dauskardt, Materials Science and Engineering, Stanford University

NNIN REU Mentor(s): Taek-Soo Kim, Mechanical Engineering, Stanford University

Contact: molinj1@umbc.edu, dauskardt@stanford.edu, tskim1@stanford.edu

Abstract:

The fabrication of nanochannels for analyzing molecular behavior at the single-molecule level is a rising phenomenon in material science. This methodology has been applied in research areas including the controlled transport of biological species, nanoelectromechanical systems (NEMS) studies, and the stabilization of the release rates of small molecules in drug delivery. Interest in the distinctive mechanical, electrical, and optical properties of the conductive polymer poly(3,4-ethylenedioxythiophene) poly(styrenesulfonate) (PEDOT:PSS), widely used in organic electronics (sensors, solar cells, LED), induces further research concerning this molecule under a nano-confining environment. In this work, we fabricate nanochannels on a quartz substrate using electron beam lithography, and furthermore, use these nano-devices to characterize the diffusivity of PEDOT:PSS. Observation under an optical microscope allows for characterization of the molecule's diffusivity, while images obtained from the SEM will confirm existence of these molecules confined in the nanochannels. The ability to characterize PEDOT:PSS in such nano-confinement will impose a strong foundation on further research on this conductive polymer.

Introduction:

The study of diffusion in nanochannel confinement is a rising phenomena in nanotechnology research. Nanochannels provide an environment in which biological species can be controlled at the single-molecule level. Furthermore, they are easily integrated with other detection device units such as nanowires, transistors, and optical waveguides [1]. The diffusion of molecules into nanochannels is commonly used in research areas including deoxyribonucleic acid (DNA) stretching studies.

We have applied this idea for characterizing the polymer, PEDOT:PSS. PEDOT:PSS is a conductive, transparent polymer with unique electrical and optical properties, making it ideal for organic electronics research [2]. However, there is no research on the diffusivity properties of PEDOT:PSS. Therefore, in this work, we have designed and fabricated a nanochannel device for characterizing the diffusivity properties of PEDOT:PSS under nanoscopic confinement.

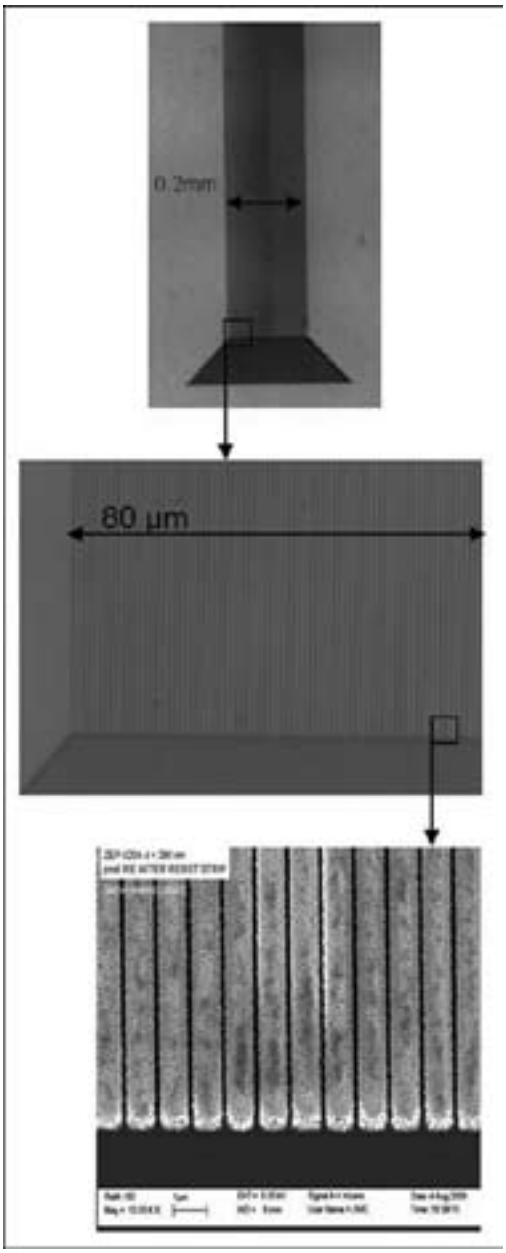

Figure 1: Top: Optical image of 120 nm channel width nanochannel device. Middle: Optical image of 120 nm channel width nanochannel. Bottom: SEM image of 140 nm channel width nanochannel device at 10KX magnification (5KV).

Experimental Procedure:

A 100 mm wafer was first spin-coated with ZEP-520A photoresist (~ 300 nm thickness). Next, a 20 nm layer of the conductive polymer,

Espacer 300Z, was spin-coated onto the wafer to prevent any charging of the quartz substrate while exposed under the electron beam [3,4]. The pattern that was to be written on the wafer was created using the RAITH 150 Software. The nanochannel device we designed and used in this work can be seen in Figure 1a.

The wafer consisted of a set of ten of the nanochannel devices. Each consisted of various channel widths ranging from 20 nm to 200 nm in increments of 20 nm. There were two sets of these patterns to show consistency. They were then written onto the ZEP-coated quartz substrate using the RAITH electron beam (e-beam). Following the e-beam exposure, the espacer was removed using a spin-rinse dryer, and the wafer was developed in xylenes. When submerged in xylenes, the areas of the ZEP resist that were exposed to the electron beam during exposure, were removed. Finally, the substrate was etched using the AMT etcher (oxide etcher) creating a 500-600 nm depth for the nanochannels. The ZEP resist was stripped by submerging the wafer in sulfuric acid for 20 minutes and the fabrication process was complete.

To characterize the diffusivity properties of PEDOT:PSS using these nanochannel devices, using a syringe, we deposited the PEDOT:PSS solution into the trapezoidal area of the nanochannel device. As the solution diffused into the nanochannels, its diffusion and mobility could be characterized in various ways.

Results and Discussion:

After the first e-beam write, there were three major issues that we encountered. First, there was poor adhesion of the ZEP resist. Weak bonding between the resist and the quartz substrate caused areas of deformation in the pattern. Our solution to this problem was to prime the wafer with hexamethyldisilazane (HMDS) to create better adhesion of the ZEP resist. Secondly, we noticed stitch breaks in the pattern. The e-beam writes in 40 μm write fields. At every shift in write field, due to the properties of the quartz substrate, the wafer would begin charging and slightly deflect the electron beam, causing a shift in the pattern write. To compensate for this charging, we coated a second layer of espacer. Finally, we noticed that after the e-beam write, the strips of ZEP resist between the nanochannels were so thin (< 300 nm) that during development, they would be easily shifted off of the pattern leaving hairy-like structures of ZEP resist on the wafer surface. The solution to this issue was to increase the spacing between the nanochannels to one micron.

After making these adjustments, the patterns were written again under the e-beam. Results can be observed at different magnifications in Figure 1. The write was successful and we had completed nanochannel devices to be used for diffusion characterization.

Following the etching of the pattern and stripping of the photoresist, the nanochannel devices were used for the diffusion tests. Preliminary diffusion results show the PEDOT:PSS solution diffused into the channels of the nanochannels devices with channel widths of 180 nm and 200 nm. The results of the diffusion using the nanochannel devices with channel widths of 180 nm can be seen in the optical image in Figure 2.

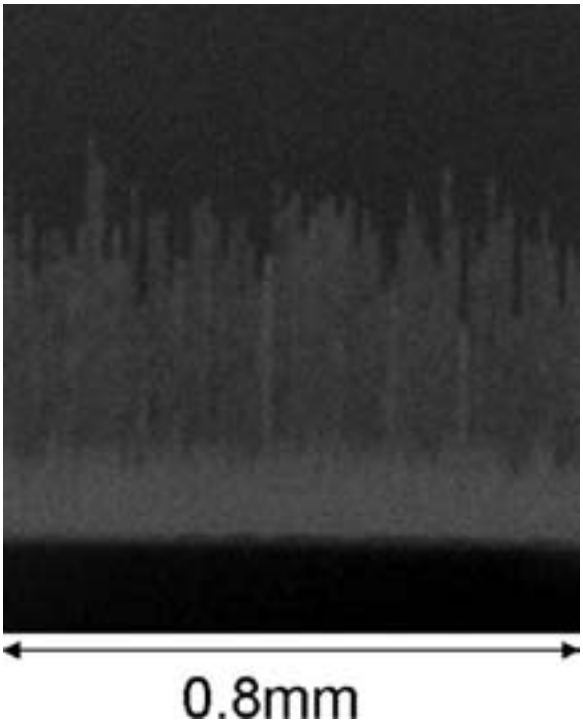

Figure 2: Optical image of 180 nm channel width nanochannel device after preliminary diffusion test.

Conclusions and Future Work:

We successfully fabricated a nanochannel device on a quartz substrate to be used for diffusion purposes. Moreover, we were able to begin preliminary diffusion work with PEDOT:PSS using these nanochannel devices. In the future, we would like to attempt to fabricate these nanochannel devices on other substrates. We would also like to characterize the diffusion properties of other polymers and DNA, using these nanochannel devices.

Acknowledgements:

Taek-Soo Kim, REU Mentor; Prof. Rienhold H. Dauskardt, PI; Michael Deal, Maureen Baran, and the Stanford Nano-fabrication staff; James Conway, SNF Staff; National Science Foundation; Intel Foundation; National Nano-technology Infrastructure Network Research Experience for Undergraduates (NNIN REU) Program.

References:

[1] Perry, J. Kandlikar, Satish G. "Review of fabrication of nanochannels for single phase liquid flow." Microfluid Nanofluid. 2005.

[2] Nardes, A. M. Eindhoven. "On the Conductivity of PEDOT:PSS Thin Films." 2007.

[3] Chou, S. Y. "Methods for Making Continuous Nanochannels." 2008.

[4] Choonsup L. E. "A Nanochannel Fabrication Technique without Nanolithography." Nano Letters. Vol. 3, No. 10. 2003.

Atomic Layer Deposition of High Constant Gate Dielectrics for Thin Film Transistors

Du Nguyen

Physics, Michigan State University

NNIN REU Site: Lurie Nanofabrication Facility, University of Michigan, Ann Arbor, MI

NNIN REU Principal Investigator(s): Jamie Phillips, Electrical Engr. and Computer Science, University of Michigan

NNIN REU Mentor(s): Jeffrey Siddiqui, Electrical Engineering and Computer Science, University of Michigan

Contact: nguye191@msu.edu, jphilli@umich.edu, jjameel@umich.edu

Abstract:

Transparent insulating oxides with high dielectric constant (κ) are desired for thin film transistors that form the basis of current flat panel displays and future flexible and transparent electronics. This project uses atomic layer deposition (ALD) in order to grow these oxide films. ALD deposits precisely one monolayer of film with every cycle so that thicknesses can be controlled at the atomic level. An Oxford OpAL ALD tool was used in this work to deposit thin films of aluminum oxide (Al_2O_3) and hafnium oxide (HfO_2) under varying parameters of temperature, plasma power, and pressure. In addition, the effects of thermal annealing the films after deposition were examined. Optimal growth parameters were found in order to maximize the dielectric constant and minimize leakage current density through the films, as these parameters are critical in determining the ultimate performance of thin film transistors. By maximizing the dielectric constant and maintaining low leakage in a thin dielectric layer, a higher capacitance from the oxide is achieved which allows for better gate control of the drain current in a thin film transistor. The results of the study will be applied to current research on zinc oxide and zinc telluride thin film transistors.

Experimental Procedure:

In the ALD process, the films are grown with repeated cycles of precursor doses and purging stages shown in Figure 1. The film growth is self limiting and based on surface reactions, which allows for the atomic scale control of the deposition. For the oxides grown in this project, two precursors are used: one for the oxide and one for the other element (Al or Hf). In order to improve the oxidation of the thin film, some of the depositions were aided by oxygen plasma. An alternative oxygen-providing precursor used was water. The other precursors for Al_2O_3 and HfO_2 were tri-methyl aluminum and tetrakis(ethylmethylamino) hafnium respectively.

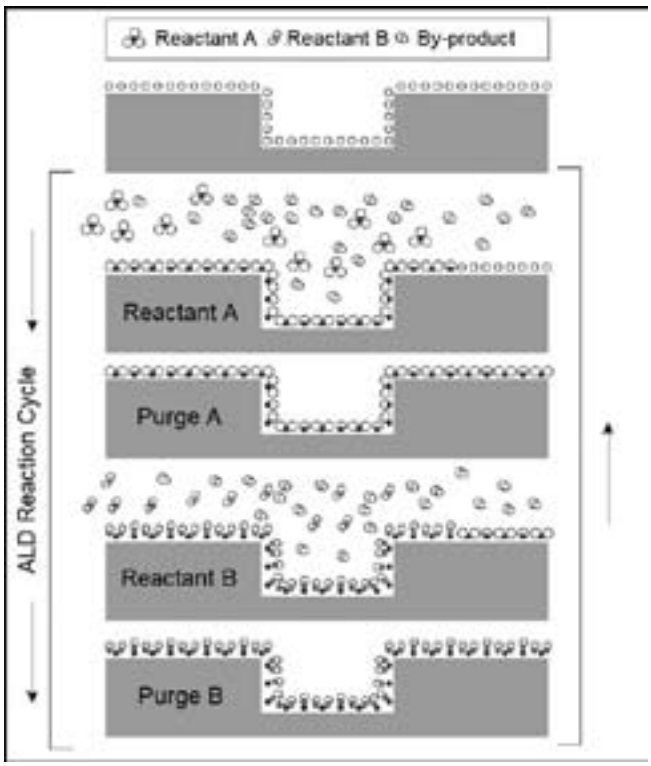

Figure 1: Basic ALD growth cycle.

Oxide thin films were deposited on silicon wafers, including HfO_2 with plasma, Al_2O_3 with plasma, and Al_2O_3 with water. The films were grown with varying parameters of temperature, plasma power, and pressure. The temperatures ranged from 100°C to 300°C in increments of 50°C and were controlled through a table heater within the growth chamber. The plasma power was directly controlled through the tool software and ranged from 100W to 300W in increments of 50W. The last parameter of pressure was controlled by the precursor and purging gas flows of the chamber. The pressure ranged from 100 mTorr to 500 mTorr in increments of 100 mTorr. Each film was grown for 300 cycles and nominally 300 Å thick.

Capacitors were fabricated to test the electrical properties of the oxide thin films. Capacitors were fabricated by depositing metal contacts with radii of 340 μm, consisting of a layer titanium and platinum 200 Å and 1000 Å in thickness respectively. The dielectric constants of the thin films were determined by measuring the capacitance, using known

values for the film thickness and contact area. In addition, the leakage current was measured for a voltage sweep ranging from -20 V to 20 V.

The optimal growth parameters for HfO_2 were found to be 300°C at 250W using the default pressure, but both the plasma power and pressures were found to have little effect on the electrical properties of the films. For Al_2O_3 with plasma, the optimal parameters were 250°C at 100W at 300 mTorr.

With Al_2O_3, the pressure had little effect as well. However, higher plasma powers had significantly higher leakage current in the films. This was likely due to a larger amount of reflected power as the plasma power increased. Finally, for Al_2O_3 with water, the optimal parameters were 300°C at default pressure. Again, pressure did not have a significant effect on film growth. Results of the experiment are summarized in Figures 2 to 7.

Summary Results and Future Work:

Initial work on the effects of annealing was begun with anneals at 400°C and 500°C for 30 minutes with oxygen gas. In addition, literature was found indicating that an anneal can decrease leakage current by orders of magnitude, but experiments have only been run for HfO_2 grown with water and anneals using forming (N_2/H_2) gas. No conclusive results have been found currently for HfO_2 with plasma or thermally grown Al_2O_3. In addition, initial zinc oxide thin film transistors will be created using the optimal parameters for the films.

Future work will apply results of the study to improved zinc oxide and zinc telluride thin film transistors. Applications of these may be used for low power electronic displays and potentially in flexible electronics.

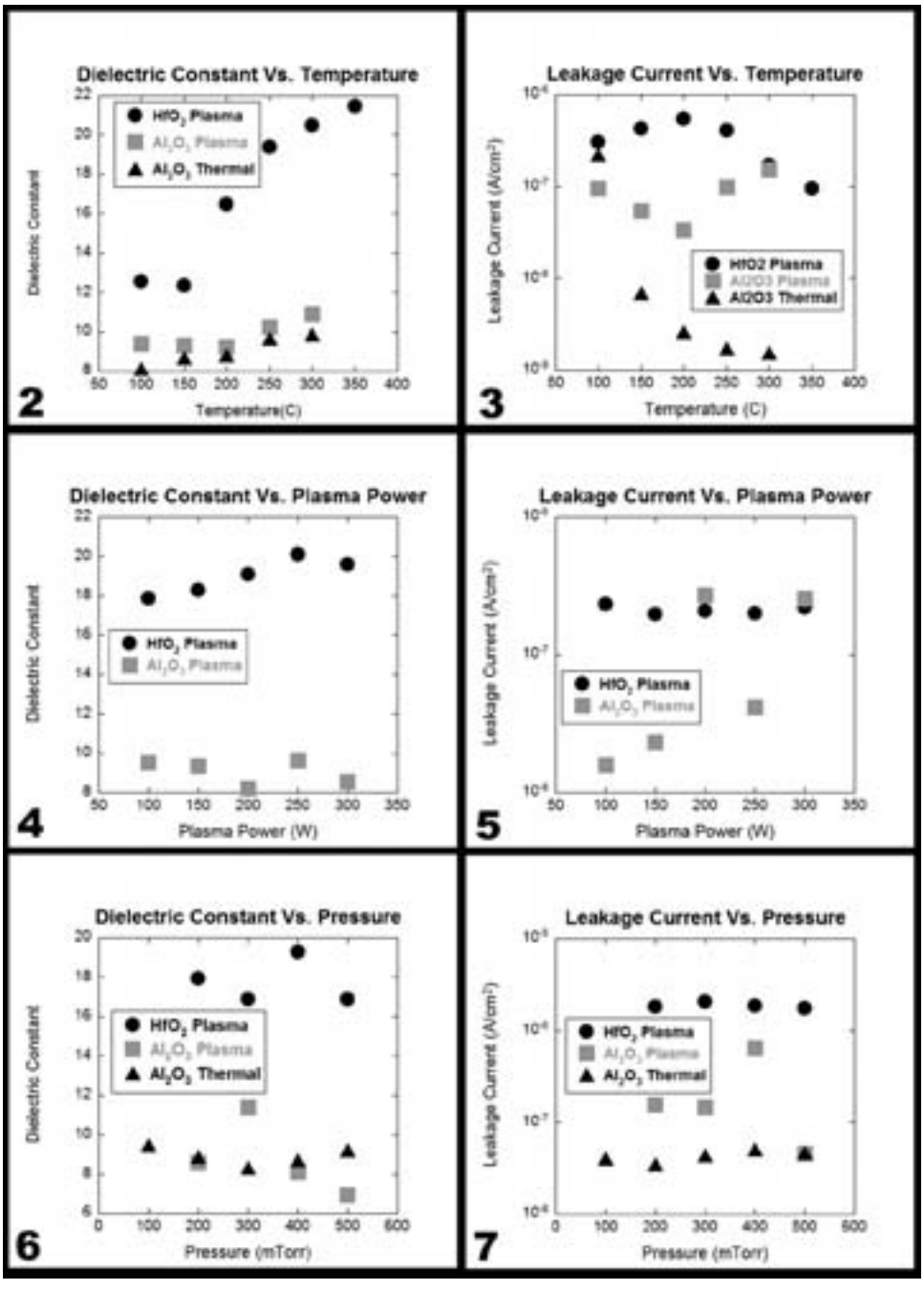

Acknowledgements:

I would like to thank my mentors Jeffrey Siddiqui and Emine Cagin for training and teaching me during this REU as well as my advisor Jamie Phillips. I would also like to thank Sandrine Martin, Brandon Lucas, and the staff of the Lurie Nanofabrication Facility for their assistance and coordination of the program. Finally, I would like to thank the National Nanotechnology Infrastructure Network Research Experience for Undergraduates Program and National Science Foundation for funding this program.

References:

[1] P.Carcia, R. McLean, and M.Reilly; "High-performance ZnO thin-film transistors on gate dielectrics grown by atomic layer deposition"; Applied Physics Letters, 88, 123509 (2006).

[2] Ritala, M. and M. Leskelä; "Atomic layer epitaxy - a valuable tool for nanotechnology?"; Nanotechnology, 10, 19-24 (1999).

[3] Puurunen, R.; "Surface chemistry of ALD: A case study for C_3H_9Al/water process"; Journal of Applied Physics, 97, 121301 (2005).

Figures 2 through 7: 2. Dielectric constant data for temperature variance; 3. Leakage data for temperature variance; 4. Dielectric constant data for plasma power variance; 5. Leakage data for plasma power variance; 6. Dielectric constant data for pressure variance; 7. Leakage data for pressure variance.

Characterization and Acid Diffusion Studies of Cyclodextrin and its Carborane Inclusion Complex

Amanda Oehrlein

Chemistry, Hamline University

NNIN REU Site: Cornell NanoScale Science and Technology Facility, Cornell University, Ithaca, NY

NNIN REU Principal Investigator(s): Christopher Ober, Materials Science, Cornell University

NNIN REU Mentor(s): Marie Krysak, Chemistry, Cornell University; Jing Sha, Materials Science, Cornell University

Contact: ao252@cornell.edu, cober@ccmr.cornell.edu, mek97@cornell.edu, js545@cornell.edu

Abstract:

In order to move forward, the semiconductor industry is dependent on improvements in the lithographic process, most importantly the development of new resist materials. As pattern dimensions continue to decrease, issues of line edge roughness arise. Molecular glasses are an attractive alternative to polymeric resists, as they are able to incorporate an amorphous structure and high transition temperature (T_g) with a small size that can show improved line edge roughness. Cyclodextrin has shown promise as a 193 nm resist, though it exhibits poor etch resistance. By introducing carborane into the cyclodextrin core, we have shown that the etch resistance of cyclodextrin is around that of PHOST, an industry standard photoresist. However, we also see an increase in line edge roughness. We intend to observe the differences in acid diffusion between the non-carborane and carborane resist by creating bilayers and measuring film thicknesses before and after development. Using this data, we can now modify cyclodextrin core with carborane to inhibit acid diffusion and show improved patterning capability with high etch resistance.

Introduction:

tert-butyl ester protected methyl β cyclodextrin has been used as a 193 nm molecular glass resist and has good patterning abilities. Unfortunately, this resist exhibits poor etch resistance, so carborane was added. The addition of carborane increased the etch resistance to the equivalence of polyhydroxystyrene but increased the line edge roughness. We believe that the photoacid generator sits in the pocket of the cyclodextrin molecule, which inhibits the acid from diffusing beyond exposed regions. We hypothesize that the carborane sits in the cyclodextrin pocket, which blocks the photoacid generator's ability to do so, increasing the acid diffusion.

Experimantal Procedure:

Our studies were carried out using *tert*-butyl ester protected methyl β cyclodextrin, shown in Figure 1. Carborane was added to the cyclodextrin core, creating a host-guest complex. The complex was dissolved in Ethyl-l-Lactate to make a 5% weight solution. The photoacid generator used was triphenylsulfonium triflate (5% weight with respect to resist). We then spun this solution on HMDS primed silicon wafers. In order to find optimal post application bake (PAB) and post exposure bake (PEB) temperatures, we used a combinatorial tool. The setup consists of an aluminum plate with an ice bath and a hot plate on either end. The combinatorial tool allows us to have a temperature gradient across the wafer, so we can find the optimal PAB and PEB temperatures on one patterned wafer. The optimal exposure dose used for patterning was 30.45 mJ/cm^2. An ABM contact aligner with a 254 nm mirror was used to expose the resist and create patterns. Supercritical carbon dioxide ($scCO_2$) was used to develop the exposed resist, at 5000 psi for 5 minutes.

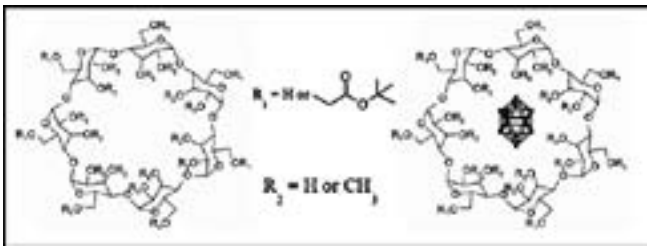

Figure 1: tert-butyl ester protected methyl β cyclodextrin without carborane (left) and tert-butyl ester protected methyl β cyclodextrin with carborane (right).

The acid diffusion studies were done using bilayers of resist, with and with out photoacid generator (PAG). Bilayers of resist were made by spinning the cyclodextrin resist with PAG on a silicon wafer. Next we spun cyclodextrin without PAG on a polydimethylsiloxane stamp that had been cleaned using oxygen plasma. The wafer and stamp were pressed together and let sit until fully wetted. Pressure and heat were applied for twenty seconds, and then the set was cooled. Finally the stamp was peeled off, leaving two layers of resist on the wafer, with the resist with PAG on the bottom. These were then exposed at varying doses and post exposure baked which started the diffusion of the acid. The wafer was then

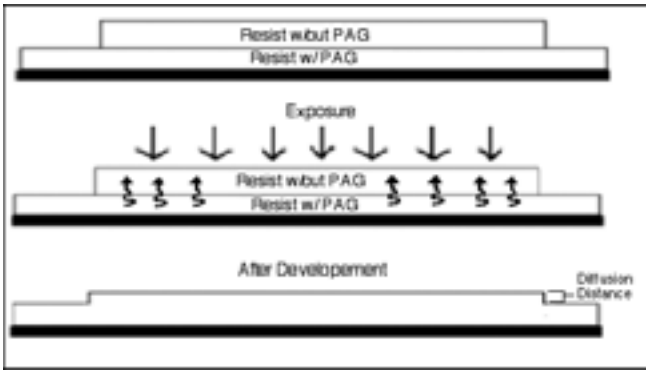

Figure 2: Patterns generated from the ABM contact aligner. Cyclodextrin without carborane on left and carborane complex on right.

developed using $scCO_2$ at 5000 psi for 5 minutes. With this type of development, the polar, or exposed portion of the resist remains, so the areas where the acid had traveled would also remain allowing us to see how far the acid diffused (Figure 2). Measurements were taken on the wafer with only the bottom layer containing resist with PAG, the wafer with both layers of resist, and after development on each exposure section. The vertical diffusion will replicate the horizontal diffusion, and we should be able to see a difference in diffusion between cyclodextrin with and without carborane.

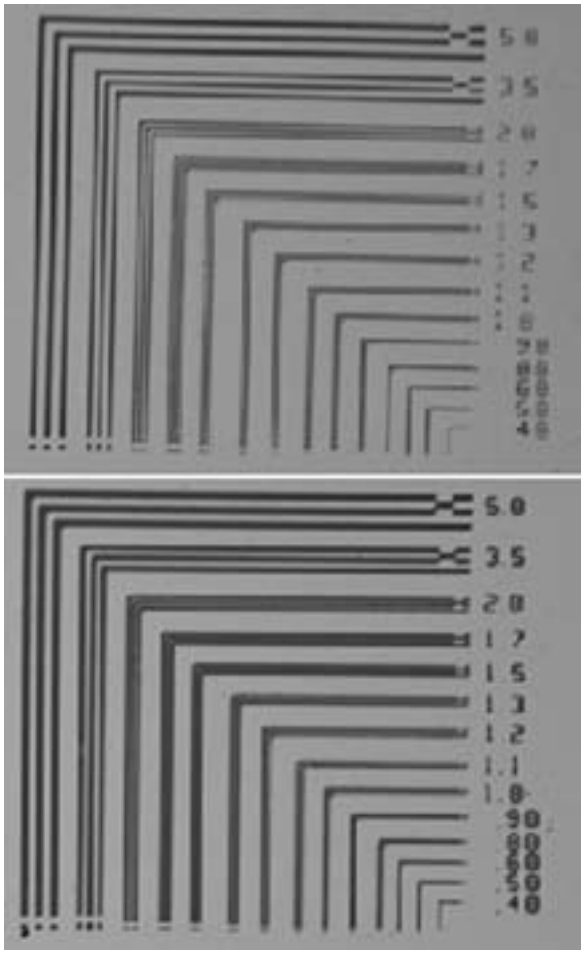

Figure 3: Diagram of bilayers.

Results:

Based on results obtained using the combinatorial technique, the optimal patterns for cyclodextrin without carborane (Figure 3, top) were observed at PAB of 109°C and PEB 99°C. The optimal patterns for cyclodextrin with carborane (Figure 3, bottom) were observed at a PAB of 107°C and a PEB of 99°C.

In order to obtain the data for the acid diffusion tests, we subtracted the resist thickness with PAG (no bilayer) from the resist thickness after development. We ran the experiment with the first batch of cyclodextrin, but the results were inconclusive. The second batch of cyclodextrin was more consistent and we can definitively say that the diffusion of acid is greater in the carborane complex than without carborane (Figure 4). Even when the swelling from development was taken into account, the data still showed that the acid diffusion was greater in the carborane complex.

Future Work:

Now that we have proven that acid diffusion is the cause of the patterns having greater line edge roughness, we can modify our cyclodextrin molecule to include PAG groups incorporated in the structure. This should decrease the acid diffusion so we can have a resist that is both etch resistant and produces high resolution patterns.

Acknowledgements:

I would like to thank Dr. Christopher Ober, Marie Krysak, Jing Sha, the Ober Research Group, Cornell NanoScale Science & Technology Facility staff, Melanie-Claire Mallison, and Lynn Rathbun for all their assistance with my project. I also would like to thank the NNIN Research Experience for Undergraduates Program and National Science Foundation for funding and the opportunity to do this research.

References:

[1] Ito, Hiroshi. Chemical Amplification Resists for Microlithography, Advanced Polymer Science (2005) 172: 37–245.

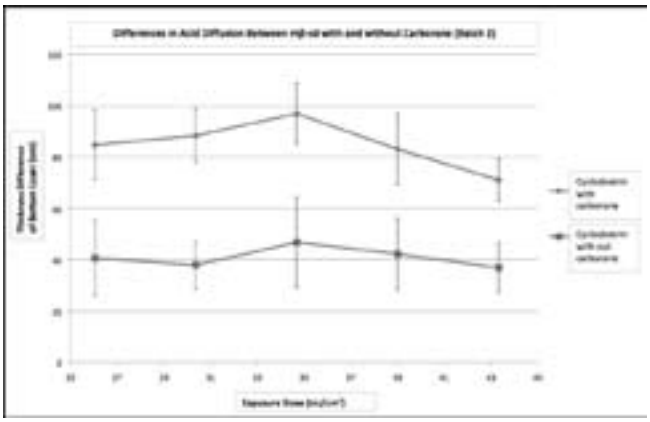

Figure 4: Batch 2 diffusion results.

Elemental Analysis of Ge-Si$_x$Ge$_{1-x}$ Core-Shell Nanowire Heterostructures

Arrielle Opotowsky

Physics and Astronomy, Louisiana State University

NNIN REU Site: Microelectronics Research Center, University of Texas, Austin, TX

NNIN REU Principal Investigator(s): Prof. Emanuel Tutuc, Electrical Engineering, University of Texas at Austin

NNIN REU Mentor(s): Kamran Varahramyan, Electrical Engineering, University of Texas at Austin

Contact: aopoto1@tigers.lsu.edu, etutuc@mer.utexas.edu

Abstract:

We investigate Ge-Si$_x$Ge$_{1-x}$ core-shell nanowire heterostructures, where the silicon germanium (Si$_x$Ge$_{1-x}$) shell is grown *in situ* on the Ge nanowire core using ultra-high-vacuum chemical vapor deposition. Transmission electron microscopy shows that the Si$_x$Ge$_{1-x}$ shell is single crystal and grows epitaxially on the Ge cores. To determine the shell thickness and elemental composition of these nanowire heterostructures, we employ energy dispersive x-ray spectroscopy and electron energy-loss spectroscopy. We show that by tuning the growth conditions, the shell thickness and the relative content of the Si$_x$Ge$_{1-x}$ shell can be controlled, enabling radial band engineering in these nanowire heterostructures.

Introduction:

Semiconductor nanowires are of interest for electronic, photonic, and sensing applications. Nanowire heterostructures are attractive building blocks for low-power, high-speed electronics, due to their reduced dimensionality and the ability to engineer their electronic properties. Here we study Ge-Si$_x$Ge$_{1-x}$ core-shell nanowire heterostructures, and characterized their dimensions and content in order to enable radial strain and band engineering in this system. The valence band of the Si$_x$Ge$_{1-x}$ shell lies below the valence band of the Ge core, which allows for the engineering of one-dimensional hole gases confined to the Ge core [1,2]. We employ high-resolution transmission electron microscopy (TEM) to analyze the crystal structure of the Ge-Si$_x$Ge$_{1-x}$ core-shell heterostructure, and energy dispersive x-ray spectroscopy (EDX) and electron energy-loss spectroscopy (EELS) to determine the elemental content [3,4].

Experimental Procedure:

The Ge-Si$_x$Ge$_{1-x}$ core-shell nanowires are grown using a combination of low pressure and ultra-high-vacuum (UHV) chemical vapor deposition (CVD). The Ge cores are grown via the vapor-liquid-solid (VLS) mechanism and using Au catalysts [5,6]. The Si$_x$Ge$_{1-x}$ shell is then grown epitaxially on the Ge core using UHVCVD techniques and with various molar ratios of SiH_4 and GeH_4 (Figure1) [5].

After growth the nanowires are harvested in an ethanol solution and deposited on a TEM copper grid. For analysis we use an FEI Tecnai TF20 microscope, equipped with high-angle annular dark field (HAADF) detectors and EDX and EELS spectrometers. The EDX and EELS data were collected using scanning TEM (STEM) linescans (Figure 2).

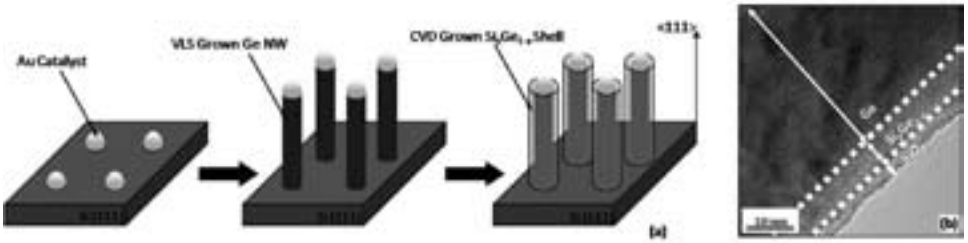

Figure 1: (a) Ge-Si$_x$Ge$_{1-x}$ nanowire core-shell growth. (b) Transmission electron micrograph of a Ge-Si$_x$Ge$_{1-x}$ core-shell heterostructure.

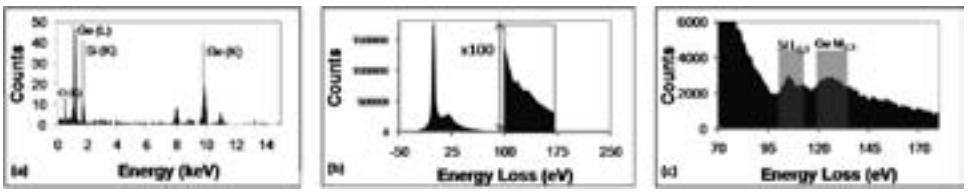

Figure 2: EDX/EELS point spectra (a) EDX spectrum showing the Si and Ge K-lines; (b) EEL-spectrum showing the zero-loss and plasmon peaks and the Si $L_{2,3}$/Ge $M_{2,3}$ edges; (c) The EEL-spectrum after background subtraction, showing the edges more clearly.

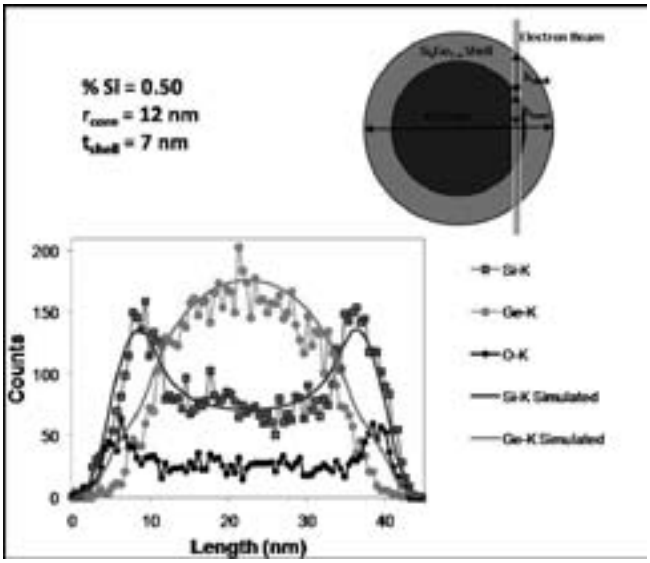

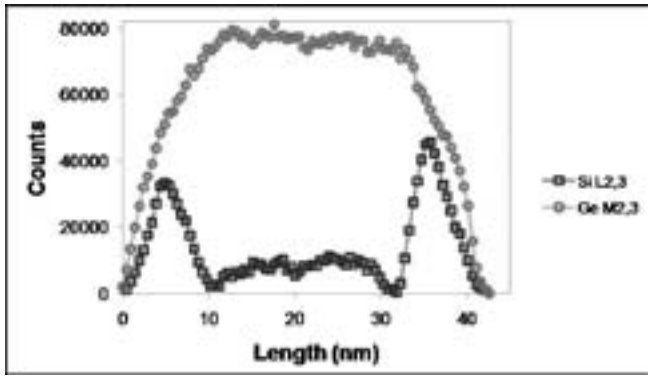

Figure 3, left: EDX linescan showing the Ge, Si, and O K-line counts as a function of beam position along nanowire cross-section. The inset diagram depicts the cross-section of the wire, and illustrates the electron beam's position along the linescan.

Figure 4, above: EELS linescan shows clear Si peaks in the shell, qualitatively consistent with the EDX data.

Results:

In order to analyze the EDX data, the Si and Ge concentrations are modeled as following: $\psi_{Si}(x) = 2X_{Si} \bullet h_{shell}(x)$ and $\psi_{Ge}(x) = 2X_{Ge} \bullet h_{shell}(x) + 2h_{core}(x)$. Here X_{Si} represents the percentage of Si in the shell, and $h_{shell}(x)$ the nanowire thickness spanned by the electron beam at position x. The concentrations are then convoluted with a Gaussian beam profile in order to compare with the measured EDX data [5].

The data of Figure 3 reveals the formation of a ~ 5 nm thick SiO_2 layer on the nanowire surface, which we associated with the O_2 plasma clean of the TEM sample. Interestingly, this causes the Ge atoms in the shell to move towards the core, a phenomenon known as Ge condensation [7]. This accumulation of Si atoms at the shell surface leads to larger and wider Si peaks than expected.

The EELS data shown in Figure 4 agrees qualitatively with the EDX data of Figure 3. However, we note the EELS analysis is sensitive to background subtraction, and the Ge $M_{2,3}$ edge is not suitable for core thickness measurements because of its weakness and proximity to the stronger Si $L_{2,3}$ edge [3].

Conclusions:

Transmission electron microscopy reveals single crystal Si_xGe_{1-x} shells epitaxially grown on the Ge cores. The EDX data allows a quantitative determination of the Si_xGe_{1-x} shell content and shell thickness. The EELS elemental analysis data is qualitatively consistent with EDX, and reveals the core-shell boundary more clearly.

Acknowledgements:

This work has been supported by the National Science Foundation and National Nanotechnology Infrastructure Network Research Experience for Undergraduates (NNIN REU) Program. Thanks to The University of Texas at Austin Microelectronics Research Center for hosting me. Jean Toll provided much assistance here. Kamran Varahramyan and Dr. Domingo Ferrer were wonderful mentors. Prof. Emanuel Tutuc and Prof. Sanjay Banerjee provided me with an amazing educational experience.

References:

[1] K. M. Varahramyan, D. Ferrer, E. Tutuc, & S. K. Banerjee, Band Engineered Epitaxial Ge-Si_xGe_{1-x} Core-Shell Nanowire Heterostructures. Applied Physics Letters. 95, 1. (2009).

[2] W. Lu, J. Xiang, B. P. Timko, Y. Wu, & C. M. Lieber, One-Dimensional Hole Gas in Germanium/Silicon Nanowire Heterostructures. Proc. Natl. Acad. Sci. U.S.A. 102, 10046 (2005).

[3] Ahn, C. C. & O. L. Krivanek, EELS Atlas: A reference guide of all electron energy loss spectra covering all stable elements. Arizona State University and Gatan, Inc.

[4] J. J. Hren, J. I. Goldstein, & D. C. Joy, Introduction to Analytical Electron Microscopy. 1979, New York: Plenum Press. p. 223-302.

[5] Kamran M. Varahramyan, Chemical Vapor Deposition Growth of Silicon and Germanium Nanowires, and Nanowire Heterostructures. MA Thesis, University of Texas at Austin. (2008).

[6] R. S. Wagner & W.C. Ellis, Vapor-Liquid-Solid Mechanism of Single Crystal Growth. Applied Physics Letters. 4(5): p. 89-90 (1964).

[7] F. K. LeGoues, R. Rosenberg, T. Nguyen, F. Himpsel, & B. S. Meyerson. Oxidation studies of Ge. Journal of Applied Physics. 65, 4 (1989).

Visible Optical Properties of Pulse-Laser-Melted Silicon with S, Se, Te, B, P and As

Si Hui Athena Pan

Martin A. Fisher School of Physics, Brandeis University

NNIN REU Site: Center for Nanoscale Systems, Harvard University, Cambridge, MA

NNIN REU Principal Investigator(s): Michael Aziz, School of Engineering and Applied Sciences, Harvard University

NNIN REU Mentor(s): Daniel Recht, School of Engineering and Applied Sciences, Harvard University

Contact: fromaspan@gmail.com, aziz@seas.harvard.edu, drecht@fas.harvard.edu

Introduction:

Recent research has demonstrated that laser-structured chalcogen-laden silicon (Si) exhibits enhanced electro-optical properties when compared with ordinary Si [1-3]. On the other hand, unstructured Si is more desirable for a wide variety of device architectures. Ion implantation followed by pulsed-laser-melting-induced rapid solidification provides a method to fabricate chalcogen-laden Si with a smooth surface and crystalline interior structure [4,5]. Sulfur-laden Si, fabricated through ion implantation and pulsed-laser-melting, has been shown to absorb light strongly in the near infrared region [5]. Until this work, the properties of laser-melted, chalcogen-laden Si in the visible spectrum have not been characterized. Furthermore, little has been done to compare these materials with Si supersaturated with common dopants such as boron. Here we present the preliminary results on the visible optical properties of pulse-laser-melted Si implanted with sulfur, selenium, tellurium, boron, arsenic and phosphorus (S, Se, Te, B, As and P, respectively).

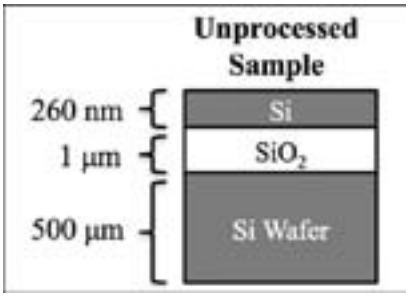

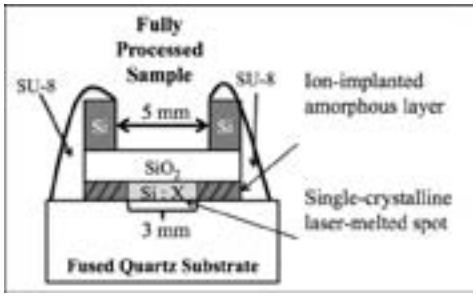

Figure 1, left: The schematic of the original SOI wafer.
Figure 2, right: The schematic of a completed processed sample.

Experimental Techniques:

Silicon on insulator (SOI) with dimensions shown in Figure 1 was used in this experiment. The 260 nm layer of p-Si(100) was ion implanted at room temperature with either $^{32}S^+$ at 80 keV, $^{80}Se^+$ at 125 keV, $^{130}Te^+$ at 120 keV, $^{11}B^+$ at 35 keV, $^{75}As^+$ at 110 keV or $^{31}P^+$ at 65 keV. Samples to be implanted at 1×10^{14} and 1×10^{15} S^+/cm^2 were first implanted with 3×10^{15} atom/cm^2 Si at 70 keV to produce a uniform amorphous layer.

The implantation dose ranged from 1×10^{14} to 3×10^{16} ions/cm^2. The ion-implanted samples were melted via irradiation with a pulsed $XeCl^+$ excimer laser (308 nm, 25 ns FWHM and 50 ns total duration) with a spatially homogenized beam. The laser fluence was controlled to be around 0.6~0.7 J/cm^2, which was chosen to melt to a depth between 210 and 250 nm. Time-resolved reflectivity of a low-power Ar^+ ion laser (488 nm) was used to monitor the melt duration [6].

After melting, the molten layer re-solidifies as a single crystal within a few nanoseconds so that a large amount of impurity atoms remain trapped within the alloy. The concentrations of implanted impurities were typically 2~4 orders of magnitude higher than equilibrium solubility [7]. Electron backscattering diffraction on a scanning electron microscope was conducted to confirm the single-crystal nature of the laser-melted layer of each sample.

In order to measure the visible optical properties of the ion-implanted layer, the bottom layer of plain Si (500 μm thick) must be removed. We polished this layer down to roughly 200 μm. The polished sample was then mounted onto a fused quartz substrate with SU-8 photoresist. The rest of the plain Si layer was removed by inductively-coupled plasma reactive ion etching. The schematic of a fully processed sample is shown in Figure 2.

We measured the transmittance of each sample with a Hitachi U-4001 spectrophotometer. A reflectance free method from Swanepoel was adopted to calculate the optical constants from transmittance only [8]. This method exploits the dependency of thin film interference fringes on the real (n) and imaginary (k) refractive indices. Such dependency allows the determination of n, k and the absorption coefficient α ($\alpha = 4\pi k/\lambda$), by simply interpolating smooth curves along the maxima and the minima of the fringes [8].

Results and Discussion:

Table 1 shows the real refractive indices n and the absorption coefficients α at 700 nm of samples implanted with different elements to different doses. All implanted samples have

refractive indices smaller than ordinary Si. The α of a low dose (1×10^{15} ions/cm^2) sulfur-implanted sample exhibits little difference from ordinary Si. However, the α of a high dose (1×10^{16} ions/cm^2) sulfur-implanted sample is increased by approximately 400% compared to ordinary Si at 700 nm. Figure 3 illustrates the α(λ) curves of both pure Si [9] and S-implanted Si at 1×10^{16} ions/cm^2 from 500 nm to 1.2 μm, which again shows the significant in-crease in absorption coefficient of the S-implanted sample.

Similarly, low dose selenium-implanted samples (1×10^{14} and 1×10^{15} ions/cm^2) exhibit only a small increase in the α compared to ordinary Si, while the difference in the α becomes more significant for high implantation doses. In particular, the absorption coefficient increases with the implantation dose. For the 3×10^{16} ion/cm^2 Se-implanted sample, α is an order of magnitude higher than that of ordinary Si.

Only high dose (1×10^{16} ion/cm^2) samples were processed and measured for Si supersaturated with Te, P, As and B. As shown in Table 1, high dose Te-implanted Si also possesses a much higher α than ordinary Si. Samples implanted with P, As and B also exhibit some increase in the α. However, such increase is relatively small compared to the three chalcogen elements investigated.

Comparing only the samples with an implantation dose of 1×10^{16} ion/cm^2, Se-implanted Si exhibits highest absorption among all elements, which is followed by S-implanted Si and Te-implanted Si. These preliminary results demonstrate chalcogen-laden Si absorbs visible light much more strongly than ordinary Si. The absorption mechanism is unknown, but hypotheses exist about the formation of an impurity band and about the formation of dopant nano-clusters. Potential applications of these strong-light-absorbing materials include the fabrication of low-cost photodetectors and photovoltaics since a thinner (and thus cheaper) layer could absorb all of the relevant light. Opto-electronic conversion for photodetectors has been demonstrated for laser-structured chalcogen-laden Si, but not yet in other settings.

Acknowledgements:

I would like to offer sincere thanks to my mentor, Daniel Recht, my P. I., Michael Aziz, and the rest of the Aziz group for their guidance and support, to the NNIN REU Program for providing me with this opportunity and to the NSF for funding this project.

References:

[1] C. Wu, C. H. Crouch, L. Zhao, J. E. Carey, R. Younkin, J. A. Levinson, E. Mazur, R.M. Farrell, P. Gothoskar, and A. Karger, Appl. Phs. Lett. 78, 1850 (2001).

[2] C. H. Crouch, J. E. Carey, J. M. Warrender, E. Mazur, M. J. Aziz, and F. Genin, Appl. Phys. Lett. 84, 1850 (2004).

[3] J. E. Carey, C. H. Crouch, M. A. Sheehy, M. Shen, C. M. Friend, and E. Mazur, Opt.Lett. 30, 1773 (2005).

[4] M. Tabbal, T. Kim, J. M. Warrender, M. J. Aziz, B. L. Cardozo, R. S. Goldman, J.Vac. Sci. Technol. B 25(6), 1847 (2007).

[5] T. G. Kim, J. M. Warrender, M. J. Aziz, Appl. Phys. Lett., 88, 241902 (2006).

[6] R. Reitano, P. M. Smith, and M. J. Aziz, J. Appl. Phys. 76, 1518 (1994).

[7] R. G. Wilson, J. Appl. Phys. 55, 3490 (1984).

[8] R. Swanepoel, J. Phys. E: Sci. Instrum. 16, 1214 (1983).

[9] R. Hull, Properties of crystalline silicon (IET, London, UK, 1999).

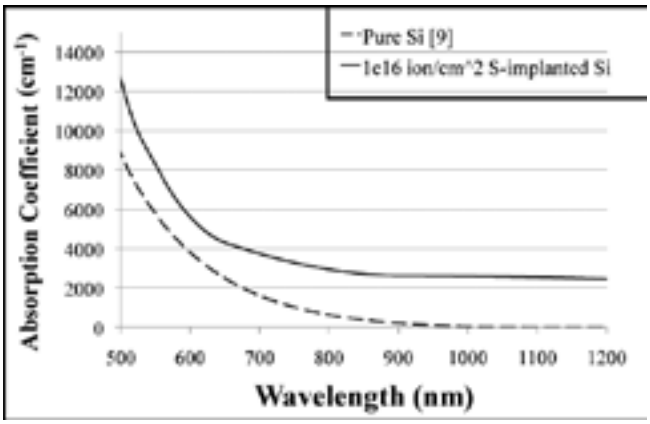

Figure 3, above: The α(λ) curves of pure silicon and 1×10^{16} ions/cm^2 S-implanted silicon.

Table 1, below: Refractive index and absorption coefficient at α = 700 nm.

Implanted Element	Implantation Dose (ions/cm^2)	Refractive Index	Absorption Coefficient (cm^{-1})	% Difference from Ordinary Si
Ordinary Si	—	3.769	1560	—
Sulfur	1×10^{15} ion/cm^2 ~ 0.08 at. %	3.045	1688	~ 8%
	1×10^{16} ion/cm^2 ~ 0.8 at. %	2.775	7440	~ 400%
Selenium	1×10^{14} ion/cm^2 ~ 0.008 at. %	3.017	2687	~ 70%
	1×10^{15} ion/cm^2 ~ 0.08 at. %	3.094	2814	~ 80%
	1×10^{16} ion/cm^2 ~ 0.8 at. %	2.969	9692	~ 500%
	3×10^{16} ion/cm^2 ~ 2.3 at. %	2.758	15775	~ 1000%
Tellurium	1×10^{16} ion/cm^2 ~ 0.8 at. %	3.17	7029	~ 400%
Phosphorous	1×10^{16} ion/cm^2 ~ 0.8 at. %	3.055	5088	~ 200%
Arsenic	1×10^{16} ion/cm^2 ~ 0.8 at. %	3.255	3440	~ 100%
Boron	1×10^{16} ion/cm^2 ~ 0.8 at. %	3.383	2583	~ 70%

Synthesis and Properties of Manganese Oxide Nanoparticles for Environmental Applications

Alexandra Rutz

Chemistry and Molecular & Cellular Biology, University of Illinois Urbana-Champaign

NNIN REU Site: Nano Research Facility, Washington University in St. Louis, St. Louis, MO

NNIN REU Principal Investigator and Mentor: Young-Shin Jun, Energy, Environmental, and Chemical Engineering, Washington University in St. Louis

Contact: arutz2@illinois.edu, ysjun@seas.wustl.edu

Abstract and Introduction:

Manganese oxide nanoparticles (MnO_2 NPs) can be utilized for advanced materials in batteries, as well as other applications, such as water treatment and imaging contrast agents [1]. To have more efficient performance, these materials need particles of defined size, while remaining benign to the environment. In this work, we synthesized NPs with a biomineralization approach and investigated antimicrobial effects. MnO_2 NPs were synthesized using the iron storage protein ferritin that provides an 8 nm cavity in which these particles form.

We compared the sizes and morphologies of biomimetically synthesized NPs to those from inorganic synthesis using dynamic light scattering (DLS), transmission electron microscopy (TEM), high resolution TEM (HR-TEM), and atomic force microscopy (AFM). DLS showed sizes of particle aggregates as a function of reaction time. Electron diffraction patterns were collected by HR-TEM to identify the phase of NPs and determine particle size. AFM was used to investigate morphologies and sizes of the particles. To study antimicrobial effects of both synthetic methods, *Shewanella* was studied while in solution with MnO_2 NPs. Our findings from this work will provide fundamental information of the potential toxicities of NPs generated by different pathways.

Materials and Methods:

To synthesize MnO_2 NPs biomimetically, apoferritin and manganese (II) tetrahydrate were added to doubly filtered deionized water. The pH of the reaction volume was brought to 9 with sodium hydroxide, and the reaction was rotated in a test tube for six hours. The inorganic synthesis was prepared in the same manner but without the protein. To investigate particle morphologies, TEM imaging was performed using a FEI Tecnai G^2 Spirit microscope. Samples were prepared by drying the reaction mixture on carbon-coated Formvar-covered copper TEM grids. HR-TEM imaging was performed on JEOL JEM-2100F with imaging using Gatan Orius SD1000B camera to determine particle size and phase by calculating d-spacing. To determine hydrodynamic particle size, DLS data was taken over time during the synthesis incubation using Malvern 1011155 Zetasizer Nanoseries. The particle morphology, before and after trypsin treatment, was examined by AFM with a Veeco Nanoscope microscope.

The protein layer was digested by adding trypsin 1:20 (w:w) to the reaction volume and was incubated for fifteen minutes. To study antimicrobial effects of NPs from different syntheses, manganese oxides at concentrations of 100 μg/mL, 20 μg/mL and 2 μg/mL were incubated in MR-1 media

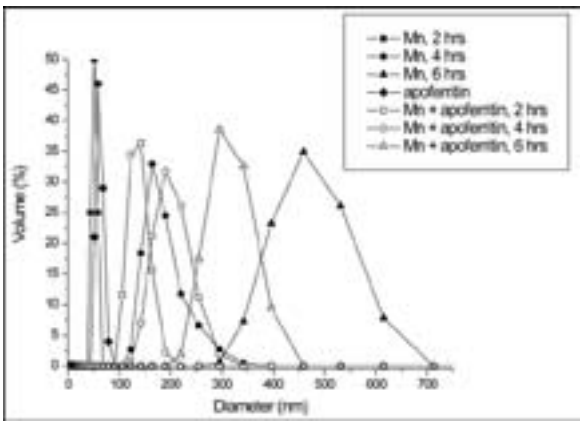

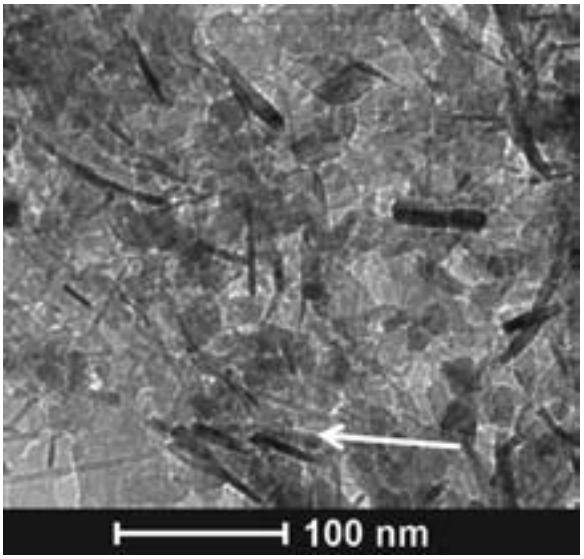

Figure 1, left: DLS data of inorganic synthesis as labeled "Mn" and biomimetic synthesis as labeled "Mn+apoferritin" with the corresponding incubation times. Figure 2, above: TEM image of inorganic synthesis displaying crystalline nanorods of various sizes.

with *Shewanella oneidensis* MR-1 at 32°C. Bacteria was added until the media had an optical density of 0.2 A at 600 nm. Optical density measurements were taken over 24 hours on ThermoScientific Genesys UV spectrophotometer.

Results and Discussion:

DLS data indicated particles measured were of aggregate size, not individual particle size. The gradual increase of size during the reaction showed aggregation as a function of time. At final incubation time, the biomimetic synthesis yielded smaller particle aggregates than the inorganic synthesis. This trend can be explained by the amount of available aqueous manganese ions in solution for nanoparticle formation.

Crystalline nanorods of various sizes in the inorganic synthesis were observed by TEM while few nanorods and spherical nanoparticles were found in the biomimetic synthesis. Particle size of 7-8 nm was verified by HR-TEM and was consistent with the limits of the protein cavity. The particles showed lattice fringes indicating crystalline material while previous work reported amorphous particles [2]. The d-spacing was calculated to be 3.407 Å corresponding to manganite. Unlike our synthesis, previous work used buffer at pH 9 as the reaction volume. The contribution of the buffer to the crystallinity of MnO_2 needs to be investigated further. Using AFM, we concluded trypsin removed the protein layer. The data of the biomimetic synthesis demonstrated peaks with particle height of 12 nm corresponding to protein and larger heights indicating protein aggregates. Digestion of biomimetic synthesis displayed height peaks at 8 nm indicating manganese oxide nanoparticles without the protein shell.

Antimicrobial studies on *Shewanella* were performed using particles of the biomimetic synthesis with and without the protein layer. The inorganic synthesis was also studied using incubation times of one and six hours. The bacteria exposed to particles of both synthetic methods showed minor inhibition in the lag and log phases of the growth curve, but recovered from the stress in the stable phase. In the log phase at eight hours, the inorganic synthesis showed greater inhibition than the biomimetic synthesis.

Conclusion:

Biomimetic manganese oxides were successfully synthesized from the adopted synthetic method [2]. TEM images indicated the nanoparticles formed within protein shells. We determined the sizes of hydrodynamic and individual nanoparticles by DLS and HR-TEM respectively. The particle morphologies were probed with AFM before and after protein digestion confirming the protein layer was removed from the nanoparticles. Antimicrobial studies of both the biomimetic and inorganic synthesis with respect to *Shewanella* indicated only minor inhibition in the lag and log phases of the growth curve.

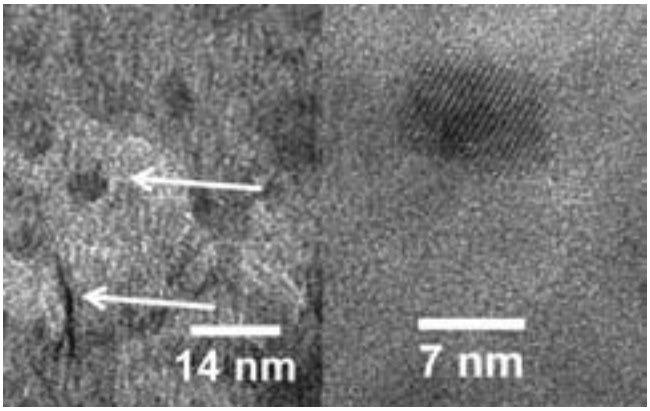

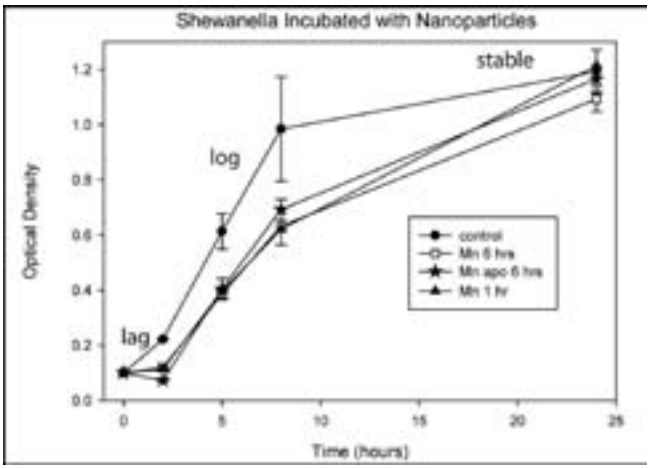

Figure 3, top: HR-TEM images from biomimetic synthesis showing crystalline nanorods and nanoparticles within protein layer.

Figure 4, bottom: Antimicrobial studies of Shewanella measured by optical densities taken over 24 hours.

Our findings report MnO_2 NPs synthesized from a controlled biomimetic method show promise for use in advanced materials that are friendly to the environment.

Acknowledgments:

I would like to thank my Principal Investigator, Dr. Young-Shin Jun, as well as the Jun Group, Kristy Wendt, Amy Sears, Dr. Dong Qin, Dr. Yinjie Tang, and Dr. Bing Wu. I would also like to thank the National Nanotechnology Infrastructure Network Research Experiences for Undergraduates Program and the National Science Foundation for their efforts and support.

References:

[1] Chen, H, et. al; "Facile Synthesis of Monodisperse Manganese Oxide Nanostructures and Their Application in Water Treatment"; J. Phys. Chem., 112, 17540–17545 (2008).

[2] Meldrum, F, et. al; "Synthesis of inorganic nanomaterials in supramolecular protein cages"; Nature, 349, 684-687 (1991).

Large-Area Chemical Vapor Deposition of Graphene over Thin Films of Cobalt

Devanand Sukhdeo

Electrical Engineering, Columbia University

NNIN REU Site: Microelectronics Research Center, University of Texas, Austin, TX

NNIN REU Principal Investigator(s): Dr. Sanjay Banerjee, Electrical Engineering, The University of Texas at Austin

NNIN REU Mentor(s): Shagandeep Kaur, Electrical Engineering, The University of Texas at Austin

Contact: dss2129@columbia.edu, banerjee@ece.utexas.edu, skaur@mail.utexas.edu

Abstract:

The synthesis of graphene over thin films of cobalt was demonstrated by chemical vapor deposition, using methane as a precursor. At sufficiently high temperatures, decomposition of methane led to dissolution of carbon in the cobalt film. Upon subsequent cooling of the metal film to room temperature, the solubility of carbon in cobalt is reduced, leading to segregation of some carbon atoms to the surface in the form of graphene. Subsequently, etching away the underlying cobalt made it possible to transfer the graphene film to arbitrary substrates, including insulator substrates such as silicon dioxide. Further analysis of the graphene films revealed that they generally consisted of a large continuous region of thin few-layer graphene, with many patches of thicker multi-layer graphene present throughout the film. Raman spectroscopy confirmed the presence of single-layer regions, as well as the presence of defects pervasive throughout the films.

Introduction:

Graphene, first identified in 2004, is a one-atom thick sheet of carbon atoms, wherein the carbon atoms are arranged in a 2-dimensional hexagonal lattice. The common material graphite can be viewed as a large number of graphene sheets stacked together.

Single-layer graphene has many favorable electronic properties, such as a high electron mobility, that may lead to transistors that operate much faster than conventional silicon devices. However, these properties are substantially degraded when graphene is present in multiple layers.

Unfortunately, it is very difficult to produce large, continuous layers of single-layer or even few-layer graphene. Most graphene used in research is obtained by "mechanical exfoliation," a process that is inefficient, labor-intensive, and non-scalable. For this project, we sought to develop a practical method to synthesize large graphene films using chemical vapor deposition.

Experimental Procedure:

For this project, we began by depositing a 100 nm film of polycrystalline cobalt on a silicon dioxide substrate using electron-beam evaporation. We then exposed this cobalt to methane and hydrogen at approximately 850°C for a few seconds. Methane molecules (CH_4) were adsorbed at the cobalt surface and hydrogen was then desorbed from the surface, leaving the remaining carbon atoms to dissolve in the cobalt film. The methane had thus decomposed into carbon and hydrogen according to the reaction:

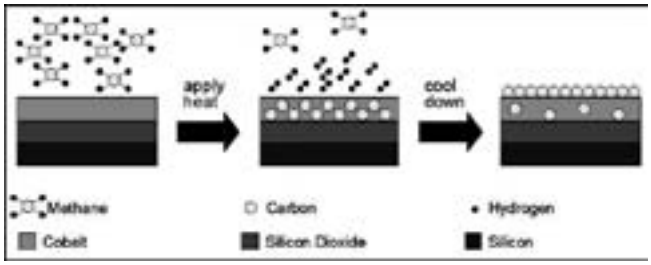

Figure 1: Graphene synthesis mechanism.

$$CH_4 \rightarrow C + 2H_2$$

Any amorphous carbon on the surface was etched away by the high-temperature hydrogen gas. Afterwards, as the cobalt cools to room temperature, the solubility of carbon in the cobalt decreases. This causes some of the dissolved carbon to segregate out to the surface, forming a continuous film of graphene, as shown in Figure 1.

The cobalt was subsequently etched away, and the graphene was transferred to a new silicon dioxide substrate. Further analysis was then performed using optical microscopy, scanning electron microscopy, atomic force microscopy, and Raman spectroscopy.

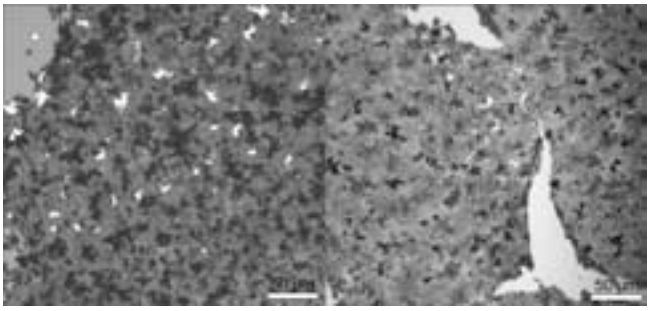

Figure 2: Optical comparison of nickel-grown graphene (left) and cobalt-grown graphene (right). Bright white indicates the thickest, most undesirable graphitic regions. All scale bars 50 µm.

Results and Conclusions:

Researchers have already successfully grown graphene over thin films of nickel [1]. We therefore began by growing graphene both over nickel and over cobalt, and compared the results as shown in Figure 2. From this comparison, we found that using cobalt instead of nickel virtually eliminated the thickest, most undesirable regions.

Ultimately, we found that drastically shorter growth processes, on the order of minutes instead of hours, yielded significantly better results, as shown in Figure 3. Unfortunately, thicker patches were still present throughout, which we believed to be due to the polycrystalline nature of the original cobalt surface. Scanning electron microscopy revealed microscopic cracks in the graphene, while atomic force microscopy revealed small growths over the graphene.

We also analyzed our films using Raman spectroscopy over a region that we thought might be single-layer graphene, with the Raman spectrum shown in Figure 4. The relative strength of the 2D peak (~ 2700 cm^{-1}) to the G peak (~ 1581 cm^{-1}) suggests the presence of single-layer or bilayer graphene. Further analysis of the 2D peak revealed that it could be fit to a single Lorentzian curve, which strongly suggests the presence of single-layer graphene. However, the strength of the D peak (~ 1350 cm^{-1}) indicates a substantial presence of microscopic defects throughout our film. This is in addition to the thicker multilayer patches previously mentioned.

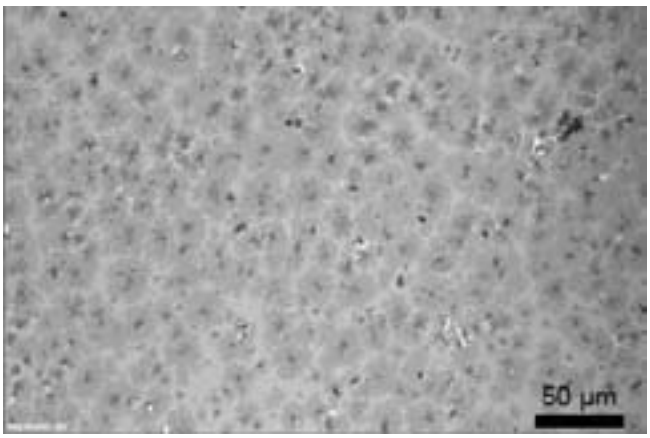

Future Work:

Most crucially, the electronic properties of these films must be measured by fabricating devices. As well, continued Raman studies may allow us to estimate what percentage of the total graphene films is single-layer, bilayer, multilayer, etc. Furthermore, since Raman spectroscopy indicates a strong presence of defects, the source of these defects must be determined so as to minimize them. It is likely that these defects arise during the transfer process, however this is not yet confirmed.

Acknowledgements:

I would like to thank my principal investigator, Dr. Sanjay Banerjee, and my mentor, Ms. Shagandeep Kaur, of the University of Texas at Austin for their guidance and assistance throughout this project. I also wish to acknowledge the contributions of Nicholas Angelou and Michael Ramon, as well as fruitful discussions with Seyoung Kim, Christopher Corbet, Micah Points, and Sayan Saha, all of the University of Texas at Austin. I also wish to thank Ms. Jean Toll for her administrative assistance. I would also like to thank the National Science Foundation and the National Nanotechnology Infrastructure Network Research Experience for Undergraduates (NNIN REU) Program for funding this project.

References:

[1] Alfonso Reina et.al., "Large Area, Few-Layer Graphene Films on Arbitrary Substrates by Chemical Vapor Deposition", Nano Letters 2009 9 (1), 30-35.

[2] D. Graf et.al., "Spatially Resolved Raman Spectroscopy of Single-and Few-Layer Graphene", Nano Letters 2007 7 (2), 238-242.

[3] Xuesong Li et.al., "Large-Area Synthesis of High-Quality and Uniform Graphene Films on Copper Foils", Science [DOI: 10.1126/science.1171245], 7 May 2009.

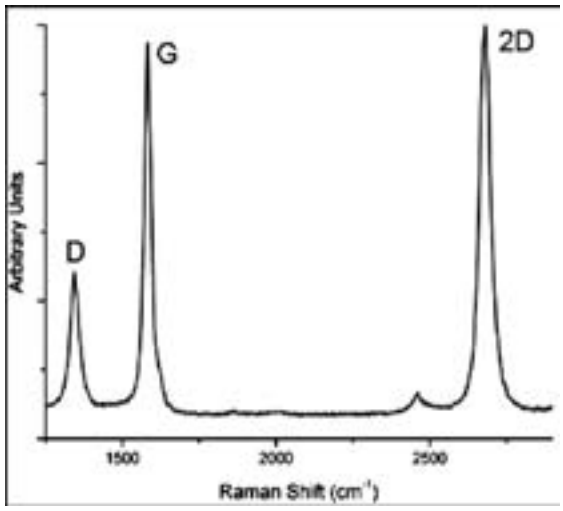

Figure 3, left: Graphene synthesized after shortening the growth process. Note the greater uniformity of the film compared to those shown in Fig. 2.

Figure 4, above: Raman spectrum of a region of monolayer graphene.

Fabricating Mechanically Adjustable Single Molecule Electrical Contacts

Matthew T. Hershberger

Physics, Bethel College, Kansas

NNIN REU Site: Colorado Nanofabrication Laboratory, University of Colorado, Boulder, CO
NNIN REU Principal Investigator(s): Professor Charles Rogers, Physics, University of Colorado at Boulder
NNIN REU Mentor(s): Jason Gray, Department of Physics, University of Colorado at Boulder
Contact: matthewher@bethelks.edu, charles.rogers@colorado.edu, jason.gray@colorado.edu

Abstract:

We investigated the fabrication parameters for mechanically-adjustable break junctions on a phosphor bronze substrate. Mechanically-adjustable break junctions have applications in studying the electron transport of molecules, which could lead to molecule sized circuit components. We have fabricated bridge structures that can be used to form break junctions, were able to measure stable resistances while bending the substrate, and have broken apart and reconnected the break junctions.

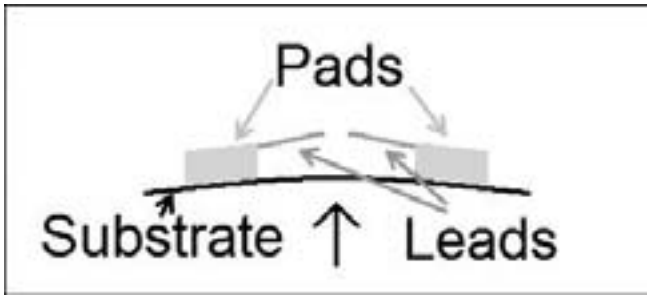

Figure 1: Diagram of break junction.

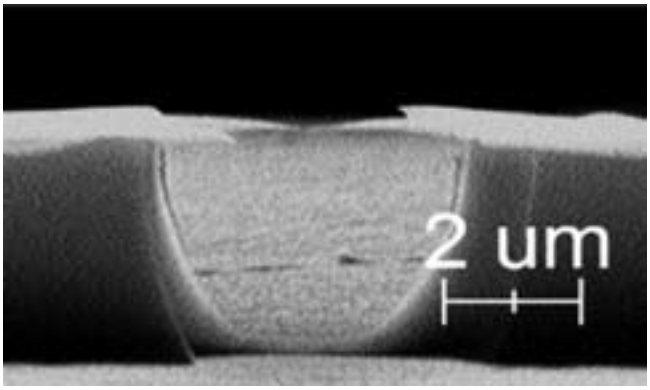

Figure 2: SEM image of bridge (side).

Introduction:

Transistors are approaching a size where it is difficult to make them perform uniformly. Making transistors and other circuit components out of molecules would allow smaller, uniform components, but the electrical properties of the molecules would need to be known. There are many techniques using nanolithography and scanning probe instruments to study the electrical properties of single molecules. Scanning probe instruments are used to take measurements of molecules in solution, but are limited to a temperature range of tens of degrees. Mechanically-adjustable break junctions can be operated at cryogenic temperatures in a vacuum environment [1]. A break junction is formed by pushing up on the substrate, which stretches the bridge until it breaks, forming two leads. Figure 1 shows a schematic diagram of a break junction. Figure 2 shows one of the fabricated bridges from the side in a scanning electron microscope (SEM). The electrical properties of a molecule are examined by trapping a molecule between the leads of the break junction in a known orientation and measuring its resistance.

Ideally, a break junction can be broken and reconnected repeatedly so multiple trials can be run using one device. Our project focused on the fabrication of mechanically-adjustable single molecule break junctions.

Procedure:

The 510 phosphor bronze substrate was polished with 3 μm alumina oxide then diced into a three inch circular wafer with a machine shop shear. The wafer was covered by a layer of MicroSystem's VM652 adhesion promoter then PI2611 polyimide spun at 3,000 rpm. The wafer was raised from room temperature to 310°C over 25 minutes, baked at 310-318°C in air, then allowed to cool with the hot plate for 35 minutes. The photolithography pattern used Futurrex NR7-1500PY resist and had 10 nm of chromium deposited at 2.0 Å per second (Å/s) followed by 80 nm of gold deposited at 5.0 to 6.0 Å/s in a thermal evaporator.

We used a bilayer electron beam resist of MircoChem's MMA 8.5 MAA-EL9 Copolymer, then 950 PMMA-A4; both spun at 3,000 rpm to develop a large undercut. The resist was developed with methyl isobutyl ketone diluted 1:3 with

isopropyl alcohol for high resolution. The electron beam lithography pattern had 2.0 nm of chromium deposited at 1.5 Å/s and 80 nm of gold deposited at 5.0 to 6.0 Å/s in a thermal evaporator. The polyimide was etched from underneath the wire using a reactive ion etch.

Many recipes were examined, but the best etch investigated was 80 standard cubic centimeters (sccm) of O_2, 20 sccm CF_4, and 400 watts. The average etch rate for this recipe was 107 ± 15.8 nm per minute for depth and 35.6 ± 5.74 nm per minute for undercut, and the average pressure was 221 milliTorr. (Note: all ± values are sample standard deviations.)

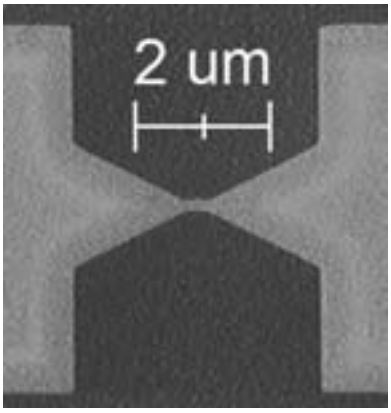

Figure 3: SEM image of bridge (overhead).

Figure 2 shows a bridge right after etching, from the side. Figure 3 shows a bridge from directly overhead. The white lines are the edge of the polyimide on the underside of the gold. The break junctions were formed by bending the substrate in a cryostat with fulcrums pushing down at the ends of the 2.5 cm by 1.0 cm wafer and a screw with a 250 μm pitch pushing from the opposite side.

Results and Conclusions:

The average bridge dimensions were 397 ± 90.2 nm long and 212 ± 64.3 nm wide with the smallest bridge by area being 281 nm long and 112 nm wide. The average resistance was 83.8 ± 7.0 ohms. We were able to load three chips into the cryostat. For each chip, we turned the cryostat screw a quarter turn every twenty seconds until the bridge broke. Due to undiagnosed internal noise, our recording setup would not read any resistances higher than 400,000 ohms, and once the impedance went above 100,000, we knew we had broken the bridge. The first chip we bent had this impedance spike, but did not reconnect as we moved the screw back. It was confirmed broken in the SEM.

The second chip we bent was broken and reconnected twice, then on the third bending, it stayed broken. Figure 4 shows the data from the second bending and reconnection of the second chip. Take note of the breaks in the graph where the data jumped and dropped from 100 ohms to over 100,000 ohms. The last chip bent was broken and did not reconnect as the screw was moved back.

We have concluded that it is possible to make the break junction structures, but several additional tests and adjustments need to be made, including: bending while cooled and under vacuum, automating the bending, refining the sensitivity of the setup to the gigaOhm range, and developing methods for isolating single molecules.

Acknowledgements:

I would like to thank Professor Charles Rogers, Jason Gray, the Roger's Group, Bart Van Zeghbroeck, Deborah Stratton, and David Alchenberger. All SEM pictures were taken in the JILA/NIST Keck Laboratory. Funding was provided by the University of Colorado, the National Nanotechnology Infrastructure Network Research Experience for Undergraduates Program, and the National Science Foundation.

References:

[1] Martin et. Al.; "Lithographic Mechanical Break Junction for Single-Molecule Measurements in Vacuum: Possibilities and Limitations"; New J. of Physics, 10 No. 6 (2008) <http://www.iop.org/EJ/njp>.

[2] Grüter et. Al.; "Electrical Conductance of Atomic Contacts in Liquid Environments."; Small, 1 No.11, 1067-1070 (2005).

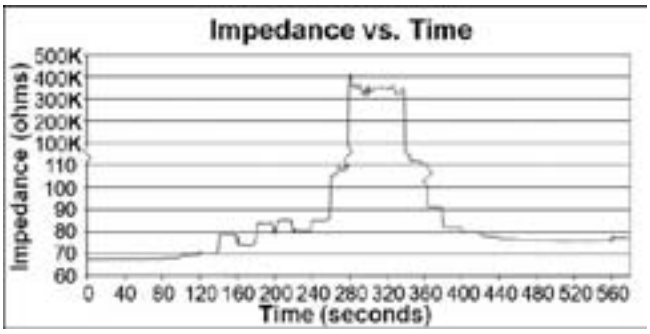

Figure 4: Data from reconnected break junction.

Horizontally Aligned Carbon Nanotube Composite Beams

Alexander Hryn

Materials Science and Engineering, University of Illinois at Urbana-Champaign

NNIN REU Site: Lurie Nanofabrication Facility, University of Michigan, Ann Arbor, MI
NNIN REU Principal Investigator(s): John Hart, Mechanical Engineering, University of Michigan at Ann Arbor
NNIN REU Mentor(s): Sameh Tawfick, Mechanical Engineering, University of Michigan at Ann Arbor
Contact: ahryn2@illinois.edu, ajohnh@umich.edu, stawfick@umich.edu

Abstract:

Microelectromechanical systems (MEMS) resonators have many applications in a variety of fields from biosensors, to radio frequency (RF) filters and transmitters. Materials suitable for nanostructured beams include metals, ceramics, aligned carbon nanotubes (CNTs), and CNT composites. It has been proposed that the high strength per low density of CNT composite beams could yield higher strengths and resonant frequencies. As an initial step toward this goal, this project focuses on creating micro-beams of horizontally aligned CNTs (HA-CNTs). This is achieved by growing vertically aligned CNTs and then, by mechanically rolling them, they adhere to the substrate and become horizontally aligned with ~ 25% packing density. Atomic layer deposition (ALD) of alumina then creates the matrix of the CNT composite material. We are able to control the CNT density and thickness of ALD coating, and future work will aim to control beam modulus and stiffness.

Introduction:

MEMS have many applications in a variety of fields from biosensors, to RF filters and transmitters. One of the most important components in a MEMS device and one of the most difficult to manufacture is a cantilever or suspended beam. The cantilever is used as a resonator that, depending on material properties, will respond to or create vibrations only at a specific frequency. Current MEMS devices make use of traditional beams composed of metal or ceramic. Others have shown that aligned carbon nanotubes (CNTs) [1], and CNT composites [2] can function as resonators.

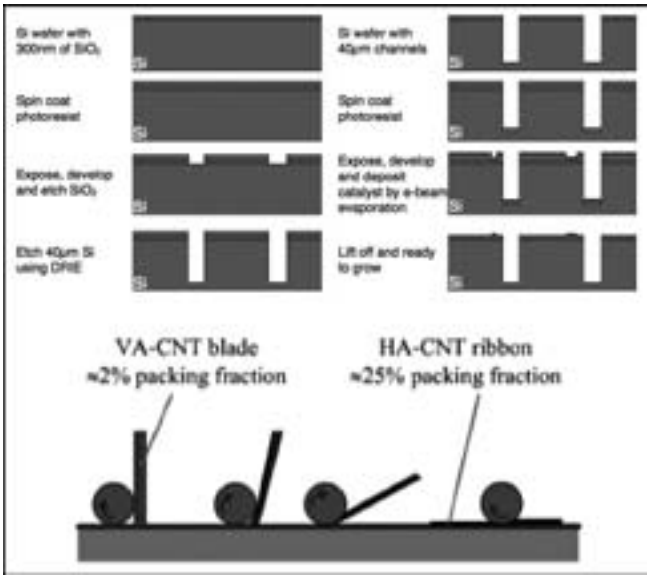

Figure 1: Processes for fabricating wafer and rolling VA-CNTs.

Experimental Procedure:

The fabrication process begins with a 4-inch silicon (Si) wafer coated with 300 nm of SiO_2 grown by thermal oxidation at 1100°C. Then, lithographic patterning was done twice on the wafer to make channels 200 to 1000 μm long and 5 to 50 μm wide, and CNT growth catalyst islands 100 to 900 μm long and 20 or 100 μm wide as shown in Figure 1. 10 nm aluminum oxide and 1 nm iron was the catalyst for CNT growth.

Once the substrate was fabricated, it was cut into 15 × 15 mm samples. CNTs were then grown in a tube furnace by first annealing the substrate in 100 sccm He and 400 sccm H2 at 775°C for 10 min. and then growing with 400 sccm He, 100 sccm H_2, and 100 sccm C_2H_4 at 775°C for 30 min. This process resulted in vertically aligned CNTs (VA-CNTs) characterized by their low areal density (2.5×10^{10} CNTs/cm^2) and the presence of entanglement along their length (Figure 2).

CNTs were then rolled [3] onto the substrate, forming horizontally aligned CNT (HA-CNT) beams (Figure 1), increasing their density and preparing them for mechanical beam characterization. When grown on substrates with etched channels, they were rolled over the channels forming suspended HA-CNT beams. The length and width of the beams corresponded to the dimensions of the catalyst island, and the channels defined the beam span. This device design allowed for beams with thicknesses below 1 μm, depending on the width of the VA-CNT bundles.

Material Characterization:

ALD can be used to create composite CNT beams by growing the deposited material via gas precursors from the CNTs at

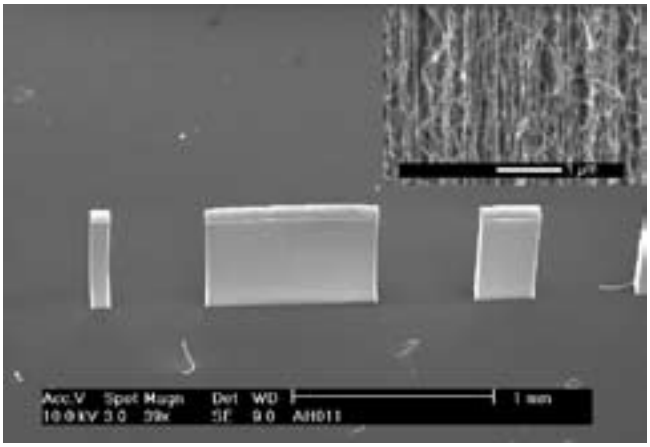

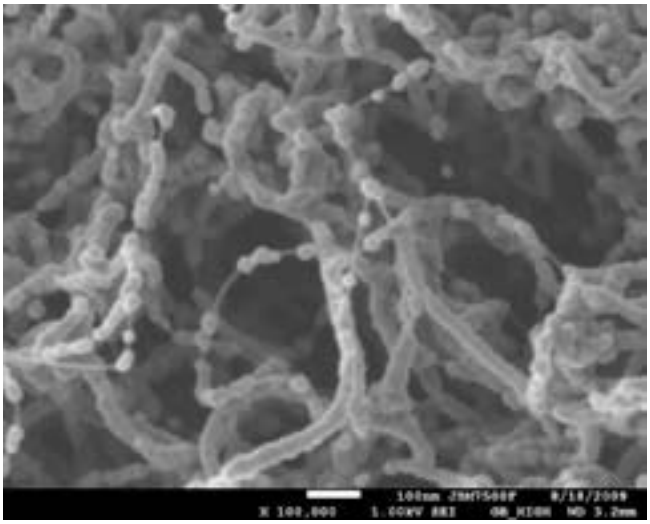

Figure 2, top: HA-CNT pattern with close up of CNTs.

Figure 3, bottom: Al2O3 coated CNTs by ALD.

variable thicknesses. The resulting matrix is expected to have higher strength based on the volume fraction of CNTs in the composite. A major challenge with designing ALD-coated CNT assemblies is penetration depth of the gases, which would yield a uniform coating throughout the CNT bundles.

Depth of aluminum oxide coatings on the nanotube beams was characterized with thermogravimetric analysis (TGA). A series VA-CNTs were grown in patterns of pillars with diameters ranging from 30 μm to 600 μm. These CNT samples were coated with alumina by 100 ALD cycles of trimethylaluminum and H2O at 250°C. These samples were then analyzed with TGA to determine the penetration depth of the alumina coating.

Results and Conclusions:

VA-CNTs were successfully grown on substrates that had been fabricated with the channels and rolled to form suspended HA-CNTs. The alumina coating of the CNT bundles was characterized using TGA, for pillars with diameters of 30 μm and 600 μm. The results of TGA (Figure 4) show clearly that at around 700°C, the CNTs burn away, decreasing the mass of the sample. Based on the CNT aerial density (2.5×10^{10} CNTs/cm^2), the diameter of CNTs (12-15 nm), and the thickness of the alumina coating (~ 12 nm); an ideal, fully coated sample of CNTs would have ~ 83% mass remaining after the CNTs burned away. Based on this, the 30 μm pillars seemed to be fully coated while the 600 μm pillars were not. Assuming that CNTs were either fully coated or not coated at all, it can be estimated that the ALD gasses penetrated ~200 μm into the 600 μm pillars.

Future Work:

Further characterization of the ALD coating needs to be done to determine the maximum size of a fully coated CNT buddle. Also, the suspended CNTs must be tested for strength and stiffness. Experiments can also be done to determine an appropriate thickness of alumina to maximize device properties.

Acknowledgements:

I would like to thank my mentor, Sameh Tawfick, and Professor John Hart and his research group for guiding me throughout this research program, and Pilar Herrera-Fierro for taking SEM images. Also, I give thanks to the site coordinators: Sandrine Martin, Brandon Lucas, and Trasa Burkhardt, and the clean room staff at the University of Michigan for all of their help. Finally, I'd like to acknowledge the National Nanotechnology Infrastructure Network Research Experience for Undergraduates Program and the National Science Foundation for funding.

References:

[1] Hayamizu, Y. et. al. Integrated three-dimensional microelectro-mechanical devices from processable carbon nanotube wafers. Nature Nanotechnology 3, 289-294 (2008).

[2] Bak, J.H., et. al. High-frequency micromechanical resonators from aluminium–carbon nanotube nanolaminates. Nature Materials 7, 459-463 (2008).

[3] S. Tawfick, K.P. O'Brien, A.J. Hart. Flexible high conductivity carbon nanotube interconnects made by rolling and printing. Small (in press), (2009).

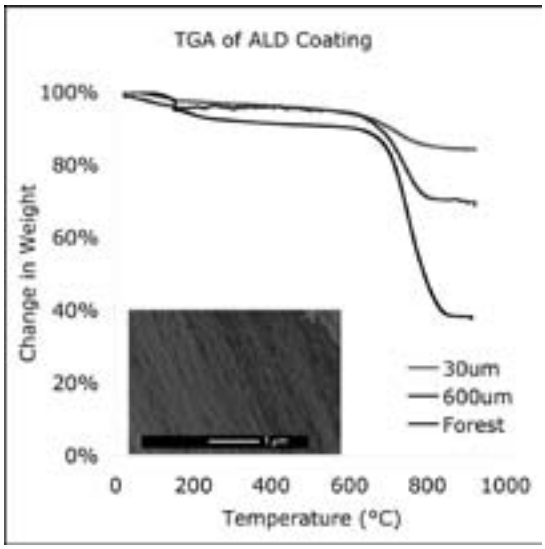

Figure 4: Results of TGA analysis and residual alumina coatings after TGA.

Microfabrication of Heaters and Resistance Thermal Detectors for Simulation of Hotspots

Julia Sokol

Mechanical Engineering, Harvard University

NNIN REU Site: Nanotechnology Research Center, Georgia Institute of Technology, Atlanta, GA
NNIN REU Principal Investigator(s): Dr. Andrei Fedorov, Mechanical Engineering, Georgia Institute of Technology
NNIN REU Mentor(s): Shankar Narayanan, Mechanical Engineering, Georgia Institute of Technology
Contact: jsokol@fas.harvard.edu, andrei.fedorov@me.gatech.edu, shankar.narayanan@gatech.edu

Abstract:

A steady decrease in feature sizes and increase in transistor density has resulted in microprocessors with increased power density and non-uniform heat generation. This has led to the development of hotspots, whose elevated temperatures necessitate the application of localized cooling solutions. This project was concerned with the development of a cooling system (called Nanopatch) for hotspots, capable of dissipating high heat fluxes using evaporation of a thin liquid film. Specifically, devices consisting of a heater and sensor system were fabricated to test the operation of the Nanopatch. Each device consisted of a central hotspot heater surrounded by multiple sensors, fabricated on a Pyrex® substrate using metal deposition and lift-off techniques. The sensors were resistance temperature detectors that, after temperature calibration, can be used to provide an accurate thermal map of the substrate while the central heater is activated.

Introduction:

Advances in semiconductor technologies are leading to the creation of more powerful microprocessors with decreasing transistor sizes and higher power density. Furthermore, the clustering of transistors results in significant spatial variations in temperature across the chip, leading to the development of hotspots, which can be damaging to microprocessor performance. Traditional cooling systems, consisting of a heat sink and a fan, are ineffective at dealing with hotspot cooling due to their large size. A more efficient, localized cooling mechanism that can be integrated with background cooling is necessary in order to manage hotspot temperatures.

Phase change heat transfer is more advantageous for dissipating hotspot heat fluxes than single phase convention cooling due to the high latent heat of vaporization. A solution to the hotspot cooling problem was proposed in the form of a Nanopatch that employs the evaporation of a thin liquid film through a porous membrane [1]. A heater and sensor system was designed in order to test the effectiveness of the Nanopatch. This device, containing a central hot spot heater and 35 resistance temperature detectors around it, allows distinguishing between the amount of heat dissipated by the cooling patch and that lost to the substrate and the ambient.

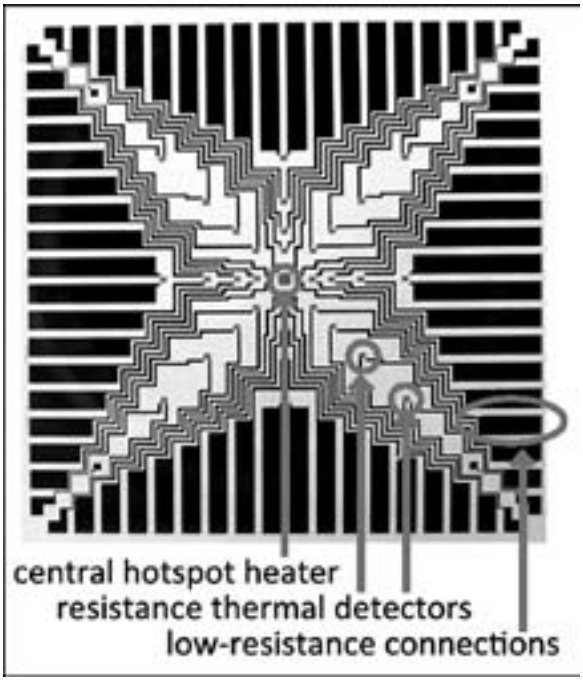

Figure 1: Diagram of heater and resistance thermal detector device.

Experimental Procedure:

The devices containing the heaters and resistance thermal detectors were designed as illustrated in Figure 1, and fabricated on a 4-inch Pyrex wafer. All sensors had 250 μm side lengths, while the heaters were of three different sizes (250, 500, and 750 μm). An illustration of the process for an individual sensor is in Figure 2. The first step consisted of laying down a layer of platinum to create the heaters, sensors, and connections. This was done using a typical photolithography process, followed by electron beam evaporation of 300 nm of platinum (along with a thin layer of titanium for adhesion), and a lift-off process. The second step consisted of adding copper and gold—metals with lower

resistivity—on top of all the connections. This was done with an analogous process of photolithography with adjusted baking times due to the partial conductance of the substrate, followed by deposition and lift-off of 300 nm of copper and 200 nm of gold (Figure 3).

Once the metal pattern was formed, a 0.5 μm layer of silicon dioxide was deposited, and a third photolithography process was done to expose the ends of the connections along the perimeter of the device. At these ends, the silicon dioxide was etched through to the gold layer, in order to enable wire-bonding between the device and the printed circuit board (PCB). A multi-meter was used to check for electrical connectivity to ensure the completion of the etching process.

Results and Conclusions:

One successfully fabricated device was set up for temperature calibration. A copper block with an embedded cartridge heater was placed inside an insulated enclosure. A fan was used to ensure uniform heating of surrounding air. While the copper block was heated using a variac, air temperature was monitored using three thermocouples at different locations inside the enclosure. The resistances of 16 sensors were monitored using a data acquisition system while the copper block was continuously heated with varying power. The resistances were recorded every 30 seconds as the temperature was raised from 25 to 80°C.

Combining temperature data from the thermocouple closest to the substrate with the resistance data, a calibration curve for each sensor was created, graphing the temperature of the sensor as a function of its resistance (Figure 4). The equation of a linear fit is used to calculate temperature at that sensor from any measured resistance value. Thus, the fabricated device will be used to test the effectiveness of the cooling Nanopatch by providing a thermal map of the substrate when the central heater is in operation and the patch is applied to hotspots of different sizes.

Future Work:

An addition to present work could be the inclusion of a background heating capability in order to completely mimic a microprocessor's heat generation. This could be done with an additional photolithography step on the back side of the substrate, followed by metal evaporation and lift-off. Silicon rather than Pyrex would be used in order to enable efficient heat transfer through the substrate.

Acknowledgments:

I would like to thank Dr. Andrei Fedorov and Shankar Narayanan for their guidance and kindness; Nancy Healy and Katherine Hutchison for making the program enjoyable; and the staff of the Georgia Tech Nanotechnology Research Center for their help in the cleanroom. Finally, thank you to the NNIN Research Experience for Undergraduates Program and the National Science Foundation for making this experience possible.

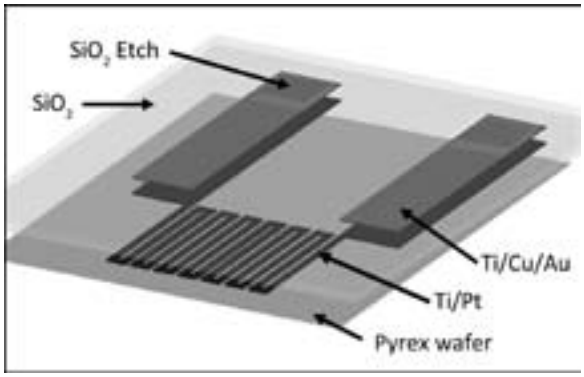

Figure 2: Fabrication layers for an individual sensor with connections.

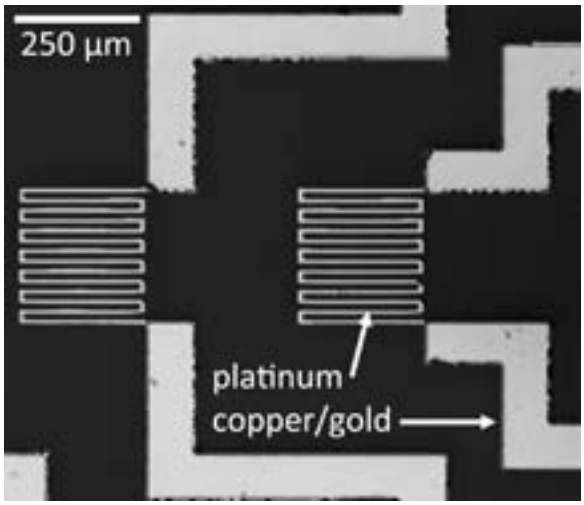

Figure 3: Microscope image of two sensors after Cu/Au deposition and lift-off.

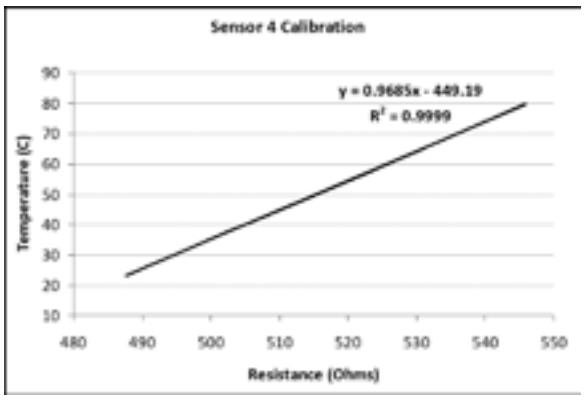

Figure 4: Calibration curve for one of the sensors.

References:

[1] S. Narayanan, A. G. Fedorov, Y. K. Joshi, "Gas-Assisted Thin-Film Evaporation from Confined Spaces for Dissipation of High Heat Fluxes," Nanoscale and Microscale Thermophysical Engineering, 13: 30-53, 2009.

Fracture at the Nanoscale

Denys Zhuo

Material Science and Engineering, Massachusetts Institute of Technology

NNIN REU Site: Penn State Nanofabrication Laboratory, Pennsylvania State University, State College, PA
NNIN REU Principal Investigator(s): Dr. Aman Haque, Mechanical and Nuclear Engineering, Penn State University
NNIN REU Mentor(s): Sandeep Kumar, Mechanical and Nuclear Engineering, Pennsylvania State University
Contact: dzhuo@mit.edu, mah37@engr.psu.edu, suk191@psu.edu

Abstract:

The objective of this research was to develop a micro-electro-mechanical systems (MEMS)-based tensile and fracture testing device for ultra thin specimens *in situ* in the transmission electron microscope (TEM). In particular, we used nanofabrication and innovative design principles to miniaturize a mechanical testing device to a 3 × 5 mm size.

The technical contribution of this research is a unique experimental technique that can perform tensile/fracture testing of nanoscale materials with virtually no restriction on specimen thickness/size. The scientific contribution of this research is that the fundamentals of fracture at extreme (1-10 nm) length-scales will be explored, both qualitatively and quantitatively. Using this technique, we studied the mechanics of fracture in ultra thin films of titanium-titanium nitride. Our experimental results indicate that the titanium-titanium nitride interface is quite strong and that there is a lack of a plastic zone traveling ahead of the crack tip, which is typically seen in bulk materials.

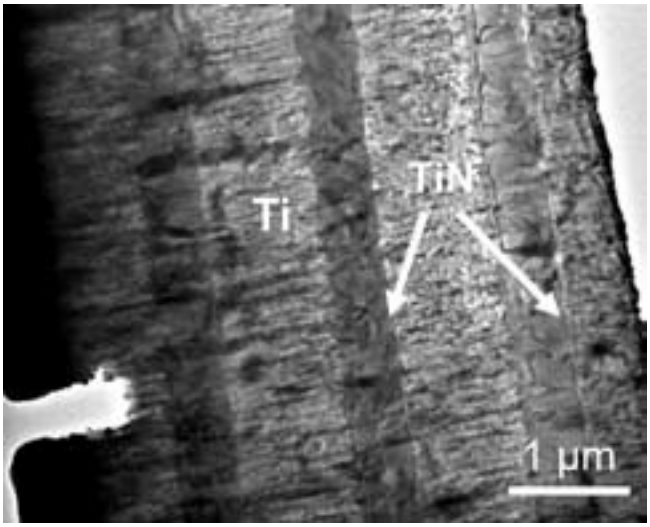

Figure 1: Titanium-titanium nitride multilayer system.

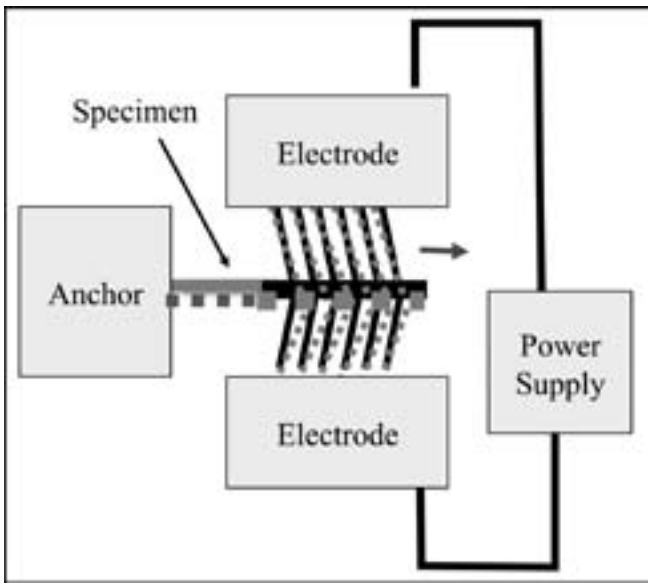

Figure 2: Tensile testing device schematic.

Introduction:

Advanced coating systems include alternating layers of hard and tough materials to achieve these two mutually exclusive properties. These layers can be only a few nanometers thin, and their interfaces make the deformation and fracture mechanics difficult to ascertain by conventional laws. Since transmission electron microscopes (TEM) visualize such small microstructures, we aimed to perform fracture testing of nanoscale thin sections inside the TEM. Our system was comprised of titanium and titanium nitride (Ti-TiN) (Figure 1), which is used as erosion resistant coatings in turbine engine compressor airfoils.

Experimental Procedure:

The tensile testing device design (Figure 2) featured bent beam thermal actuators to apply the stress on a freestanding specimen. Current would be passed through the electrodes

and Joule heating would expand the beams, applying tensile stress on the specimen. Force sensors measure the applied stress and displacement sensors measure strain.

The devices were fabricated by deviceside and backside patterning of silicon-on-insulator (SOI) wafers using photolithography. Both sides of the wafer were then etched with deep reactive ion etching. The devices were released with hydrofluoric vapor etching.

The Ti-TiN specimen was milled with an ion beam from bulk substrate in focused ion beam/scanning electron microscope. The specimen was then integrated onto the tensile testing device with the Omniprobe nanomanipulator and platinum was deposited as a glue to hold the specimen to the sample. A notch was milled into the specimen as an initial point for crack formation.

Results and Conclusions:

We hypothesized that the crack would initiate at the notch which was milled into the sample with the focused ion beam. The crack should have propagated through the titanium layer, but arrested at the Ti-TiN interface since the boundary between the two would require higher energies in order to be crossed. If more energy in the form of increased stress was supplied, then the interface could be breached and the crack cold propagate through the next layer.

In our experiment, the crack initiated at a point below the notch and propagated through the Ti layer (Figure 3). No arrestation at the interface was noted and the crack traveled into the TiN layer (Figure 4). The crack was arrested in the TiN layer when the platinum glue holding the specimen to the device failed and stress was no longer being applied to the specimen.

Although the crack was not arrested at the interface as we had predicted, that the crack crossed the interface rather than traveling along the interface suggests that it is quite strong. In our experiment, we also noted the absence of a plastic zone ahead of the crack tip. In bulk materials, dislocations are typically noted traveling ahead of the crack tip. This demonstrated an interesting difference between fracture behavior in bulk and nanoscale materials.

Future Work:

Further research in Ti-TiN multilayer systems should be completed, including the effect of varying thicknesses of the two materials. Other areas of research include integrated specimen and device processing, which would eliminate the most challenging step—integrating the device and the specimen, as well as fracture testing using the described techniques on a wide range of other materials.

Acknowledgments:

I would like to thank my graduate mentor Sandeep Kumar, advisor Dr. Haque, the Penn State Nanofabrication Lab, as well as the National Nanotechnology Infrastructure Network Research Experience for Undergraduates Program.

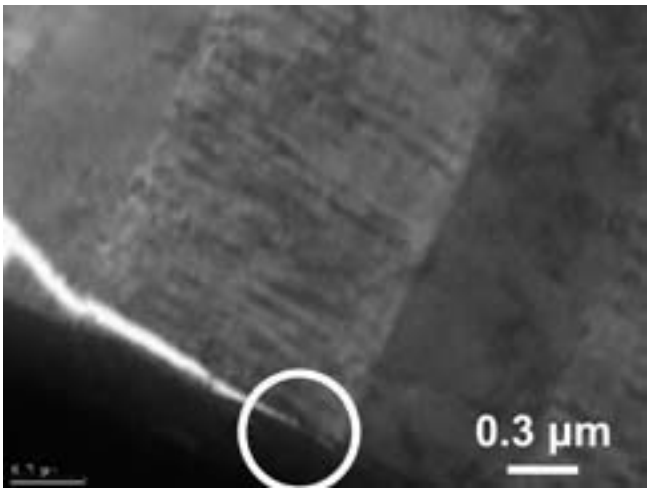

Figure 3: Crack propagating through titanium layer.

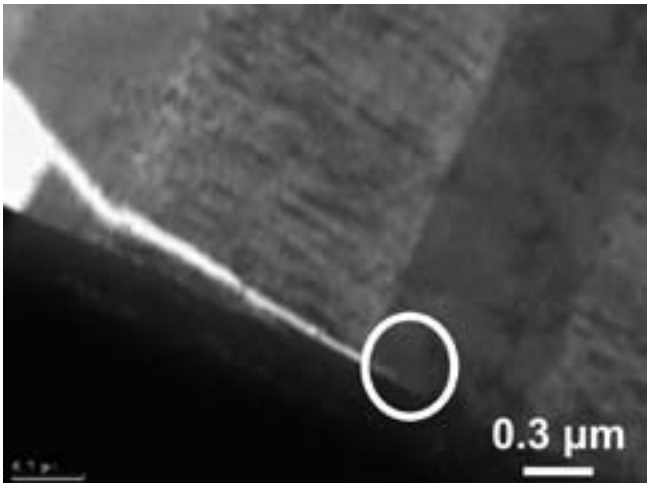

Figure 4: Crack propagating through titanium nitride layer.

Fabrication and Characterization of Nanobeam Resonators with Waveguides

Arolyn Conwill

Physics, Pomona College

NNIN REU Site: Center for Nanoscale Systems, Harvard University, Cambridge, MA

NNIN REU Principal Investigator(s): Prof. Marko Lončar, Engineering and Applied Sciences, Harvard University

NNIN REU Mentor(s): Ian Frank (2007 NNIN REU at Harvard), Engineering and Applied Sciences, Harvard

Contact: amc02006@mymail.pomona.edu, loncar@seas.harvard.edu, ifrank@seas.harvard.edu

Introduction:

Photonics research involves the manipulation and characterization of light flow through materials with engineered geometries. Like electronics, which seeks to control the behavior of electrons, photonics seeks to control the behavior of photons. Photonic crystals employ periodic changes in refractive index to elicit specific behaviors from photons. Recently, photonics researchers have made progress in confining and guiding light at sub-wavelength scales in photonic crystal resonators with high quality factors. These devices have potential applications in chemical sensing, optical switching, nanoscale lasers, low power nonlinear optics, cavity quantum electrodynamics, and light-matter coupling [1].

This project involved the fabrication and characterization of silicon nanobeam cavities, a type of one-dimensional photonic crystal resonator, and its aim was to optimize a new method of probing the optical resonance modes of these cavities. Our cavity design extended the work done by Deotare, et al, who have improved fabrication quality of nanobeam cavities and have achieved quality factors as high as 7.5×10^5 [2].

The quality factor, Q, is related to how long a resonant photon remains contained within the cavity. Practically speaking, fabrication quality prevents the realization of the maximum theoretical quality factors which are on the order of 2.0×10^7. Typical near-IR resonators (see Figure 1) are approximately 500 nm wide, 10 μm long, and 220 nm deep.

The periodic, uniform holes along the silicon nanobeam are Bragg mirrors, which act as ideal mirrors over a range of frequencies and define the characteristic optical bandgap of the cavity. By introducing a defect in this series, typically done by perturbing the spacing at the center of the series of holes, resonance modes emerge. Thus, when the cavity is probed with an appropriately polarized resonant wavelength, photons are trapped near the defect for a relatively long period of time. Tapering the size and spacing of the holes nearby the defect allows for impedance matching which is necessary to achieve high Qs.

Currently, the group employs a resonant scattering technique to probe the optical properties of these cavities. However, the coupling of the laser light from free space at normal incidence restricts the number of modes available for excitation.

In order to probe modes with a wider range of polarizations, our new design incorporated waveguides, solid beams of silicon, onto both ends of the resonator. The waveguides provided a new way to direct the pump beam which excited the resonance modes to the cavity. It was then possible to couple the end of a waveguide to a pulled optical fiber-taper carrying a large evanescent field. We also inserted an intermediate SU-8 waveguide to reduce scattering losses between the silicon waveguide and the optical fiber.

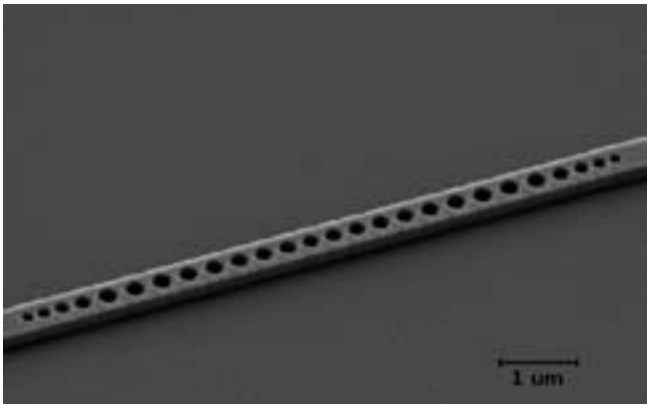

Figure 1: Fabricated resonator.

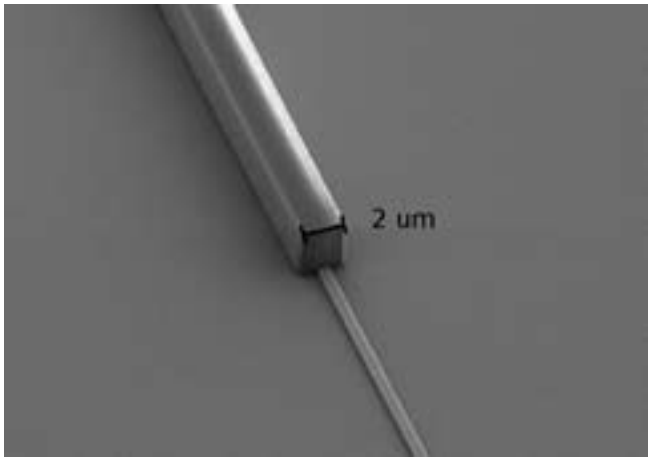

Figure 2: Fabricated waveguides.

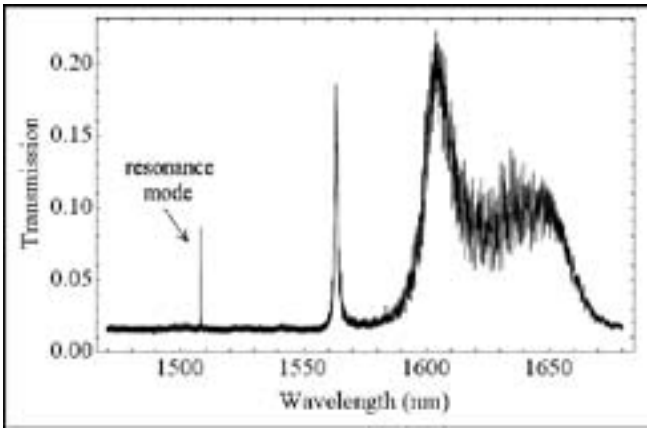

Figure 3: Transmission spectrum.

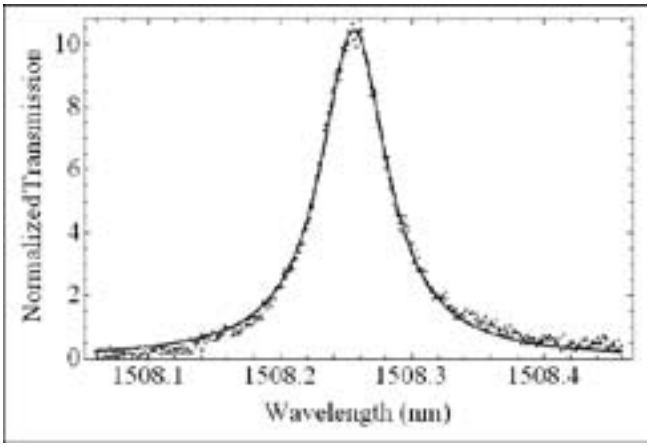

Figure 4: Resonance mode.

Experimental Procedure:

The cavity design was simulated using finite difference time domain (FDTD) software, and we expected a resonant wavelength around 1.51 μm. We transferred the design geometry to AutoCAD in order to produce a file readable by the Elionix electron-beam lithography tool. We wrote the pattern to an silicon-on-insulator (SOI) wafer covered in FOx-17 (HSQ), a negative electron-beam resist. Reactive ion etching (RIE) allowed us to transfer the pattern to the silicon device layer of the wafer. The RIE recipe consisted of C_4F_8, SF_6, and H_2 plasmas and had two steps, a silicon etch phase and a silicon oxide etch phase; this helped prevent undercutting which could become a problem when the substrate etched at uneven rates. Subsequently, we wrote SU-8 waveguides using a similar electron-beam lithography technique. We used scanning electron microscopy (SEM) to image the results of the fabrication procedure.

To characterize the fabricated cavities, we input a tunable near-IR laser beam into an optical fiber which carried the probe beam to our sample. We brought the probe beam from the fiber to the cavity through the SU-8 waveguide and the silicon waveguide. Resonant photons tunnel through the cavity and may emerge at the other side. Then, they pass through an identical series of waveguides and fiber to a photodetector where we measured the transmission spectrum of the cavity. Hence a peak in the spectrum indicated a resonance mode.

Results and Conclusions:

Figure 1 is an SEM image of a silicon resonator resting on an oxide substrate, taken at a 45 degree angle from the surface to inspect the quality of the silicon dry etch. Figure 2 shows the interface between a silicon waveguide and an SU8 waveguide.

We have demonstrated that it is possible to measure resonance modes by probing through waveguides. Figure 3 is a sample measured transmission spectrum, which has a resonance peak that is more easily detectable than typically observed using the resonant scattering technique. We fit the resonance peak to a Lorentzian distribution function in Figure 4, allowing us to determine the quality factor of this cavity to be 25000.

Future Work:

Future work includes continuing to optimize this characterization technique, through improving the waveguide fabrication procedure and investigating cavity resonance modes that have not been measured previously. This technique can also be applied to investigate the resonance modes of more complicated structures such as coupled resonators [1]. In this case, a hydroflouric acid (HF) vapor etch would be used to fabricate suspended cavities anchored to an oxide substrate via the extended silicon waveguides.

Acknowledgments:

I would like to thank the National Nanotechnology Infrastructure Network Research Experience for Undergraduates (NNIN REU) Program and the National Science Foundation (NSF) for funding, as well as my group members including Ian Frank (mentor) and Marko Lončar (principal investigator).

References:

[1] P. B. Deotare, M. W. McCutcheon, I. W. Frank, M. Khan, and M. Loncar. Coupled photonic crystal nanobeam cavities. Applied Physics Letters, 95, 2009.

[2] P. B. Deotare, M. W. McCutcheon, I. W. Frank, M. Khan, and M. Loncar. High quality factor photonic crystal nanobeam cavities. Applied Physics Letters, 94:121106, 2009.

Fabrication of Grating Couplers and Optical Waveguide Sensors

Edgar Garay

Electrical Engineering and Physics, Florida International University

NNIN REU Site: Nanotechnology Research Center, Georgia Institute of Technology, Atlanta, GA
NNIN REU Principal Investigator(s): David S. Gottfried, Nanotechnology Research Center, Georgia Tech
NNIN REU Mentor(s): Janet Cobb-Sullivan, Nanotechnology Research Center, Georgia Institute of Technology
Contact: efgaray@hotmail.com, david.gottfried@mirc.gatech.edu

Introduction:

Interest in chemical sensors has been rapidly increasing due to the need for a low cost, high sensitivity, and portable sensor that could provide a rapid response for detecting different chemicals and biological agents. In the past, different techniques and methods have been investigated in order to create real time sensors, such as acoustic wave-based devices, magnetoelastic sensors, electrochemical sensors based on conductometric or impedance methods, and optical sensors [1].

Optical systems are one of the most accepted techniques in order to perform detection of chemicals. The main reasons behind their popularity are the simplicity of the fabrication methods and the many different environments in which they can be used [2]. Several optical sensors are based on measuring changes in the index of refraction of a sensing material as analytes are adsorbed. Different methods using optical sensors have been reported. Ymeti *et al*. proposed a technique using interferometry in order to detect herpes simplex virus type 1. This method offers a rapid approach that increases the sensitivity and selectivity previously reported by other groups.

In this work we describe a novel method for fabricating grating couplers and optical waveguides that can be used as the base for an optical interferometric chemical sensor. This method is based on a technique developed previously [3], in which electron beam lithography (EBL) is used to create grating structures on a silicon substrate, which is then utilized as a template in order to transfer the pattern to a quartz substrate via imprinting and plasma etching. New findings suggest that the UV curable polymer that acted as an etch mask can be used directly as the substrate for the grating couplers, reducing the amount of steps in the fabrication process.

mr-UVCr06	Before	After
Index of Refraction	1.5355	1.5427
Film Thickness	216.26 nm	193.83 nm

Table 1: Measurements of mr-UVCur 06 before and after baking.

Materials And Methods:

In order to create the grating couplers and optical waveguides the fabrication process was divided into three main steps. The first step was to create the grating template on a silicon substrate using EBL, the second step was to imprint the grating structures into the UV curable polymer by using nanoimprint lithography (NIL). The last step was to deposit the silicon nitride waveguide by plasma enhanced chemical vapor deposition (PECVD). The deposition of silicon nitride is done at 300°C, and for this reason, a number of tests had to be performed prior to the fabrication of the device in order to determine if the transition temperature of the UV curable polymer was greater than the fabrication temperature.

UV Curable Polymer Evaluation:

An UV curable resist was purchased from Micro Resist Technology (mr-UVCur06). The UV curable resist was spun into a silicon wafer at 3000 rpm for 60 seconds. Next, the UV curable polymer was exposed to 365 nm light at room temperature for 75 seconds. The power density of the UV lamp used was 13 mW/cm^2. Subsequently, the substrate was baked in vacuum for 2 hours at 350°C. The thickness and index of refraction of the UV curable resist was measured before and after baking (Table 1).

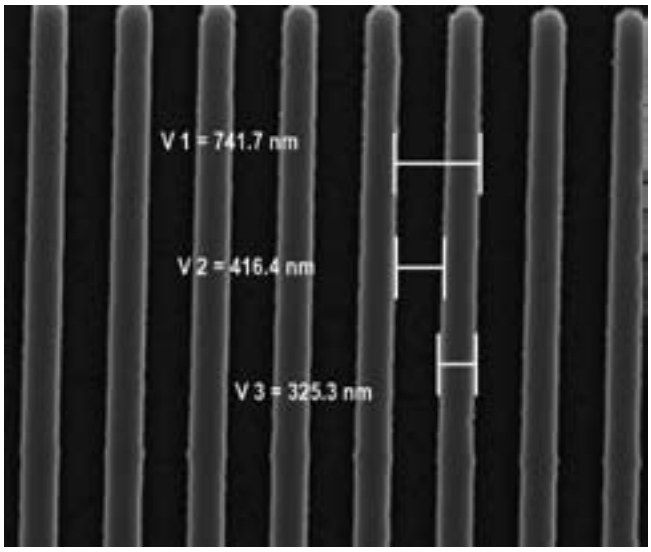

Figure 1: SEM image of the silicon template.

Fabrication Process:

A 4″ silicon wafer was patterned using a standard EBL process with hydrogen silsesquioxane (HSQ) as the resist. The etching was performed using the Plasmatherm ICP. Before use, the silicon template was dipped in hydrofluoric acid (HF) for 10 seconds in order to remove the native oxide layer. Subsequently, a fluorine based polymer was deposited by exposing the silicon template to C_4F_8 plasma for 30 seconds in the ICP (Plasmatherm). The fluorine based polymer acted as a release layer for the nanoimprint process. Figure 1 shows the final silicon template with the grating structures having a period of 740 nm. The depth of the gratings was measured to be 50 nm using an atomic force microscope.

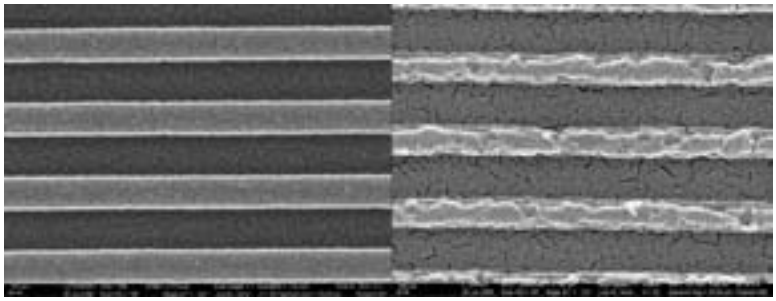

Figure 3: Pattern transfer improvement.

Fused quartz was used as the substrate for the nanoimprint step. The quartz substrate was cleaned by dipping it in sulfuric acid at 80°C for 1 hour. After rinsing the quartz with deionized water, it was baked at 200°C for 1 hour. Next, the UV curable resist was spun into the quartz substrate at 3000 rpm for 60 seconds. After this, the silicon template was placed on top of the quartz substrate and pressure was applied by hand in order to prevent them from separating. Next, they were placed on a hot plate at 85°C for 1 minute.

UV based nanoimprint lithography was performed using a commercial nanoimprinter (Obducat). The UV curable resist was imprinted by applying a pressure of 15 bars for 180 seconds at room temperature, followed by UV light exposure; the UV dose was 1000 mJ/cm^2. After release of the imprinted gratings, a 1500 Å layer of silicon nitride (Si_3N_4) was deposited by PECVD at 300°C.

Results and Discussions:

An improved fabrication process was developed in order to create grating couplers and optical waveguide using an UV curable polymer as the substrate. By using the new material as the substrate for the gratings, one third of the steps in the fabrication process (plasma etching and resist stripping) were eliminated, reducing time and cost of the fabrication.

Figure 2 shows an optical image of the grating couplers and waveguide guiding 633 nm light from a HeNe laser. Furthermore, transfer of the pattern into the UV curable polymer was improved by applying a thicker layer of a fluorine based polymer to the surface of the silicon template (Figure 3).

Additional testing is needed in order to obtain the coupling efficiency of the gratings and the optical intensity loss of the waveguide, but qualitative evidence so far indicates that devices made using this process will provide a viable alternative to the standard fabrication methods.

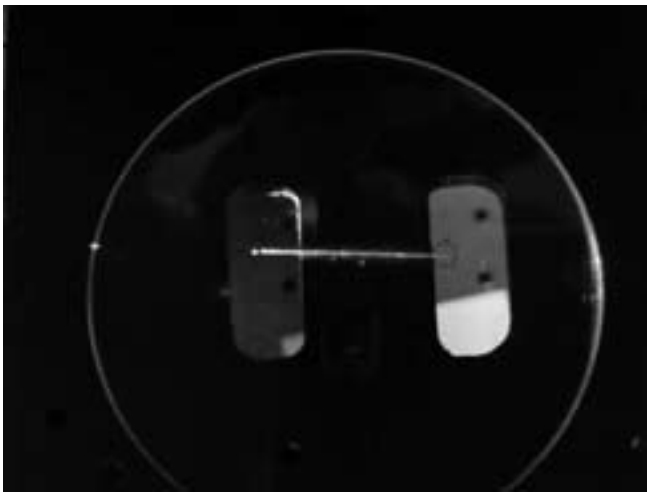

Figure 2: Optical image of final device.

Acknowledgements:

This work was performed under the auspices of the National Nanotechnology Infrastructure Network Research Experience for Undergraduates (NNIN REU) Program and the National Science Foundation. Thanks to all the members of the Microelectronics Research Center at Georgia Institute of Technology. Special thanks to Dr. David S. Gottfried and Janet Cobb-Sullivan for providing such a challenging project.

References:

[1] J. Xu, D. Suarez, D.S. Gottfried; "Detection of avian influenza virus using an interferometric biosensor Analytical and Bioanalytical Chemistry"; 2007 Oct; 389(4): 1193-9.

[2] S. Mandal and D. Erickson; "Nanoscale optofluidic sensor arrays"; Opt. Express 16, 1623-1631 (2008).

[3] A. Scofield; "Optical Waveguide Couplers Fabricated by Nano-Imprint Lithography"; 2009 NNIN REU Research Accomplishments, 112, Nov. 2008. http://www.nnin.org/nnin_reu.html.

3D Photonic Crystals Fabricated Through Direct Laser Writing

Meredith Henstridge
Physics, Xavier University

NNIN REU Site: Colorado Nanofabrication Laboratory, University of Colorado, Boulder, CO
NNIN REU Principal Investigator(s): Dr. Rafael Piestun, Electrical & Computer Engr, Physics, University of Colorado
NNIN REU Mentor(s): Timothy Gerke, Electrical & Computer Engineering, University of Colorado at Boulder
Contact: henstridgem@xavier.edu, rafael.piestun@colorado.edu, gerke@colorado.edu

Abstract:

We developed a procedure for fabricating woodpile photonic crystals which involved writing structures into AZ P4210 positive photoresist and a subsequent gold electroplating process.

Introduction:

A photonic crystal is a periodic structure in which the period is on the order of the wavelength. In a three-dimensional (3D) photonic crystal, a 3D photonic band gap is possible. A band gap is the range of frequencies in which light cannot penetrate the crystal regardless of incident angle and polarization. Defects can be engineered in the structures for which light at band gap frequencies can be guided or confined within the crystal, in principle, without loss [1]. Photonic crystals with designed defects enable new types of optical integrated circuits, the analog of electrical integrated circuits. Routing signals optically can eliminate performance problems caused by nanowire capacitance and signal crosstalk in nanoscale electrical signal processing systems [1].

Our photonic crystal fabrication process included direct laser writing, in which 800 nm laser pulses with durations less than 100 femtoseconds were tightly focused in order to expose a photosensitive sample [2]. Each focused pulse had a power density of 400GW/cm^2, which was enough for two photon nonlinear absorption process. Direct laser writing was capable of fabricating 3D structures into photoresist and feature sizes were controlled by modulating the output power. Our setup employed a shutter and a PI Nanocube 3D piezo translation stage, both of which were computer controlled through a Labview program (see Figure 1).

Experimental Procedure and Results:

Sample Preparation. The first step of sample preparation was to use a three boat thermal evaporator to deposit a 50 nm layer of titanium followed by a 50 nm layer of gold onto a glass microscope coverslip. The gold served as the seed layer necessary for a subsequent electroplating process, and the titanium layer was necessary for adhesion of the gold to the substrate. The final sample preparation step was to spin-coat a layer of AZ P4210 positive photoresist onto the substrate.

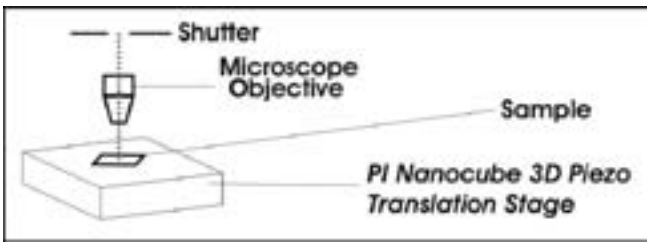

Figure 1: Direct laser writing setup.

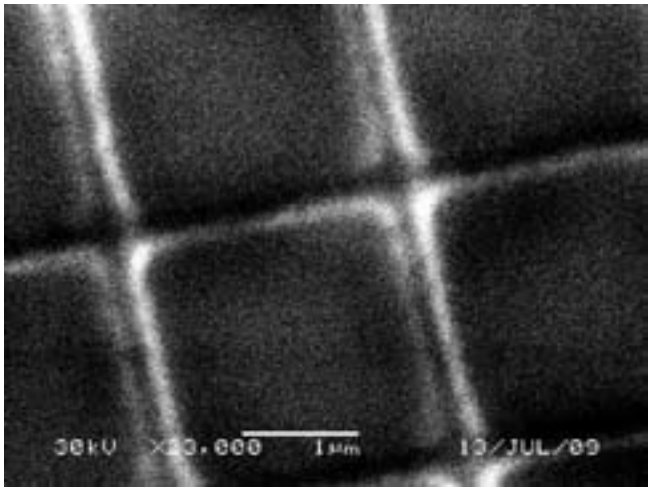

Figure 2: A grid sample written with 100 μW of output power, stage velocity of 0.1 mm/s.

Determining the Writing Power. Since we desired to create the smallest features possible, the output power that resulted in the smallest feature in the photoresist was the optimal writing power. Test structures to determine this were written into a 2 μm layer of photoresist at output powers ranging 50-200 μW with a stage velocity of 0.1 mm/s. When attempting to measure the feature size of these test samples, however, we encountered a problem: the gold seed layer had a lower modification threshold than the AZ P4210 photoresist, and under an optical microscope, modified gold and properly exposed photoresist were indistinguishable. A sample written with 100 μW of output power exhibited only seed layer

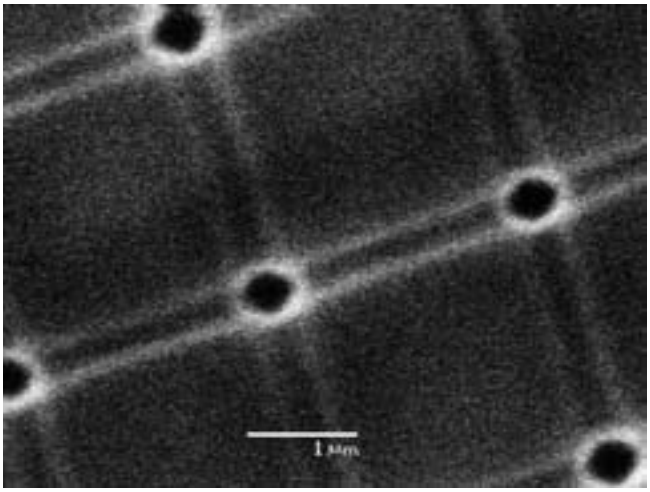

Figure 3: A grid sample written with 125 μW of output power, stage velocity of 0.1 mm/s.

modifications, as seen in Figure 2. When the output power was increased to 125 μW, dark holes appeared in the sample (Figure 3). These holes were locations where the photoresist was developed away because of a double exposure dose due to the crossing of written lines. The visible lines in the image were seed layer modifications, not developed photoresist, whereas a properly written structure would be lines of developed photoresist.

To eliminate the visibility of seed layer modifications, we sputtered a thin gold layer onto the sample surface. After applying the gold coating, only the locations where the photoresist was developed away were visible in the SEM. To fix the underexposure without increasing feature size we reduced the velocity of the PI stage, which increased the exposure dose of the material. When the stage velocity was reduced to 0.025 mm/s, 75 μW of output power yielded proper exposure and a desired feature size of 100-300 nm (see Figure 4).

Gold Electroplating Process. Infiltrating the written structures with gold was the final step of our fabrication process. 6 μm tall test structures were electroplated for different time durations and 1 mA of current.

Only 150 nm filling occurred for durations under five minutes, and overfilling occurred after a duration of 30 minutes. Thus, the time it took to fill a 6 μm tall structure was between 5 and 30 minutes. Once this time was determined, it could be used to extrapolate the filling times for taller structures.

Conclusion:

We developed a procedure using a direct laser writing system to fabricate gold woodpile photonic crystals through two-photon absorption in photoresist and a subsequent electroplating process. We prepared substrates by evaporating gold and titanium, then spin-coating a layer of positive photoresist. We determined the writing power and stage velocity that yielded a desired 100-300 nm feature size. Finally, we investigated the electroplating process and determined that it takes between 5 and 30 minutes to fill a 6 μm structure.

Future Work:

Further investigation into the correct time parameters of the electroplating process is necessary. Once correct time parameters are established, the woodpile photonic crystal structures written into the photoresist can be infiltrated with gold. The resulting gold woodpile photonic crystals are expected to have 3D photonic band gaps. Defects can then be engineered in the crystals to pursue applications such as optical circuitry.

Acknowledgements:

Thanks to the National Nanotechnology Infrastructure Network Research Experience for Undergraduates Program and the National Science Foundation for funding this opportunity. Thanks to Bart Van Zeghbroeck and Debbie Stratton for organizing the program at the University of Colorado at Boulder. Finally, I would like to acknowledge Rafael Piestun, Tim Gerke, Tomoko Borsa, and Jan Van Zeghbroeck for their guidance on this project.

References:

[1] John Joannopoulos, et al. (2008). Photonic Crystals: Molding the Flow of Light (2nd ed.). Princeton: Princeton University Press.

[2] M. Deubel et al. (2006). 3D–2D–3D photonic crystal heterostructures fabricated by direct laser writing. Optics Letters, 31, 805-807.

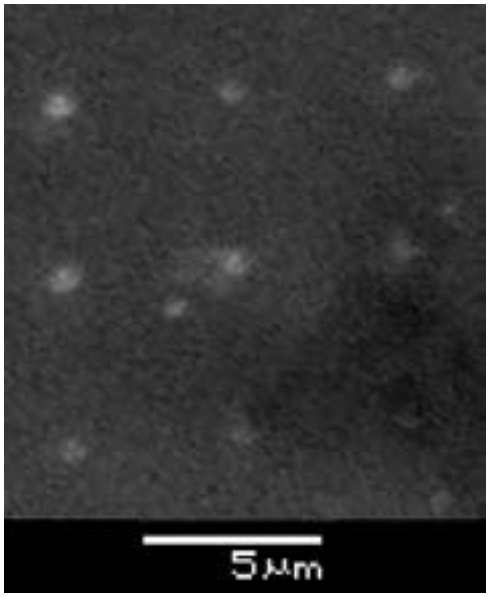

Figure 4: A sample of holes with diameter 100-300 nm, written with 75 μW of output power, stage velocity of .025 mm/s.

Patterning Soft Materials with Light-on-Tip

Richard Purvis
Engineering Physics, Tulane University

NNIN REU Site: Microelectronics Research Center, University of Texas, Austin, TX
NNIN REU Principal Investigator(s): Dr. Xiaojing Zhang, Biomedical Engineering, University of Texas at Austin
NNIN REU Mentor(s): Dr. Yuyan Wang, Department of Biomedical Engineering, University of Texas at Austin
Contact: rpurvis@tulane.edu, john.zhang@engr.utexas.edu, yuyan.wang@engr.utexas.edu

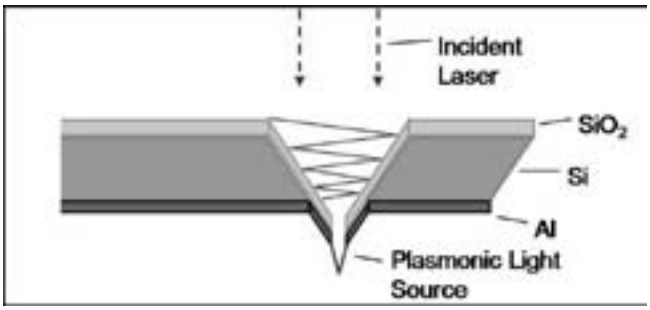

Figure 1: Cross section of the plasmonic scanning probe.

Abstract and Introduction:

The objective of this project is to stimulate cell membrane proteins, through a nanofabricated plasmonic scanning probe tip mounted in near-field scanning optical microscopy. Near-field scanning optical microscopy is a method that allows for sub-wavelength resolution optical imaging and collection along with spectral and topographical information. This is made possible by using light emitted in the near field from a sub-wavelength aperture on a scanning probe tip. Since the far field resolvable spot size is limited due to the Abbe diffraction limit [1], our probe utilizes surface plasmon resonance [2] to emit light from the aperture. Since these fields are attenuated, this effect can only be utilized within the decay range. Our group has attained aperture sizes as small as 66 nm. Figure 1 shows a cross-section of the plasmonic probe, with surface Plasmon resonance occurring at the aluminum-silicon dioxide interface.

For this Research Experience for Undergraduates Program, calibration of the plasmonic enhanced scanning probe tip was performed by measuring the dependence of exposure depth on exposure time in photoresist spun onto a glass substrate. Models were constructed using COMSOL finite element method for comparison. To prepare to stimulate proteins using the plasmonic tip, we also demonstrated a microcontact printing technique to pattern protein on glass substrate using a polydimethylsiloxane stamp. Using the near-field light source from our probe to locally stimulate cell proteins will allow us to examine gene expression with high precision.

Experimental Procedure:

The major focus of this summer research program was calibration and simulation of the plasmonic probe, as well as the demonstration of a protein sample preparation method. Demonstration of a method to prepare protein monolayer samples is important to test the probe's ability to isolate proteins for stimulation before it is used on living cells. To prepare the monolayers, we employed a microcontact printing technique. Rabbit Immunoglobulin G-Fluorescein isothiocyanate conjugated protein was micropipetted onto a hydrophobic polydimethylsiloxane (PDMS) stamp, rinsed in phosphate buffered saline and then deionized water, air dried, and depressed onto either a glass or porous silica substrate. Figure 2 depicts the stamped protein monolayer in a 20 μm diameter circle pattern and scanning electron microscope closeup.

To calibrate our probe and evaluate the plasmonic effect, a near-field photolithography experiment was performed. A 1.4 μm layer of AZ-5209 E positive photoresist was spun onto a glass substrate and mounted in our near-field scanning optical microscopy setup. A plasmonic probe with a 500 nm aperture diameter fed with 405 nm light was used to expose photoresist point by point with exposure times varied between 0-8 minutes. The resulting exposure pattern was developed and evaluated using atomic force microscopy.

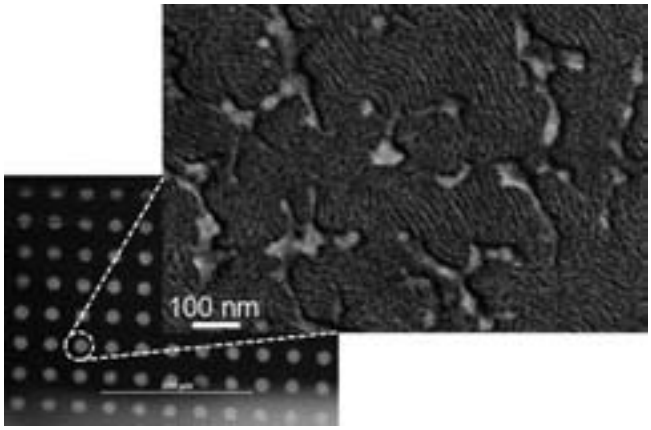

Figure 2: Optical and scanning electron microscope image of stamped protein monolayers.

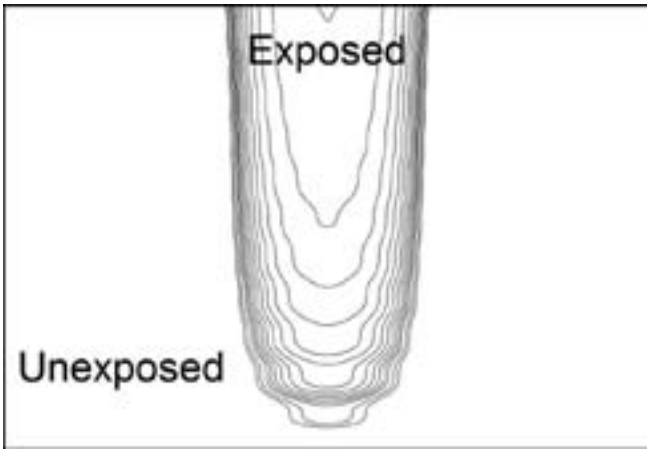

Figure 3: Simulated exposure contours for unexposed photoresist.

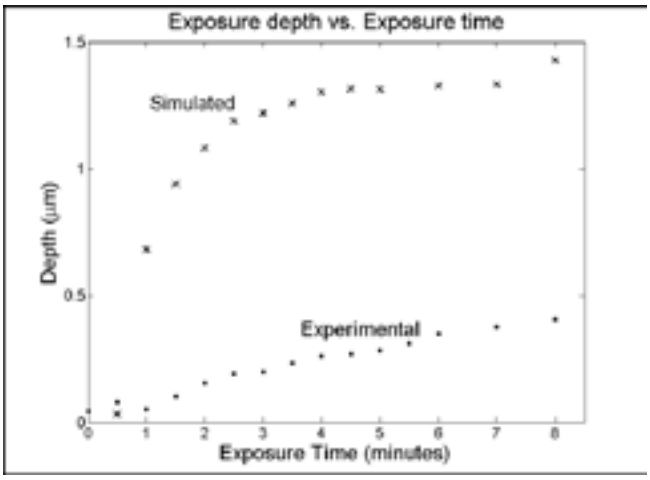

Figure 4: Exposure Depth vs. Exposure Time for near-field photolithography experiment.

Comsol finite element method software was utilized to simulate the near-field photolithography experiment. The photoresist layer was modeled two dimensionally as a rectangle with a height of 1.381 μm and a 500 nm-full width half maximum Gaussian source opposed at the center of the upper side. The power of the light source was calibrated to a value on the same order of magnitude as the first experimental value, which was 6.5 microwatts. To simulate the light transmission within the photoresist, iterated steady-state solutions were performed for each time step. Using the clearing dose parameter for AZ-5209 E photoresist, we calculated the minimum power flow required to expose the photoresist for each time step. The exposure contours calculated for completely unexposed photoresist are shown in Figure 3. A "cone" of exposed photoresist with the same depth and radius as the previous time step's contour was defined using two second-degree Bezier curves for each iteration to approximate the index change from exposed to unexposed photoresist. The resulting depth values were recorded and compared to the experimental values.

Results and Conclusions:

Simulated and experimental exposure time-depth relationships are shown in Figure 4. For the first depth value, simulated and experimental results are comparable. This is to be expected, as it is the calibration point. We have determined several possible sources for the disparity in the rest of the depth values. Contact of the plasmonic tip with the photoresist, the inability of the optical simulation to account for the development process, and limited probing depth of the atomic force microscope tip are some possible sources of error. We can conclude that one of the significant source of error is the inability of the simulation to account for near-field waves with a transmitted Gaussian source. If the source included the decaying component, the simulated values for the first few depths would be higher, allowing for a lower power value in the simulation, which would in turn bring the rest of the data points down closer to the experimental data. We therefore conclude that the plasmonic effect occurred during the near-field photolithography experiment.

Future experiments involve photosynthetic reaction center membrane proteins from *Rhodobacter sphaeroides* bacteria [3], where these proteins will be arranged in a monolayer where each isolated proteins or protein groups will be stimulated with high spatial-temporal resolution with subsequent photosynthetic current measured.

Acknowledgements:

I would like to thank Dr. Xiaojing Zhang, Dr. Yuyan Wang, Eric Huang, and the rest of Zhang research group for their guidance and support. I would also like to thank Jean Toll and Melanie-Claire Mallison for their excellent job in coordinating the research program. Funding was provided by both the National Nanotechnology Infrastructure Network Research Experience for Undergraduates Program and National Science Foundation.

References:

[1] Betzig, E. and Trautman, J. K. "Near-field optics: Microscopy, spectroscopy, and surface modification beyond the diffraction limit." Science 257, 189–194 (1992).

[2] Y.Y. Wang, Y.Y. Huang, K. Hoshino, Yujan Shrestha, David Giese, X.J. Zhang, " Plasmonic Nanoprobe Integrated with Near-field Scanning Microscope", Optical MEMS 2009, August 17-19 (accepted).

[3] G. Feher, J. P. Allen, M. Y. Okamura, D. C. Rees. "Structure and function of bacterial photosynthetic reaction centres." Nature 339, 111 (1989).

Hybrid Silicon Microring Lasers

Daryl Spencer

Engineering Physics, University of Tulsa

NNIN REU Site: Nanotech@UCSB, University of California, Santa Barbara, CA

NNIN REU Principal Investigator(s): Dr. John Bowers, Electrical and Computer Engineering, University of California, Santa Barbara

NNIN REU Mentor(s): Dr. Di Liang, Electrical and Computer Engineering, University of California, Santa Barbara

Contact: daryl-spencer@utulsa.edu, bowers@ece.ucsb.edu, dliang@ece.ucsb.edu

Abstract:

We demonstrate a hybrid silicon microring laser device utilizing active indium phosphide (InP)-based epitaxial layers integrated on a silicon-on-insulator (SOI) substrate. The ring resonators exhibit compact structure with diameters of ≤ 50 μm. Laser emission is evanescently coupled to a Si waveguide and captured by on-chip photodetectors. Successful continuous-wave lasing has been observed with a minimum electrical pump current of ~ 5 mA at 10°C and maximum power output > 500 μW at 20°C. Temperature dependent studies were also conducted up to a safe operating temperature of 65°C. Lasing at 1.53 μm shows good spectrum purity with a < 0.04 nm linewidth (limited by the resolution of the optical spectrum analyzer) and a 4.2 nm free spectral range at 20°C. Unidirectional lasing bistability, a unique characteristic of circular lasers, is also observed. The devices are a promising candidate for future applications in optical interconnects, memory, and all optical processing.

Introduction:

Silicon photonics is an important and progressive field for developing low-cost, high-speed optical devices on a Si substrate. Integrating on-chip optical interconnects with modern Si electronics can realize faster and more power efficient data communications in future microprocessors and other emerging applications.

Our research focused on developing a microring laser based on the hybrid silicon platform [1] developed by a joint effort between the University of California Santa Barbara and Intel Corporation. The hybrid silicon platform realizes active optical components on a well developed silicon manufacturing base. The goal of this project was to characterize the microring lasers across design parameters and optimize the fabrication procedure.

Device Layout:

Figure 1 shows the 3D schematic (a) as well as the 2D cross section (b) of the hybrid silicon microring laser. The ring resonator consisted of an active gain region: InAlGaAs-based quantum wells and a separate confinement heterostructure sandwiched by InP p-cladding and n-contact layer, which were then integrated through a wafer bonding technique onto an SOI substrate. The active region generated photons when electrical carriers were injected, which were guided along the ring resonator to achieve optical gain. The ring resonator had a compact structure with a variable radius, R, of ≤ 25 μm. The laser emission was evanescently coupled across a gap, s (50-500 nm), to a Si bus waveguide of width, w (600-1000 nm), for characterization via on-chip photodetectors.

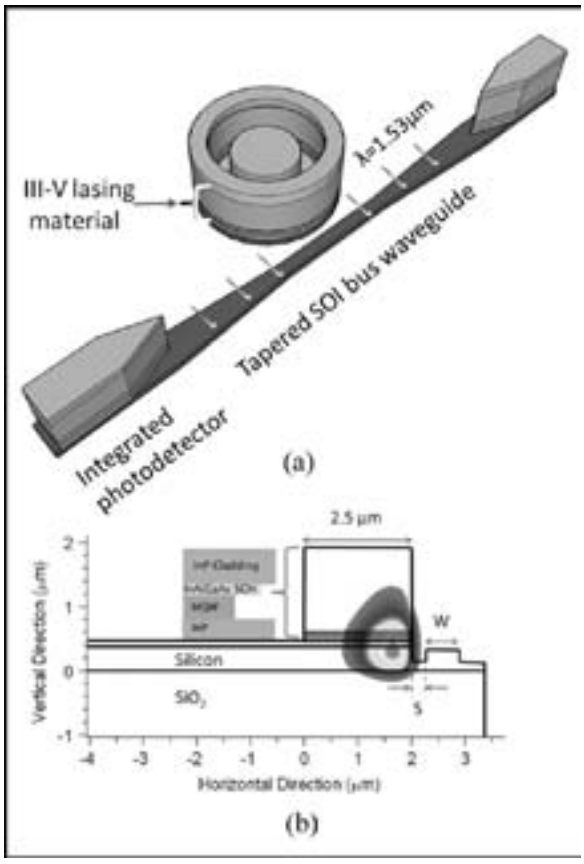

Figure 1: (a) 3D schematic ring resonator, waveguide, and photodetectors, and (b) 2D cross section with optical mode profile and epitaxial layers.

Results:

Figure 2 shows a typical continuous-wave, temperature-dependent output power vs. injected current (L-I) characteristic for devices

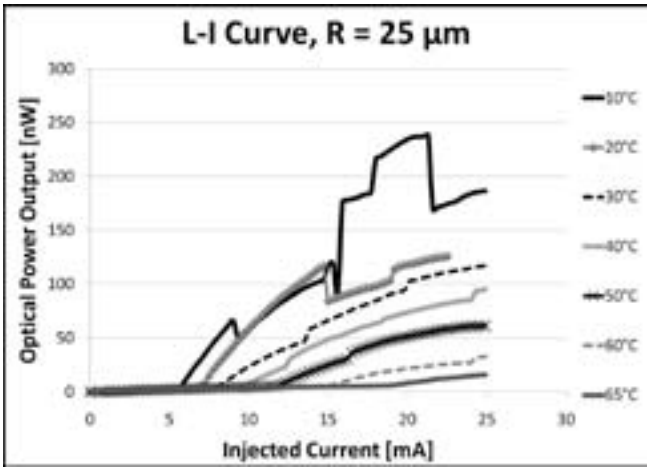

Figure 2: Detail of typical L-I curve for R = 25 µm devices.

with R = 25 μm. Once the required threshold was met, the output light power increased dramatically and was the sign of lasing. Successful lasing was achieved at thresholds as low as 5.4 mA (R = 12.5 μm, s = 250 nm, w = 600 nm) at 10°C and output light power > 500 μW (R = 25 μm, s = 50 nm, s = 600 nm) at 20°C. Experiments increasing the coupling gap from 50 nm to 500 nm showed a trend of decreasing threshold (I_{TH}) with a reduction of out-coupled power collected at the photodetectors. The maximum lasing temperature was recorded under safe operating conditions of up to 25 mA pump current, and yielded a maximum temperature of 65°C. Devices fabricated with a coupling gap of 500 nm had too low of a optical power coupled to the waveguide to be consistently measured with the photodetectors.

Figure 3 shows the primary longitudinal mode in the lasing spectrum collected from the silicon waveguide. Full-width at half-maximum is < 0.04 nm (limited by the resolution of the optical spectrum analyzer) and the free spectral range between higher order modes is 4.2 nm (not shown), which agrees well with a predicted value of 4.3 nm.

Figure 4 shows the L-I curves for unidirectional lasing, a feature unique to ring/disk resonators. Without introducing nonreciprocal gain or loss in the resonator cavity, lasing was observed in both clock-wise (CW) and counter-clock-wise (CCW) simultaneously. In order to break the balance, the right photodetector (PDR) was forward-biased as a light source at 500 mV to force laser emission in a CW direction. The output was measured at the left photodetector (PDL) as the pump current was increased. When threshold was reached, it was clear that the majority of the laser emission was detected at the PDL, thus demonstrating unidirectional lasing.

Conclusions:

We have demonstrated a compact hybrid silicon microring laser with low threshold down to 5.4 mA and output power > 500 μW at 10°C. Good spectrum purity was observed with a linewidth < 0.04 nm and a free spectral range of 4.2 nm. Additionally, unidirectional lasing was achieved utilizing the on chip photodetectors and unique geometry of the ring resonator.

These results show that the hybrid silicon microring laser is a promising candidate for optical interconnects, memory, and all optical processing.

Acknowledgements:

I would like to thank the ultrafast optoelectronics research group at the University of California Santa Barbara under Dr. John Bowers, Mentor Di Liang for his advising and design/fabrication of devices, and Tadashi Okumura. I also acknowledge our funding agencies: the National Nanotechnology Infrastructure Network Research Experience for Undergraduates Program, the National Science Foundation, Hewlett Packard Labs, and the Defense Advanced Research Projects Agency.

References:

[1] A. W. Fang, H. Park, O. Cohen, R. Jones, M. J. Paniccia, and J. E. Bowers, "Electrically pumped hybrid AlGaInAs-silicon evanescent laser," OE 14, 9203-9210, (2006).

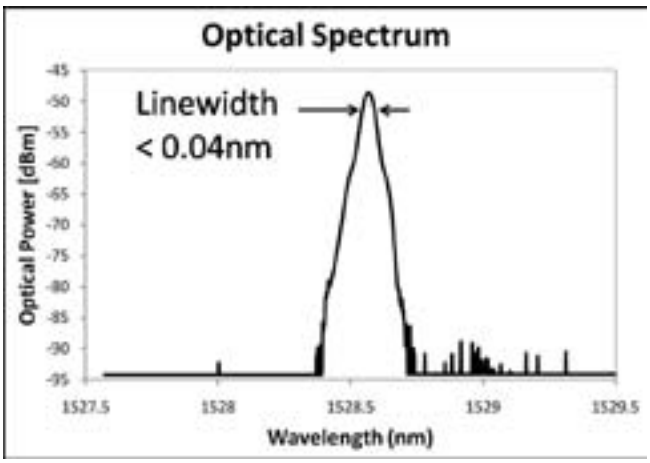

Figure 3: 1st order mode lasing spectrum and measured linewidth.

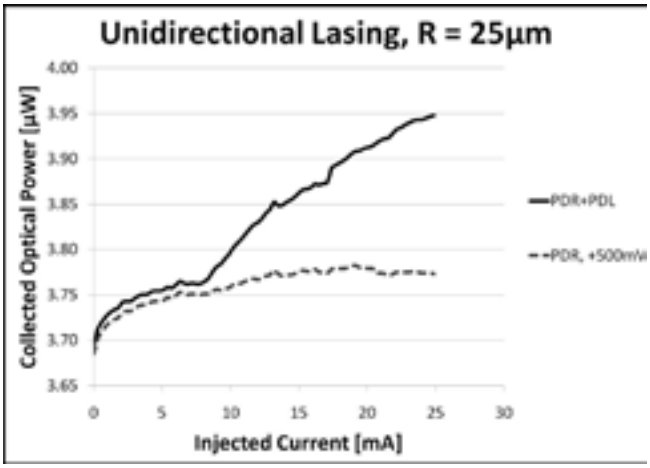

Figure 4: Unidirectional lasing in the microring structure.

Fabrication of Single Crystal Silicon Photonic Crystals

Matthew Strathman

Electrical Engineering, Montana State University

NNIN REU Site: Stanford Nanofabrication Facility, Stanford University, Stanford, CA

NNIN REU Principal Investigator(s): Prof. Roger T. Howe, Prof. Olav Solgaard; Electrical Engineering, Stanford University

NNIN REU Mentor(s): Dr. J. Provine, Dr. Il Woong Jung; Electrical Engineering, Stanford University

Contact: matt827657@gmail.com, rthowe@stanford.edu

Abstract:

Photonic crystals are periodic arrangements of dielectric materials, in our case a two-dimensional array of holes etched into a silicon substrate, that have special optical properties. We fabricated these photonic crystals out of single crystal silicon using the GOPHER process, which stands for the Generation Of PHotonic Elements by RIE (reactive ion etching) [1]. These photonic crystals have been shown to have high reflectance over a broad wavelength range and therefore are useful as broadband mirrors. They also are made from single crystal silicon so the effects of silicon migration to improve the performance of the photonic crystals can be tested.

Introduction:

Photonic crystals made from single crystal silicon can be fabricated to have high reflectivity over a large wavelength range and therefore be very useful as broadband mirrors [2]. Photonic crystals or PCs are periodic arrangements of dielectric materials that, because of their structure, have interesting optical properties. Photonic crystals can be fabricated that are one, two or three dimensional.

An example of a one dimensional photonic crystal is a Distributed Bragg Reflector or DBR. A DBR is a layered structure that has films of alternating high and low indexes of refraction and very precise thicknesses. Two dimensional photonic crystals have a periodic structure in two dimensions. The photonic crystal fabricated using the GOPHER process is an array of holes etched out of a single crystal silicon substrate. The benefits of using the GOPHER process over other methods of fabrication include that the final photonic crystal is stress free and fabricated from a silicon wafer, which is inexpensive when compared to silicon-on-insulator (SOI) substrates. Another benefit of the GOPHER process is that the finished photonic crystals are single crystal silicon. This is important because silicon migration experiments can be performed on single crystal silicon structures.

Procedure:

To fabricate these photonic crystals using the GOPHER process, we started by thermally oxidizing the wafer. The wafer was then coated with photoresist, the photoresist patterned and developed, and the pattern was etched through the oxide to create a mask for the etching steps. After the resist was stripped, holes were etched into the substrate with the first directional silicon etch, then the sidewalls were oxidized, and the oxide on the bottom of the holes was etched. The second directional silicon etch then deepened the holes, and an isotropic silicon etch undercut the photonic crystal. An SEM image of the finished GOPHER photonic crystals that were fabricated is shown in Figure 1.

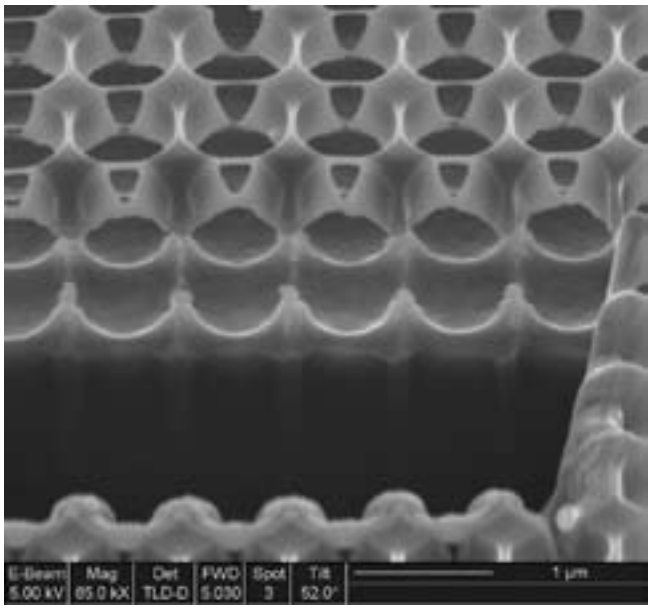

Figure 1: SEM image of the finished GOPHER photonic crystal.

After fabrication, the reflectivity of these photonic crystals were tested using a broadband light source and an optical spectrum analyzer. Light from the broadband source was focused onto the photonic crystal and the reflected light was fed into the optical spectrum analyzer. The reflectivity was obtained by comparing this data to a measurement of the reflectance of bare silicon which is known to be 31% in the frequency range that was measured.

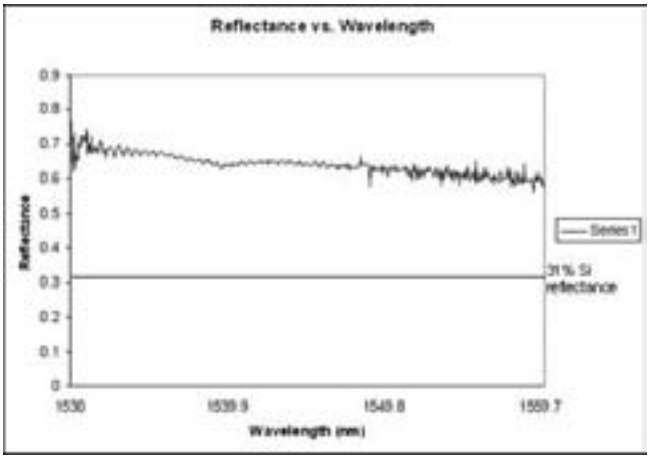

Figure 2: Plot of reflectance vs. wavelength for the fabricated photonic crystal. Line shows the 31% reflectivity of bare Si.

Results and Discussion:

The fabricated photonic crystals performed as expected in the tests. The reflectivity was above 60% over the range that we measured as shown in Figure 2. Wavelength regions with higher reflectivity could have been out of the wavelength range that we measured, but due to a limited range broadband light source, we were unable to verify this. After looking at the devices in an SEM we noticed that the holes that made up the periodic structure of the photonic crystal were longer in one direction than the other. Although we did not see any effects from this, further polarization testing on these photonic crystals could show a polarization effect from this difference.

Future Work:

The photonic crystals that we fabricated are going to be used to test the effects of the migration of single crystal silicon on the optical performance of the photonic crystals. Silicon migration can be used to reflow single crystal silicon structures and cause them to go to a low surface energy state. This can be done by annealing at high temperatures in a non-reactive ambient such as hydrogen. This improves the efficiency of the photonic crystals by smoothing out sharp edges and rough surfaces from etching. Figure 3 shows a GOPHER PC before and after annealing, and after the structure was annealed almost all of the rough edges have been smoothed out which will decrease the amount of light that is scattered. The photonic crystals that we fabricated will be used to further test this process and try to optimize its use for these photonic crystals.

Summary and Conclusions:

Photonic crystals are periodic arrangements of dielectric materials fabricated to have interesting optical properties. The photonic crystals that we fabricated and tested had high broadband reflectivity which is useful for broadband mirror applications. The GOPHER process was used to fabricate these crystals using reactive ion etching to etch holes into a silicon substrate. The resultant photonic crystal was stress free and composed of single crystal silicon.

The photonic crystals that we successfully fabricated this summer were tested and shown to have the high reflectivity characteristics that we were striving for. In the future the PCs that we have made will be used to further test the hydrogen annealing process to improve the performance of the phonic crystals.

Acknowledgements:

The National Nanotechnology Infrastructure Network Research Experience for Undergraduates Program.

References:

[1] Sanja Hadzialic, Sora Kim, Shrestha Basu Mallick, Aasmund Sudbø, and Olav Solgaard, "Monolithic Photonic Crystals", 2007 LEOS.

[2] I. W. Jung, S. Kim, and O. Solgaard, "High Reflectivity Broadband Photonic Crystal Mirror MEMS Scanner With Low Dependence on Incident Angle and Polarization," IEEE Journal of Microelectromechanical Systems, Vol. 18, No. 4, August, 2009.

[3] Sora Kim, Rishi Kant, Sanja Hadzialic, Roger T. Howe, and Olav Solgaard, "Interface Quality Control of Monolithic Photonic Crystals by Hydrogen Annealing", 2008 OSA / CLEO/QELS.

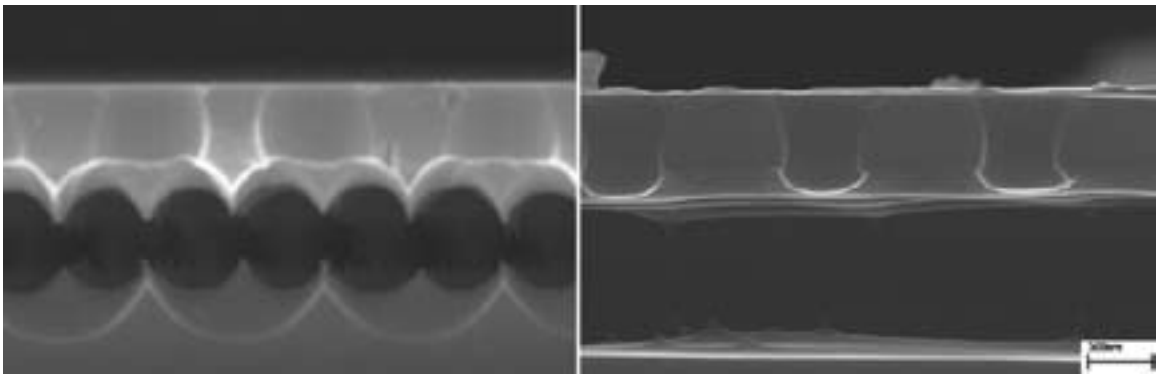

Figure 3: An GOPHER photonic crystal before annealing (left) and after annealing (right) [3].

Fabrication of Silicon Nitride Waveguides

Takia Wheat

Chemistry, Jackson State University

NNIN REU Site: Center for Nanoscale Systems, Harvard University, Cambridge, MA

NNIN REU Principal Investigator(s): Marko Lončar, School of Engineering and Applied Sciences, Harvard University

NNIN REU Mentor(s): Parag B. Deotare, School of Engineering and Applied Sciences, Harvard University

Contact: takia.m.wheat@jsums.edu, loncar@seas.harvard.edu

Abstract:

Over the years there has been an ongoing demand for faster, better, and less expensive computer systems. Microelectronics have so far offered quality solutions, but have now reached their limitations. Nanophotonics is one alternative to microelectronics. Owing to its much larger bandwidth, it has high potential for providing solutions to faster computer systems through the manipulation of light, which is channeled using a waveguide. These waveguides, based on total internal reflection, are able to transport light from one area to another. Once light is between two mediums of lower refractive indices, it is reflected back and trapped, and can then be used in integrated optics to link together various optical devices and components. In this work, we report the fabrication of silicon nitride waveguides which can operate at standard telecom wavelengths. The fabrication of this waveguide mainly involved nanofabrication processes like e-beam lithography, which was used for defining the waveguides, followed by reactive ion etching (RIE) to transfer the pattern onto the silicon nitride surface. Optimization of the RIE etch chemistry was carried out to generated straight and smooth walled waveguides.

Introduction:

In the technology of integrated circuits, it is advantageous to transport photons rather than electrons. Photons generate less heat, are less costly and travel faster. The technology has many applications ranging from: transporting light over long distances, and connecting components of miniaturized optical and optoelectronic devices and systems. The theory of waveguides operates on a principle of reflection which is achieved through a medium of refractive index n_1 embedded in a medium of a lower index of refraction n_2. Therefore $n_2 < n_1$. The medium of lower index of refraction traps the light within, confining multiple total internal reflections [1]. Through this concept, it is possible to transport light from one area to another. Optical waveguides are used in the technology of integrated optics for generating, focusing, coupling and detecting light [2]. The light in the waveguides can be guided in different modes depending on the geometry.

The experimental waveguides were designed to be single-mode with step refractive index distribution, composed of silicon nitride. The wafer had three different layers; silicon (base), silicon oxide (insulating layer), and silicon nitride (waveguide layer).

Experimental Methods:

The reactive ion etch (RIE) profile optimization was done with basic photolithography due to the time consuming fabrication of electron-beam written waveguides. During the basic photolithography, the wafer was properly prepared and cleaned, increasing the photoresist's ability to adhere to the surface of the wafer. Photoresist 1813 was spun on the surface of the wafer, followed by baking at 115°C for 90 seconds. The sample was exposed for five seconds and developed in MF-319 for 45 seconds. Silicon nitride was etched using a H_2, C_4F_8 and SF_6 chemistry. The gas ratios along with platen and coil power were optimized to generate straight walled etch profiles.

First, the sample was subjected to four runs, which started with varying H_2 and pressure while maintaining C_4F_8 (60 standard cubic centimeters per minute, sccm), SF_6 (35 sccm), and coil (ICP)-1000 W, at constant values. After studying the sample, a second set of four runs were done on the sample without using H_2 while keeping C_4F_8 (130 sccm), coil (ICP)-1000 W, and pressure-10 mTorr, constant. A third set of four runs were done with further increasing of the SF_6 while keeping the same parameters constant. Then a fourth trial of three runs was done with increasing platen and coil, while holding C_4F_8 and SF_6 constant.

Results and Discussion:

The recipe with H_2 etched faster into the SiO_2 layer. It was found from the second run that the etch rate of silicon nitride was much slower without H_2. Due to the fact that the Si_3N_4 was only 200 nm thick and the etching with the H_2 recipe was quite fast, we discarded the use of H_2 in further recipes. Further optimization of the recipe was done by varying

the other parameters. During trial II, the etching produced ranged from approximately 200-350 nm in five minutes. Runs two through four were excluded since run one (Figure 1) portrayed straighter walls than all the runs in trial I.

Trial III optimization followed that of trial II with variation of SF_6 and platen since in trial II it was discovered that decreasing the SF_6 and increasing the platen was not successful. We decided to increase SF_6, because in trial II decreasing the parameter did not straighten the walls, but achieved a reasonable etch rate. Run two of the recipe—SF_6 (100 sccm) and Platen (12 W)—portrayed the straightest walls and most proper etch depth over the other three runs. Figure 2 shows the etching done in run 1 (runs 3 and 4 show similar characteristics) and the walls are not straighter than the walls of the image in Figure 1, which led to run 1 having a better etch profile for trial III.

After finding an approximate value for parameter C_4F_8 and SF_6, we wanted to see the affect platen and coil had on the etching of Si_3N_4. We discovered that increasing the platen and coil, which are the power, created a deeper etch in the Si_3N_4 surface, see Figure 3. The image shows a darker line that separates the Si_3N_4 and SiO_2 layer.

After manipulating the recipe, it was found to produce a good anisotropic etch profile with C_4F_8 (130 sccm), SF_6 (100 sccm), platen (1000 W), coil (12 W), and chamber pressure (10 mTorr).

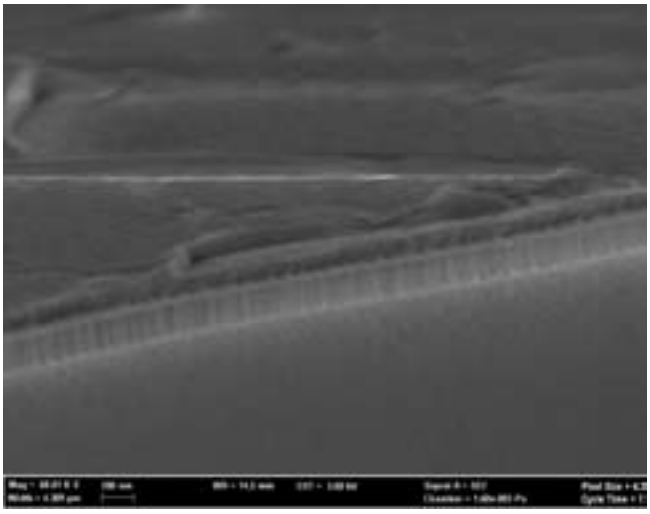

Figure 1: SEM image of Si_3N_4 sample from run 1 of trial II; etched 200 nm. Note: Photoresist not fully removed.

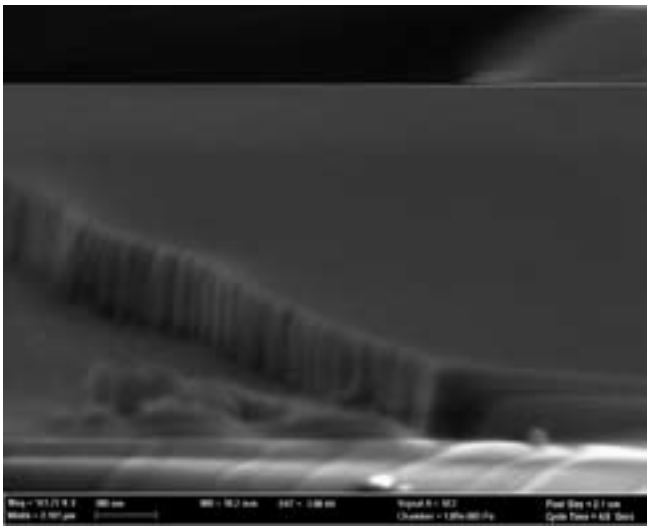

Figure 2: SEM image of Si_3N_4 sample from run 1 of trial III; etched 200 nm.

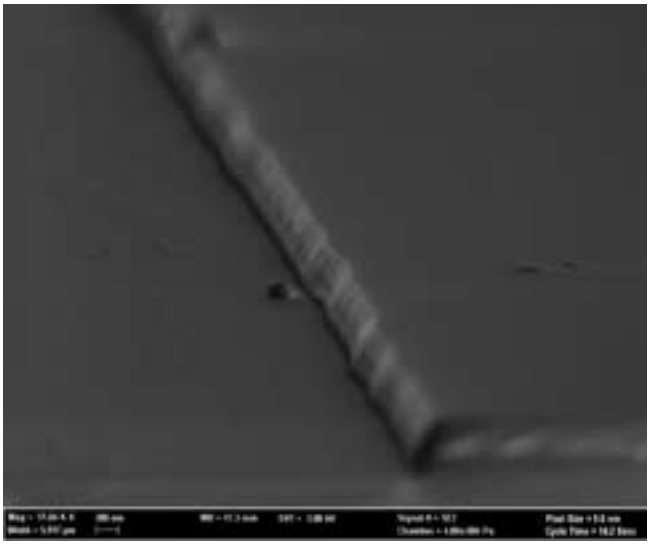

Figure 3: SEM image of Si_3N_4 sample from run 1 of trial IV; etched 450 nm.

Conclusions:

H_2 bonds with the fluorine in C_4F_8 producing hydrofluoric acid (HF), which is known to etch Si_3N_4. It is suspected that this reaction is what caused the deep etching in the Si_3N_4 layer and into the SiO_2 layer. The RF power platen and coil are the powers which generate the plasma. As they were increased, it also caused an increase in etching, because it increased the acceleration of ions as they were accelerated upon the surface of the Si_3N_4. With a straight wall etch recipe for Si_3N_4, the etch rate was determined to be 50 nm/sec. This etch rate will be used in future research to etch e-beam written samples to fabricate the actual waveguides.

Acknowledgements:

National Nanotechnology Infrastructure Network Research Experience for Undergraduates (NNIN REU) Program.

References:

[1] Madou, Marc J., (1997), Fundamentals of Microfabrication, Ron Powers, Boca Raton, Florida, 1, pp.14.

[2] Saleh, B.E.A and Teich, M.C. (2007) Fundamentals of Photonics, John Wiley & Sons, Inc. Hoboken, New Jersey, 8, pp.308-311.

Novel Fabrication Method for a High-Q Capillary-Based Whispering-Gallery-Mode Biosensor

Michael Zakrewsky

Chemical Engineering, Rensselaer Polytechnic Institute

NNIN REU Site: Nano Research Facility, Washington University in St. Louis, St. Louis, MO
NNIN REU Principal Investigator(s): Dr. Lan Yang, Electrical & Systems Engr., Washington University in St. Louis
NNIN REU Mentor(s): Dr. Sahin Ozdemir, Electrical & Systems Engineering, Washington University in St. Louis
Contact: zakrem@rpi.edu, yang@ese.wustl.edu, ozdemir@ese.wustl.edu

Abstract:

We developed a novel fabrication method for a capillary-based Whispering-Gallery-Mode (WGM) resonator by employing pressurized inert gas to overcome the effects of surface tension during the capillary pulling process. Current fabrication protocols employing hydrofluoric acid (HF) etching of the capillary wall produce rough interior surfaces resulting in lower quality factors due to scattering losses. Using our protocol, we produced capillaries with less interior roughness and higher quality factors, showed a near-linear relationship between gas pressure and wall-thickness, and laid out a plan for further improvements.

Introduction:

Optical sensors rely on the light/molecule interaction, which is significantly enhanced by a resonant structure. A variety of optical resonators have been investigated for ultra-sensitive and label-free sensing [1-3]. Among them, WGM resonators, in which light is trapped in circulating orbits by total internal reflections, hold the highest quality. The quality (Q-factor) of a resonator is an important parameter reflecting the power dissipation rate of a resonant system, and is defined as Q = ω•Stored Energy/Power Loss = ω•τ, where ω is the resonant frequency and τ denotes the photon lifetime in the resonator. Higher Q-factor implies stronger light-matter interactions [4], and Q-factors in excess of 100 million have been achieved in WGM resonators. Light can circulate around a WGM resonator millions of times allowing a single particle/molecule to cause a noticeable change in the transmission spectrum of outgoing light.

Over the past couple years, there has been a growing interest in the application of WGM resonators as biosensors, and they have been used for single molecule and label-free detection of a wide range of biomolecules; however, they also have the potential to quantify the behavior of amyloids and prions like never before. Unlike current analytical techniques, WGM biosensors are not limited to specific sample environments and large sample concentrations, which make them appealing for studying aggregate species. WGM biosensors provide real-time quantitative data on the change in refractive index and polarizability from which a particle's mass, conformation, and shape can be deduced, offering high-resolution kinetic data of amyloid nucleation and the conformation changes that occur during aggregation-all of which, to the best of the author's knowledge, have not been analyzed quantitatively, or at least not to the level of resolution possible with a WGM biosensor.

Before these experiments can be realized improvements need to be made to the resonators; in particular, higher Q-factors for water based samples and higher sensitivities to refractive index changes need to be achieved in a device that incorporates both the WGM resonator and fluidics to introduce our biological sample. For this reason, a capillary architecture was chosen as the sensor platform: the channel supports fluidics and the cross-sectional ring supports WGM.

Experimental Procedure:

Current fabrication methods call for tapering a glass capillary from an initial diameter of 1 mm down to 100 μm. Afterwards, the interior is etched with HF to reduce wall-thickness and achieve a desired sensitivity; however, doing so causes roughness to the interior surface, which increases scattering loss and subsequently diminishes the Q-factor.

To increase the Q-factor and sensitivity of capillary resonators, we developed a novel fabrication protocol by employing pressurized inert gas. By employing pressurized inert gas during fabrication, three improvements to the capillary resonator are achieved. First, we can fabricate thin-walled capillaries without the interior roughness attributed to acid etching. Second, we can fabricate capillaries with smaller mode volumes by decreasing the wall-thickness, thereby increasing the intensity and particle interaction of light within the resonator. Third, reflow of the resonator exterior, similar to procedures that made toroids with ultra-high Q-factors, can be performed to increase the Q-factors of capillary resonators.

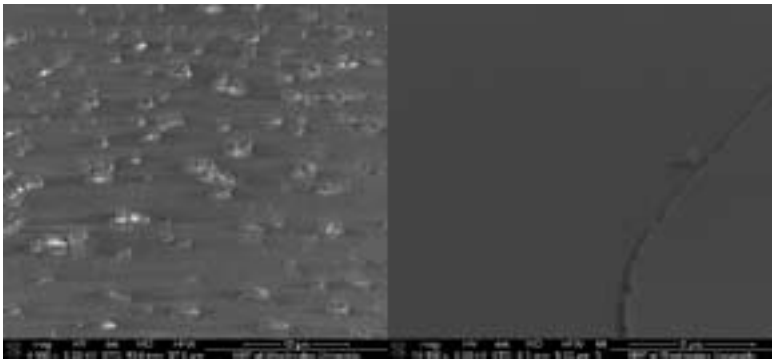

Figure 1: SEM images of capillary interior surfaces; acid etched (left), and pressurized with inert gas (right).

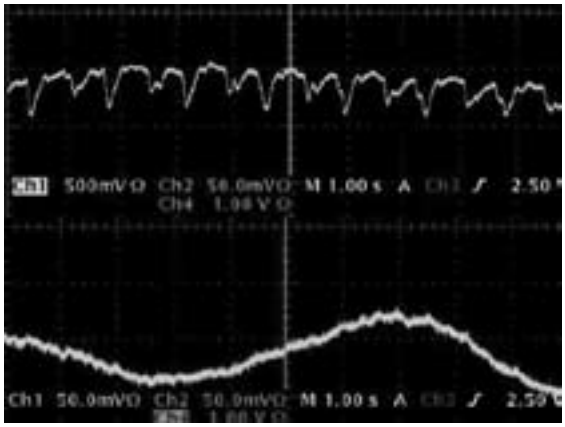

Figure 2: Transmission spectrum of a smooth capillary, before (top) and after acid etching (bottom).

Using our protocol, we produced capillaries with much less interior roughness than is possible with current HF etching methods (Figure 1). As expected, smooth capillaries showed a dramatic increase in *Q*-factor over acid etched capillaries.

The *Q*-factors of capillaries fabricated with pressurized inert gas were measured before and after etching with HF. Before etching, *Q*-factors around 10^4 were observed. After etching, resonance nearly disappears (Figure 2).

Next, capillaries were fabricated at various pressures to study the effect of gas pressure on wall-thickness, and showed a near-linear relationship (Figure 3). As gas pressure increased, the ratio of outer to inner diameter decreased.

Results and Conclusions:

Currently, fabrication of capillaries with sub-micron wall-thicknesses is being attempted, and the *Q*-factor and sensitivity of smooth capillaries supporting WGM are being tested. In the near future, reproducibility will be improved by using CO_2 lasers instead of a hydrogen flame to allow finer control of the glass temperature during pulling, and smooth capillaries will be fabricated using glass that is nearly exclusively preferred by others working with capillary WGM resonators due to its high quality, fused-quartz.

In conclusion, high-*Q* capillary-based WGM biosensors have the potential to further our understanding of both the light/molecule interaction in WGM resonators, and misfolding proteins and their diseases. We took the first step toward realizing this capability by developing a novel fabrication method that employs pressurized inert gas during the pulling process. Using our protocol we produced capillaries with smoother interior surfaces and higher *Q*-factors, showed a near-linear relationship between gas pressure and wall-thickness, and laid the groundwork for further improvements.

Acknowledgements:

National Science Foundation, National Nanotechnology Infrastructure Network Research Experience for Undergraduates (NNIN REU) Program, Amy Sears.

References:

[1] Armani, Kulkarni, Fraser, and Vahala. "Label-free, single-molecule detection with optical microcavities", Science, 317, pp.783-787, 2007.

[2] Vollmer and Arnold. "Whispering-Gallery-Mode Biosensing: Label-Free Detection Down to Single Molecules." Nature Methods 5 7 (2008): 591-96.

[3] Fan X.D. et al. "Opto-Fluidic Micro-Ring Resonator for Sensitive Label-Free Viral Detection." Analyst 133 3 (2008): 356-60.

[4] M.L. Gorodetsky, A.A. Savchenkov and V.S. Ilchenko, "Ultimate Q of optical microsphere resonators", Opt. Letters. Vol. 21, 453-455, 1996.

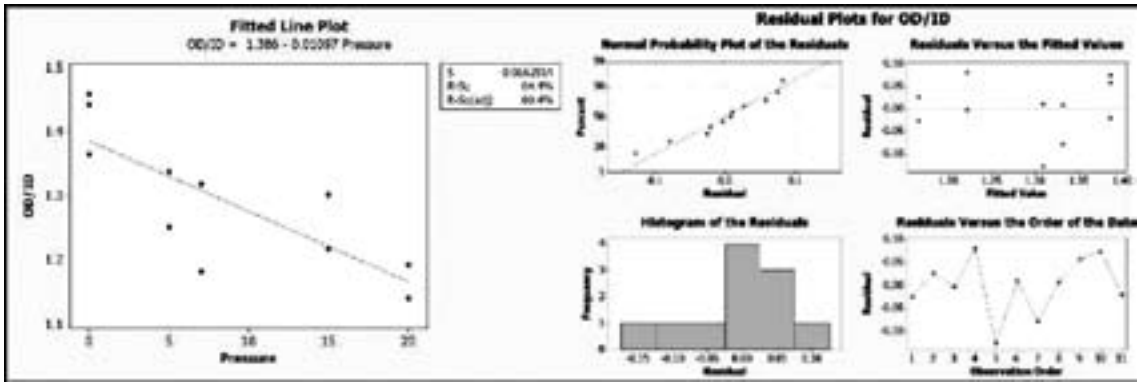

Figure 3: Near-linear relationship of gas pressure to wall-thickness.

Space-Charge Limited Current Calculations in Nanowires

Ian Braly

Chemical Engineering, Oregon State University

NNIN REU Site: Center for Nanotechnology, University of Washington, Seattle, WA
NNIN REU Principal Investigator(s): David S. Ginger, Chemistry, University of Washington
NNIN REU Mentor(s): Obadiah Reid, Chemistry, University of Washington
Contact: bralyi@onid.orst.edu, ginger@chem.washington.edu, obadiah@gmail.com

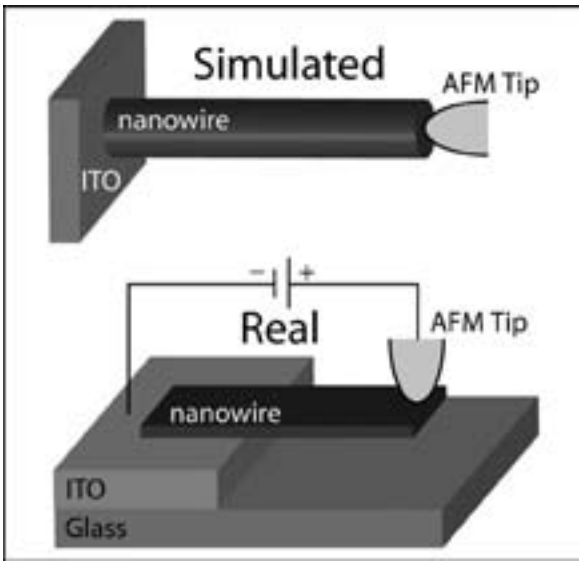

Figure 1: (top) The geometry of existing numerical models for space-charge limited current through a nanowire. (bottom) The geometry of AFM experiments on which space-charge limited currents are measured.

Abstract and Introduction:

Existing models of a space-charge limited current through a single polymer nanowire do not agree with experimental data from conductive-atomic force microscopy measurements. A better theoretical understanding of space-charge limited transport in these polymer nanowires [1] would allow for quantitative carrier mobility measurements [2]. Our hypothesis was that the disagreement between existing models and experiments was due to differences in the geometry. In this work we developed a numerical model that has a geometry conforming much more closely to that found in experimental measurements (see Figure 1). Our results suggest that the discrepancy between our models and experiments cannot be explained by this difference in geometry.

Procedure:

We used two coupled differential equations to simulate charge transport in our model: the drift-diffusion equation and the Poisson equation. The drift-diffusion equation describes how charge-carriers move through an electric field and in response to charge density gradients, while the Poisson equation describes how the electric field is affected by the charge-carriers.

We used COMSOL Multiphysics 3.5a to solve this coupled system of equations in a variety of geometries. This software solves differential equations by breaking up the geometry into smaller pieces and finding self-consistent solutions in each piece. This method is called the finite element method.

Our model development was centered on constructing a realistic geometry for the simulation. Control geometries were used in order to test that the model could reproduce understood scenarios such as the plane-parallel electrode case. Then, while only changing one element of the geometry at a time, more complicated cases (geometries) could be solved.

Results:

Figure 2 shows simulation results for the most experimentally conformal geometry we produced. The current density is much higher along the corners of the nanowire near the injection point, and then funnels towards the center of the nanowire near the extraction surface.

Figure 3 shows current-density voltage curves from an AFM experiment (circles) and our simulation (squares). The current density is dependant on the square of the injection voltage for both the experiment and the updated simulation, strongly suggesting a space-charge limited current.

Figure 4 shows current density-transport distance curves from an AFM experiment (circles), original simulation (triangles), and updated simulation (squares). Both of the simulated results show an inverse-square relationship between current density and charge-carrier transport distance. This is much different than the sub-linear dependence on length that the experimental results show.

Discussion:

It is unclear why the current density is higher at the corners in the nanowire in Figure 2. We speculate that this may not be a physical phenomenon, but rather an artifact in the simulation. This feature has been found in both the updated geometry model and in original simulations. Further investigation

is required to understand the origin of this feature, and whether it effects our results for total current density.

The dependence of current density on the square of the voltage suggests that both the simulated and experimental currents are space-charge limited (see Equation 1). There is still a lack of agreement between the experimental results from the single nanowire space-charge limited current experiment and the theoretical results from the model, even after the model geometry was made to better match the conductive-atomic force microscopy experiment. Both the original model and the updated model show a length dependence on the current density of L^{-2}. This suggests that the orientation of the atomic force microscope tip does not affect the current density's length dependence.

Conclusion:

Space-charge limited current measurements have been made in the past in order to measure the charge-carrier mobility of a single semiconducting polymer nanowire [2]. The simulations that were run in parallel to this experiment did not yield results that agreed with the experimental results. It was hypothesized that this lack of agreement was due to the model geometry not being realistic enough. We have developed a new model that reorients the atomic force microscope tip to touch the nanowire on the side of the wire instead of the end, and changes its shape from cylindrical to prism shaped.

Once the geometry was updated we verified that our model still produced a quadratic relationship between current density and voltage. This is evidence that the current remains space-charge limited. The length dependence of the current density was found to be L^{-2}. This relationship is very similar to the current density-length relationship that was found in the original model. From these results we conclude that neither the orientation of the atomic force microscope tip on the nanowire, nor the exact shape of the nanowire significantly affect the charge transport characteristics.

Further modeling of alternate geometries and investigation of the experimental conditions are required in order to explain the present discrepancy between our experiment and models.

Acknowledgements:

We thank the University of Washington NNIN Site Coordinator Ethan Allen. We thank the National Nanotechnology Infrastructure Network Research Experience for Undergraduates Program and National Science Foundation for funding.

References:

[1] H. Xin, F. Kim and S. Jenekhe. J.Am.Chem.Soc., 130(16), pp 5424-25 (2008).

[2] O. Reid, K. Munechika and D. Ginger. NanoLett., 8 (6), pp 1602-1609 (2008).

[3] A. Talin, F. Léonard, B. Swartzentruber, X. Wang, and S. Hersee, Phys. Rev. Lett., 101 (076802), 2008.

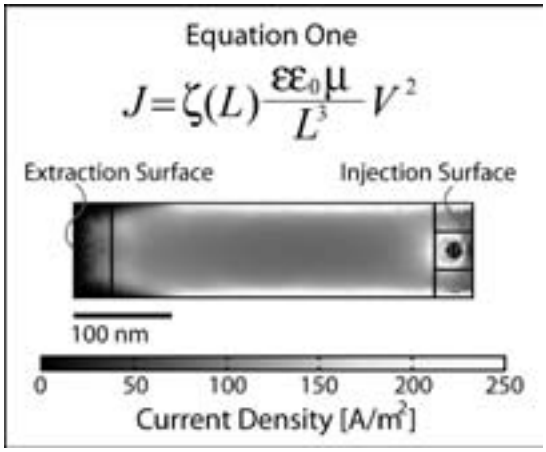

Figure 2: (top) The generalized equation for describing a space-charge limited current [3], where J is current density, ζ(L) is a geometry dependent function of length, $\varepsilon\varepsilon_0$ is the permittivity, μ is the charge-carrier mobility, V is injection voltage, and L is transport distance (wire length). (bottom) The solution of the updated model, showing current density.

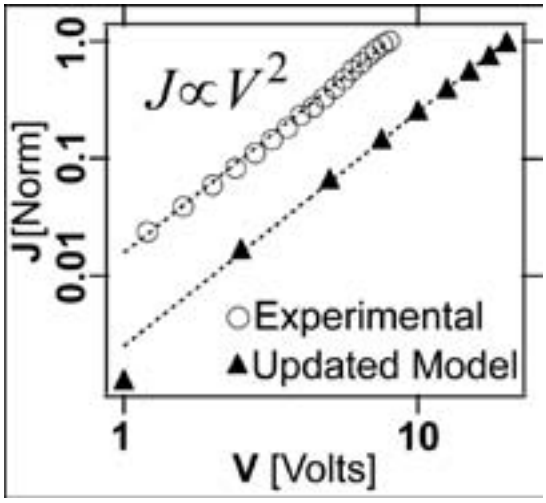

Figure 3: Current density versus injection voltage, with the experimental data (open circles), and the updated model data (closed triangles).

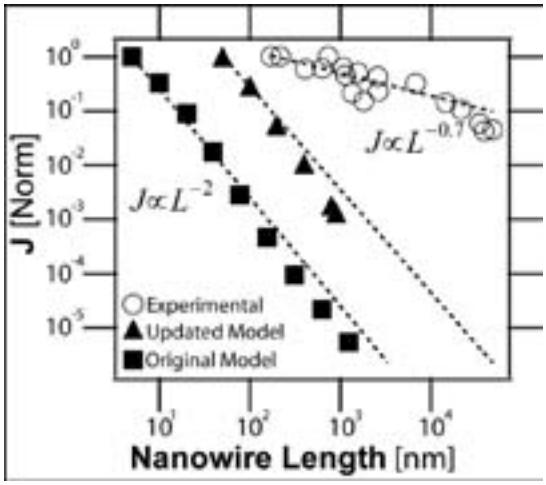

Figure 4: Current density versus wire length, with the experimental data (open circles), the updated model data (closed triangles), and the original model data (closed squares).

Raman Topography Studies of Eutectic Systems of Strontium Ruthenate and Ruthenium

Eric Hao

Engineering, University of California, Berkeley

NNIN REU Site: Penn State Nanofabrication Laboratory, Pennsylvania State University, State College, PA
NNIN REU Principal Investigator(s): Dr. Ying Liu, Department of Physics, The Pennsylvania State University
NNIN REU Mentor(s): Yiqun A. Ying, Neal Staley, Conor Puls; Physics, The Pennsylvania State University
Contact: eric_hao@berkeley.edu, liu@phys.psu.edu, yzy116@psu.edu

Abstract:

We report unexpected phenomena observed on the Sr_2RuO_4-Ru eutectic system featuring ruthenium (Ru) islands embedded in *p*-wave superconductor strontium ruthenate (Sr_2RuO_4) with a superconducting transition temperature (T_c) nearly twice that of pure Sr_2RuO_4. This enhancement of a *p*-wave superconductor is significant because of its similar structure (perovskite) compared to *d*-wave superconductors (high T_c superconductors). It occurs at the atomically sharp interface between the two materials, with the electronic states modified strongly. To examine this, we employed Raman spectroscopy, a convenient method of measuring phonon stiffness. A laser was shone onto the sample, where excited electrons scatter phonons—energy dependent on specific bonding structure—and the emitted photon was recaptured and analyzed. As we performed line scans across the interface, we noticed the phonons hardened near the interface, suggesting the T_c of the eutectic phase correlates with phonons.

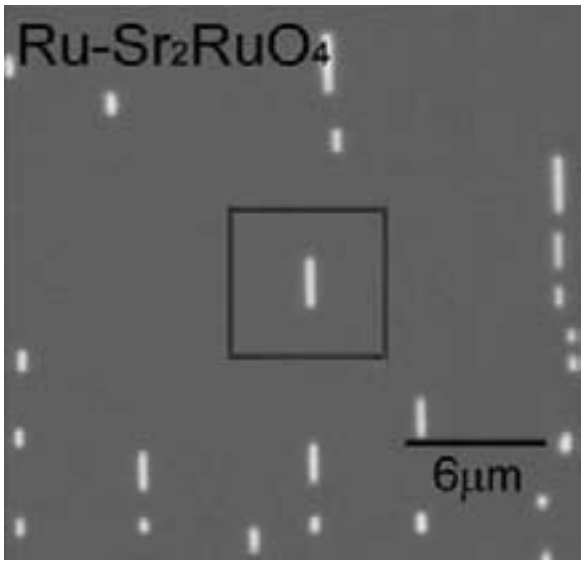

Figure 1: Eutectic system consisting of ruthenium (brightly lit areas) and Sr_2RuO_4.

Types of Superconductors:

The main theory for explaining superconductivity is the BCS Theory (named after Bardeen, Cooper, and Schrieffer), which, to put it simply, says that superconductivity relies on special electron-phonon interactions that create Cooper Pairs. If these Cooper Pairs can survive the vibrations of the crystal lattice (below a certain temperature T_c), then the material is superconducting. This theory, however, only explains the simplest type of superconductor—*s*-wave—which constitutes a majority of all superconductors. These *s*-wave superconductors typically have critical temperatures in the range of 0-10K. Another type of superconductor—*d*-wave—is well-known and studied for its high critical temperature characteristics (highest 140K); however these have extremely complicated crystal structures. The superconductor system we are interested in composes of Sr_2RuO_4—a chiral *p*-wave superconductor [1-4] that has T_c in range of *s*-wave (1.5K), but exhibits similar structure as *d*-wave—and ruthenium metal —a conventional *s*-wave superconductor (T_c = 0.5K). This eutectic system [5] is grown by adding ruthenium oxide to a strontium ruthenate substrate, with excess ruthenium forming islands about 1-2 μm in width and as long as 10 μm in length. The interface between these two materials exhibit an enhanced region of superconductivity: T_c = 3K. This is interesting because Sr_2RuO_4 usually is extremely sensitive to impurities, which destroy its superconductivity. This project aims to find evidence of crystal restructuring through use of phonon detection.

Procedure:

Raman spectroscopy discriminates materials based on bonding structure. To summarize, it works by shooting a photon at the sample, and collecting the inelastically reflected photon containing the "molecular imprint." This is quantified by measuring its resulting shift in energy.

A 514.5 nm wavelength laser, operating at 13 milliWatts of power, was shone onto a sample of the eutectic phase of

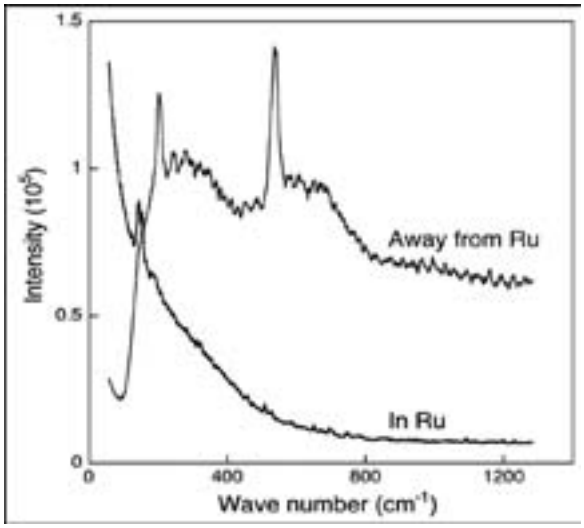

Figure 2: Spectrum of bulk ruthenium (bottom curve) and bulk Sr_2RuO_4 (top curve).

Sr_2RuO_4-Ru. Its spot size was determined using an optics formula, which came out to a 349 nm lateral resolution. First, we measured the Raman spectrum at bulk Sr_2RuO_4, which exhibited apex oxygen vibrations at 537.5 cm^{-1} and strontium vibrations at 203.11 cm^{-1}. We then measured the Raman spectrum at bulk ruthenium, which exhibited vibrations at 190 cm^{-1}. Since the enhanced phase occurs outside of the ruthenium island, we chose to measure the vibrational shift of Sr_2RuO_4.

We first performed line scans, starting at bulk Sr_2RuO_4 and moving in 349 nm increments, collecting spectra at each point, until the strontium and oxygen vibrational modes disappeared inside the ruthenium island.

Results:

We received data ranging from 50 cm^{-1} to 1300 cm^{-1}. First, we cropped out the irrelevant data, obtaining two sets (one for strontium and one for oxygen). We removed the linear bias associated with each region, and fit Gaussian peaks, recording its central peak position. We noticed a shift of about 8.3 cm^{-1} in the oxygen vibration, a change of about 1.3%, as well as a shift of about 1.6 cm^{-1} in the strontium vibration, corresponding to a change of about 0.8%. We were also successful at reproducing this phenomenon, through repeated line scans in different areas, and different islands.

Conclusion:

Raman spectroscopy data gave evidence of so-called "phonon stiffening." The change in the vibrational frequencies of both the strontium and oxygen reflected a change in the phonons associated with the crystal structure. This change in crystal structure was correlated with the change in the critical temperature of the 3K enhanced phase, suggesting that phonons play an important role in the enhancement of the eutectic system.

Further suggested experiments include temperature-dependent as well as polarization dependent Raman spectroscopy measurements in order to further quantify this "phonon stiffening."

Acknowledgments:

The author would like to thank Dr. Y. Liu; Y. A. Ying; N. Staley; C. Puls; J. Stitt; Dr. J. Robinson; Dr. R. Redwing, as well as the National Science Foundation; The NNIN REU Program; the Department of Energy; and the Department of Defense, Army Research Office for funding.

References:

[1] A. P. Mackenzie, Y. Maeno, Rev. Mod. Phys. 75, 657 (2003).

[2] K.D. Nelson, Z.Q. Mao, Y. Maeno, Y. Liu, Science 306, 1151 (2004).

[3] J. Xia, Y. Maeno, P. T. Beyersdorf, M. M. Fejer, A. Kapitulnik, Phys. Rev. Lett. 97, 167002 (2006).

[4] F. Kidwingira, J. D. Strand, D. J. van Harlingen, Y. Maeno, Science 314, 1267 (2006).

[5] Y. Maeno et al., Phys. Rev. Lett. 81, 3765 (1998).

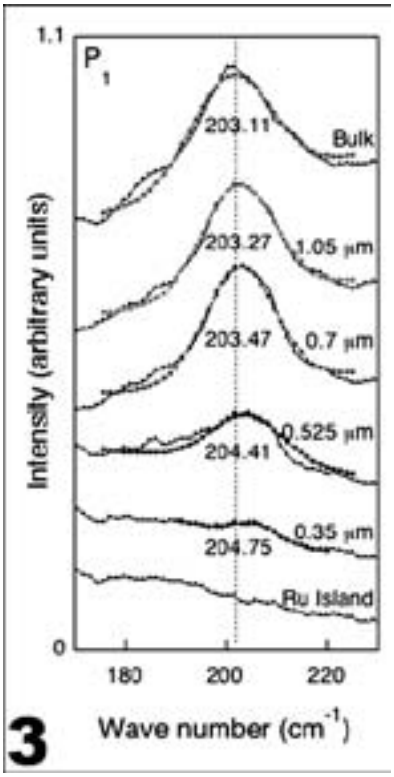

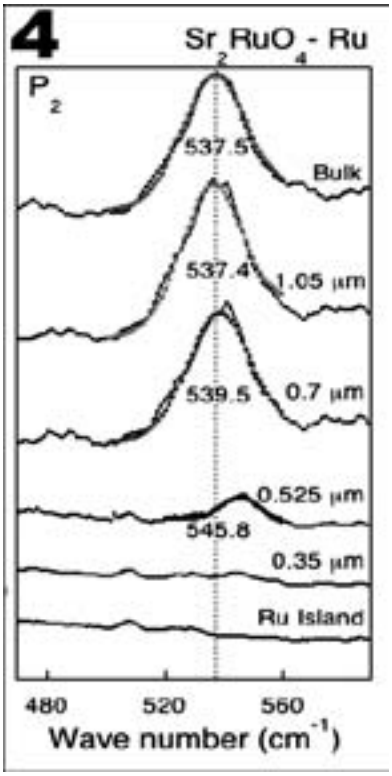

Figure 3: Sr vibration line scans with peak positions and distance from island.

Figure 4: Oxygen vibration line scans with peak positions and distance from island.

Fabrication of Sub-Micron Lateral Spin Valves

Alayne M. Lawrence

Chemical Engineering, Xavier University of Louisiana

NNIN REU Site: Nanofabrication Center, University of Minnesota-Twin Cities, Minneapolis, MN
NNIN REU Principal Investigator(s): Professor Paul Crowell, Physics, University of Minnesota-Twin Cities
NNIN REU Mentor(s): Michael Erickson, Physics, University of Minnesota-Twin Cities
Contact: alawren1@xula.edu, crowell@physics.umn.edu, erickson@physics.umn.edu

Introduction:

This research project focused on the fabrication of sub-micron lateral spin valves, which are devices consisting of two or more conducting materials that allow us to measure spin injection and relaxation in metallic structures. These spin valves modulate electrical transport depending on the alignment of two magnetic electrodes. In this case, the two magnetic electrodes are separated by a channel of a normal metal, which can be copper, silver or aluminum. One of the major problems with these spin valves is that the resistivity of the normal metal channel, which is grown by evaporation, is dominated by defects. We suspect that if we make these spin valves out of better materials then the spin lifetime will increase. Progress on the fabrication of lateral spin valves of high purity, high conductivity transport channels of copper, aluminum, and silver will be presented.

Experimental Procedure:

Different methods were employed to increase the diffusion length by reducing the resistivity using high purity wires and foils. First, we selected high purity wires and foils on which we intended to deposit ferromagnetic contacts. The aluminum, copper and silver wires used were all approximately 99.99% pure. The aluminum and copper foils were both approximately 99.999% pure and the silver sample used was approximately 99.998% pure. We then measured the residual resistivity ratio of the wires and foils before and after annealing.

Residual Resistivity Ratio:

The measurement we were most concerned with was the residual resistivity ratio (RRR). RRR is measured by the resistance of a sample at room temperature divided by the resistance at a low temperature. At a low temperature, the resistance of an ordinary metal is determined by scattering from defects, while at room temperature the resistivity is dominated by scattering from lattice vibrations. A cleaner sample will therefore have a higher RRR. (See Figure 1.)

Dunk Probe:

At first we were measuring a crude RRR number by measuring the resistance at room temperature and then measuring the resistance at 77K by dunking it into liquid nitrogen. As the measurements progressed, it was clear we needed to examine the temperature dependence of the resistivity below 77K; so in order to do so we decided to use a liquid helium dunk probe to get more accurate data.

The dunk probe works by simply attaching a sample to a large probe and then actually dunking it in a helium Dewar. Figure 2 shows data obtained using the dunk probe.

Annealing:

In order to fabricate better spin valves, we explored improving the properties of the normal metal by annealing. Annealing is a heat treatment that is used to change the grain structure of samples in order to increase the electron transport.

The first anneal was conducted in vacuum. Samples of high purity wires were placed in a quartz tube inside a furnace which was connected to a turbo-molecular pump. Inside the furnace the temperature was brought up to 350°C at a pressure of 4×10^{-6} Torr. After approximately six hours of annealing, we discovered that the RRR did not change significantly and therefore we decided to try annealing in an

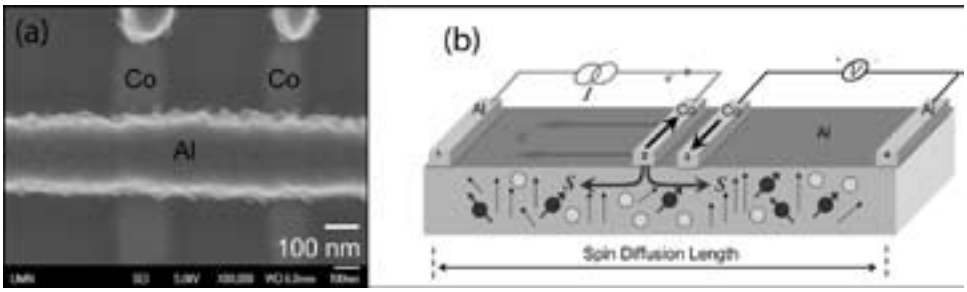

Figure 1: (a) SEM micrograph of a lateral spin valve; (b) Schematic diagram of the device.

oxygen atmosphere. The oxygen annealing was basically conducted in the same manner as the vacuum annealing; the only difference was that a furnace was connected to an oxygen tank instead of a vacuum pump. In addition, a slightly higher temperature of 400°C was used.

Photolithography:

The annealing processes were both done on high purity wires. Eventually we decided to test on high purity foils. Astonishingly, the high purity foils gave RRR's that were significantly larger. We decided to use these foils as the channel for our future spin valves. Since the foil area was very large and the channels for these devices are very small, photolithography was used to etch micron scale wires from foils.

For this process, first the high purity metal foils were mounted on a glass substrate with wax. A thin layer of photoresist (S1818) was then spun followed by a two minute soft bake at 105°C. Second, a wire was mounted onto the foil as a photolithography mask and the same resist was spun again and baked. Third, after the second soft bake was done the sample sat under an ultraviolet light for two minutes in order to keep only the small wire that we wanted. The wire was removed then the resist was developed and a wet etch was done through the metal foils so that a wire was created.

Results and Conclusions:

A comparison of the RRR's amongst different samples suggests that we can improve the transport properties of high purity metal foils. The ability to fabricate spin valves from these materials may lead to better understanding of the role of defects and grain structure on spin relaxation. Additionally SEM micrographs suggest that we may have been able to change the grain structure of metals through annealing. With this knowledge we will be able to go forth and make spin valves out of high purity materials in hope of increasing the spin lifetime. In addition, this work may serve to ultimately develop a new process to deposit ferromagnetic contacts on a single crystal wire.

Acknowledgements

I would like to acknowledge Professor Paul Crowell, Michael Erickson, Eric Garlid and Mun Chan from the Physics Department at University of Minnesota-Twin Cities. I would also like to acknowledge Christopher Leighton Lab in Materials Science at the University of Minnesota-Twin Cities. Lastly, I would like to acknowledge National Nanotechnology Infrastructure Network Research Experience for Undergraduates Program and National Science Foundation for funding.

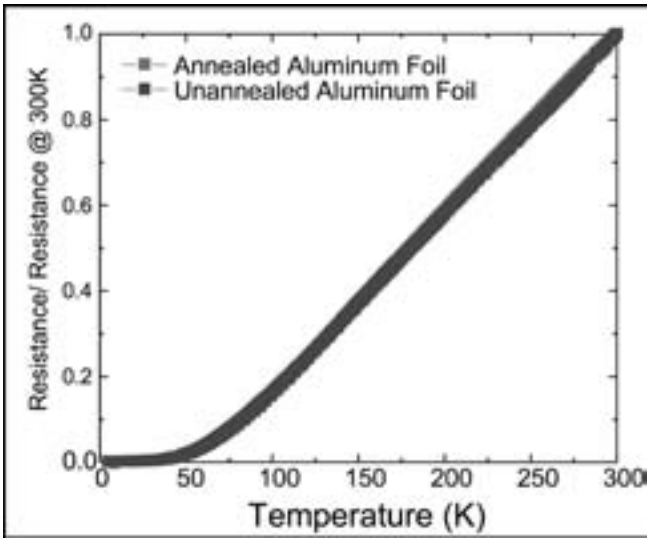

Figure 2: Typical resistivity data for an Al foil.

Sample	Unannealed	Vacuum Annealed	Oxygen Annealed
Aluminum Wire	10.554	11.455	16.203
Copper Wire	7.114	7.635	7.843
Silver Wire	5.129	5.54	5.222
	Unannealed	Annealed	
Aluminum Foil	840	1090	
Copper Foil	271	563	
Silver Foil	25	32	

Figure 3: Table of all RRR measurements.

Magneto-Transport in Photoexcited Diamond

Sarah Reiff

Physics, Marquette University

NNIN REU Site: Nanotech@UCSB, University of California, Santa Barbara, CA

NNIN REU Principal Investigator(s): Professor David Awschalom, Center for Spintronics and Quantum Computation, University of California Santa Barbara

NNIN REU Mentor(s): Joseph Heremans (2005 NNIN REU at Cornell), Center for Spintronics and Quantum Computation, University of California Santa Barbara

Contact: sarah.reiff@marquette.edu, awsch@physics.ucsb.edu, jheremans@umail.ucsb.edu

Abstract and Introduction:

Diamonds are uniquely suited for electronic and spintronic device applications. Ultrahardness, a wide band-gap of 5.5 eV, and a high thermal conductivity are ideal material properties for electronic devices requiring high power, high frequency, or high temperature. Additionally, defects in diamond are a single-spin system and single photon source, with potential for room temperature quantum computation. However, little is known about certain electrical properties in diamond. Here, we attempt to determine the carrier type and density of a single-crystal, nitrogen-rich diamond, by measuring the photoexcited Hall effect. Using a physical properties measurement system (PPMS), it is possible to take these measurements over varied temperatures and magnetic fields.

Experimental Procedure:

In this investigation, we explored single crystal, type Ib diamond, grown by the high-temperature, high-pressure method with a substitutional nitrogen concentration of 10^{19} atoms/cm^3. Using small-scale photolithography techniques and electron-beam deposition, we evaporated 100/500/900 Å of titanium/platinum/gold in a four pad Van der Pauw geometry (Figure 1). Each contact pad was 1 mm^2 and the gaps between neighboring contacts were 50 μm. The large contact pads allowed for an optical fiber to be glued to the area at the center of the pads in a process known as pig-tailing. The fiber was attached directly onto the sample with optical glue [1]. After metallization, one sample was annealed at 230°C for 36 hours to eliminate any surface conduction effects caused by hydrogen-terminated bonds.

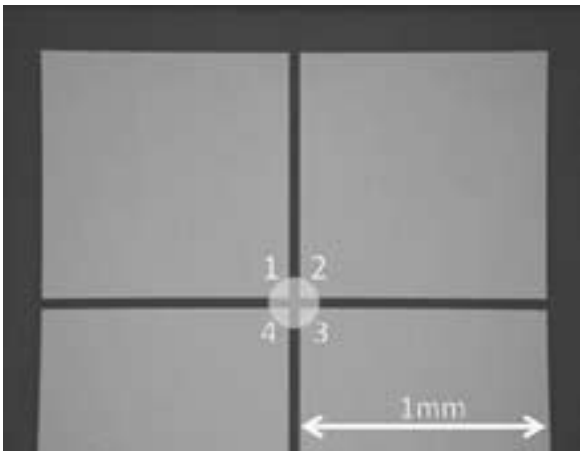

Figure 1: An optical micrograph of a diamond sample (dark color) with 1 mm x 1 mm Ti/Pt/Au contact pads (light squares). The contact pads are numbered in the Van der Pauw geometry. The lightest circle represents the photoexcited area.

The measurements were taken using a PPMS, which is a cryogenic chamber capable of cooling down to temperatures as low as 1.8 K. A superconducting electromagnet, within the PPMS, can apply magnetic fields to the sample up to 14 T normal, which is optimal for Hall effect measurements. The integrated electronics in the PPMS allow for a large array of measurement capabilities; however, it does not provide a system for optical illumination. Two modifications were critical for photoexcitation with a powerful, external laser.

First, a custom probe stick insert was designed and fabricated to lower the fiber and sample down the length of the sample chamber and into the measurement space (Figure 2 a,b). The stick was made of G-10 fiberglass with non-magnetic brass fixtures. The G-10 pieces were bonded together using cryogenic epoxy. The thermal expansion of all materials used was carefully considered for cycling from room temperature to 10 K to ensure that the stick insert remained shorter than the PPMS sample chamber.

Once the fiber was fed through the probe stick, it was pig-tailed directly onto the sample (Figure 2c). The diamond was photoexcited using a sub-bandgap 532 nm (2.3eV) laser beam which passed through a series of expansion optics and focused into a 105 μm core fiber. To withstand temperatures as low as 4.2 K, the fiber had aluminum cladding. The other end of the fiber was directed via a Teflon® ferrule out of the PPMS through the second modification: a specialized vacuum fitting consisting of a Swagelok and KF flange [2].

In our setup, the 2.3 eV laser was used to optically bridge the center region between the pads, and excite carriers from within the diamond. These nitrogen-rich diamonds have

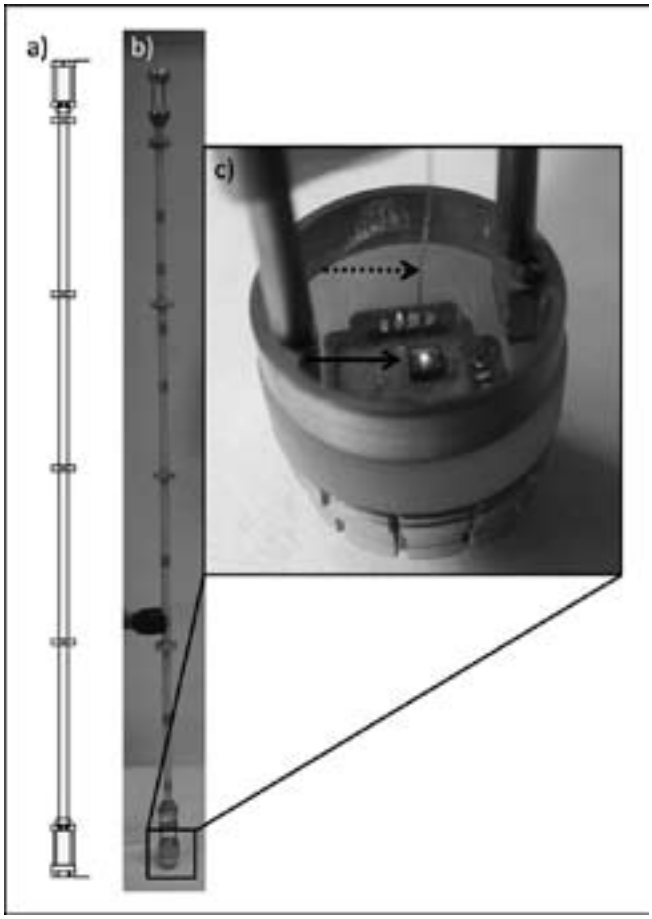

Figure 2: a) A schematic drawing of probe stick insert design. b) Image of the fabricated probe stick insert. c) View of the lower portion of stick insert including sample (solid arrow) and pigtailed optical fiber (dotted arrow).

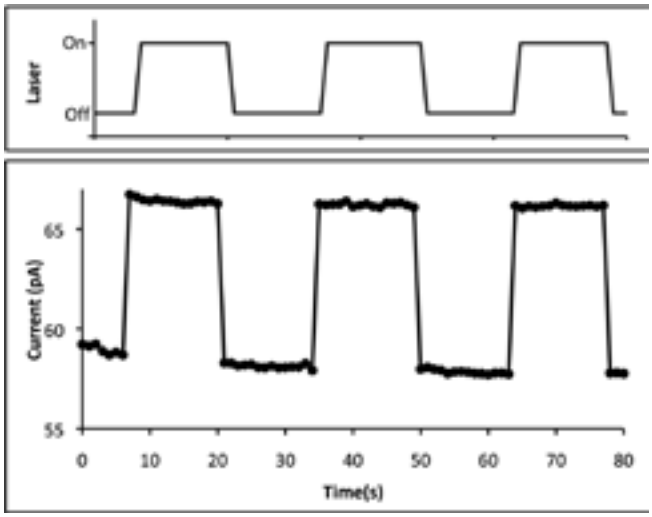

Figure 3: Plot of current (pA) and laser state vs. time (s) showing an increased current corresponding to times when the laser is used to photoexcite the sample.

shown photoinduced charge storage effects likely due to the presence of substitutional nitrogen defects, believed to reside 1.9eV below the conduction band [3]. To verify photoconductivity, the stick assembly was tested at room temperature by applying a DC voltage across two pads, between which the current was measured using a current preamplifier. Figure 3 shows the measured current between pads 2 and 4, dependent on the laser illumination as plotted on a time axis. Under illumination, there should be an increase in the current due to the excitation of carriers and a decrease when the laser is blocked. This is a successful proof of concept that the pig-tailed fiber can indeed demonstrate photoconductivity in type Ib diamond.

Conclusions:

We have demonstrated a successful photoconductivity technique using a custom designed PPMS probe stick insert and pig-tailed optical fiber on single crystal, nitrogen rich diamond. With this, we are now able to subject samples to normal incident magnetic fields of a few Tesla over a large range of temperatures. Having successfully seen photoconductivity in this system, we can begin to investigate the photoexcited Hall effect in type Ib diamond.

Acknowledgements:

I would like to thank my mentors, Joseph Heremans and Shawn Mack, my principal investigator, Prof. David Awschalom, fellow cohort, Matthew Brehove, and the rest of the Awschalom group for their constant support and guidance during the program. I would also like to thank Angela Berenstein, the UCSB REU site coordinator. This work was sponsored by the National Science Foundation, the Air Force Office of Scientific Research, and the National Nanotechnology Infrastructure Network Research Experience for Undergraduates Program.

References:

[1] F. M. Mendoza, Ph.D. thesis, UC Santa Barbara, 2008.
[2] E.R. Abraham, E.A. Cornell, Applied Optics, 37, pp.1762 (1998).
[3] F. J. Heremans, et al., Appl. Phys. Lett. 94, 152102 (2009)

Fabrication of a Stable Tunable Fabry-Perot Interferometer in the Fractional Quantum Hall Regime

Paden Roder

Physics, Grinnell College

NNIN REU Site: Center for Nanoscale Systems, Harvard University, Cambridge, MA
NNIN REU Principal Investigator(s): Dr. Charles Marcus, Physics, Harvard University
NNIN REU Mentor(s): Angela Kou, Douglas McClure; Physics, Harvard University
Contact: roderpad@grinnell.edu, marcus@harvard.edu, akou@physics.harvard.edu, dmcclure@fas.harvard.edu

Abstract:

Electronic Fabry-Perot interferometers on high mobility gallium arsenide / aluminum gallium arsenide heterostructures have recently been used in attempts to detect non-Abelian statistics in the fractional quantum Hall regime. Though successful in the integer quantum Hall regime, these devices appear to lack the electrostatic stability needed for interference measurements at fractional filling factors. This is likely due to the fact that the doping of the material is optimized for high mobility, leading to poor gateability. Here we report on the development of a new generation of devices where gates are deposited in etched trenches rather than on the surface of the chip, allowing them to operate at smaller voltages where they are more stable.

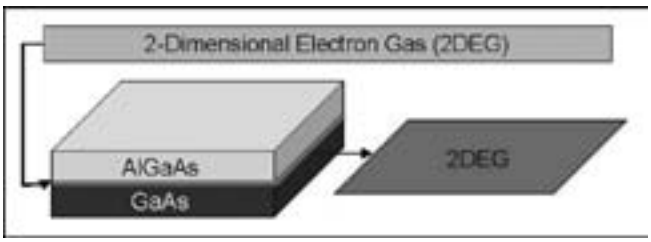

Figure 1: A two-dimensional electron gas.

Introduction:

Under exchange of identical particles, fermions have an anti-symmetric wave function whereas bosons have a symmetric wave function. This difference in symmetry properties is responsible for the characteristics of different particles, such as photons and electrons. However, particles that are neither fermionic nor bosonic, termed anyons, have been hypothesized to occur in the fractional quantum Hall regime [1]. The filling factor 5/2 has received particular attention since the anyons there are believed to be non-Abelian and therefore potential building blocks for a topological quantum computer [2].

In the Hall effect, a current in a two-dimensional (2D) electron gas (Figure 1) running orthogonal to a magnetic field generates a Hall resistance, perpendicular to both the current and the magnetic field, due to the Lorentz force. At low enough temperatures and high enough magnetic fields, quantization of the energy spectrum leads to plateaus in the Hall resistance known as the quantum Hall effect.

Furthermore, it has been observed that certain quantized Hall resistances most likely result from the formation of correlated states where charge is carried by anyonic quasiparticles whose charge is a fraction of an electron's. For these fractional quantum Hall states to form, a high-mobility 2D electron gas is required. Such a 2D electron gas can be created at the interface of a gallium arsenide/aluminum gallium arsenide heterostructure [3]. An interference device, seen in Figure 2, defined by negative voltages applied to metal gates on the surface of the chip, has been proposed to detect the non-Abelian anyons required for topological quantum computing via their effect on the relative phase of interfering trajectories. So far, a major obstacle has been the electrostatic stability of the device.

Here, etching the interferometer into the chip is explored as a possible way to reduce the needed gate voltages, possibly increasing stability.

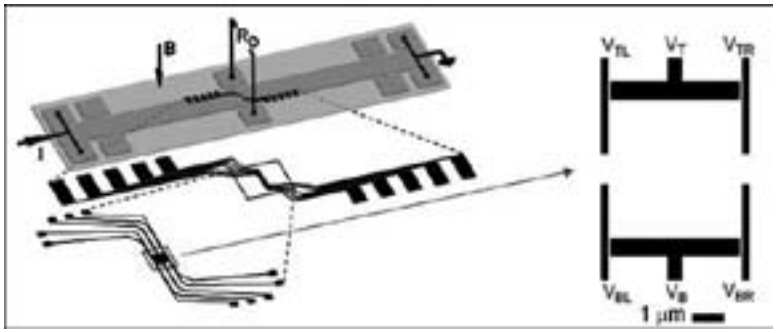

Figure 2: An electronic interferometer device is shown on typical Hall bar used in quantum Hall measurements [4].

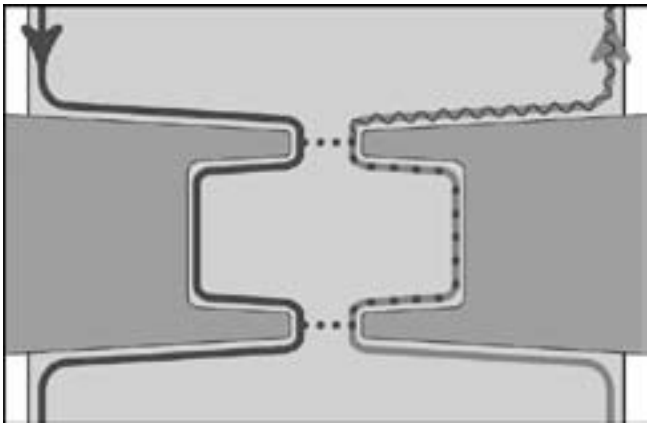

Figure 3: Charges in the two-dimensional electron gas travel along the edges of the device. Tunneling at the two quantum point contacts leads to interference [5].

Methods:

Previous fabrication methods of the electronic interferometer deposited the gates on the surface of the heterostructure. The gates' large distance to the 2D electron gas and screening from the donor layer necessitate the use of relatively large gate voltages, resulting in unstable, "switchy" device behavior. By depositing the gates in etched trenches instead of on the surface, both of these problems may be alleviated. The drawback of this method is that etching the interferometer features becomes difficult when dealing with separations of short distances (in our case, 140 nm). If etched too far, the gates could become shorted due to lateral etching. If etched too little, no advantage is observed.

In order to find the optimal fabrication parameters, multiple devices were written onto a chip using electron beam lithography at different exposure doses. After developing, the chip was then etched some distance. This procedure was repeated using multiple chips, where for each chip, the distance etched was varied. Finally, titanium/gold gates were deposited via thermal evaporation.

After fabricating devices that passed visual inspection in the scanning electron microscope, the gates were tested by measuring the device resistance as a function of gate voltage at 4 K. A sharp rise in resistance signals depletion of the 2D electron gas under the gates. Comparing the gate voltage at which depletion occurs in etched versus unetched samples provides a quantitative measure of the effect of the etching.

Results and Conclusions:

The farthest distance etched so far was 115 nm. Since the distance from 2D electron gas to the surface of the heterostructure is 200 nm, the distance to the gates is 85 nm. As seen in Figure 4, despite the etched features being connected, the gates do not short. Modeling the gates and the 2D electron gas as a parallel plate capacitor suggests that the absolute value of the depletion voltage in the etched device should be reduced by 0.386V from that in the unetched device. Experimentally, a decrease of 0.3 V is observed. However, the depletion voltage in both cases is roughly 1 V more negative than that predicted from this simple model, suggesting that screening from the donor layer may still be an issue.

Future Work:

The next set of devices can be etched farther in order to further reduce the gate voltages needed. Once an optimal etch depth is chosen, the device will be cooled in a dilution refrigerator and used for fractional quantum Hall interferometry. If the etching has led to increased stability, non-Abelian statistics may finally be observed.

Acknowledgements:

I would like to thank the Charles Marcus group, specifically my mentors Angela Kou and Douglas McClure, for providing an immense amount of guidance, knowledge, experience, and patience during the summer. Also, I would like to thank Kathryn Hollar, the Harvard CNS staff, the NSF, and the NNIN REU program for an unparalleled summer experience.

References:

[1] Wilczek, F. Fractional Statistics and Anyon Superconductivity. World Scientific, Singapore, 1990.

[2] Kitaev, A. Y. "Fault Tolerant Quantum Computation by Anyons", Annals of Physics, 303, 2- 30 (2003).

[3] Stormer, H. "Nobel Lecture: The Fractional Quantum Hall Effect" Reviews of Modern Physics, 71, 875-889 (1999).

[4] McClure, D. et al. "Edge-State Velocity and Coherence in a Quantum Hall Fabry-Perot Interferometer" (2009), arXiv:0903.5097 [5] Illustration by Douglas McClure.

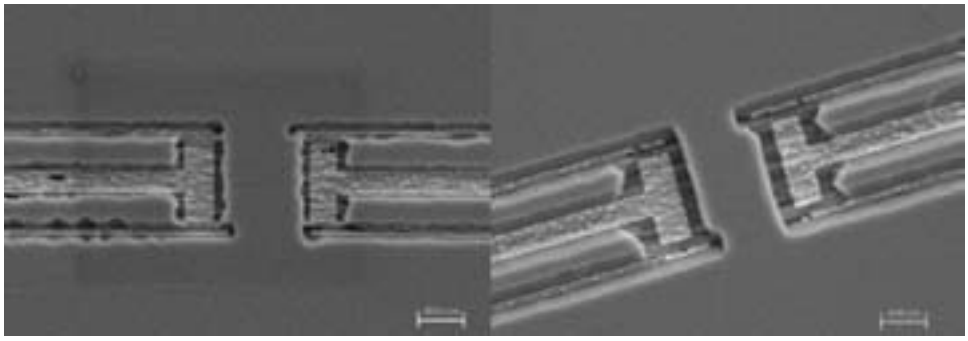

Figure 4: The left device is etched ~ 60 nm and the right device is etched ~ 115 nm.

Imaging and Characterization of Carbon Nanotube Growth and Transfer

Stephanie Bojarski

Material Science and Engineering, Lehigh University

NNIN REU Site: Stanford Nanofabrication Facility, Stanford University, Stanford, CA
NNIN REU Principal Investigator(s): H.-S. Philip Wong, Electrical Engineering, Stanford University
NNIN REU Mentor(s): Arash Hazeghi, Electrical Engineering, Stanford University
Contact: sab410@lehigh.edu, hspwong@stanford.edu, ahazeghi@stanford.edu

Abstract:

Carbon nanotubes (CNTs) have extremely high strength, flexibility, and excellent electrical properties as either a metallic or semiconducting material. Semiconducting CNTs are thus potential candidates for logic devices, such as carbon nanotube field effect transistors. Dense parallel arrays of CNTs are grown by chemical vapor deposition (CVD) on a quartz substrate and then transferred onto a silicon wafer, while, ideally, maintaining the same high density and alignment as the growth. However, issues with the current process include incomplete nucleation of CNTs at the catalyst strip along with a lower percentage of multiple transferred CNTs. We use atomic force microscopy (AFM) and scanning electron microscopy (SEM) to measure the approximate diameters and densities of CNTs and nanoparticles present during various stages of the growth and transfer.

In this work we characterized the diameters of carbon nanotubes and other nanoparticles present on the surface of various growth samples. We also characterized the surfaces of various lithography treatments to determine the plausibility of patterned ferritin as a CNT catalyst. This helped us to better understand these processes by determining how complete the chemical nucleation of CNTs was during the growth and how to improve future growths. A more complete understanding and further optimization of the growth and transfer processes parameters will allow for fabrication of devices with high CNT density, which is desirable for logic applications.

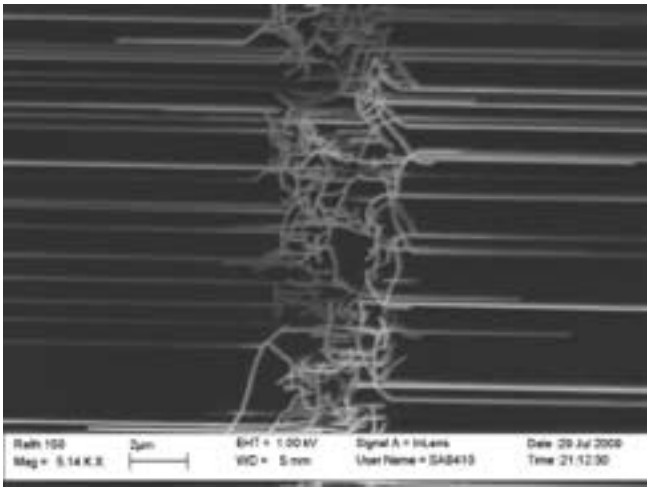

Figure 1: Catalyst strip with dense parallel growth.

Background:

Carbon nanotubes are essentially tubes of rolled up graphene with a typical diameter of 1-5 nm. In this work, we used tapping mode atomic force microscopy to obtain a topographical image of the CNT growth and transfer surfaces. The SEM was also utilized as a larger scale imaging tool to determine CNT density, Figure 1.

Methodology:

CNTs were grown onto a single crystalline quartz wafer and later transferred onto a silicon wafer to allow for complementary metal oxide semiconductor (CMOS) processing.

Iron nanoparticles were patterned into 5 μm wide strips on a quartz wafer. The wafer was then calcined at 900°C to remove any contamination. CNTs were then grown by CVD in a methane atmosphere which was raised to about 850°C. After the growth was complete, a gold thin film (~1500Å) was evaporated on the quartz, covering the CNTs. Thermally releasing tape was then applied to the gold/CNT combination, peeled off, and transferred to the silicon wafer. The wafer was then placed in an oven at 130°C, at which the tape released. The wafer then underwent three minutes of oxygen plasma cleaning and four minutes of argon plasma cleaning to remove any contamination from the tape.

After three minutes of liquid gold etch (sodium iodide, iodine, and water), parallel arrays of CNTs should be present on the silicon wafer.

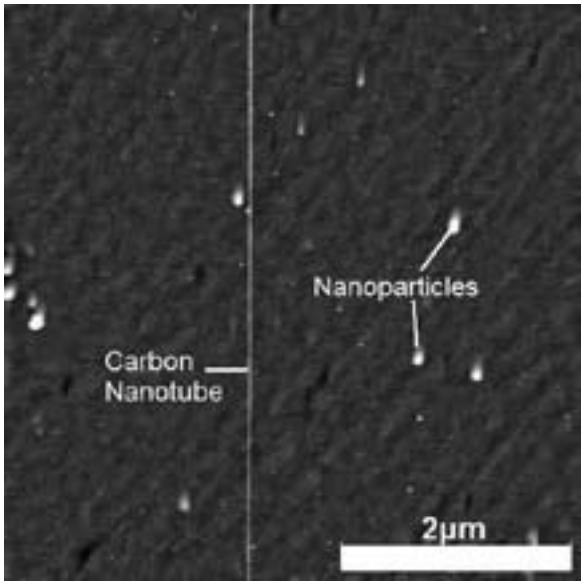

Figure 2: AFM image of CNT and nanoparticles.

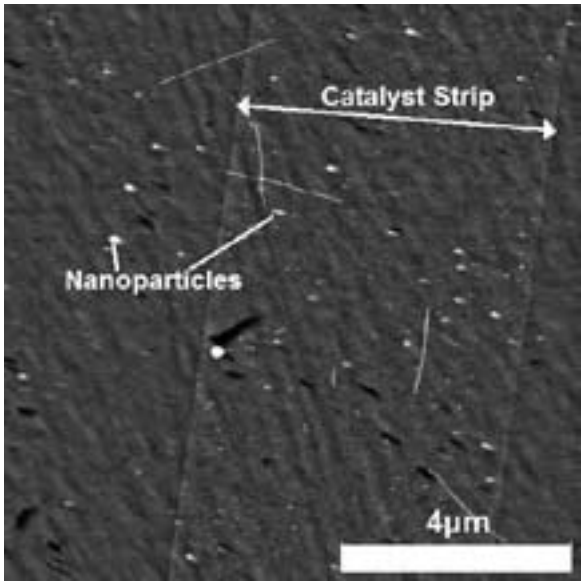

Figure 3: AFM of nanoparticles in and around the catalyst strip.

Results and Discussion:

Unsuccessful growths were investigated using the AFM to measure the diameters of the CNTs in areas of sparse growth. These diameters were then compared to the diameters of particles within the growth area, Figure 2. The average height of the CNTs was ~ 1.7 nm while the average particle height was ~ 2.4 nm.

Particles on and around catalyst strips with no nucleation, Figure 3, were then imaged with the AFM. These also had an average diameter of about 2.5 nm. It was concluded that these contaminant particles were amorphous carbon. This was supported by the relatively large diameter of particles, location of particles throughout the growth area, and the fact that amorphous carbon is a common impurity in CVD growth which indicates incomplete nucleation at the catalyst sites [1].

Issues with the current growth process led us to investigate ferritin, a globular protein complex that encompasses an iron nanoparticle, for patterned CNT growth. Ferritin has already been proven as catalyst for robust CNT growth [2], however traditional iron nanoparticle patterning techniques cannot be used and an alternative method of patterning has not been developed. Our goal was to pattern ferritin using the photoresist LOL2000 in order to yield a more patterned and aligned growth.

To test the solubility of ferritin in photoresist, we used AFM to image the following samples: ferritin with distilled water, patterned ferritin with two layers of photoresist, and patterned ferritin with the top layer of resist removed to determine the surface texture and roughness. We also imaged a lift off area of resist, as a surface texture control, and the areas close to the patterned region, to see if any particles were present on this un-patterned area.

By comparing the topographical images from the AFM, we were able to determine if the samples contained ferritin nanoparticles. The results of this experiment can be seen in Table 1. It was found that ferritin nanoparticles were clearly evident in the ferritin water solution. However, there was no evidence of ferritin nanoparticles in the patterned resist area or on the area adjacent to the patterned resist.

Conclusion:

In conclusion, it was determined that particles on catalyst strips and around CNTs of sparse growths were most likely amorphous carbon. It was also determined that ferritin is only soluble in water, not in the photoresist LOL2000, therefore a new method is required to pattern ferritin for growth.

Acknowledgments:

I would like to thank Arash Hazeghi for his patience and confidence in my abilities. I would also like to thank Professor H.-S. Philip Wong, Mike Deal, Maureen Baran, and all of the SNF staff members for their support and help. Finally thank you to the National Science Foundation, NNIN Research Experience for Undergraduates, and Stanford Nanofabrication Facility.

References:

[1] Franklin, N., Li, Y., Chen, R., Javey, A., and Dai, H. "Patterned growth of single-walled carbon nanotubes on full 4-inch wafers" Applied Physics Letters, Vol. 79, No. 27, pp. 4571-4573, 31 December 2001.

[2] Patil N., Lin A., Myers E., Wong H.-S.P., Mitra S. "Integrated Wafer-Scale Growth and Transfer of Directional Carbon Nanotubes and Misaligned-Carbon-Nanotube-Immune Logic Structures"; VLSI Technology, 2008 Symposium on, pp. 205-206, (2008).

Sample	Average Height (nm)	Peak Height (nm)	Ferritin Particles? (Y/N)
Forming DI Water	1.7	5.5	Yes
2 Layers of Resist	1	2.6	No
1 Layer of Resist	0.8	2	No
Blank Area (next to Dual Layer)	0.6	0.7	No
Blank Area (next to Single Layer)	0.6	0.9	No
Lift Off Only	0.6	0.7	No

Table 1: Average heights of AFM scans for ferritin test.

Fabrication and Characterization of Catalytic Nanomotors

Christine Burdett

Chemical Engineering, North Carolina State University

NNIN REU Site: ASU NanoFab, Arizona State University, Tempe, AZ

NNIN REU Principal Investigator(s): Dr. Jonathan D. Posner, Mechanical Engineering, Chemical Engineering, Arizona State University

NNIN REU Mentor(s): Jeffrey Moran, Mechanical Engineering, Arizona State University

Contact: cmburdet@ncsu.edu, jposner@asu.edu, jeffrey.moran@asu.edu

Introduction:

Platinum-gold bimetallic nanorods swim autonomously in aqueous hydrogen peroxide solutions. These synthetic nanomotors consist of one platinum (Pt) segment and one gold (Au) segment, each 1 μm long and approximately 200 nm in diameter. The platinum and gold react with the peroxide to form water and oxygen, propelling the nanomotor in the process. A theory called self-electrophoresis has been proposed to describe this movement. In this theory, platinum catalytically oxidizes the hydrogen peroxide to create protons, electrons, and oxygen, and gold catalytically combines the protons and electrons with peroxide to form water. Nanorod locomotion is therefore caused by the asymmetric electrochemical reactions on the platinum and gold surfaces. The charged particles transferred in these reactions generate an electric body force that drives the nanomotor through the surrounding viscous liquid.

In our study, we fabricated nanomotors and attempted to control their direction of motion. This was done by incorporating a nickel (Ni) segment and using magnetic fields to orient them; additionally, alternating current (AC) electric fields were employed to align the nanomotors. We also analyzed the variation of nanomotor velocity with time.

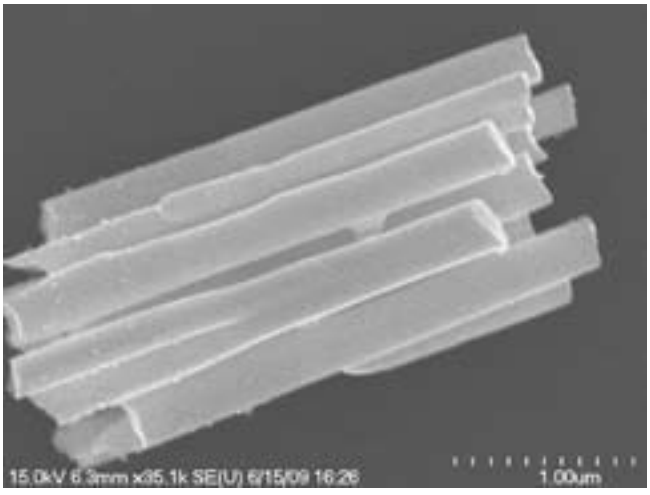

Figure 1: Nanomotors imaged by (FESEM).

Experimental Procedure:

Our nanomotors were fabricated according to the method described elsewhere in detail [1]. Nanomotors were imaged for characterization using a field emission scanning electron microscope (FESEM); see Figure 1. The objective of our first experiments was to directionally control Pt-Ni-Au nanomotors with magnetic fields. The nanomotors were always added to the hydrogen peroxide solution just before the experiment began, and peroxide concentration was always 5 wt%. After the solution was in place in the capillary or microchannel, magnets were placed near the surface to control nanomotor orientation. For the AC electric field experiments, we filled a capillary with nanomotor solution and placed gold electrodes in wells on both ends; we then ran an AC electric field of 200 V/cm at 1 kHz through the capillary to align the nanomotors.

We also studied how nanomotor velocity changed over time for several different volume fractions. Videos were taken of the nanomotors' motion until they appeared to be moving with only Brownian motion, using a Nikon TE-2000 microscope with 60× magnification. Images and videos were captured with a CoolSnap CCD scientific camera.

Results and Discussion:

Upon FESEM imaging of the nickel nanomotors, we discovered that the nickel segments were breaking apart from the platinum segments and were also being etched away, possibly due to the sodium hydroxide (NaOH) rinse step. To remedy this, we shortened the duration of the NaOH rinse and added a short gold segment on either end of the nickel segment. This reduced nickel etching and the nickel segments adhered more strongly to the gold segments, preventing breakage. However, we had some difficulty imaging the nanomotors and controlling the direction of their movement with magnets, without blocking the transmission light source. It was because of these obstacles that we also used an AC electric field to orient the nanomotors. Not only did this method work for Au-Ni-Au-Pt nanomotors, but when 200 V/cm at 1 kHz was applied to Pt-Au nanomotors, they oriented along the electric field as well. Thus, the use of AC electric fields enables directional control of nanomotor movement without the need for nickel segments. Figure 2

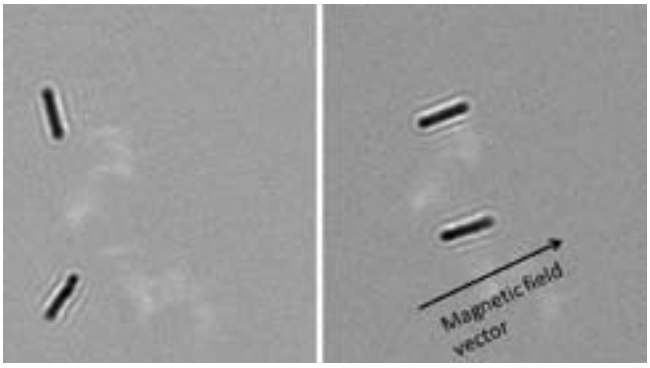

Figure 2: Left, unoriented Au-Ni-Au-Pt nanomotors. Right, nanomotors aligned by magnetic field.

shows a grouping of unoriented Au-Ni-Au-Pt nanomotors, followed by an image of the nanomotors once they had been aligned by magnetic field.

In our study of nanomotor velocity as a function of volume fraction, we found that nanomotors tended to slow down over time. We believe this was due to the local hydrogen peroxide concentration decreasing over time. As the nanomotors remain in peroxide for longer periods of time, the amount of oxygen and water being produced increases and the amount of peroxide left in the solution decreases, causing nanomotor speed to decrease as well.

To support this hypothesis, we considered the advection-diffusion equation for hydrogen peroxide, which is Equation 1 in Figure 3. We assumed that the variation of the total concentration of peroxide with time is more significant than spatial variations of concentration at any given instant in time; therefore the advection and diffusion terms are negligible. For simplicity, we assumed a first order reaction, such that $R \sim -AC$, yielding Equation 2. Integrating this equation resulted in $C = C_0 e^{-At}$. Since we knew velocity to be roughly linearly dependent on concentration [2] (for concentrations up to 5% H_2O_2), such that $V \sim BC$, it followed that velocity decreases exponentially over time according to Equation 3. These free model parameters were adjusted to reproduce the envelope matching the experimental data, which is shown with our velocity/time data for different volume fractions of nanomotors in Figure 4.

In our experimental setup, oxygen bubble formation caused by the decomposition of H_2O_2 into oxygen and water occasionally forced nanomotors to settle to the surface. This made it necessary to move the microscope field of view to a new location to view unsettled nanomotors, which were moving faster due to more peroxide being present locally. This is the cause of the spikes in velocity values over time in the graph.

Equations:

$$(1): \quad \frac{\partial C}{\partial t} + \vec{u} \bullet \nabla C = D\nabla^2 C + R$$

$$(2): \quad \frac{\partial C}{\partial t} = -AC$$

$$(3): \quad v(t) \propto BC_0 e^{-At}$$

Conclusion and Future Work:

Our results suggest that velocity decreases exponentially with time due to depletion of hydrogen peroxide fuel. While we were able to successfully fabricate nanomotors that could be directionally controlled, the experimental method still needs to be modified to ensure more reliable results. Currently, work is being done to observe nanomotors without oxygen bubble interference.

Acknowledgments:

I would like to thank Dr. Jonathan Posner, Jeff Moran, Philip Wheat, and the rest of Posner Research Group for their help and guidance. Thanks also to the National Nanotechnology Infrastructure Network Research Experience for Undergraduates Program, the National Science Foundation, and the Center for Solid State Electronics Research at Arizona State University for research support and funding.

References:

[1] Martin, R.B.; Dermody, D. J.; Reiss, B.D.; Fang, M.; Lyon, L.A.; Natan, M.J.; Mallouk, T.E.; "Orthogonal Self-Assembly on Colloidal Gold-Platinum Nanorods"; Adv. Mater., II, 1021-1025 (1999).

[2] Laocharoensuk, R.; Burdick, J.; Wang, J.; "Carbon-Nanotube-Induced Acceleration of Catalytic Nanomotors"; ACS Nano, II, 1069-1075 (2008).

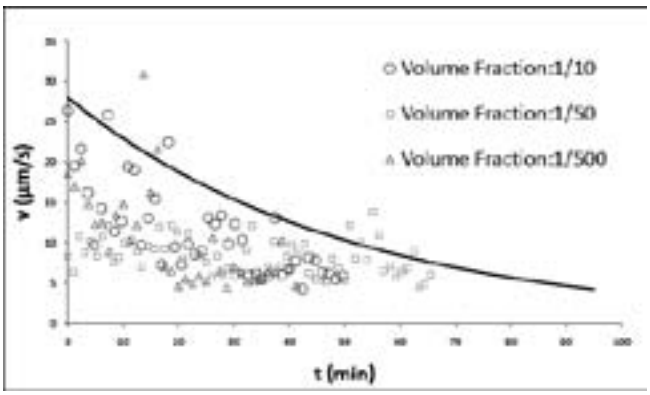

Figure 4: Velocity/time data for different volume fractions of nanomotors.

Structure Optimization of Semiconducting Nanowires with AFM Direct-Write

Jacqueline Collette

Materials Science and Engineering, Arizona State University

NNIN REU Site: Center for Nanotechnology, University of Washington, Seattle, WA

NNIN REU Principal Investigator(s): Professor Marco Rolandi, Materials Science and Engineering, University of Washington at Seattle

NNIN REU Mentor(s): Dr. Jessica Torrey, Materials Science and Engineering, University of Washington at Seattle

Contact: jacqueline.collette@asu.edu, rolandi@u.washington.edu, torreyjd@u.washington.edu

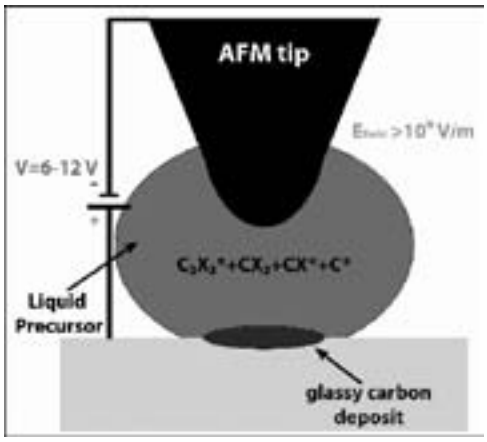

Figure 1: Schematic of AFM direct-write process.

Abstract and Introduction:

Conventional semiconductor device fabrication is reaching its resolution limits as devices become ever smaller. Fabrication of nanoscale devices requires precise positioning of nanometer-size components into complex geometries. Several patterning methods affording nanoscale resolution have been explored. Local oxidation nanolithography facilitates surface modification through field-induced water menisci [1]. Dip-pen nanolithography uses molecular "inks" to coat the tip of a scanning probe, which are transferred to the surface in a condensed water vapor meniscus [2]. Both are useful techniques, but are often limited by low throughput and material selectivity. Atomic force microscope (AFM) direct deposition of nanofeatures occurs via field-induced localized chemical reactions of a liquid precursor in the region between the AFM tip and the substrate. AFM direct-write is a quick, versatile patterning method for carbon nanowires (CNWs) using organic solvents as precursors. Field-induced patterning of large areas at high velocities has been demonstrated in perfluorooctane [3]. This work focuses on the direct deposition of CNWs from n-octane, their processing and characterization.

The electrical behavior of carbon materials spans a wide range, making them attractive for use in electronic devices. Depending on their bonding structure, they can be insulating, semiconducting, or fully conductive. Conductivities are a function of the ratio of sp^3 (diamond-like) to sp^2 (graphite-like) bonds [4]. Amorphous CNWs (sp^3 rich) are expected to be wide band-gap semiconductors.

In order to optimize conductivity of CNWs, we annealed at temperatures of 550°C and 900°C to induce graphitization [6,7]. Electron delocalization in graphitic carbon permited electron flow within planes of π-bonds. Annealing was used to facilitate transformation from sp^3 to sp^2 bonding, enhancing conductivity. In order to accomplish device integration of CNWs, it was necessary to understand how the morphology and bonding structure change with annealing temperature. Previous unpublished work of the Rolandi group uses photoelectron emission microscopy (PEEM) to examine changes in sp^2/sp^3 bond ratios as a function of annealing temperature and will be used as bases for these studies.

Experimental:

Two categories of experiments were performed: the fabrication of nanolines for morphological examination, and the fabrication of devices for electrical characterization. P-type, boron-doped, silicon (Si) <100> substrates were used for all the measurements. For morphological analysis, carbon nanolines were fabricated on a thin (ca. 2 nm) native oxide

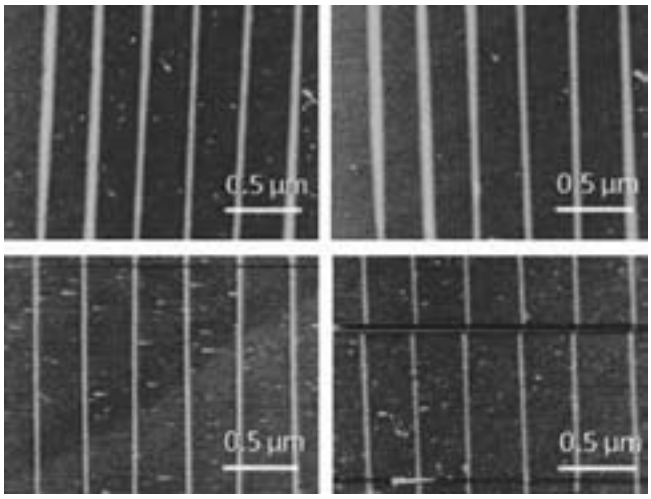

Figure 2: AFM images of nanolines, in pristine state (on left), after annealing at 550°C (upper right), and after annealing at 900°C (lower right).

layer. Lines were patterned by AFM direct-write at 10-12V bias and 1 μm/s write speed. Imaging was performed using a Veeco Multimode IV atomic force microscope operated in tapping mode and scanning electron microscopy. For device fabrication, a thick oxide layer, ca. 10 nm, was dry-grown on the Si substrate. Contacts (5 nm Cr and 20 nm Pt) were patterned via positive resist photolithography and ion beam sputtering. Wires were deposited using high-field AFM with a 30V bias at 1 μm/s. Electron beam lithography was used to complete the device contacts. Both lines and wires were annealed under argon in a tube furnace at 550°C and 900°C. Conductivity testing was performed on a probe station connected to an Agilent 4155C Semiconductor Parameter Analyzer.

Results and Discussion:

Nanoline deposition for morphology consideration was easily accomplished on thin (2 nm) oxide substrates. The average height of the pristine 10V lines was 1.8 nm, and that of the 12V lines was 2.4 nm. After annealing at 550°C for one hour, the height of the 10V lines decreased by 3%, while the 12V lines exhibited no height reduction. A 900°C anneal produced height reductions in the 10V and 12V lines of 80% and 62%, respectively. As expected, due to the planar constraint of the substrate, widths of the lines did not show a noticeable trend with annealing temperature.

The volume loss in the lines annealed at 900°C merits speculation. While annealing at 550°C did not noticeably affect the height of the lines, the higher temperature reduced their height significantly. This can partly be explained as a transformation of the carbon to sp^2 bonding at the higher temperature. Graphitic carbon's planar geometry is more compact than that of tetrahedral amorphous carbon. Theoretical densities of amorphous carbon and graphite enable predictions of 7%-20% volume loss upon complete graphitization. The observed volume loss was much greater, indicating that an intermediate temperature between the chosen 550°C and 900°C will likely procure the desired sp^2 rich carbon. Also of interest is the fact that the 12V lines appear to retain more of their height than the 10V lines. Although annealing was performed under argon to eliminate the possibility of oxide formation, it's possible that trace oxygen contamination exists in the furnace. It's reasonable to assume that volume loss is due both to decomposition of the lines upon carbon oxidation and densification of the material with graphitization.

Annealing Temperature	% of original height (10V)	% of original height (12V)
25°C	100%	100%
550°C	97%	100%
900°C	20%	38%

Figure 3: Percent height loss of nanowires deposited at 10 and 12 volts after annealing at 550° and 900°C.

In order to deposit CNWs into devices, it is necessary to use a substrate with a thick (10 nm) oxide layer to prevent leakage of current through the back gate. However, the thickness of this oxide hinders the deposition of the nanowires. It's also possible that the oxide incurs damage during writing. We can determine if this is the case by performing electrical and transmission electron microscopy (TEM) analysis. Although we were unable to ultimately test the wires in devices, foundations were set for the standardization of the direct-write parameters. Threshold voltages on the order of 28-32 volts and write speeds of 0.1-0.5 μm/s were found to deposit clean, uniform wires. This knowledge enables us to further our exploration of conductivity as a function of annealing temperature.

Conclusions:

We were able to deposit CNWs on both native and thick (10 nm) oxides using high-field AFM. The wires exhibited significant size reductions upon high temperature annealing. We have provided a foundation for the integration of CNWs into devices for the purpose of measuring electrical conductivity.

Acknowledgements:

National Science Foundation; National Nanotechnology Infrastructure Network Research Experience for Undergraduates (NNIN REU) Program; Center for Nanotechnology, University of Washington.

References:

[1] R. Garcia, R. V. Martinez, J. Martinez, Chem. Soc. Rev., 2006, 35, 29-38.

[2] B. Basnar, I. Willner, Small, 2009, 5, No. 1, 28-44.

[3] M. Rolandi, I. Suez, A. Scholl, J.M.J. Frachet, Angew. Chem. Int. Ed. 2007, 46, 7477-7480.

[4] A. C. Ferrari, J. Robertson, Phil.Trans. R.Soc. Lond. A, 2004, 362, 2477-2512.

[5] I. Suez, M. Rolandi et. al., Adv. Mater. 2007, 19, 3570-3573.

[6] D. Wesner, S. Krummacher et. al., Phys. Rev. B, 1983, 28, No. 4, 2152-2156.

[7] Y. H. Tang, P. Zhang et. al., Appl. Phys. Letters, 2001, 79, No. 23, 3773-3775.

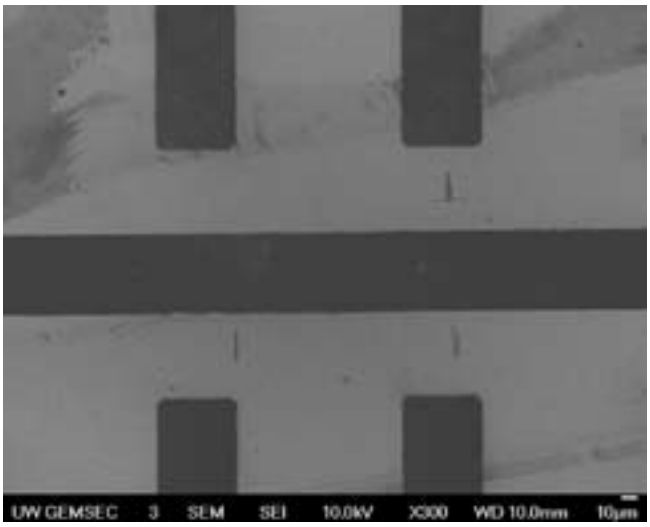

Figure 4: SEM image of pre-EBL device with CNWs obtained with AFM direct-write in n-octane.

Atomic Layer Deposition on Surfaces Modified with Thin Interfacial Organic Layers

Scott Isaacson

Chemical Engineering, University of Minnesota

NNIN REU Site: Cornell NanoScale Science and Technology Facility, Cornell University, Ithaca, NY
NNIN REU Principal Investigator(s): James R. Engstrom, Chemical and Biomolecular Engr., Cornell University
NNIN REU Mentor(s): Kevin J. Hughes, Chemical and Biomolecular Engineering, Cornell University
Contact: isaac145@umn.edu, jre7@cornell.edu, kjh47@cornell.edu

Abstract:

Atomic layer deposition (ALD) of aluminum oxide (Al_2O_3) has been performed on bare silicon dioxide (SiO_2) and on SiO_2 modified with thin interfacial organic layers. The Al_2O_3 films have been characterized using ellipsometry, atomic force microscopy (AFM), and x-ray photoelectron spectroscopy (XPS). We find that Al_2O_3 films grown on SiO_2 modified with a nitrogen-containing organic layer or a polyethylene glycol based self-assembled monolayer (SAM) grow at a rate of approximately 1 Å per cycle, equal to the deposition rate of Al_2O_3 on bare SiO_2, while a fluorinated hydrocarbon SAM strongly attenuates the rate of growth in the initial ~ 15 cycles. AFM of the Al_2O_3 films indicates a surface roughness of less than 0.5 nm, and XPS analysis confirms the presence of the organic layer at the Al_2O_3/substrate interface after ALD.

Introduction:

In order to continue to increase the performance and decrease the size of integrated circuits, capacitance within the interconnect structure must be reduced [1]. Several porous materials with a low dielectric constant (low-κ materials) have been proposed to address this issue. Unfortunately, the copper used in the interconnects can easily diffuse through these materials, severely shortening their usable lifetime [1].

Atomic layer deposition (ALD) is a technique that enables the deposition of thin, smooth, and conformal films with atomic layer precision [2]. Because of these desirable properties, ALD can be used to create a copper diffusion barrier on low-κ substrates. However, problems arise from infiltration of the gas-phase ALD precursors into the pores of the low-κ material. It has been proposed that an interfacial organic layer (IOL) could be used to seal the surface pores in these materials against gas-phase precursors before ALD is performed. Appropriately designed organic layers may have the added benefit of controlling the kinetics of the early stages of ALD. The objective of the work presented here is to determine how the structure and reactivity of the organic layer affects the growth rate and morphology of an Al_2O_3 film deposited on that layer.

Experimental Procedures:

ALD of Al_2O_3 was performed using an Oxford Instruments FlexAL atomic layer deposition tool. To deposit an Al_2O_3 film, a substrate was sequentially exposed to two alternating precursor gases, trimethylaluminium and water. The deposition chamber was purged with argon gas between precursor exposure. Films were deposited on bare SiO_2 and on SiO_2 modified with thin interfacial organic layers (IOLs).

The IOLs can be separated into two classes, based on whether or not they contain functional groups which are reactive towards the ALD precursors. The reactive IOLs used in this study were a polyethylene glycol (PEG) based SAM and a nitrogen-containing organic layer (referred to as "Layer N" below). (1H,1H,2H,2H-perfluorooctyl) trichlorosilane (FOTS), which contains only CH_2, CF_2, and CF_3 groups, is not expected to be reactive toward the ALD precursors. A cross-sectional view of a generalized sample after modification with an IOL and film deposition by ALD is shown in Figure 1 (thicknesses not to scale).

The thickness of the deposited films and IOLs were measured with a Woollam variable angle spectroscopic ellipsometer. Film morphology was characterized using a Digital Instruments Dimension 3100 atomic force microscope.

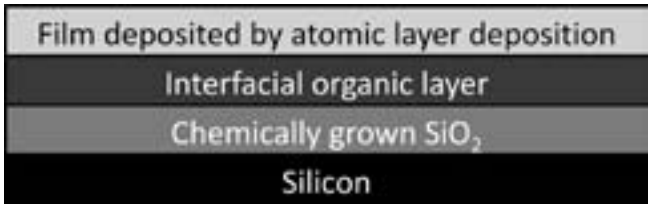

Figure 1: A cross-sectional view of a generalized and idealized sample.

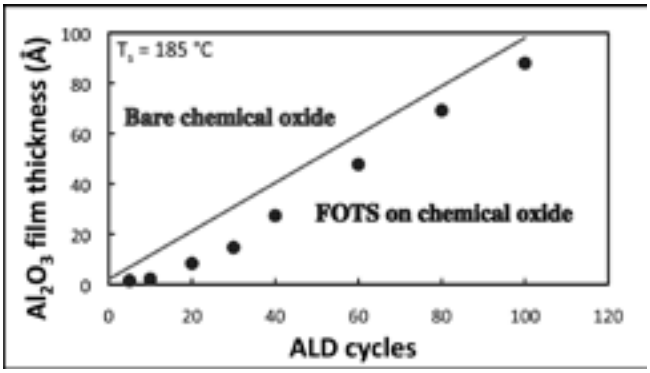

Figure 2: Deposited thickness of Al_2O_3 as a function of the number of ALD cycles for growth on SiO_2 and the FOTS SAM.

Results and Conclusions:

To establish an ideal growth rate, Al_2O_3 was deposited on bare, chemically grown SiO_2. Film growth on SiO_2 is considered to be ideal because this substrate is smooth and has an excess of active sites on which the Al_2O_3 film may nucleate. A constant growth rate of 0.96 Å/cycle at a substrate temperature (T_s) of 185 °C was observed, consistent with previous measurements [3].

An FOTS SAM attenuated growth of Al_2O_3 on SiO_2 in the first ~ 15 cycles (Figure 2). However, after about 30 cycles, the film growth rate returned to ~ 1 Å/cycle. This behavior suggests that the unreactive FOTS layer presents relatively few active sites on which the Al_2O_3 film can nucleate. This would lead to the film initially growing in patches, or islands [4]. After about 30 ALD cycles, however, it appears that these islands coalesce into a continuous Al_2O_3 film, masking the attenuating effect of the unreactive FOTS layer and returning the film growth rate to the ideal ~ 1 Å/cycle.

Al_2O_3 films were deposited at a rate of 0.96 Å/cycle on the reactive Layer N material, identical to Al_2O_3 films grown on SiO_2. Films deposited on the reactive PEG layer grew at a rate of 1.14 Å/cycle, slightly faster than on SiO_2. These results suggest that Layer N and PEG have an excess of active sites upon which the Al_2O_3 film can nucleate [4]. These results are summarized in Figure 3.

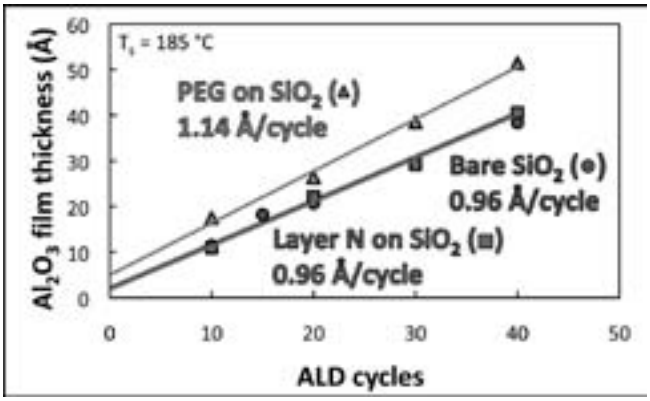

Figure 3: Deposited thickness of Al_2O_3 as a function of ALD cycles for growth on SiO_2 and reactive organic layers.

Ex situ x-ray photoelectron spectroscopy analysis of these films confirmed that, at minimum, some remnant of the Layer N material remained and waws confined to the Al_2O_3/SiO_2 interface after deposition.

Through qualitative analysis of AFM images of these films, we found that films exhibit similar morphology, independent of the reactivity or presence of an interfacial organic layer. In Figure 4, we present an AFM image of a 41 Å thick Al_2O_3 ALD film on Layer N. This film is representative of other Al_2O_3 films deposited on SiO_2 modified with IOLs or SAMs. Quantitatively, we found that all films were very smooth, with root-mean-square roughness values between 2.5 Å and 5.5 Å.

Acknowledgements:

This work was sponsored by the National Nanotechnology Infrastructure Network Research Experience for Undergraduates Program and the National Science Foundation. The author would like to thank Kevin Hughes, James Engstrom, Deirdre Manion-Fischer, and Melanie-Claire Mallison for their guidance and support.

References:

[1] International Technology Roadmap for Semiconductors. http://www.itrs.net, 2007.

[2] Puurunen, R. L. Applied Physics Reviews. 2005, 97, 121301.

[3] George, S. M.; Ott, A. W.; Klaus J. W. J. Phys. Chem. 1996, 100, 13121-13131.

[4] Dube, A.; Sharma, M.; Ma, P. F.; Ercius, P. A.; Muller, D. A.; Engstrom, J. R. J. Phys. Chem. C 2007, 111, 11045-11058.

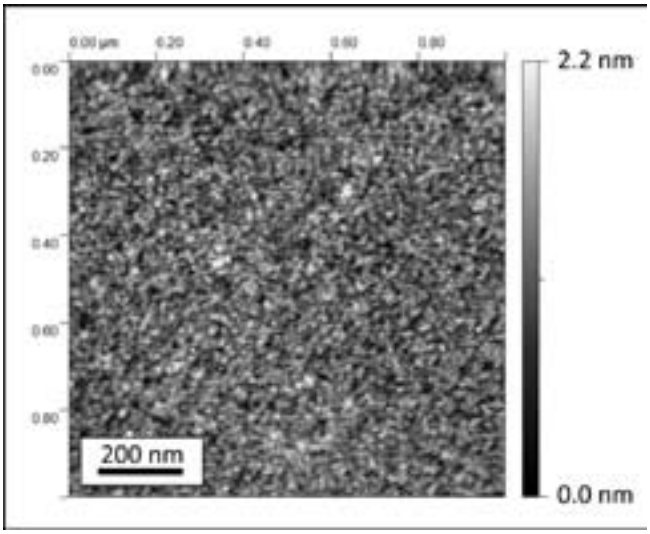

Figure 4: AFM of a 41 Å thick Al_2O_3 film deposited by ALD on Layer N.

Process Development for a Traveling Wave Terahertz Detector

Benjamin D. McPheron

Electrical Engineering, Ohio Northern University

NNIN REU Site: Colorado Nanofabrication Laboratory, University of Colorado, Boulder, CO

NNIN REU Principal Investigator(s): Dr. Garret Moddel, Electrical Engineering, University of Colorado

NNIN REU Mentor(s): Sachit Grover, Electrical Engineering, University of Colorado

Contact: b-mcpheron.1@onu.edu, moddel@colorado.edu, sachitelectric@gmail.com

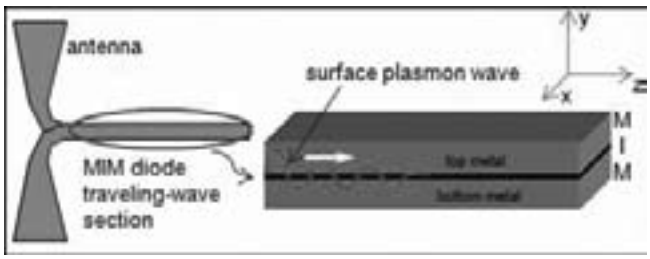

Figure 1: Traveling wave detector.

Abstract and Introduction:

The terahertz region has been untapped in the electromagnetic spectrum due to limitations in photonic and semiconductor devices. It has been proposed to use antenna coupled traveling-wave diode detectors to achieve high performance in the infrared. These devices channel radiation received by an antenna into a parallel plate waveguide: a metal-insulator-metal (MIM) diode that rectifies the carrier, producing a signal voltage. This arrangement facilitates a better impedance match between the antenna and the rectifying MIM diode than a lumped-element diode connected to the antenna.

The focus of this project was to develop process steps to fabricate these detectors. An example of such a detector can be seen in Figure 1. These were designed to receive radiation in the wavelength range of 9 to 12 μm. Potential applications for these devices include communications and infrared imaging.

Theory:

One of the essential components of these detectors is the MIM diode, which relies on the quantum tunneling of electrons. Tunneling implies that an electron will travel between metal electrodes without being excited over the insulator's band-gap barrier. This allows MIM diodes exhibit the non-linear I(V) characteristic required for signal rectification: the conversion of an alternating current (AC) signal into a direct current (DC) level. Tunneling characteristics vary with shape and size of the insulator barrier [1].

We chose a bow-tie antenna for its wider bandwidth and greater response. We designed an arm length of 6 μm, which should respond to wavelengths, including the 10.6 μm radiation of the CO_2 laser test radiation.

To achieve maximum power output, the antenna and waveguide should have reasonably matched impedance. The characteristic impedance of the 120° bow-tie antennas we fabricated can be calculated to be 40Ω. [2-3] The MIM waveguide used has an expected impedance of 20Ω at the testing frequency.

Process Development:

The first step was to deposit contacts and electron-beam alignment marks. We spun NR9-1000PY negative resist and exposed for 10 seconds. After developing the resist, we used a thermal evaporator to deposit a 10 nm chromium adhesion layer followed by 40 nm of gold. We performed the lift off in acetone and isopropyl alcohol.

We extensively employed electron-beam lithography for the next steps. For every e-beam step, we used a bi-layer resist recipe with 9% MMA/MAA co-polymer and 2.75% MMA in anisole. To develop, we used 1:3 MIBK:IPA and developed

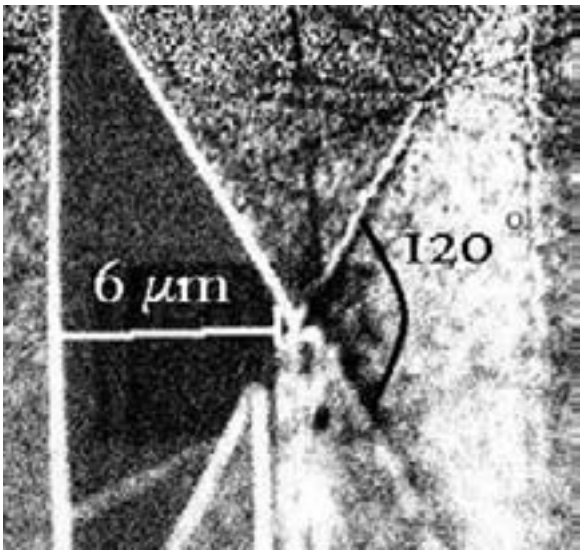

Figure 2: Dimensions of antenna arm.

for two minutes. With each e-beam layer, we deposited a new set of alignment marks in order to align future steps. We also wrote dosing patterns with e-beam lithography to find proper exposure conditions.

The first antenna arm was patterned using e-beam lithography and 10 nm of chromium (Cr), and 40 nm of gold (Au) were deposited after a short oxygen plasma ash, then lifted off. We confirmed that the antenna arm was 6 μm in length using a scanning electron microscope (SEM). This image can be seen in Figure 2.

Next, the MIM stack was deposited everywhere using an RF sputter system. We used a Nb/Nb_2O_5-Ta_2O_5/Nb MIM recipe with an oxide thickness of 2 nm and a total stack height of 82 nm. Subsequently, we used e-beam lithography to pattern a reactive ion etch (RIE) mask for the MIM waveguide on the first antenna arm. We deposited 40 nm of aluminium (Al), etched the excess MIM away, and passivated the sidewalls in the RIE.

Another experiment in the development of the process outlined parameters for removing the Al etch mask using the weak acid AZ-400K developer. After removing the etch mask, SiO_2 was deposited everywhere using an RF sputter system, and etched down in the RIE to prevent the final metal from shorting the diode. We experimented with etch parameters for the SiO_2 to avoid over-etching.

The final antenna arm was patterned and an atomic force microscope confirmed that the antenna was aligned properly. This alignment verification can be seen in Figure 3. We etched away aluminum oxide from the substrate with an ion mill and deposited and lifted off 10 nm of Cr and 40 nm of Au. Finally, we etched away excess MIM to achieve an undercut waveguide width of 100 nm.

We also fabricated large area MIM diodes using photo-lithography techniques and the same MIM recipe as the antenna to test and characterize them.

Results and Conclusions:

While developing the process for fabricating traveling wave detectors for the terahertz frequency range, we learned several lessons related to the optimization of the process. We had initially planned to use a Cr mask for the RIE etch of the MIM, but we realized that we would not be able to remove the Cr mask and then would not achieve the waveguide feature size that we desired, so Al was substituted. We found that dipping the substrate for 5 seconds in AZ-400K removed the Al mask completely. Also, we found that it would be beneficial to deposit larger alignment marks for the e-beam lithography steps with an 'L' shape to aid in the alignment of the waveguide and second antenna arm.

Acknowledgments:

This project has taught me essential fabrication skills and has improved my understanding of micro-electronic circuits, as well as introduced me to the quantum physical theory of electron tunneling. Ultimately we were successful in developing a process to fabricate these detectors.

Thanks to: National Science Foundation, National Nano-technology Infrastructure Network Research Experience for Undergraduates, Dr. Garret Moddel, Sachit Grover, Olga Dmitriyeva, James Zhu, David Doroski, University of Colorado at Boulder, Colorado Nanofabrication Laboratory, Dr. Van Zeghbroeck, Dr. Filipovic.

References:

[1] Van Zeghbroeck, B; "Principles of Semiconductor Devices", Section 2.3 (2007).

[2] Balanis, C; "Antenna Theory and Design", Equation 9-14 (2005).

[3] Fumeaux, C, et al; "Nanometer thin-film Ni-NiO-Ni diodes for detection and mixing of 30 THz radiation", Infrared Physics & Technology, Volume 39, Issue 3, pp. 123-183 (1998).

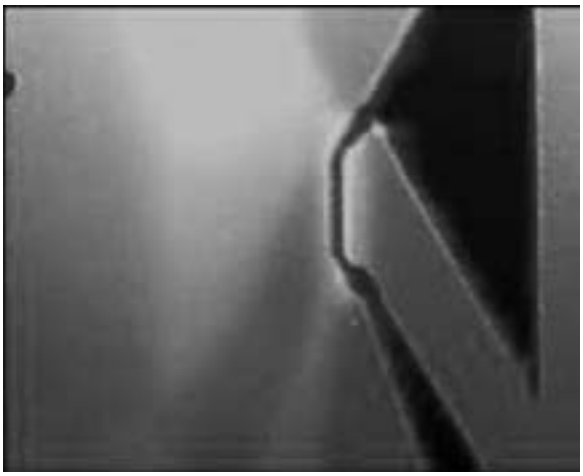

Figure 3: AFM verified arm alignment.

Fabrication of Nanohole Arrays with Nano-Imprint Lithography

Axel Palmstrom

Chemical Engineering, University of California, Santa Barbara

NNIN REU Site: Nanofabrication Center, University of Minnesota-Twin Cities, Minneapolis, MN

NNIN REU Principal Investigator(s): Prof. Sang-Hyun Oh, Electrical and Computer Engr., University of Minnesota

NNIN REU Mentor(s): Si Hoon Lee, Biomedical Engineering; Hyungsoon Im, Electrical and Computer Engineering, University of Minnesota

Contact: apalms1@gmail.com, sang@umn.edu, leex3487@umn.edu, imxxx019@umn.edu

Abstract and Introduction:

Sub-wavelength metallic nanostructures can excite surface plasmons, which are electromagnetic waves at the metal interface. When light is incident on a periodic array of sub-wavelength holes in a noble metal film, more light passes through the array than predicted by aperture theory. This is called extraordinary optical transmission (EOT) and believed to be a result of surface plasmon resonance (SPR). SPR biosensors have been used in measuring the binding kinetics of biomolecules [1].

A method for fabricating nanostructures, specifically nanohole arrays, is necessary for this biosensing application. Current fabrication methods for nanohole arrays include focused ion beam (FIB) milling and e-beam lithography (EBL). These techniques are not practical for large-scale production. Nanosphere lithography can do this [1]; however, the process requires numerous steps and uniformity is limited. Another technique, nano-imprint lithography, offers the advantages of low cost, high throughput, and uniformity.

This research focused on nano-imprint for the fabrication of nanohole arrays in metal films, and three methods for mold fabrication: (a) polystyrene nanospheres, (b) double imprinting, and (c) metal masking.

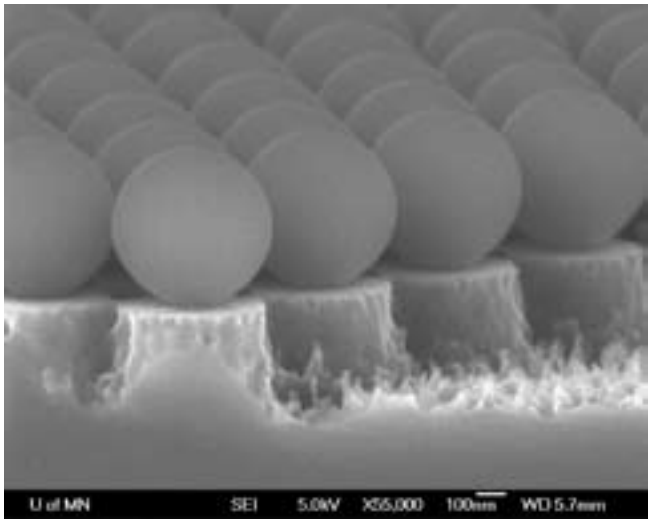

Figure 1: Nanopillars etched with nanosphere mask.

Mold Fabrication:

Reactive ion etches used:

NIL: 10 sccm O_2 at 50W RF power and 20 mtorr

OXIDE: 50 sccm Ar, 25 sccm CF_4 and 50 sccm CHF_3 at 150W RF power and 75 mtorr

O2SHRINK: 10 sccm Ar and 35 sccm O_2 at 60W RF power and 100 mtorr

SISLW: 40 sccm CF_4 and 4 sccm O_2 at 25W RF power and 100 mtorr

Nanosphere Lithography. A solution of nanospheres was prepared with 5:5:1 ratio of ethanol, de-ionized water and polystyrene nanospheres. A droplet of nanosphere solution was applied to a silicon wafer, resulting in nanosphere self-assembly. The patterned nanospheres were then shrunk with 1 min of O2SHRINK and etched with SISLW for 150 sec, resulting in silicon pillar nanostructures (Figure 1). The nanospheres were removed with a 30 min piranha clean (1:1 H_2SO_4:H_2O_2). The mold was placed in a desiccator with 4 drops of (heptadecafluoro-1,1,2,2- tetrahydrodecyl) trichlorosilane for 1 hour, forming a self-assembled monolayer (SAM) release layer.

Double Imprinting. Polymethylmethacrylate (PMMA) resist was spin coated on a thermally oxidized (100 nm) silicon wafer (EBL#1) at 3000 RPM for 30 sec and baked at 180°C for 90 sec. A dot array was exposed using electron beam lithography at 20 kV and with a 10 μm aperture. The PMMA was developed for 15 sec in a bath of 1:3 methyl isobutyl ketone (MIBK) and isopropyl alcohol, leaving holes in the resist. EBL#1 was etched with two RIE recipes— 4 min of OXIDE and 3 min with SISLW— then cleaned for 30 min in piranha. A trichlorosilane release layer was applied to EBL#1. Another 100 nm thermally oxidized wafer (NIL#1) was coated in NXR-1025 thermal resist by spin coating at 1000 RPM and baking at 155°C for 1 min. This gave a 300 nm resist layer. The mold EBL#1 was imprinted to the new wafer at 175°C and 300 psi for 1 min. Three RIE recipes were applied to NIL#1—3 min NIL, 4 min of OXIDE, and 4 min of SISLW—leaving pillar features in SiO_2/Si. The SAM trichlorosilane release layer was applied to NIL#1.

Metal Masking. EBL was employed to pattern PMMA on a silicon wafer with 100 nm of thermally grown oxide, EBL#2. 30Å of Au/Pt was slowly deposited using sputtering over the PMMA and bare wafer. The resist was then stripped using acetone and sonication for 10 min, leaving dots of Au/Pt. Two RIE recipes were used on EBL#2; first, 3 min of OXIDE followed by 3 min of SISLW. EBL#2 was coated with the trichlorosilane release layer.

Imprinting and Etching to Metal Film. A wafer with a 200 nm silver (or gold) film, deposited with electron beam evaporation, was coated with NXR-1025 thermal resist and placed on top of the nano-imprint mold. The two wafers were placed in the nano-imprinter and run for 1 min at 175°C and 300 psi. After imprinting, the mold was removed by carefully creating a gap with a razorblade and separating with a gust from a nitrogen jet. After imprinting, there was a residual layer of resist. The residual layer was removed with the RIE recipe: NIL. This recipe gave an etch rate of approximately 900Å/min for the NXR-1025 thermal resist. Etch times varied depending upon the features imprinted. When the residual layer of resist was removed, the silver (Ag) or gold (Au) layer below was etched using argon ion sputtering.

Results and Conclusions:

In this research, nano-imprint lithography was capable of transferring nanoscale features from one mold to a substrate. It was used to replicate molds, requiring only one master mold. Imprinting was performed with pieces as small as 2 × 2cm^2, and has the potential to efficiently fabricate nanohole array patterns to be etched into a metallic film. Both EBL and NSL were capable of nanohole array molds with varying periodicities. Nanosphere lithography (Fig.2) eliminated EBL patterning at the loss of precise feature design, and has possibilities for cheap large-scale patterning. There was no significant difference in image quality between the metal masking (Fig.3) and double imprinting (Fig.4) techniques.

The double imprinting method was preferred because it was cheaper and created a master mold in the process. The EBL patterning incorporated in the metal masking and double imprinting processes allowed for more pattern control, with options for alternative features. All three molds lost feature quality when the pattern was transferred to the metallic layer. No method was clearly superior.

Future Research:

Future research should focus on; 1) optimization of the Au/Ag etch process for improved feature quality, and 2) nanosphere self-assembly for increased patterning area.

Acknowledgements:

I would like to thank Si Hoon Lee, Hyungsoon Im, and Prof. Sang-Hyun Oh for their support and assistance. I would also like to thank the UMN NFC staff for help and training I needed for this project and the NSF NNIN REU Program for funding for this research.

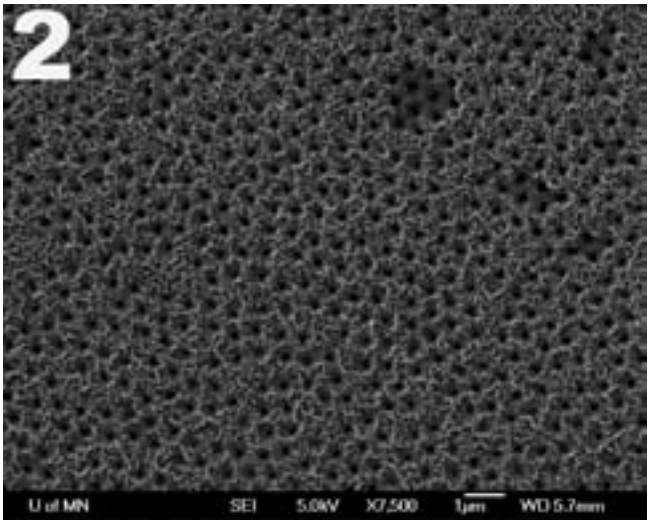

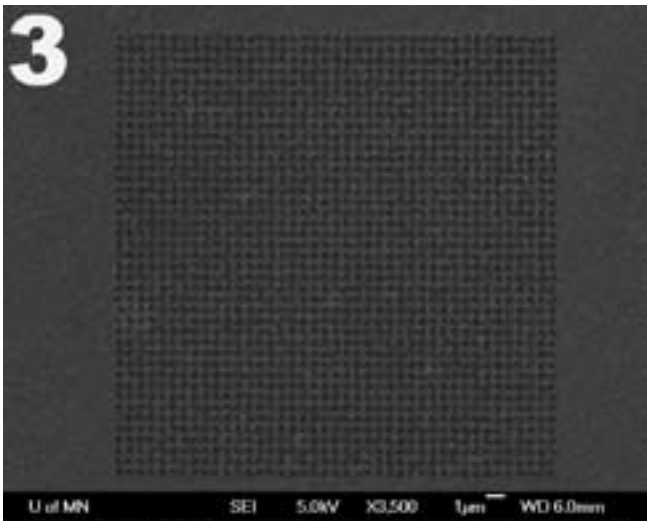

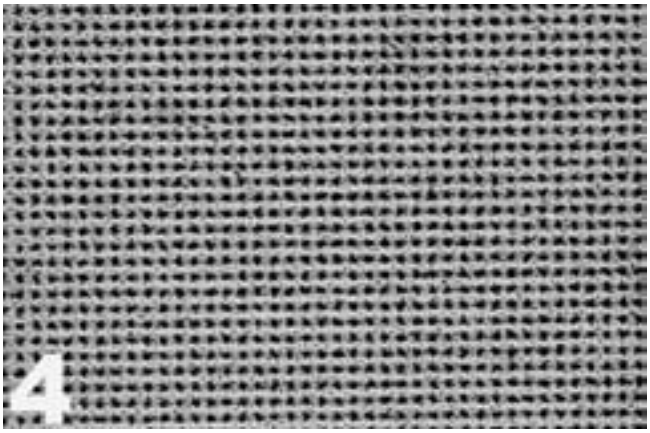

Figure 2: Nanoholes in silver patterned by nanosphere mold.

Figure 3: Nanoholes in silver patterned by metal masking mold.

Figure 4: Nanoholes in Ag patterned by double imprinting mold.

References:

[1] Lindquist et al. Lab Chip, 9, 382-387 (2009).

[2] T.W. Ebbesen et al. Nature, 391, 667-669 (1998).

DNA Electrophoresis in Sparse Ordered Obstacle Arrays

Alyssa Terry

Biomedical Engineering, Mississippi State University

NNIN REU Site: Nanofabrication Center, University of Minnesota-Twin Cities, Minneapolis, MN

NNIN REU Principal Investigator(s): Dr. Kevin Dorfman, Chemical Engineering and Materials Science, University of Minnesota-Twin Cities

NNIN REU Mentor(s): Dr. Jia Ou, Daniel Olson; Chemical Engineering and Materials Science, University of Minnesota-Twin Cities

Contact: abt66@msstate.edu, dorfman@umn.edu, ouxxx023@umn.edu, olso1887@umn.edu

Abstract and Introduction:

Engineering faster methods for deoxyribonucleic acid (DNA) separation is critical for the future of disease diagnosis and forensic work. To date, electrophoresis for DNA separation can only be performed on samples with fewer than around 20,000 base pairs using constant field gel electrophoresis. By increasing the pore size of traditional electrophoresis media, longer DNA with more base pairs can also be separated under a direct current (DC) field in microfluidic devices.

This study focuses on two main challenges: optimizing fabrication methods for creating micro-features on silica using the facilities available in the University of Minnesota fabrication center and understanding the post-collision mechanism of the DNA molecules. To study the DNA collision, first a procedure for creating an ordered hexagonal array in silica with 1 mm features had to be developed. Scanning electron microscopy (SEM) was used to inspect the effectiveness of the fabrication procedure. For the electrophoresis experiments, the DNA was dyed with YOYO-1 and then placed in the chip under an electric field. An inverted microscope controlled by LabVIEW, in addition to MATLAB software, was used to image and analyze the DNA during separation. Using the images recorded from the experiments, the DNA was analyzed for collisions, shape upon impact, velocity and time to relaxation.

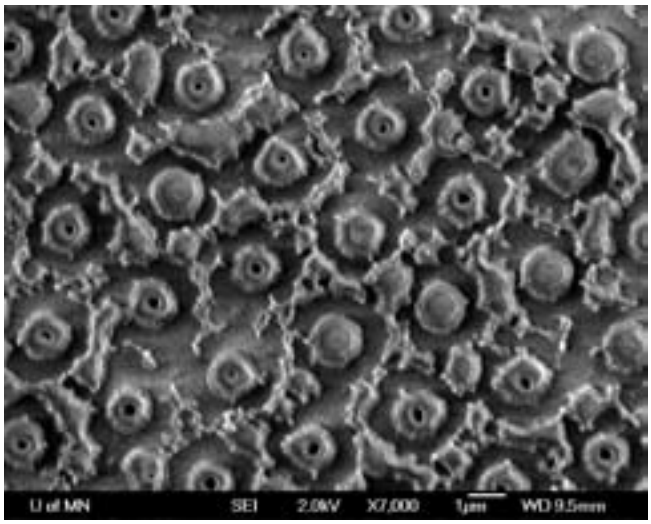

Figure 1: SEM of Method 1.

Device Fabrication:

A device consisting of a channel with posts 1 μm in diameter spaced 3 μm apart was needed to examine DNA collisions during electrophoresis. The chip consisted of a channel with the aforementioned specifications and two ports into which to load the DNA.

Method 1. Wafers were patterned using Shipley 1805 photoresist, exposed using a MA/BA6 contact aligner, and developed using 351 developer. Unwanted photoresist was removed using an oxygen plasma etch on the STS etcher. Posts were produced by etching through the silicon wafer in a deep trench etcher. Then 400 nm of silicon dioxide (SiO_2) was grown on the chips to provide electrical insulation.

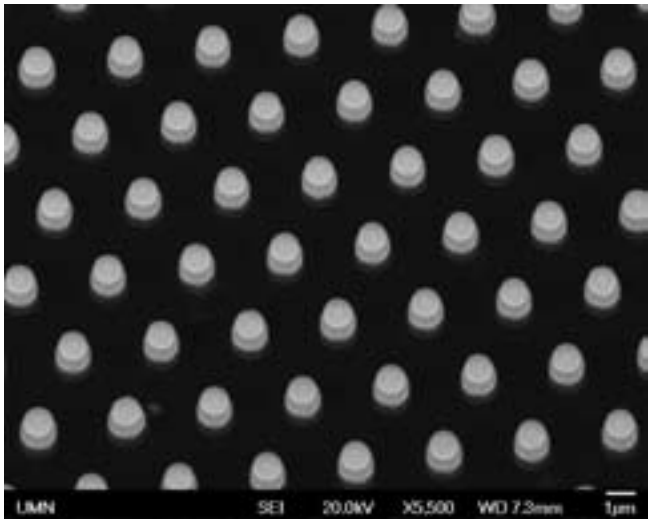

Figure 2: SEM of Method 2.

Method 2. A 25 nm layer of SiO_2 was grown on an Si wafer and then patterned using 0.5 μm of Shipley 1805 photoresist and developed in 351 developer. The wafers were then coated with 300 Å of chromium (Cr) in the e-beam metal evaporator. Acetone was used to remove all of the photoresist, including the photoresist coated with Cr. A pattern of Cr dots remained. Then buffer oxide etch (BOE) was used to etch through the SiO_2 layer, and Cr-125 etch was used to remove the Cr, leaving small posts of SiO_2. Deep trench etching was then used to etch through the Si and create 2 μm high posts. Then 400 nm of SiO_2 was grown on the wafer to provide electrical insulation. After the silicon was patterned, the chips were cut and holes were drilled into them at each of the ports. A glass slide with ports at the same location was adhered to the silicon using an epoxy.

DNA Electrophoresis. Lambda DNA was dyed using YOYO-1. Dyed DNA was loaded into one port on the device and 60 volts applied to the chip to make the DNA move from one side of the channel to the other. DNA was examined using a camera and microscope controlled by LabVIEW and analyzed with MATLAB.

Results and Discussion:

Method 1 produced inconsistently sized and spaced posts. Photoresist remained in the channel, therefore blocking the flow of DNA through the chip. The photoresist may have been a artifact of the photolithography procedure. Figure 1 depicts the final results of Method 1.

As shown in Figure 2, the second method produced consistently sized and spaced posts. No photoresist remained in the channel, and DNA was free to flow between and collide with the posts.

Figure 3 shows the position of a single molecule of DNA through the channel in time. Two collisions are visible: one at ~ 0.75 seconds and another at ~ 1.75 seconds. Velocity was constant as the DNA approached and left a post, but was reduced to 0 frames/sec upon impact.

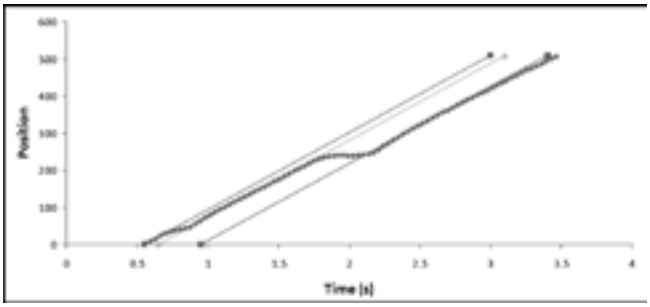

Figure 3: DNA time vs. position through channel.

Conclusions and Future Work:

Method 2 created ordered arrays of posts that can be used effectively for analysis of DNA collisions in electrophoresis. In the future, Method 2 will be used to fabricate chips for DNA separation and collisions.

Acknowledgements:

Thanks to Dr. Kevin Dorfman for this opportunity, Dr. Jia Ou and Dan Olson for their guidance and support, and the National Nanotechnology Infrastructure Network Research Experience for Undergraduates (NNIN REU) Program for funding.

References:

[1] S. A. Campbell, The Science and Engineering of Microelectronic Fabrication, Vol. 2: Oxford University Press, 2001.

[2] M. J. Madou, Fundamentals of Microfabrication: The Science of Miniaturization, 2nd edition. Boca Raton, FL: Taylor & Francis, Inc, 2002.

[3] J. L., Vivoy, "Electrophoresis of DNA and other polyelectrolytes: Physical mechanisms." Reviews of Modern Physics, vol 72, pp 813-872, 2000.

Photoconductivity and Photolumniescence of $Al_{0.3}Ga_{0.7}As$/GaAs p-i-n Junction Quantum Well Solar Cells

David J. Christle

Physics and Mathematics, University of Minnesota-Twin Cities

NNIN iREU Site: National Institute for Materials Science (NIMS), Tsukuba, Ibaraki, Japan

NNIN iREU Principal Investigator(s): Prof. Hiroyuki Sakaki, NIMS, Quantum Dot Research Center; Toyota Technological Institute, 201201 Hisakata, Tempaku-ku, Nagoya 468-8511, Japan

NNIN iREU Mentor(s): Dr. Takeshi Noda, National Institute for Materials Science, Quantum Dot Research Center, 1-2-1 Sengen, Tsukuba, Ibaraki 305-0047, Japan

Contact: christle@cnsi.ucsb.edu, h-sakaki@toyota-ti.ac.jp, noda.takeshi@nims.go.jp

Abstract:

Single-junction gallium arsenide (GaAs) photovoltaic devices are thermodynamically limited to roughly 30% efficiencies in Air Mass (AM) 1.5 conditions via the well-known Shockley-Quesslier limit. Under idealistic assumptions, a photovoltaic device containing an intermediate energy band between the edges of the conduction and valence bands has been shown to have an efficiency limit upwards of 60%, primarily due to the absorption of sub-bandgap photons [1]. An $Al_{0.3}Ga_{0.7}As$/GaAs-based quantum well solar cell realizes this special electronic structure by alternating growth layers between $Al_{0.3}Ga_{0.7}As$ (E_g = 1.8 eV) and GaAs (E_g = 1.42 eV). This growth of repeating heterojunctions forms a series of quantum wells (QWs) known as a superlattice, which admits a large number of bound states at energies between the GaAs/$Al_{0.3}Ga_{0.7}As$ band edges. Adjusting the width and separation of these quantum wells controls both the width and the depth of this intermediate band, meaning this technique is also tunable.

Introduction and Experimental Procedure:

In this paper, we attempt to understand the dynamics of photogenerated carriers in such a device by measuring the photoconductivity and photoluminescence of $Al_{0.3}Ga_{0.7}As$/GaAs quantum wells embedded in the intrinsic region of standard p-i-n junction solar cells. These measurements are germane since carriers can either be swept away by the internal electric field, creating a current, or recombine radiatively or non-radiatively, with the former being observed as photoluminescence.

We grew four films with 1, 10, 25 and 50 quantum wells, along with a control sample containing no quantum wells, via molecular beam epitaxy. All films were grown on an *n*-type GaAs (100) substrate at a substrate temperature (temp) of 580-600°C, and consisted of 300 nm *n*-GaAs ($n = 1 \times 10^{18}$ cm^{-3}), and 300 nm of *n*-$Al_{0.3}Ga_{0.7}As$ ($n = 5 \times 10^{17}$ cm^{-3}) for the n-doped region. The intrinsic region was a variable layer of 150 nm to 493 nm of *i*-$Al_{0.3}Ga_{0.7}As$ with repeated pair layers of 3 nm *i*-$Al_{0.3}Ga_{0.7}As$ and 4 nm *i*-GaAs to create *N* QWs, and 500 nm of *i*-$Al_{0.3}Ga_{0.7}As$.

The variable layer thickness was adjusted so that the entire intrinsic region thickness was fixed at 1 μm in all samples. The top *p*-region was 200 nm *p*-$Al_{0.3}Ga_{0.7}As$ ($p = 5 \times 10^{17}$ cm^{-3}), 20 nm *p*-$Al_{0.3}Ga_{0.7}As$ ($p = 2 \times 10^{18}$ cm^{-3}), and 20 nm of *p*-GaAs ($p = 2 \times 10^{19}$ cm^{-3}). A 20 nm, 1 mm diameter chromium gold (CrAu) ring was patterned by photolithography and deposited using thermal deposition. We used a wet etch to create a mesa structure and finally made electrical contact by pressing indium or Au wedge bonding.

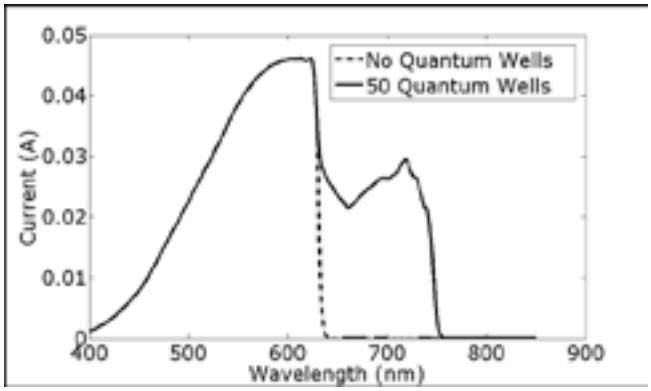

Figure 1: A plot of data obtained from the 50 QW sample versus the control.

In our photocurrent apparatus, a halogen lamp light was incident through a slit into a standard monochromator that emitted monochromatic light with a spectral width of ≈ 3 nm. The light was modulated via a mechanical chopper and lens-focused onto the mesa of the sample, which was mounted in a nitrogen flow cryostat. We used an SR530 lock-in amplifier in current-sensing mode to recover the emitted current due to photovoltaic action. We scanned the monochromator wavelength from 400 nm to 850 nm and measured the current through the device to produce spectra as in Figure 1.

Our photoluminescence apparatus consisted of a fiber-coupled Andor iDus spectrometer lens—focused to samples mounted in a closed-cycle (6-300 K) cryostat. A 550 nm laser at oblique incidence excited carriers within the $Al_{0.3}Ga_{0.7}As$

region, which diffused and relaxed into the QWs where they may radiatively recombine.

Figure 4 shows the AM 1.5 I-V characteristics of our devices that had an expected increase in the short-circuit current I_{sc} roughly linear with the number of QWs in accordance with sub-bandgap absorption, with the 50 QW sample showing a ~ 45% increase. We also observed a reduction in the open-circuit voltage that kept each device's efficiency near 10%.

Results and Conclusions:

We discuss in detail here photoluminescence for the 25 QW sample since it had the most complete dataset. PL spectra versus temp showed the QW emission peak energy decreased with increasing temp for all QW samples, and that this decrease was Varshni-like for the 25 QW sample.

An Arrhenius plot of PL versus temp in Figure 3 shows significant thermal quenching of the integrated PL intensity for the same sample. The behavior is well-described by a Boltzmann three-level model with activation energies of (27.7 ± 1.2) meV and (119 ± 6) meV. The low-energy quenching mechanism is unclear to us, however other groups with similar structures attribute a similar activation energy to thermal delocalization of excitons trapped in potential fluctuations of the well layers [2,3]. The high energy quenching mechanism we attribute to carrier thermal escape, since this energy is consistent with our theoretical band structure calculations [2,4]. Our data show the low-energy quenching mechanism is more pronounced than quenching associated with thermal escape. Quenching is observed qualitatively in all samples.

Measuring the photocurrent served as a probe of the underlying energy-dependent device physics. We first extracted the higher energy full-width half-maximum wavelength from the photoluminescence data. We then calculated the ratio between the spectrum-corrected photocurrent at this energy and the top of the band edge associated with $Al_{0.3}Ga_{0.7}As$, which had negligible temp dependence, to eliminate measurement-to-measurement light intensity fluctuations. Measurement at the upper FWHM energy corrected for the Stokes shift, the energy difference between the emission peak and the effective QW joint density of states edge observed in semiconductors with alloy disorder [5].

Figure 2 shows a semilogarithmic plot of this ratio versus temp. The single and ten QW samples both show saturation with increasing temp, while both the 25 and 50 QW samples are saturated above 77 K. The PL intensity for the 25 QW sample shows an order of magnitude decrease in radiative recombination while the photocurrent remains essentially constant, indicating that excitons previously localized by potential fluctuations in the well structures instead undergo a non-radiative recombination process unidentified in the present experiment. We also observe what appears to be an increase in the photocurrent with decreasing temp near 77-90 K in the unsaturated samples, the unclear origin of which requires more investigation.

We have characterized the photoluminescence and photocurrent properties of QW and multi-QW $Al_{0.3}Ga_{0.7}As/GaAs$ solar cells in addition to observing a promising increase in the short-circuit current. We have measured two distinct thermally-activated quenching mechanisms and highlighted future avenues of investigation into understanding the physics of these and other confinement-based devices, such as the quantum dot solar cell.

Acknowledgements:

David Christle would like to gratefully acknowledge mentor Dr. T. Noda, Dr. T. Mano, and principal investigator Dr. H. Sakaki for their generous support and tutelage throughout the program. This work was supported by the NSF, NIMS, and the NNIN iREU program.

References:

[1] A. Luque and A. Marti, Phys. Rev. Lett. 78 (1997).
[2] I. Friel et al., Appl. Phys. Lett. 85, 3068 (2004).
[3] J. D. Lambkin et al., Appl. Phys. Lett. 56 (1990).
[4] S. Birner et al., IEEE T. Electron. Dev. 54 (2007).
[5] M. Gurioli et al., Phys. Rev. B 50 (1994).

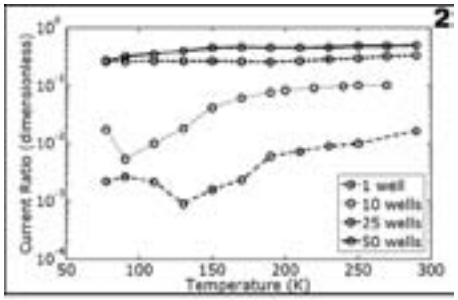

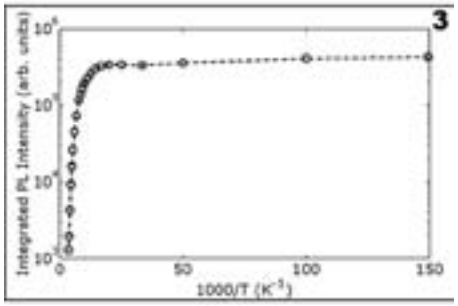

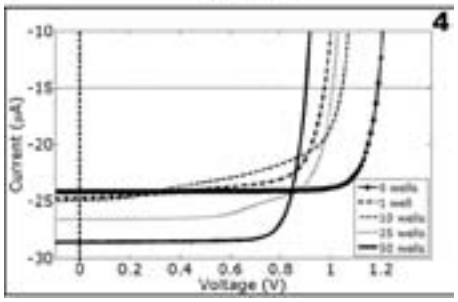

Figure 2: A semilogarthmic plot of the ratio between the upper FWHM and band-edge currents.

Figure 3: An Arrhenius plot for the 25 QW sample photoluminescence intensity.

Figure 4: I-V characteristics in AM 1.5 conditions. Dashed and dotted axes aide in showing the short-circuit current/open-circuit voltages.

Preparation of Collagen-Glycosaminoglycan Scaffolds Using Ice Templates for Tissue Engineering

Sarah Grice

Mechanical Engineering, University of Maryland, College Park

NNIN iREU Site: National Institute for Materials Science (NIMS), Tsukuba, Ibaraki, Japan
NNIN iREU Principal Investigator(s): Dr. Guoping Chen, Biomaterials Center, NIMS
NNIN iREU Mentor(s): Dr. Young-Gwang Ko, Biomaterials Center, National Institute for Materials Science
Contact: sgrice@gmail.com, guoping.chen@nims.go.jp, ko.young-gwang@nims.go.jp

Abstract:

Conventional methods of repairing or replacing lost or damaged tissues, such as transplants, surgical reconstruction, artificial prostheses, and medication, help to restore some functionality, but are rarely fully integrated into the body's processes. Tissue engineering, in contrast, implants prostheses that are seeded with cells of the appropriate type. These prostheses, typically in the form of porous scaffolds, will ideally become indistinguishable from natural tissue.

Scaffolds that can mimic the structure and chemistry of the extracellular matrix (ECM) are the most compatible with implantation. To this end, this project prepared scaffolds using an ice template technique that incorporated chondroitin-6-sulfate, a glycosaminoglycan (GAG) that is an important component of cartilage. The structure and performance of the collagen-GAG scaffolds were compared with standard collagen scaffolds.

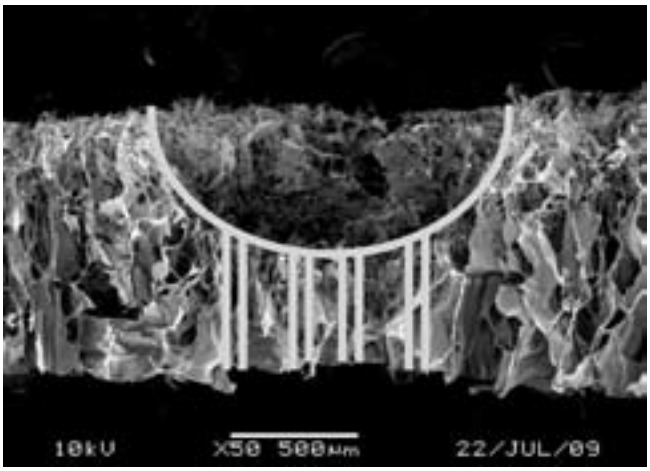

Figure 1: Cross-section of an ice template scaffold with funnel structure.

Experimental Procedure:

Scaffold Fabrication. Porous scaffolds are typically fabricated using a uniform solution of the material that will make up the structure, resulting in a uniform porous structure. The ice template technique used in this project resulted in a hierarchical funnel-like structure with large pores on the top surface and smaller pores leading to the interior of the scaffold, as in Figure 1.

This structure was created by depositing ice droplets of a uniform size on a substrate that had a silicone frame. A collagen or collagen-GAG solution was then poured over the ice droplets and frozen at -3°C for an hour, then at -80°C for several more hours, before being freeze-dried for 24 hours. The resulting porous scaffold was then crosslinked using glutaraldehyde gas, neutralized in glycine, washed, and freeze-dried again.

Results:

Collagen-GAG Solution Concentration. The optimal concentration for the collagen-GAG solution was determined by fabricating scaffolds using a fixed 1 wt% concentration of bovine collagen (Nippon Meat Packers) and varying concentrations of GAG in the form of chondroitin-6-sulfate (Sigma Life Sciences). These concentrations were 0.02, 0.05, 0.1, 0.25, and 0.5 wt%. The structure of the scaffolds was then observed using a scanning electron microscope (SEM). The 0.02 and 0.05 wt% GAG scaffolds were found to be too dense for efficient cell seeding, while the 0.25 and 0.5 wt% GAG scaffolds had a weak and inconsistent structure. The 0.1 wt% GAG to 1 wt% collagen solution was thus selected for further testing. Scaffolds fabricated using this solution will henceforth be referred to as collagen-GAG (CG) scaffolds.

Pore Structure Analysis. In order to perform comparative studies between collagen and CG scaffolds, 24 scaffolds were fabricated—12 scaffolds per solution type. The 12 scaffolds were divided into four groups, each of which used a different ice template diameter: control (no ice template used), 200 μm, 400 μm, and 800 μm. After fabrication, most of the scaffolds were separated into samples suitable for

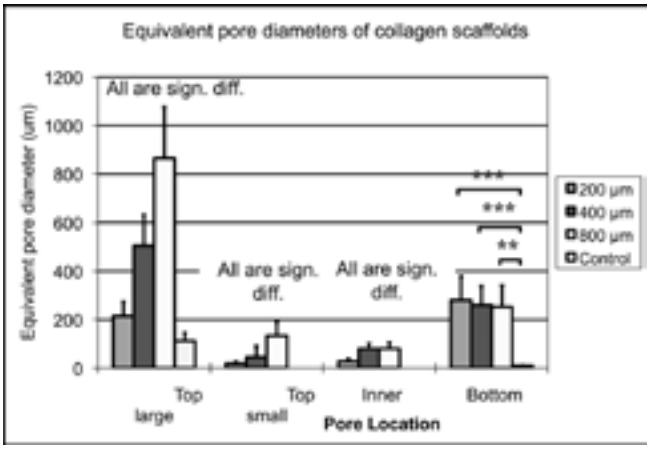

Figure 2: Mean equivalent pore diameter for collagen scaffolds.

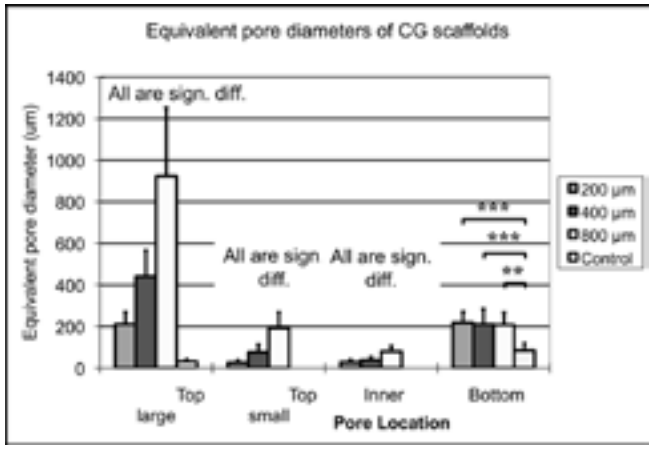

Figure 3: Mean equivalent pore diameter for collagen-GAG scaffolds.

cell culture experiments, with the remainder used to create samples for SEM imaging.

SEM images were taken of the top, bottom, and cross-section of each scaffold. The equivalent diameters of the large and small pores on the top surface, inner bulk pores, and bottom pores were sampled (n = 100) using MetaVue. The results are shown in Figures 2 and 3.

The pore equivalent diameters of the collagen and CG scaffolds were compared using a one-factor analysis of variance (ANOVA). The results are shown in Figure 3. As can be seen in Figure 3, only the 400 μm scaffolds had statistically significant differences in equivalent diameters for all pore types when comparing the collagen and CG scaffolds ($p \leq 1.22E\text{-}3$). The control scaffolds also had significantly different large top and bottom pore equivalent diameters ($p \leq 1.24E\text{-}57$), but the inner bulk and small top pores were not measured. The 200 and 800 μm scaffolds had statistically significant differences in their small top and bottom pore equivalent diameters, but their top large and inner bulk pores were not significantly different in size. (See Table 1.)

Conclusions:

From this analysis, it is clear that the addition of GAG to the scaffold has an effect on the size of the small top and bottom pores. The bottom pores of the CG scaffolds are significantly smaller than those of the collagen scaffolds, while the CG small top pores are significantly larger than their counterparts on the collagen scaffolds. There does not appear to be any pattern to the relative sizes of the top large or inner bulk pores.

Although further study is needed to determine the mechanism of the pore size differences, preliminary explanations may be formed. The significant difference between the pore sizes of the 400 μm collagen and CG scaffolds is tentatively attributed to fabrication error, as the size of the large surface pores should be mainly dependent on the size of the ice template used. The difference in the size of the small surface and bottom pores, however, is not so easily dismissed—possible mechanisms include but are not limited to the interaction of the GAG with the glutaraldehyde gas during crosslinking and differences in the thermal properties of the CG solution compared with the collagen solution.

Future Work:

The samples not used for SEM sample creation will be used in cell culture experiments to determine the effect of the addition of glycosaminoglycan on cell adhesion, growth, and differentiation.

Acknowledgments:

I would like to thank my PI, Dr. Chen, my mentor, Mr. Ko, and the rest of the research group who made me feel at home and helped me with the technical aspects of my research. I am also deeply grateful to the National Nanotechnology Infrastructure Network International Research Experience for Undergraduates (NNIN iREU) Program and the National Science Foundation for making this once-in-a-lifetime experience possible.

Is CG Significantly Different from Collagen?

	200 µm	400 µm	800 µm	Control
Large surface	No	Yes; smaller	No	Yes; smaller
Small surface	Yes; larger	Yes; larger	Yes; larger	
Inner	No	Yes; smaller	No	
Bottom	Yes; smaller	Yes; smaller	Yes; smaller	Yes; smaller

Table 1: Results of one-factor ANOVA comparing collagen and collagen-GAG scaffolds ($\alpha = 0.05$).

Electrochemical Deposition of Polyaniline on Nanoelectrode CrossBar Structures

Jose Guevarra

Mechanical Engineering, University of California, Santa Barbara

NNIN iREU Site: Institut Für Bio- Und Nanosysteme (IBN), Forschungszentrum, Jülich, Germany
NNIN iREU Principal Investigator(s): Dr. Dirk Mayer, Molecular Bioelectronics, Forschungszentrum, Julich
NNIN iREU Mentor(s): Nils Sanetra, Molecular Bioelectronics, Forschungszentrum, Julich
Contact: joseg@engineering.ucsb.edu, dirk.mayer@fz-juelich.de, n.sanetra@fz-juelich.de

Abstract:

Molecular bioelectronics investigates the electronic characteristics of biomolecules, hoping to replace conventional electronic components with molecular equivalents, and produce new biosensors. Molecular electronics typically interacts with layered and even single biomolecules by metallic electrodes. Fabricating electrodes separated by a gap size comparable to the size of molecules is difficult. A convenient method of filling this space is to electrochemically deposit conducting material on the electrodes to fill the gap. Polyaniline (PANI) was electrochemically deposited on nanoelectrodes to bridge the gap between two parallel 300 nm half-pitch gold (Au) electrodes. By varying the deposition time, voltage bias, and aniline monomer concentration several different PANI morphologies were produced.

Introduction:

Molecular bioelectronics integrates biomolecules into inorganic structures in order to investigate and control charge transport phenomena in and across biomolecules. An increasingly helpful tool in investigating biomolecules electronic properties is the crossbar electrode structure. Created by intersecting nanoscale electrodes, one on top of the other, crossbar electrodes have an interjunction gap that can be filled with monolayers or individual biomolecules. Fabricating electrodes separated by tens of nanometers is difficult. A method of producing a gap size on the order of molecules is to electrochemically deposit conducting material between the electrodes. The aim of this project was to investigate if PANI could be used to bridge the gap between two parallel 300 nm half-pitch electrodes.

Aniline is an organic compound that can be oxidized into a conducting polymer, emeraldine. By applying a voltage bias between two electrodes immersed in an aniline monomer electrolyte, the aniline oxidizes on the cathode thus depositing polyaniline (emeraldine) on the electrode. As the PANI grows out from the electrode, it creates an electrically conductive "bridge" in the gap between the parallel electrodes.

Experimental Procedure:

A 0.1M aniline + 0.5M H_2SO_4 solution was made by mixing aniline monomer (Sigma-Aldridge) and sulfuric acid (H_2SO_4) in water. Aniline monomer instantly precipitates when added to H_2SO_4 solution. Shaking the mixture dissolves the precipitate.

The current between parallel electrodes was tested in air to ensure that they were not electrically connected. A micropipette was used to directly apply a drop of aniline solution onto the electrodes, then a voltage bias is applied across the electrodes for over an hour using a probe station. After the deposition was performed, the electrodes were cleaned in Milli-Q water, blown dry, and cyclic voltammetry was performed on the electrodes immersed in H_2SO_4 and in air to test their conductance. Several different voltage biases (0.95V, 0.97V, 1V) and doubling the aniline concentration were used to observe their effect on the deposition.

Results:

After the electrodeposition, a green substance was observed on the acting cathode, Figure 1. Due to the nanoscale gap

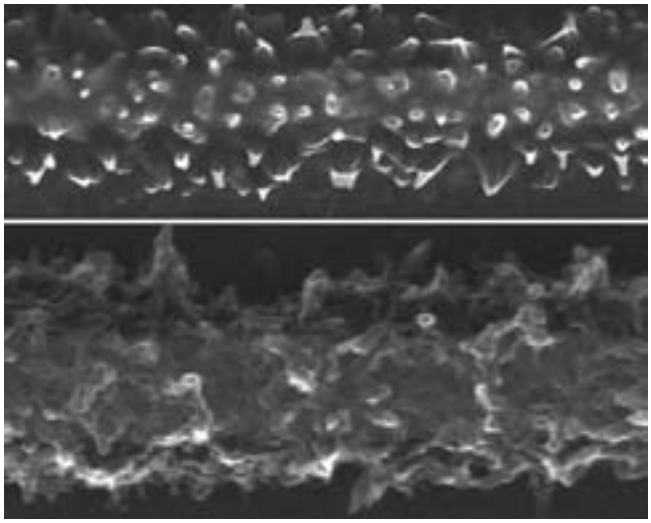

Figure 1: Depositions using 0.1M aniline (top) and 0.2M aniline (bottom) solutions.

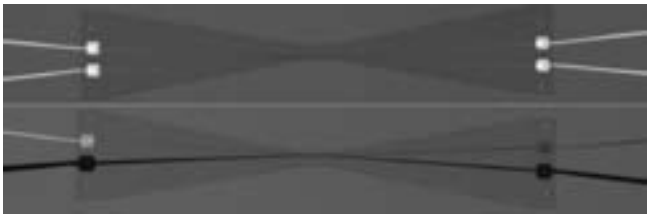

Figure 2: Parallel electrodes before the deposition of polyaniline (top) and after (bottom).

between the electrodes, it was not possible to observe if bridging between the gap had occurred with a microscope; bridging could be determined several other ways. During the deposition, the conductance would fluctuate and increase in a step-like fashion due to PANI reaching the other electrode, hence allowing current to pass between the electrodes. After rinsing the electrodes in water and blowing them dry, a voltage sweep in air could also be performed to compare the conductance before and after the deposition. The conductance ranges on the order of 10^{-8} to 10^{-6} S in air. The PANI growth between the electrodes could also be viewed by using a scanning electron microscope (SEM). Figure 2 shows an SEM image of the space between two parallel electrodes. It shows small protrusions from the cathode (bottom) crossing the gap and contacting the other electrode. By varying several parameters of the electrochemical deposition, the morphology of the deposited PANI could be changed.

The electrochemically deposited PANI has a coral-like morphology. An increase in the concentration of the aniline monomer has a tendency to decrease the emeraldine density and change the emeraldine morphology. Figure 3 shows a deposition performed using 0.1M aniline + 0.5M H_2SO_4 (top) and another performed using double the aniline concentration (bottom).

Three different voltage biases were used to deposit PANI on Au electrodes. Increasing the voltage bias had a tendency to decrease the deposition density over the electrodes. Figure 4 shows the PANI morphology for biases of 0.95V, 0.97V, and 1V (top to bottom). The coral-like features of the PANI decrease as the voltage is increased despite having similar deposition times and aniline concentrations. This may be due to oxidation of emeraldine occurring at lower voltages.

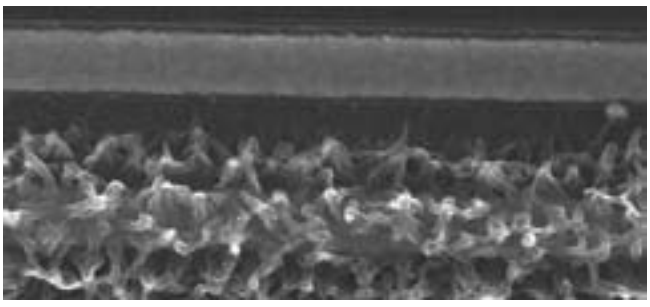

Figure 3, left: Emeraldine protrusion connecting the cathode to the anode across a 300 nm gap.

Conclusions:

The conducting polymer emeraldine was electrochemically deposited on Au electrodes. The morphology of the PANI can be modified by changing the aniline concentration or the voltage bias. The time required to bridge the 300 nm gap between electrodes ranged from 45 minutes to 1.5 hours. The expected conductance after bridging occurs ranges from 10^{-8} to 10^{-6} S when measured in air.

Future Work:

Deposition results vary with aniline concentration and solution immersed electrode surface area. To control these parameters applying a funnel structure over the electrodes is recommended. Future work will consist of applying top electrodes on polyaniline deposited bottom electrodes, measuring the resulting conductance between top and bottom electrodes, and depositing biomolecules between the interjunction gaps.

Acknowledgments:

The National Nanotechnology Infrastructure Network, The National Science Foundation, Lurie Nanofabrication Laboratory. I would like to thank Dr. Dirk Mayer, Dr. Andreas Offenhäusser, and Niles Sanetra for their guidance and help with my project. Thanks to everyone at IBN-2, Lynn Rathbun, and my fellow REU students for their motivation and making the summer such a great experience.

References:

[1] Staikov, G; "Electrochemical formation and the properties of thin polyaniline films on Au (101) and p-Si (111)"; Appl. Phys, A 87,405-409 (2007).

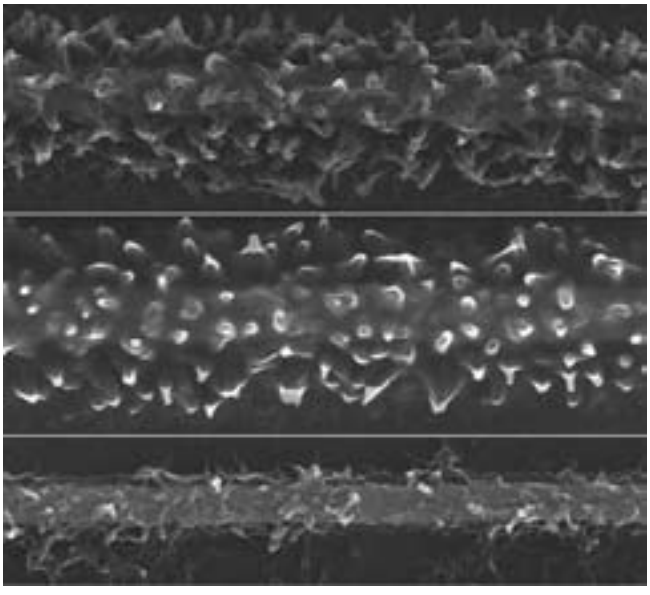

Figure 4, above: Depositions performed at 0.95V (top), 0.97V (center), and 1.0V (bottom).

Charge Transfer of Recombinant Proteins

Jennifer Hou

Molecular and Cellular Biology, Johns Hopkins University

NNIN iREU Site: Institut Für Bio- Und Nanosysteme (IBN), Forschungszentrum, Jülich, Germany

NNIN iREU Principal Investigator(s): Dr. Dirk Mayer, Institut für Bio- und Nanosysteme (IBN2); Prof. Arnd Baumann, Ph.D., Institut für Strukturbiologie und Biophysik (ISB1), Jülich Forschungszentrum

NNIN iREU Mentor(s): Zhiwei Yi, Institut für Bio- und Nanosysteme (IBN2), Jülich Forschungszentrum

Contact: jhou4@jhu.edu, dirk.mayer@fz-juelich.de, a.baumann@fz-juelich.de, z.yi@fz-juelich.de

Abstract and Introduction:

In nature, cytochrome *c* (Cyt *c*) serves a role in the synthesis of adenosine triphosphate (ATP) [1]. Cyt *c*, a mitochondrial protein [1,2], passes single electrons by oxidation and reduction of its redox center [2]. Researchers employ Cyt *c* for charge transfer research due to its solubility [1] and "accessible redox center" [3].

For charge transfer, Cyt *c* must form stable contact with electrodes and must also have a "defined orientation" in a two terminal electrode junction [3]. To increase immobilization, Schröper *et al*. placed cysteine or hexahistidine tags at either the N or C terminus of Cyt *c*, by genetically altering the pJRhrsN2 construct [4]. Immobilization improved by electro-static interactions of C-cys with "carboxy-terminated self-assembled monolayers (SAM)" [3] and by affinity binding of N-his_6 with nickel-nitrilotriacetic acid (NiNTA) SAM.

The motivation to obtain recombinant proteins arises from the desire to conduct further research on their integration into bioelectronic devices (cross bars and break junctions) and to learn more about charge transfer [3]. The focus of this work was to obtain high-yields and to characterize C-cys, C-his, N-his, and NC-his Cyt *c*.

Experimental Procedure:

To obtain Cyt *c*, first, a mixture of 1.0 μL plasmid deoxyribonucleic acid (DNA) and 50 μL [5] E.coli BL21 cells was iced for 30 minutes [6]. Then cells were heat-shocked at 42ºC [5] for 45 seconds before plating on ampicillin plates.

Since initial yields had decreased, several culturing methods were investigated to determine which modifications would increase expression, modeled after [4] and [6]. First, yields were evaluated for cultures with and without precultures (methods 1-5 [4]) as shown in Figure 1. Second, aeration (shaker speed) and medium [4] were varied (methods 1, 6, and 7). Third, larger volumes were tried (methods 8 and 9). For precultures and cultures, the incubation temperature was 37ºC overnight, and 37ºC for 2 hrs and then 30ºC for 50 hrs, respectively. For glycerol stocks [6], individual colonies were precultured in LB, screened, combined with glycerol, and stored at -80ºC. Cyt *c* was expressed from these solutions by method 4.

To purify Cyt *c*, cells were pelleted, re-suspended in protease inhibitor, lysed, and centrifuged. Next, cation exchange and affinity chromatography columns were prepared for wildtype and C-cys and for C-his and NC-his Cyt c, respectively. Wild-type and C-cys while C-his and NC-his were eluted with 0.5M NaCl buffer and 250 mM imidazole buffer, respectively.

For cyclic voltammetry (CV) of complex Cyt *c* and Cyt *c* reductase, electrodes were placed into 1 mM 4-mercatophenol (MPhOH) [3]. Also, 0.8 mg/ml of Cyt *c* reductase was combined with C-cys Cyt *c* for 2 hrs [3]. Afterwards, electrodes were placed in the complex for another 2 hrs. To measure the reaction in NADH, with a 2 mV/s scan rate, the buffer was changed to 7.5 mM NADH buffer [3]. For current-voltage characterization of C-cys Cyt *c* in a break junction, first 10 mM 11-mercaptoundecanoic acid solution (MUA) and then 10 μM C-cys Cyt *c* were applied to electrodes for at least 5 minutes each.

Method	Preculture Medium	Preculture Volume (ml)	Culture Medium	Culture Volume (ml)	Shaker Speed (rpm)	Cyt *c* Expression (Red Cultures/Total Cultures)
1	LB	5	TB	200-250	165	0/8
2	TB	5	TB	200-250	200	2/4
3	TB	25	TB	200-250	200	6/10
4	-	-	TB	200-250	200	11/18
5	-	-	LB	200-250	200	2/14
6	LB	5	TB	200-250	180	2/24
7	LB	5	LB	200-250	180	0/2
8	-	-	TB	500	200	1/9
9	TB	25	TB	500	200	0/5

Figure 1: E.coli preculture and culture methods and results.

Results and Conclusions:

Higher expression was obtained from direct culturing. As shown in Figure 1, 11/18 cultures (method 4) and 2/4 cultures (method 8) had high expression or appeared red (Cyt *c*). Also, preculturing 5 or 25 ml TB [4] (method 2 and 3) improved expression; 2/4 and 6/10

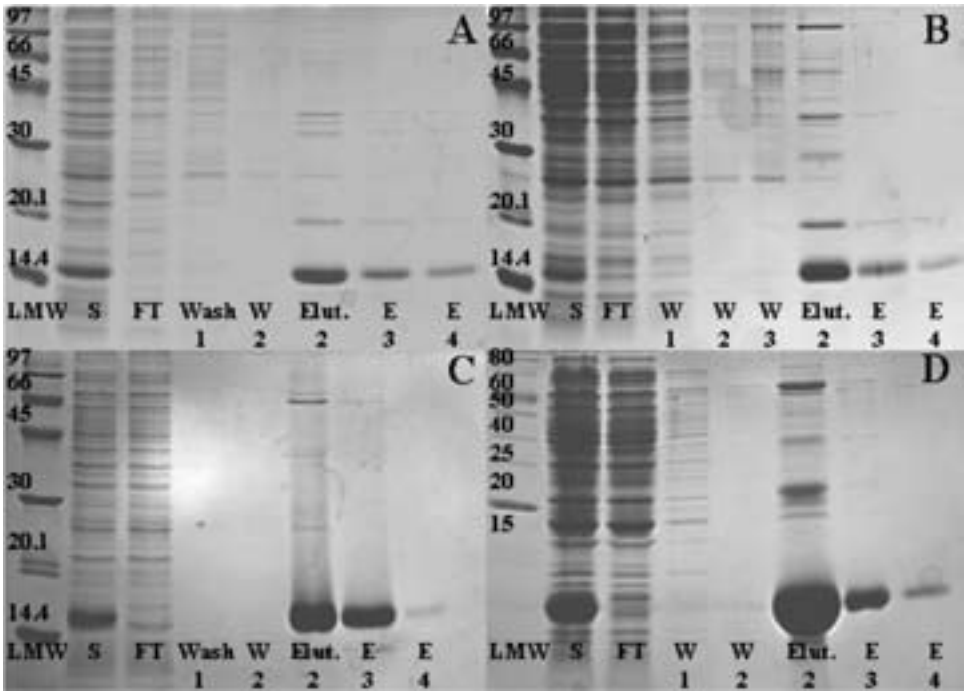

Figure 2: SDS PAGE of wildtype; (A), C-cys (B), C-his (C), and NC-his (D) Cyt c.

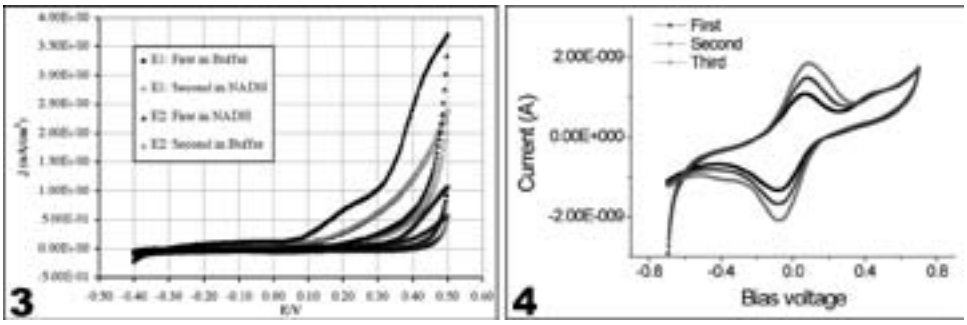

Figure 3: Electro-enzymatic reaction of C-cys Cyt c and Cyt c reductase in NADH [8].

Figure 4: Current-voltage characteristics of C-cys Cyt c integrated into a break junction [9].

red cultures. However, larger volumes (method 8 and 9) showed lower expression of 1/9 and 0/5 red cultures. Higher expression from direct culturing may be caused by an optimal 250 ml culture volume [7]. The expression of recombinant proteins from frozen glycerol stocks was consistent; 6/6 red cultures.

SDS PAGE (Figure 2) reveals distinct bands at 14.4 kilo-Daltons (kDa) [3], especially in second elution fractions. Lanes S and FT represent supernatant and flow through. UV-Vis shows absorbance peaks: 415, 520, and 550 nm, demonstrating a properly "incorporated heme group" [3]. Surface plasmon resonance (SPR) indicates "homogenous" immobilization [3]. Also, CV of C-cys Cyt *c* shows single peaks for oxidation and reduction of the redox center.

Figure 3 shows a strong peak 3.70 μA/cm^2 near 0.5V (Ag/AgCl) for the complex of C-cys Cyt *c* and Cyt *c* reductase in NADH (electrode 2, E2), compared to 1.05 μA/cm^2 near 0.5V in buffer. Since the complex was incubated before its immobilization, this may have increased its immobilization because the native binding site of C-cys Cyt *c* heme group would be more "accessible" to Cyt *c* reductase. Last, break junction data of C-cys Cyt *c* (Figure 4) show single oxidation and reduction peaks.

In conclusion, higher yields of wildtype, C-cys, C-his, and NC-his Cyt *c* were obtained through TB direct culturing or by 25 ml TB preculturing [4]. Also, glycerol stocks consistently expressed proteins.

Future Work:

The next steps are; further study of the integration of C-cys Cyt *c* into bioelectronic devices, and the expression and characterization of bifunctional N-his/C-cys Cyt *c*.

Acknowledgements:

I would like to thank Dr. Dirk Mayer for his guidance, encouragement, and for this tremendous opportunity. I would like to thank Prof. Dr. Arnd Baumann for his generosity in allowing me to use ISB1 facilities and for his valuable teaching. I would like to express my gratitude to Zhiwei Yi for his advice and support. Special thanks to Dr. Lynn Rathbun, Prof. Tobias Hanrath, Florian Schröper, the group members and staff at IBN2, IBN4, ISB1, and Jülich Forschungszentrum. I thank Prof. Dr. Andreas Offenhäusser for this profound experience. Last, I gratefully thank the NNIN iREU and NSF for their generous funding.

References:

[1] J.M. Berg et al, "Biochemistry," W.H. Freeman & Co., 1120 (2007).
[2] H. Lodish, "Cell Biology," W.H. Freeman & Co., 486, 495, 497 (2008).
[3] F. Schröper, "Optimierte Immobilisierung von Redoxproteinen an funktionale Elektrodenoberflächen für die molekulare Bioelektronik" PhD-Thesis, RWTH Aachen, Biologe (2009).
[4] J.N. Rumbley et al, "Recombinant Equine Cytochrome *c* in *Escherichia coli*: High-Level Expression, Characterization, and Folding and Assembly Mutants," Biochemistry, 13894-6 (2002).
[5] www.biomol.com.
[6] Dr. Mayer, Prof. Dr. Baumann, Florian Schröper.
[7] Prof. Arnd Baumann, Ph.D., Zhiwei Yi.
[8] Dr. Liu.
[9] Dong Xiang.

Effects of Immobilized Oligoarginine Peptides on Cellular Uptake of Gold Nanoparticles

Jillian Kiser

Mechanical Engineering, Franklin W. Olin College of Engineering

NNIN iREU Site: National Institute for Materials Science (NIMS), Tsukuba, Ibaraki, Japan

NNIN iREU Principal Investigator(s): Prof. Yukio Nagasaki, Tsukuba Research Center for Interdisciplinary Materials Science, University of Tsukuba; Satellite Lab of International Center for Materials Nanoarchitectonics, NIMS

NNIN iREU Mentor(s): Dr. Jun Nakanishi, International Center for Materials Nanoarchitectonics, NIMS

Contact: jillian.kiser@students.olin.edu, nagasaki@nagalabo.jp, nakanishi.jun@nims.go.jp

Abstract:

Developing ways to deliver cargoes past the lipid bilayer of cells is a significant field of investigation in modern nanobiology. The use of cell-penetrating peptides (CPPs) [1,2] and incubation in the presence of pyrene butyrate [3] are two methods that have gained prominence. The objective of this project was to evaluate the efficiency of oligoarginines (R_n) as a CPP intended to internalize gold nanoparticles (GNPs) into cells. The GNPs were modified with dithiol-ended poly(ethylene glycol) (PEG) and an oligoarginine-conjugated PEG-dithiol (PEG-R_n). Several parameters such as GNP diameter, the ratio of PEG to PEG-R_n, and the length of both PEG and arginine molecules were investigated in detail. Results showed that 30 nm GNPs modified with a 1:1 ratio of PEG_{5k} and PEG_{5k}-R_{12} conjugate had significant interaction with the cell walls, ultimately resulting in cellular uptake through endocytosis.

Experimental Procedure:

A bulk conjugate of dithiobis (succinimidyl undecanoate) with PEG-R_n, PEG-Tx (Texas Red conjugate), or PEG was prepared in a two hour reaction in the presence of triethylamine as a catalyst. This disulfide conjugate was then reacted directly with citrate-capped GNP to immobilize the PEG, PEG-R_n, or PEG-Tx on the nanoparticle surface in an overnight reaction. The sample was then purified through centrifugation and washed into phosphate buffer saline (PBS). After sample preparation, zeta-potential was measured to confirm successful immobilization and absorbance spectra were recorded to check the sample's dispersity.

Cell experiments were then performed to determine the sample's level of interaction with the cell membrane. Because the lissamine rhodamine fluorescent labels on the arginine peptides were found to be quenched through interaction with arginine, confocal reflectance mode microscopy [4] was used to observe the GNP's interaction with cells. HeLa cells were incubated with 7 μM pyrene butyrate in PBS for 5 minutes, followed by a 10 minute incubation with GNPs and pyrene butyrate in PBS. After incubation with GNPs, cells were washed with Hank's Balanced Salt Solution (HBSS) to remove any GNPs that had not interacted with the cells. Cells were then observed on a Leica SP5 confocal in reflectance mode, followed by further incubation and observation.

Four parameters were varied throughout the project: GNP diameter, ratio of PEG to PEG-R_n, length of PEG, and length of arginine. GNPs of 5 nm, 15 nm, and 30 nm diameter were used, and the ratio of PEG to PEG-R_n was varied from 1:1 to 1:9. For cell experiments, all samples had a 1:1 ratio of PEG to PEG-R_n. This ratio was found to be an ideal balance between the cell penetrating properties of oligoarginine and the stabilizing influence of PEG on nanoparticle dispersity. In addition, PEG of molecular weights 5000 (PEG_{5k}) and 2000 (PEG_{2k}), and oligoarginines composed of 8 (R_8) and 12 (R_{12}) arginines, were used.

Results and Discussion:

Because aggregated GNPs change from red to blue, an absorbance spectra is important in determining the stability of the sample. As seen in Figure 1, the absorbance spectra indicated no significant aggregation in the samples used in

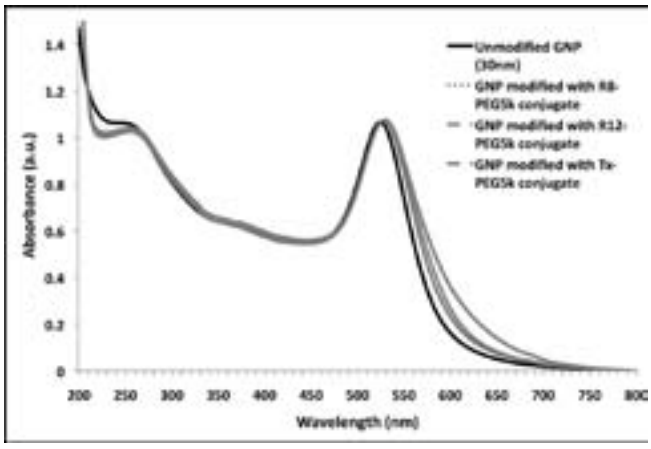

Figure 1: Absorbance spectrum of modified and unmodified particles.

cell experiments. In addition, the successful immobilization of Rn can be inferred from the slight red shift in the spectra of the modified particles due to the color of lissamine rhodamine dye. Immobilization of PEG and PEG-R_n to the GNP surface was also verified from the change in the zeta potential from -27.3 to 0.24 mV.

Of all the parameter permutations attempted, only the 30 nm GNP modified with a 1:1 ratio of PEG_{5k} to PEG_{5k}-R_{12} conjugate successfully interacted with the cells. It is important to note that, if either the particle diameter or the length of the arginine peptide is changed, the GNP ceases to have any interaction with the cells. Thus, a significant conclusion of this work is that particle diameter and peptide length are dependent parameters for inducing cellular uptake.

When GNPs modified with PEG_{5k}-Tx were incubated with cells, little to no reflectance was observed, indicating low internalizing efficiency of GNPs without oligoarginine, as shown in Figure 2. On the other hand, high reflectance was observed when GNPs modified with PEG_{5k}-R_{12} were incubated with cells (Figures 3 and 4).

In addition, it should be noted that, as seen in Figure 3, the GNPs are only found on the outside of the cell after the initial 10 min incubation. In Figure 4, however, the GNPs can be seen inside the cell after an additional 3 hour incubation. This slow uptake of the particles is most likely due to endocytosis, rather than direct membrane translocation. To achieve direct membrane translocation, the interaction between particles and the cell membrane must be further optimized.

Conclusions:

The combination of 30 nm GNPs with PEG_{5k}-R_{12} creates the strongest interaction with the cell membrane of any other attempted combination. This sample was ultimately internalized through endocytosis.

Acknowledgements:

I'd like to thank Dr. Jun Nakanishi, Dr. Yukio Nagasaki, Dr. Dolçe Fabregat, and Hidekazu Nakayama for their technical support, as well as the National Science Foundation, the National Nanotechnology Infrastructure Network iREU Program, and the National Institute of Material Science for financial support that made this project possible.

References:

[1] Pujals, S; "Shuttling Gold Nanoparticles into Tumoral Cells with an Amphipathic Proline-Rich Peptide." ChemBioChem, 10, 1025-1031, (2009).

[2] Takayama, K; "Novel System to Acheive One-Pot Modification of Cargo Molecules with Oligoarginine Vectors for Intracellular Delivery." Bioconjugate Chem, 20, 249-257, (2009).

[3] Takeuchi, T. "Direct and Rapid Cytosolic Delivery Using Cell-Penetrating Peptides Mediated by Pyrenebutyrate." ACS Chemical Biology, 5, 299-303, (2006).

[4] Pujals, S. "Shuttling Gold Nanoparticles into Tumoral Cells with an Amphipathic Proline-Rich Peptide." ChemBioChem, 10, 1025-1031 (2009).

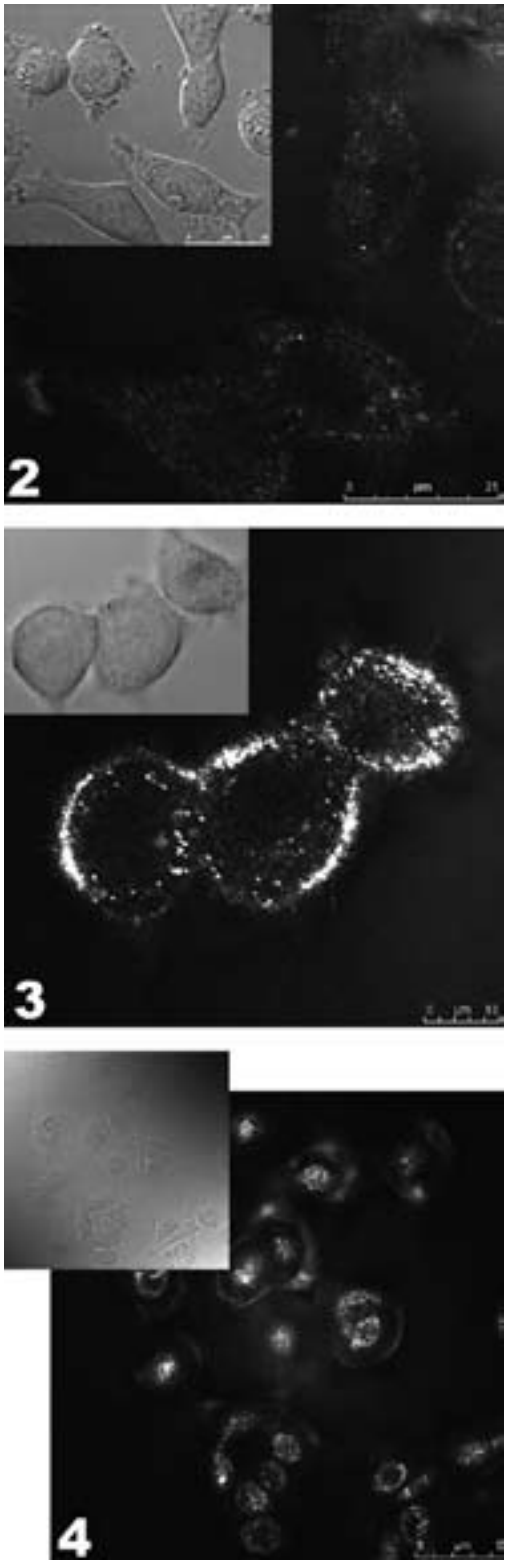

Figure 2, top: Reflectance image of HeLa cells loaded with GNP modified with 1:1 ratio of PEG_{5k} and PEG_{5k}-Tx.

Figure 3, middle: Reflectance image of HeLa cells loaded with 30 nm GNP modified with 1:1 ratio of PEG_{5k} and PEG_{5k}-R_{12} after 10 minute incubation.

Figure 4, bottom: Reflectance image of HeLa cells loaded with 30 nm GNP modified with 1:1 ratio of PEG_{5k} and PEG_{5k}-R_{12}, three hours after initial incubation.

High-κ Gate Stack for d-DotFET

Kishore Padmaraju

Electrical Engineering and Physics, University of Rochester

NNIN iREU Site: Institut Für Bio- Und Nanosysteme (IBN), Forschungszentrum, Jülich, Germany

NNIN iREU Principal Investigator(s): Dr. Jüergen Moers, Institut für Bio- und Nanosysteme (IBN-1)

NNIN iREU Mentor(s): Julian Gerharz, Institut für Bio- und Nanosysteme (IBN-1)

Contact: kpadmara@gmail.com, j.moers@fz-juelich.de, j.gerharz@fz-juelich.de

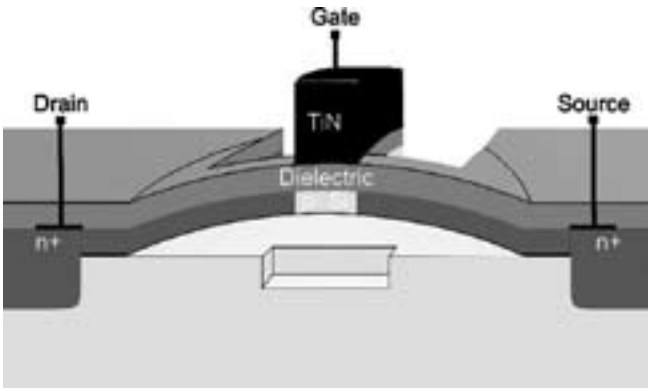

Figure 1: Schematic of the d-DotFET.

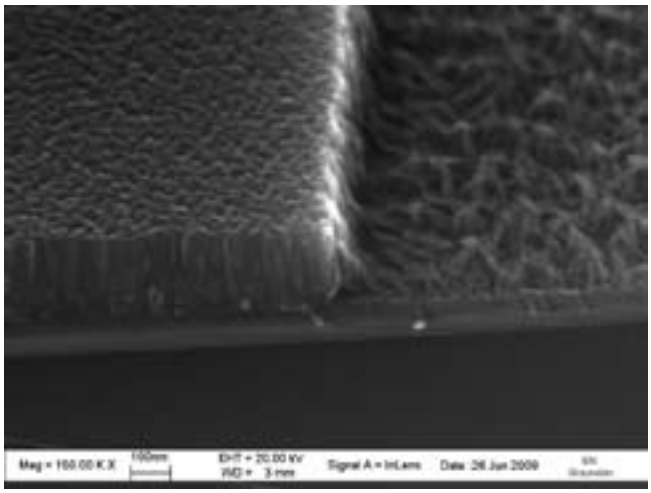

Figure 2: Cl_2 plasma etch of TiN on top of $GdScO_3$ layer.

Introduction:

The Disposable Dot Field Effect Transistor (d-DotFET) is a collaborative research project, funded by the European Commission, aimed at utilizing a strained silicon (Si) channel in a traditional metal oxide semiconductor field effect transistor (MOSFET) design; thereby achieving a faster transistor. In a strained Si layer, the interatomic distance between atoms is higher than that of normal Si. As a result, strained Si exhibits higher electron carrier mobility than normal Si. In the d-DotFET project, biaxially strained Si is achieved by growing a layer of Si over a pseudo-substrate of silicon germanium (SiGe). Specifically, the silicon is grown over a germanium dot that is later evacuated. However, the nanoscale dimensions of the d-DotFET require gate structures on the scale of 50 nm.

The goal of this project was to create a fabrication process for a high-κ gate stack consisting of 50-100 nm conducting layer of titanium nitride (TiN) and a thin dielectric layer of either silicon dioxide (SiO_2), silicon nitride (Si_3N_4), or gadolinium scandate ($GdScO_3$).

Experimental Procedure and Results:

The nanoscale dimensions of the gate stack requires that the TiN etching process produces vertical flanks—what is known as an anisotropic etch. Reactive ion etching (RIE) experiments on samples of TiN/$GdScO_3$ were conducted using a chlorine (Cl_2) plasma. The samples were prepared by depositing a layer of $GdScO_3$ on top of a Si substrate, and subsequently sputtering TiN on top of the $GdScO_3$ layer. As can be seen in Figure 2, a sample etched in a Cl_2 plasma resulted in relatively vertical flanks.

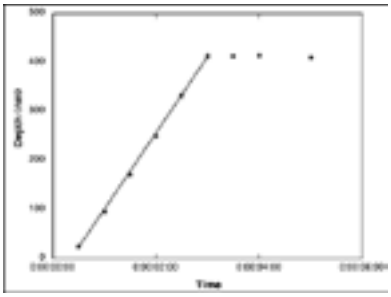

Figure 3: TiN etching with Cl_2 plasma

A profilometer was used to test the depth of the etch for increasing etch times on samples of 400/10 nm of TiN/$GdScO_3$. Figure 3 shows the results when using a Cl_2 plasma with a RF bias power of 10 W, an ICP power of 1000 W, at 20°C, with 30 sccm of Cl_2. The Cl_2 plasma etches TiN at the rate of 150 nm/min. In addition, the plasma stopped well on the $GdScO_3$ layer, failing to etch the layer after two additional minutes of etching. This indicates a selectivity greater than 30—a very high selectivity of TiN over $GdScO_3$.

When etching with Cl_2, we found that a grass-like layer of titanium oxide (TiO), most likely titanium dioxide (TiO_2),

was left after the etching of TiN. The TiO residue can be seen in Figure 4, where a Cl_2 plasma has etched away ~ 260 nm of TiN from an originally 400 nm layer of TiN. What remains on top is a ~ 170 nm grass layer of TiO.

Previous studies on the oxidation of TiN give evidence that the grass layer is composed of TiO_2 [2]. We surmised that the columnar structure of TiN lead to the creation of TiO_2 in between the TiN gaps. Hence, when TiN is etched, the TiO_2 remains as a porous grass-like layer. To further verify that the grass-like layer was titanium oxide, we performed an elemental analysis using an energy dispersive x-ray spectroscopy (EDX) measurement. The measurement was performed on a etched sample of $TiN/GdScO_3/Si$. The qualitative measurement found the sample to be composed of titanium, oxygen, gadolinium, scandium, and silicon (Ti, O, Gd, Sc, and Si). Hence, we were able to rule out several possible compounds such as titanium chlorides.

We also inferred that the top of the TiN layer had been oxidized, forming a thin layer of TiO_2. This would explain the 20-30 s of inhibition time that occurred when we etched TiN with Cl_2. This was in agreement with prior experiments using SF_6 etching, where there was no inhibition time, and subsequently no grass-like layer remaining after the TiN etch. This was a result of SF_6 etching TiO_2 much more effectively than Cl_2 [3].

One of the goals of this project was to use $GdScO_3$, a high constant (high-κ) dielectric, in conjunction with TiN. Ideally, the $GdScO_3$ layer could be etched with a process similar to the one used to etch the TiN layer. As seen previously in Figure 3, Cl_2 is very poor at etching $GdScO_3$. However, it has been shown that the selective removal of $GdScO_3$ over Si is possible using a combination of chlorination and water purging [1]. Chlorinated $GdScO_3$ is water soluble. Hence, it is removed when rinsed with water. The appropriate process is to first expose the $GdScO_3$ layer to 30 s of a Cl_2 plasma, chlorinating the surface, and then water purge the layer, removing 1-2 nm of $GdScO_3$ [1].

An experiment was conducted in which a 400/8 nm sample of $TiN/GdScO_3$ was etched for 3.5 min with a Cl_2 plasma at a plate power of 10 W. The intent of this etching was to remove the TiN layer. Then the sample was etched with a Cl_2 plasma with a plate power of 50 W to chlorinate the $GdScO_3$. The sample was then water rinsed and the procedure was repeated eight more times for a total of nine cycles. Scanning electron microscope images showed us that the $GdScO_3$ layer was removed, albeit inhomogeneously. This inhomogeneous removal is the result of a micromasking effect caused by the TiO_2 grass-like layer.

Future Work:

We have identified a process that will etch TiN with the selectivity and anisotropy required at nanoscale dimensions, and identified methods for etching the various underlying dielectrics that could be used in our gate stack. Further work needs to be conducted to remove the TiO_2 residue left from TiN etching. Future efforts will either push to prevent the oxidation of TiN or for the targeted removal of TiO_2.

Acknowledgements:

I would like to thank my mentor and PI, Julian Gerharz and Dr. Jüergen Moers, for the time and resources they dedicated throughout my research experience. I also express appreciation for the helpful staff at the Forschungszentrum, and Prof. Dr. Detlev Grützmacher in particular. Lastly, I am grateful to Lynn Rathbun and Wolfgang Albrecht for their coordination of the iREU program.

References:

[1] Shamiryan et al. "Selective Removal of Rare Earth Based High-κ Materials in a Semiconductor Device"; United States Patent Application Publication, April 2008.

[2] Naresh C. Saha, Harland G. Tompkins. "Titanium nitride oxidation chemistry: An x-ray photoelectron spectroscopy study"; J. Appl. Phys. 72, 3072 (1992).

[3] S. Norasetthekul, P.Y. Park, K.H. Baik, K.P. Lee, J.H. Shin, B.S. Jeong, V.Shishodia, E.S. Lambers, D.P. Norton, S.J. Pearton. "Dry etch chemistries for TiO_2 thin films." Appl.Surf. Sci. 185, 27-33 (2001).

[4] H. K. Chiu, T. L. Lin, Y. Hu, K. C. Leou, H. C. Lin, M. S. Tsai, T. Y. Huang. "Characterization of titanium nitride etch rate and selectivity to silicon dioxide in a Cl_2 helicon-wave plasma"; J.Vac. Sci. Technol. 19, 455-459 (2001).

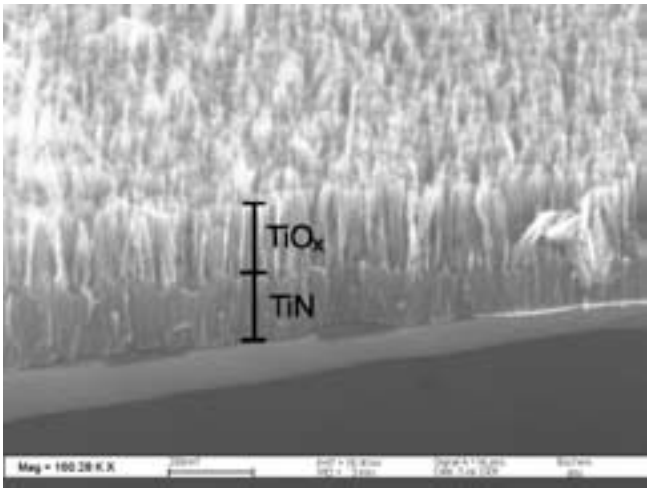

Figure 4: Titanium oxide residue after etching with Cl_2 plasma.

Resistive Switching in Ag/Cu Doped Methyl-Silsesquioxane for Future Memory Applications

Adam C. Scofield

Electrical Engineering, University of California, Los Angeles

NNIN iREU Site: Institut Für Bio- Und Nanosysteme (IBN), Forschungszentrum, Jülich, Germany

NNIN iREU Principal Investigator(s): Dr. Carsten Kügeler, Institut für Festkörperforschung (IFF), Forschungszentrum Jülich

NNIN iREU Mentor(s): Roland Rosezin, Institut für Festkörperforschung (IFF), Forschungszentrum Jülich

Contact: scofield.adam@gmail.com, c.kuegeler@fz-juelich.de, r.rosezin@fz-juelich.de

Introduction:

Increased scaling of current memory devices will soon reach a limit due to the complexity of their design and the required architecture for implementing them. Furthermore, no current technology simultaneously allows for high speed, high density, and non-volatile memory. Resistive random access memory (RRAM) offers a possible solution to fulfill all three of these requirements [1]. One such RRAM cell uses a symmetric design consisting of two inert electrodes with a methyl-silsesquioxane (MSQ) thin film in between. This symmetric metal-insulator-metal design allows for high density integration by using nano-crossbar arrays capable of being stacked in multiple layers [2]. Recently, a cell with a similar device structure demonstrated fast switching speeds of less than 10 ns, showing great promise for future memory applications [3]. However, the reliability of these devices must first be improved and the performance optimized before high density integration can be achieved.

Experimental Procedure:

The resistive switching devices used in this study were based on MSQ thin films doped with either silver (Ag) or copper (Cu). Under strong electric fields, Ag and Cu atoms within the MSQ are ionized and become mobile. The proposed mechanism for resistive switching is that the mobile ions form a filament within the MSQ film, through which is a low resistance path for current to flow. This filament can then be broken and reformed repeatedly to achieve memory function. The primary variable affecting performance in such a device then is the concentration of dopant metal within the film. In order to study the effects of doping on device performance, a total of eight samples were fabricated with different doping concentrations; four samples each for Ag and Cu.

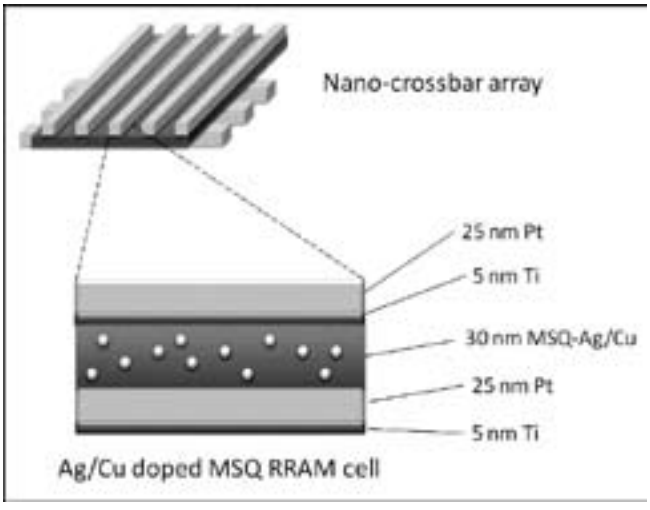

Figure 1: Diagram depicting the device structure and integration in a nano-crossbar array.

The device structure (Figure 1) was fabricated with junction areas ranging from 1 μm^2 to 150 μm^2 using standard micro-fabrication techniques. Both the top and bottom electrodes were deposited by sputtering 5 nm Ti and 25 nm Pt, and then patterned using photolithography. Prior to the fabrication of the top electrodes, the MSQ film was doped by first depositing 15 nm of either Ag or Cu and then diffusing the metal by annealing the sample at temperatures of 450, 500, 550, and 600°C for 20 minutes for each of the samples and their respective dopant.

Electrical characterization was carried out using an Agilent B1500 semiconductor. The analyzer was programmed to test the devices by repeatedly switching them and measuring the resistances as well as their I(V) response during switching. Each device was switched a total of 100 times and the results were compiled to show the effect of device performance due to doping concentration. Figures 2 and 3 show the I(V) characteristics of the Ag doped samples for the turn on and turn off voltage sweeps, respectively.

The devices were first switched on by sweeping the voltage from 0 to 2 V and back. Between 0.25 and 0.75 V, a filament was formed and the cell entered a low resistance state. During switching the current was limited to a maximum of 250 μA to prevent the immediate destruction of the filament due to joule heating. To check that the filament was stable, a small forward bias of 10 mV was applied while the leakage current was measured. The device was then switched off by sweeping the voltage from 0 to 5V with no current limit, and the resistance was checked again.

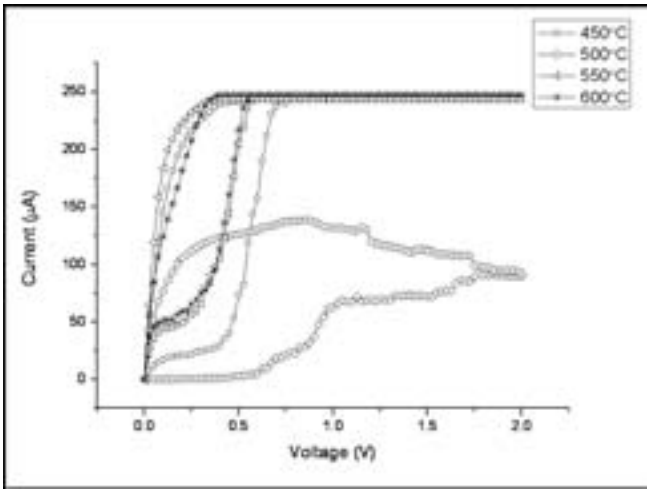

Figure 2: I(V) curves for the various Ag doped MSQ devices showing the switch from high to low resistance states.

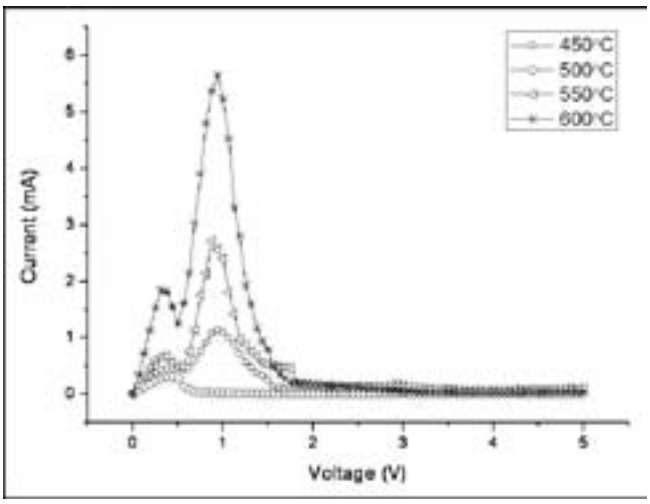

Figure 3: I(V) curves showing the switch from low to high resistance states.

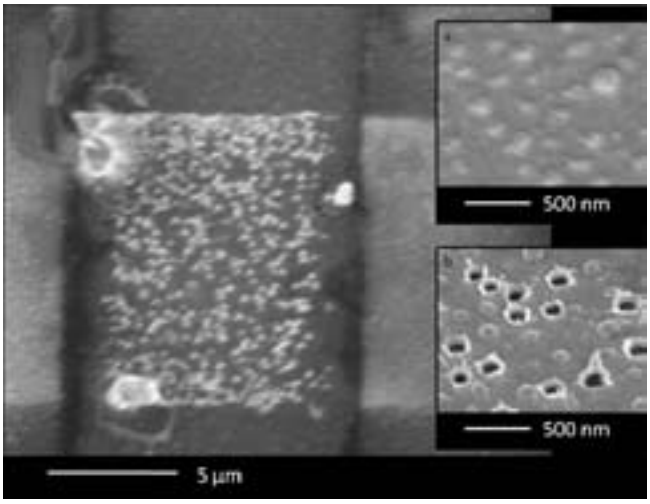

Figure 4: SEM images showing in situ switching and destruction of a device.

In addition to the repeated sweep measurements used to investigate the switching characteristics and device reliability, scanning electron microscopy (SEM) was performed while switching a device *in situ* in order to directly observe the switching effects.

Figure 4 shows an image from this experiment, where the filament breaking points can be seen as bright spots in the center of the junction. The insets show images of the top electrode at a 45° viewing angle before (a) and after (b) the device was damaged from high currents.

Results and Future Work:

Of the devices tested, only those doped with Ag showed consistent switching from less than 1 kΩ to greater than 1 MΩ. Measurements taken on the Cu doped devices indicated that the samples were under-doped. Further work will need to be done to determine whether or not Cu can be used as an effective dopant.

Comparisons were also made between Ag doped devices with different junction areas in order to observe potential scaling effects, showing a decrease in the required erase current with area. This fact, combined with an endurance test resulting in over 3000 successful on/off cycles before failure, are a strong indicator that Ag doped MSQ resistive switching devices are a promising candidate for future memory applications.

Acknowledgements:

Thanks to Dr. Carsten Kügeler, Prof. Rainer Waser, and Roland Rosezin for an interesting project in an exciting field of research. Also, thanks to Robert Weng and Rohit Soni for meaningful discussions and advice. I would also like to thank Dr. Rathbun, the NSF, and NNIN iREU Program for supporting this work, as well as everyone at the Forschungszentrum Jülich for a great experience.

References:

[1] Waser, R, Aono, M; Nature Materials 6, 833-840 (2007).
[2] Meier, M, et al.; Microelectronic Engr., 85(5-6), 870-872 (2008).
[3] Meier, M, et al.; IEEE Electron Device Letters, 30(1), 8-10 (2009).

Growth and Characterization of Graphene on Silicon Carbide

Julie Stiver

Chemical Engineering, University of Massachusetts, Amherst, MA

NNIN iREU Site: National Institute for Materials Science (NIMS), Tsukuba, Ibaraki, Japan

NNIN iREU Principal Investigator(s): Dr. Daisuke Fujita, Managing Director, Advanced Nano Characterization Center, NIMS

NNIN iREU Mentor(s): Dr. JianHua Gao, Advanced Scanning Probe Microscopy Group, NIMS

Contact: julstiver@gmail.com, FUJITA.Daisuke@nims.go.jp, GAO.Jian-Hua@nims.go.jp

Abstract:

Epitaxial graphene layers were fabricated by thermal decomposition of silicon (Si)-terminated ^{4}H-SiC(0001) in ultrahigh vacuum (UHV) at different temperatures. Raman spectra and Auger electron spectra show that graphene layers can form after annealing at 1300°C, and a heating recipe should be optimized between 1300°C and 1400°C. Scanning tunneling microscope (STM) images reveal Moiré patterns in our multi-layer graphene providing evidence of a rotated phase in which individual layers are electronically decoupled.

Introduction:

Graphene, a single monolayer of sp^2-bonded carbon atoms, has recently attracted much attention due to its novel quantum electrodynamic properties [1] and the potential of carbon-based electronics [2]. Due to a linear dispersion of energy at the constant (κ)-point, graphene's charge carriers behave as fermions with zero rest mass and mimic relativistic particles described by the Dirac equation. Graphene is a zero-gap semiconductor with charge carriers that travel ballistically through the two-dimensional material and is stable under ambient conditions [3]. However, large-scale growth of high quality graphene for both bench-top experiments and carbon-based device engineering presents a challenge. Mechanical exfoliation of HOPG produces the highest quality graphene but is not scalable [2]. Other growth methods include chemical vapor deposition [4], surface segregation of carbon doped metals [5], and thermal decomposition of silicon carbide (SiC) [6]. The latter is attractive because SiC can be integrated into silicon technology. Additionally, multi-layer graphene grown on the carbon face of ^{4}H-SiC has been shown to retain the electrical properties of a single sheet of graphene as adjacent layers are rotated and electronically decoupled [7]. Here we present preliminary work optimizing a heating procedure for graphene growth via thermal decomposition of Si-terminated ^{4}H-SiC(0001) as well as evidence that multi-layer graphene grown by our method exists as a rotated phase and may behave like a single sheet of graphene.

Experimental Procedure:

^{4}H-SiC(0001) samples roughly 1 mm × 8 mm in size were cut using a diamond scribe and cleaned ultrasonically with ethanol and acetone. The samples were heated individually in a UHV (base pressure 10^{-11} mbar) preparation chamber. At high temperature, silicon atoms sublimate from the SiC surface and the remaining carbon atoms are left to rearrange and form graphene. Samples were heated at intervals between 1150°C and 1600°C for different lengths of time. STM and atomic force microscopy (AFM) measurements were taken at room temperature in UHV. Electrochemically etched tungsten STM probes were argon sputtered for 15 minutes and used throughout. *In situ* field evaporation was used to further clean the tip apex. AES measurements were performed at room temperature with a scanning Auger microscope (ULVAC-PHI model SAM680) with a cylindrical mirror analyzer. AES spectra were recorded with a primary electron beam of 10.0 kV. Differential dN(E)/dE Auger spectra were obtained by numerical derivation of raw N(E) integrated Auger data by Savitzky-Golay differential filter using five points. Raman spectra were recorded by Raman microscope (JY-6400) at room temperature. The Ar ion laser of 532 nm was used as the excitation source with the laser power 100 mW.

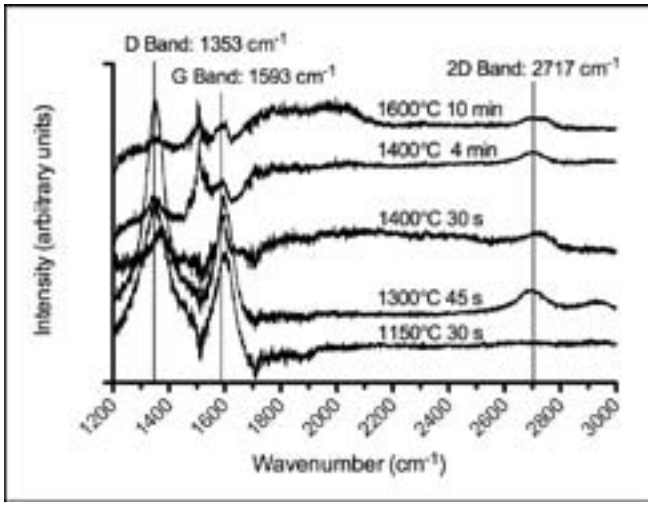

Figure 1: Normalized Raman spectra of five samples corrected by subtracting the substrate (SiC) spectra.

Results and Discussion:

Figure 1 shows the Raman spectra for ^{4}H-SiC(0001) surfaces after annealing at different temperatures. Three distinct peaks in the Raman spectra are characteristic of graphene: the defect-induced D band (~ 1353 cm^{-1}), the in-plane vibrational G band (~ 1593 cm^{-1}), and the two-phonon 2D band (~ 2717 cm^{-1}) [8].

Each of these peaks was clearly visible in all our samples with the exception of the 2D band in the 1150°C sample (Figure 1). This indicated that 1150°C was not sufficiently high a temperature for graphene growth. The defect-induced D band peak at 1353 cm^{-1} was very strong in the spectra of samples grown below 1400°C. This indicated that edge state characteristics dominated in samples heated below 1400°C because of small grapheme domains. Above 1400°C the spectra showed undesirable features. We concluded from this Raman analysis that 1400°C for a short time was a good temperature around which to optimize the heating procedure.

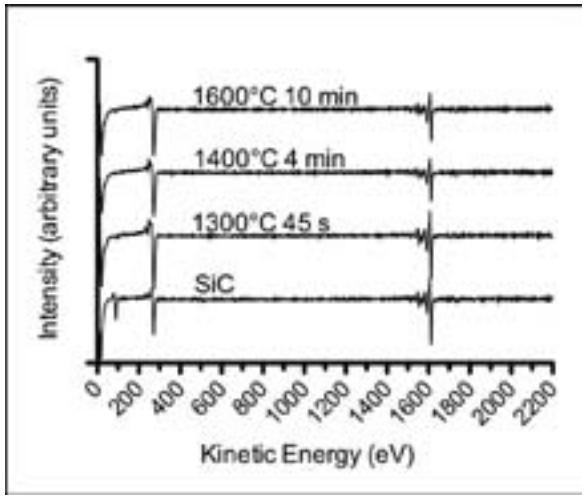

Figure 2: Differential Auger spectra for three samples and substrate.

Auger electron spectroscopy provided additional macro-scopic information about the surface. Figure 2 shows the differential Auger spectra for four samples annealed at different temperatures and the SiC surface. The spectra were characterized by three peaks: a low-energy Si LVV peak at 84 eV, a high energy Si KLL peak at 1610 eV, and a C KLL peak at 265 eV. The mean free paths of the Si LVV and the Si KLL peaks were approximately 0.5 and 2.4 to 3.0 nm respectively [9]. We concluded from the decreased Si LVV peak intensity that at 1300°C the carbon concentration had already increased on the surface and optimization of a heating procedure should begin around this temperature. The increase in background noise of the Si KLL peak as well as the relative C KLL and Si KLL peak intensities indicated increased carbon concentration at higher temperatures, as we expected.

STM images from as-received SiC following graphitization at 1400°C for 1 minute are shown in Figures 3 and 4. Individual graphene layers and islands are distinguishable in Figure 3. There were a large number of defects including carbon nanotubes which were found growing simultaneous with graphene layers. Figure 4 shows an atomic resolution image with a Moiré pattern which indicated that the top layer of graphene was rotated with respect to the layer below it; evidence that individual layers were electronically decoupled.

Future Work:

A heating recipe for graphene on ^{4}H-SiC(0001) should be optimized between 1300°C and 1400°C. A pre-heating hydrogen-etch to remove scratches from commercial polishing may be necessary. STM images should be taken at regular temperature intervals to establish a better understanding of the growth mechanism.

Acknowledgements:

I thank Dr. Daisuke Fujita, Dr. JianHua Gao, and Dr. Keisuke Sagisaka for their time and valuable discussions. Support for this research from NSF through the NNIN International REU Program and the National Institute of Materials Science is also gratefully acknowledged.

References:

[1] A. H. Castro Neto et al., Rev. Mod. Phys. 81, 109 (2009).
[2] A. K. Geim and K. S. Novoselov. Nature Materials. 6, 183 (2007).
[3] K. S. Novoselov et al., Nature. 438, 197 (2005).
[4] A. Reina et al., Nano Lett. 9, 30 (2009).
[5] D. Fujita et al., Surf. Sci. 566, 361 (2004).
[6] D. L. Miller et al., Science. 324, 924 (2009).
[7] J. Hass et al., Phys. Rev. Lett. 100, 125504 (2008).
[8] Z. H. Ni et al., Phys. Rev. B 77, 115416 (2008).
[9] M. Suleman and Salah-Ud-Din. J. Mat. Sci. Lett. 5, 1285 (1986).

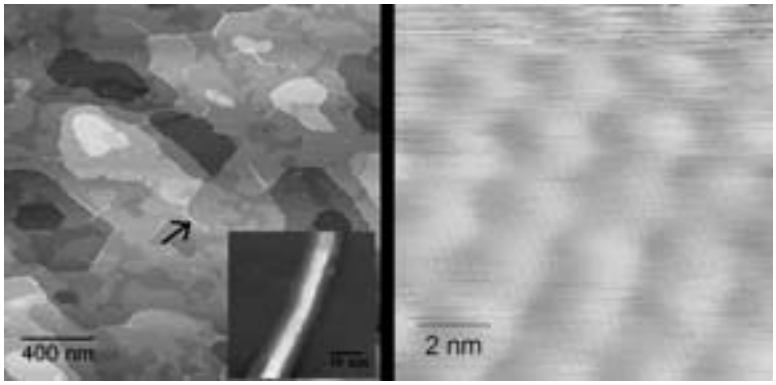

Figure 3, left: STM image of sample heated to 1400°C for one minute. Features similar to the one indicated by arrow are carbon nanotubes. Inset: UHV AFM image of a bundle of carbon nanotubes.

Figure 4, right: STM image of sample heated to 1400°C for one minute. The Moiré pattern is evident.

Study on Structural and Electronic Properties of Heavily Al-Doped Zinc Oxide Thin Films Deposited by Pulsed Laser Deposition

Arun Swain

Electrical and Computer Engineering, Cornell University, Ithaca, NY

NNIN iREU Site: National Institute for Materials Science (NIMS), Tsukuba, Ibaraki, Japan

NNIN iREU Principal Investigator(s): Dr. Naoki Ohashi, Optoelectronics Group, NIMS, Tsukuba, Japan

NNIN iREU Mentor(s): Dr. Yukata Adachi, Optoelectronics Group, NIMS, Tsukuba, Japan

Contact: aps97@cornell.edu, ohashi.naoki@nims.go.jp, adachi.yutaka@nims.go.jp

Abstract:

As zinc oxide (ZnO) crystallizes into a wurtzite structure, it exhibits spontaneous polarization due to the creation of inherent zinc terminated and oxygen terminated faces. The zinc terminated face is much more chemically stable than its oxygen terminated face. This research investigates the effect of aluminum (Al)-doping and deposition rate of ZnO thin films on (11$\bar{2}$0) sapphire substrates on the polarity and the electronic properties of the film. It is reported that Al-doping with a faster deposition rate creates a zinc terminated surface. A faster deposition rate also increases carrier concentration and optical bandgap for all samples.

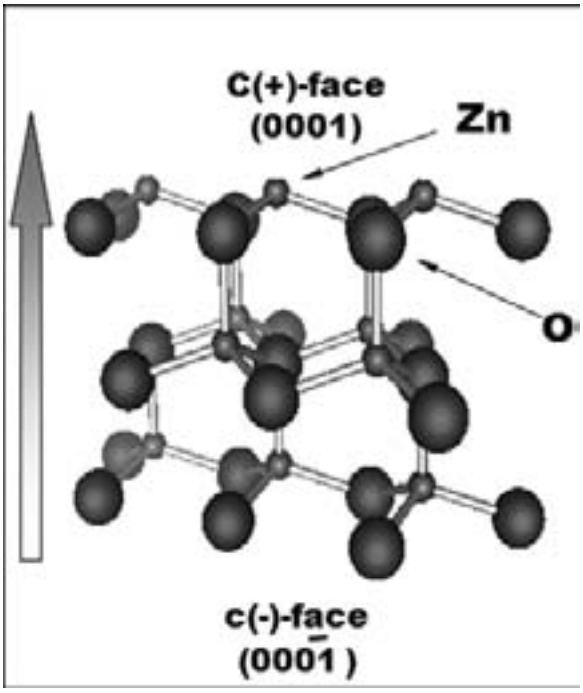

Figure 1: Crystal structure of zinc oxide.

Introduction:

Zinc oxide is a wide bandgap (3.37 eV at room temperature) semiconductor with high exciton binding energy (60 meV). Since these properties are very similar to those of gallium nitride, ZnO has been considered to be an appropriate material for light emitting diodes, which allows for bright room temperature light emission. As zinc oxide crystallizes into a hexagonal wurtzite type crystal (Figure 1), it inherently forms a (0001) zinc terminated surface or an (000$\bar{1}$) oxygen terminated surface. The zinc face is much more chemically stable and hence desirable for device applications. Under ordinary deposition methods, undoped zinc oxide has an (000$\bar{1}$) oxygen terminated surface [1]. However, it has been reported [2] that Al-doping allows for a zinc terminated surface. In this study, the effects of Al-doping and deposition rate on the electronic and structural properties of ZnO thin films will be investigated. By varying deposition rates of thin films, the surface polar orientation will be examined.

Experimental Procedure:

Four crystalline thin film samples—two 0.1 mol% Al-doped ZnO and two pure ZnO thin films—were prepared using a multi-step process. Thin films were deposited on (11$\bar{2}$0) sapphire substrates using pulsed laser deposition (PLD) at 700°C in an ultrahigh vacuum below 10^{-7} Pa. To make targets for the PLD process, ZnO and Al-doped ZnO (AZO) powders were pelletized using a hydraulic press and sintered at 1000°C for 20 hours. The (11$\bar{2}$0) sapphire substrates were cleaned in ultrasonic baths of acetone and ethylene and subsequently washed with deionized water. A pulsed laser of Nd: YAG laser (λ = 266 nm) was used at two different frequencies (10 Hz and 50 Hz) to vary deposition rate. In order to maintain equal film thickness (~ 500 nm), films were grown for 30 minutes with the 50 Hz laser and for 3 hours with the slower 10 Hz laser.

Upon film growth, electronic properties were characterized by Hall effect and transmittance measurements, while x-ray diffraction (XRD) and x-ray photoelectron spectroscopy (XPS) measured the films' structural properties.

Thin Film	Deposition Rate (nm/hr)	Laser Power (Watt)	Carrier Concentration (cm^{-3})	Optical Bandgap (eV)	Type
Pure ZnO	150	1	2.05E+16	3.33	N
Pure ZnO	690	5	2.86E+16	3.34	N
0.1 mol % Al doped ZnO	125	1	3.95E+19	3.42	N
0.1 mol % Al doped ZnO	625	5	7.24E+19	3.47	N

Table 1: Growth parameters and electronic and optical properties of doped and undoped zinc oxide thin films.

Results and Conclusion:

XRD results confirmed that all the films, regardless of doping or deposition rate, were c-axis oriented. Transmittance measurements showed that Al-doping increased the optical bandgap as listed in Table 1. Since Al-doping increases the carrier concentration in the conduction band, the optical bandgap energy increases. Hence, it was concluded that aluminum was successfully doped in the AZO thin films. Hall measurements confirmed that the AZO samples had a carrier concentration three orders of magnitude higher than the undoped ZnO samples as listed in Table 1. This further indicates that Al was successfully doped into the AZO thin films since Al has a higher carrier concentration than that of undoped ZnO.

Hall effect and transmittance measurements showed that the AZO films with a faster deposition rate had a higher carrier concentration and optical bandgap than the AZO films with a slower deposition rate as shown in Table 1. The solubility limit [3] of Al in ZnO at 800°C is 1×10^{-19} cm^{-3}. An Al concentration of 1×10^{-20} cm^{-3} indicates a complete non-equilibrium state. In a complete non-equilibrium state, Al dopants tend to react with the oxygen to form Al_2O_3 (sapphire) to return to a more equilibrium state. This is a probable explanation of the phenomenon active in these samples. The slower deposited thin films got more time for the Al dopants to condense into the sapphire substrate than the faster deposited AZO films. Hence the Al concentration in the faster deposited AZO film was higher than in the slower deposited AZO film. Since the optical bandgap is a function of the carrier concentration, it also increases with a faster deposition rate.

In this investigation, angle resolved XPS (AR-XPS) was employed to observe crystalline polarity. XPS is useful to determine the surface elemental composition and the surface chemical and electronic state of elements of an object. By varying take-off angles (tilt and rotation angles of the sample with respect to the electron energy analyzer direction), AR-XPS profiles were obtained. In particular, we obtained a tilt and rotation angle dependency of the relative intensity ratio between Zn 2p and O 1s peaks. Measuring both sides (oxygen-terminated and zinc-terminated surface) of a single crystalline ZnO crystal, a characteristic tilt angle was found which had high zinc to oxygen ratio for the zinc terminated surface and a very low zinc to oxygen ratio for an oxygen terminated surface. Note that etching the single crystal ZnO sample with nitric acid confirmed the results of the XPS data.

XPS measurements of the faster grown AZO sample showed a higher intensity ratio of zinc peaks to oxygen peaks near the previously determined optimum tilt angle as shown in Figure 2(a). Thus it was concluded that the faster grown AZO sample was zinc-terminated. However, no conclusive data on polarity could be observed for the slower grown AZO thin film (Figure 2(b)). This could be due to the fact that several crystals in the AZO thin film had mixed polarity with some grains being zinc terminated and others being oxygen terminated. Another possibility is that perhaps a different tilt angle is required to get more acute zinc and oxygen ratios from the XPS measurements.

Future Work:

The next steps are to conduct XPS measurements at several more tilt angles for the AZO samples. Also, growing more AZO thin film samples at various other deposition rates could also confirm the effect of deposition rate on polarity.

Acknowledgments:

Funding for this research has been provided by the National Nanotechnology Infrastructure Network iREU Program, the National Science Foundation and the National Institute of Materials Science. I would like to thank my PI, Dr. Naoki Ohashi, and my mentor, Dr. Yukata Adachi, for their guidance and informative discussions.

References:

[1] Ohnishi, T, et al; "Determination of surface polarity of c-axis oriented ZnO films by coaxial impact-collision ion scattering spectroscopy"; Applied Physics Letters, Vol. 72, No. 7 (1998).

[2] Adachi, Y, et al; "Change in polarity of zinc oxide films grown on sapphire substrates without insertion of any buffer layer"; Journal of Materials Research, Vol. 23, No. 12 (2008).

[3] J. Kobayashi, et al; "Properties of gallium- and aluminum-doped bulk ZnO obtained from single-crystals grown by liquid phase epitaxy"; Journal of Crystal Growth Vol. 311, No. 19 (2009).

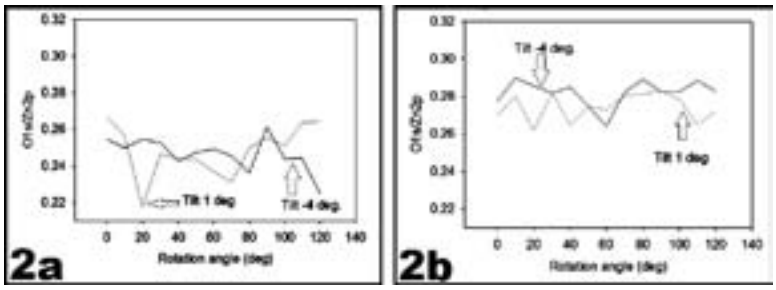

Figure 2: Relative x-ray photoelectron spectroscopy peak intensity ratio between Zn 2p and O 1s for various tilt and rotation angles of (a) the faster grown AZO film and (b) slower grown aluminum doped zinc oxide film.

Detection of DNA Hybridization Using a Field-Effect Device

Justine Yoon

Biomedical Engineering, Rensselaer Polytechnic Institute

NNIN iREU Site: National Institute for Materials Science (NIMS), Tsukuba, Ibaraki, Japan
NNIN iREU Principal Investigator(s): Dr. Yuji Miyahara, Biomaterial Systems Group, NIMS
NNIN iREU Mentor(s): Dr. Chiho Kataoka, Biomaterial Systems Group, National Institute for Materials Science
Contact: justine.yoon@gmail.com, miyahara.yuji@nims.go.jp, kataoka.chiho@nims.go.jp

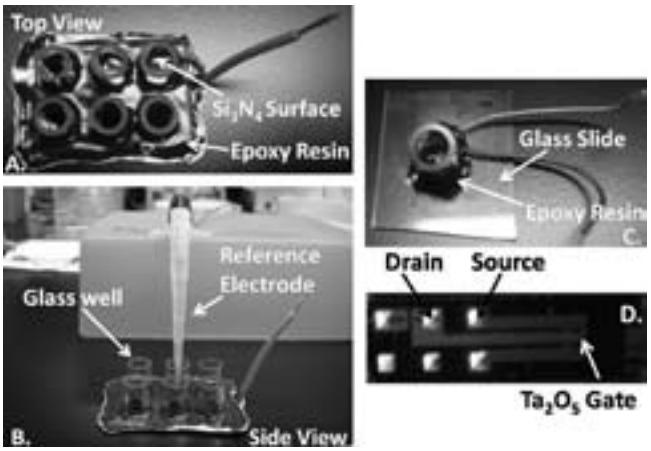

Figure 1: (A) Top view and (B) Side view of capacitive device. (C) Top view of FET. (D) Transistor used.

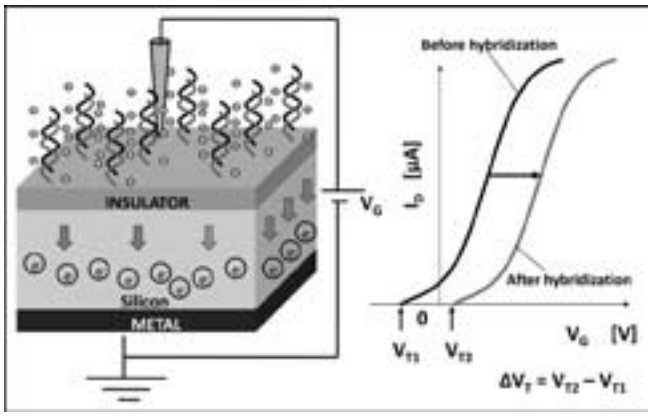

Figure 2: Concept of field-effect devices.

Abstract and Introduction:

In this study, two field-effect devices, a capacitive device with a silicon nitride (Si_3N_4) surface (Figures 1A, 1B) and a field-effect transistor (FET) with a tantalum oxide (Ta_2O_5) gate (Figures 1C, 1D) were fabricated to detect deoxyribonucleic acid (DNA) hybridization by taking potentiometric measurements using the intrinsic charge in DNA. DNA hybridization biosensors, which utilize bio-recognition between two single-stranded complementary DNA, can be used for genetic testing, clinical diagnosis, and forensic science.

The surface of each device was treated with poly(2-meth acryloyloxyethylphosphorylcholine-co-3-methacryloxy-propyltrimethoxysilane) (PMSi) to increase the charge density at the surface of the gate, 3-aminotriethoxysilane (APTES) to introduce a reactive amino group, and gluta-raldehyde to act as a bifunctional cross-linking agent [1]. Next, DNA was immobilized at the surface, and treated with glycine to block any free aldehyde groups. Contact angles were taken after every modification to ensure that the surface had been uniformly coated.

A reference electrode was used to control and fix the potential of a measurement solution and gate voltage [1]. When DNA molecules adsorb onto the surface of an insulator, electrons in the silicon substrate electrostatically interact with the immobilized DNA, affecting the electrical characteristics of the field-effect device [2]. Detection of hybridization is indicated as a shift in the flat-band voltage (V_{FB}) for the capacitive device, and a shift in interface potential (V_T) for the FET due to the increased charge density (Figure 2). Results show that the capacitive device was not sensitive enough to detect hybridization; however, the FET showed a significant shift in interface potential, successfully detecting DNA hybridization.

Experimental Procedure:

Device Fabrication. The Si_3N_4 surface of the capacitive device was washed in acetone, ethanol and water, and dried with nitrogen (N_2) gas. Six glass wells were attached to the surface using epoxy resin and baked at 120°C for 30 minutes. A wire was attached to the bottom of the device using silver paste and covered in aluminum foil. The remaining Si_3N_4 surface was covered with epoxy resin and baked for 2 hours.

The FET was fabricated using a transistor with a Ta_2O_5 gate adhered to a glass slide. Two wires were connected to the source and drain of the transistor using silver paste. A glass well was attached over the gate of the transistor. The rest of the transistor was covered with epoxy resin and baked for two hours at 120°C.

Immobilization and Hybridization of DNA. The chambers were immersed in 0.02 wt% of PMSi in ethanol for 30 minutes, dried in an ethanol atmosphere for 24 hours, and incubated at 120°C in a vacuum for one hour. Next, they were filled with 2 v/v% APTES in ethanol for 24 hours and incubated for another hour.

The chambers were then filled with 25 wt% glutaraldehyde containing 0.01 g/mL sodium cyanoborohydride ($NaBH_3CN$) for three hours. Overnight, 100 μM probe DNA in TE buffer, containing 0.01 g/mL $NaBH_3CN$, was incubated in each chamber at 50°C. Finally, chambers were incubated at 50°C for one hour with 1M glycine in TE buffer.

The probe was then hybridized with 100 μM of target DNA in 4 × SSC, 0.1% SDS buffer and incubated at room temperature for one hour.

Measurements. Contact angles were taken after each surface modification using the Kyowa Dropmaster and FAMAS software. To observe the changes in electrical characteristics, the reference electrode was submerged in the chamber solution (pH 6.86 standard).

For the capacitive device, an Agilent Precision Impedance Analyzer was used to take capacitance-voltage measurements from -5 to 3 volts. The V_{FB} was interpolated from the data at a capacitance ratio of 0.57. This predetermined value is dependent on the thickness of the insulator, carrier density, and dielectric constant of the semiconductor [3].

For the FET, a lab-developed transistor measurement system was used to measure V_T. The source-drain current was kept constant. Measurements were taken before and after hybridization, and ΔV was determined for both devices.

A. Surface Contact Angles:

Surface treatment	Contact Angle
Si_3N_4	11.6°
PMSi	41.1°
APTES	57.1°

B. ΔV_{FB} for Capacitive Device:

Trial	V_{FB} Before Hybridization (mV)	V_{FB} After Hybridization (mV)	ΔV_{FB} (mV)
Control	-668.92	-663.69	5.23
Trial 1	-608.75	-612.4	-3.65
Trial 2	-589.51	-592.98	-3.47

Table 1: (A) Contact angles after surface modification. Values are an average of six individual measurements. (B) ΔV_{FB} is the difference in V_{FB} before and after DNA hybridization.

Results and Conclusions:

Results from measurements are tabulated in Table 1. The changes in contact angle confirm that the surface had been modified. (Table 1A)

The results for the capacitive device were inconclusive because of the low, negative shift of ΔV_{FB}. ΔV_{FB} should be in the positive direction (Table 1B). This could be due to experimental error, or because the DNA had not immobilized on the surface. However, there was a significant negative

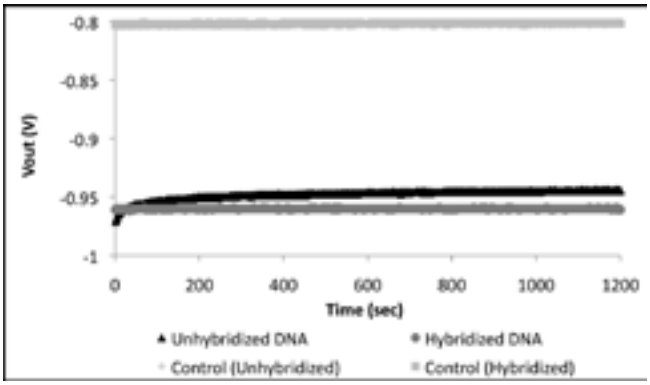

Figure 3: Time course of interface potential before and after DNA hybridization.

shift of -15 mV in V_T for the FET, while the control remained constant at -0.802 mV (Figure 3). This significant negative shift confirmed the hybridization of DNA due to the increased negative charge at the gate's surface.

Future Work:

Ta_2O_5 surfaces are rougher than Si_3N_4 surfaces and could have contributed to the unsuccessful immobilization of DNA on the silicon nitride surface. Future work could involve taking measurements regarding the surface roughness and its effects, as well as the reproducibility of the results taken from the FET device.

Acknowledgments:

The author acknowledges Dr. Yuji Miyahara, Dr. Chiho Kataoka and everyone in the Biomaterial Systems Group for giving her the opportunity to work in their lab and their helpful discussions. She also acknowledges the National Institute for Materials Science, National Nanotechnology Infrastructure Network International Research Experience for Undergraduates Program and National Science Foundation for funding this project.

References:

[1] Sakata, T., Kamahori, M., and Miyahara, Y.; "DNA analysis chip based on field-effect transistors"; Japanese Journal of Applied Physics, 44, 2854-2859 (2005).

[2] Miyahara, Y., Sakata, T., and Matsumoto, A.; "Microbial genetic analysis based on field effect transistors"; Principles of Bacterial Detection: Biosensors, Recognition Receptors and Microsystems, 311-337 (2008).

[3] Kataoka-Hamai, C., Inoue, H., and Miyahara, Y.; "Detection of supported lipid bilayers using their electric charge"; Langmuir, 24, 9916-9920 (2008).

Index

2009 NNIN REU & iREU Reports by Site

Index

2009 NNIN REU & iREU Interns, Mentors and Principal Investigators (Interns are in Bold)

H

I

J

K

L

M

N

O

The 2009 NNIN REU Research Accomplishments are also available online in PDF at: http://www.nnin.org/nnin_2009reu.html

Find information on all the NNIN REU Programs at: http://www.nnin.org/nnin_reu.html

P

R

S

T

V

W

X

Y

Z